Dissertation

submitted to the
Combined Faculty of Natural Sciences and Mathematics
of Heidelberg University, Germany
for the degree of
Doctor of Natural Sciences

Put forward by
Steffen Kühn, M. Sc.
born in Worms
Oral examination: 21. July 2021

High-precision soft X-ray transition measurements of neon-like mid-Z ions using ultra monochromatic synchrotron radiation

Referees:
apl. Prof. José Ramón Crespo López-Urrutia
Prof. Dr. André Butz

High-precision soft X-ray transition measurements of neon-like mid-Z ions using ultra monochromatic synchrotron radiation

For more than 40 years, most astrophysical observations and laboratory studies of two key soft X-ray diagnostic $2p$-$3d$ transitions, 3C and 3D, in Fe XVII ions found oscillator-strength ratios $f_{3\mathrm{C}}/f_{3\mathrm{D}}$ disagreeing with theory. This discrepancy hampered the proposed plasma diagnostic utility based on the observed intensity ratios ever since. In previous laboratory measurements, the ratio was determined by scrutinizing the photon emission of an electron-impact excited plasma. First X-ray laser spectroscopy experiments at a free-electron laser (FEL) confirmed the discrepancy between experiments and theory independently of electron-excitation cross sections that could have falsified previous laboratory measurements. In this thesis, the 3C/3D oscillator-strength ratio was measured by resonantly exciting the transitions utilizing highly brilliant and monochromatic X-ray synchrotron light. Thereby, two proposed systematical effects that could have lowered the results of the FEL measurements were excluded. The final result $f_{3\mathrm{C}}/f_{3\mathrm{D}} = 3.51(7)$ of this work is in excellent agreement with the newest state-of-the-art theoretical predictions and appears to finally resolve the long-lasting conundrum. Additionally, for the first time, the individual natural linewidths of lines 3C and 3D, among others, were determined with an uncertainty of $\approx 15\%$. The findings of this thesis now allow the observed intensity ratios of 3C and 3D to enable their usefulness in the diagnostics of astrophysical spectra.

Hochpräzise Messungen weicher Röntgenübergänge in neon-artigen Ionen mittlerer Ordnungszahl mit ultramonochromatischer Synchrotronstrahlung

Seit mehr als 40 Jahren weisen die Mehrzahl astrophysikalischer Beobachtungen und Labormessungen des Oszillatorstärkenverhältnisses zweier $2p$-$3d$ Schlüsselübergänge names 3C und 3D in Fe XVII Ionen Werte auf, die im Widerspruch zu theoretischen Modellen stehen. Seitdem beeinträchtigt diese Diskrepanz die vorgeschlagene Plasmadiagnose auf der Grundlage der beobachteten Intensitätsverhältnisse. In früheren Labormessungen wurde das Verhältnis durch Untersuchung der Photonenemission eines durch Elektronenstöße angeregten Plasmas bestimmt. Erste Röntgen Laserspektroskopie-Experimente an einem Freien-Elektronen-Laser (FEL) bestätigten die Diskrepanz zwischen Experiment und Theorie, unabhängig von den Elektronenanregungsquerschnitten, die frühere Labormessungen verfälscht haben könnten. In dieser Arbeit wurde das 3C/3D-Oszillatorstärkenverhältnis durch resonante Anregung der Übergänge mit hochbrillantem und monochromatischem Röntgensynchrotronlicht gemessen. Dadurch wurden zwei vorgeschlagene systematische Effekte, die die Ergebnisse der FEL-Messungen hätten verfälschen können, ausgeschlossen. Das Endergebnis $f_{3\mathrm{C}}/f_{3\mathrm{D}} = 3.51(7)$ dieser Arbeit ist in hervorragender Übereinstimmung mit den neuesten theoretischen Vorhersagen und scheint das jahrzehntelange Rätsel endgültig zu lösen. Zusätzlich wurden erstmals die individuellen natürlichen Linienbreiten u.a. der Linien 3C und 3D mit einer Messunsicherheit von $\approx 15\%$ bestimmt. Die Ergebnisse dieser Arbeit erlauben es nunmehr, die beobachteten Intensitätsverhältnisse von 3C und 3D für die Diagnostik von astrophysikalischen Spektren nutzbar zu machen.

Contents

1 Introduction **1**

2 Basics **7**

2.1 Atomic structure . . . 7
2.2 Highly charged ions . . . 10
2.3 Fundamental collision processes of electrons and photons with ions . . . 11
2.3.1 Ionization . . . 11
2.3.2 Recombination . . . 12
2.3.3 Excitation . . . 14
2.3.4 Deexcitation . . . 15
2.4 Methods for the calculation of the atomic structure . . . 21
2.4.1 Hartree-Fock method . . . 21
2.4.2 Configuration Interaction . . . 22
2.4.3 Multiconfiguration Dirac Hartree Fock . . . 22
2.4.4 Many Body Perturbation Theory . . . 22
2.5 Fe XVII and Fe XVI . . . 23

3 Electron beam ion traps **27**

3.1 Basics . . . 27
3.2 The PolarX-EBIT . . . 29
3.2.1 Magnetic system . . . 31
3.2.2 Vacuum system . . . 33
3.2.3 Off-axis electron gun . . . 33
3.2.4 Drift tubes . . . 38
3.2.5 Collector . . . 38
3.2.6 Injection system . . . 39
3.2.7 Detection of X-ray photons . . . 41

4 Synchrotron radiation **45**

4.1 Basics . . . 45
4.2 The variable polarization XUV beamline P04 . . . 50
4.2.1 Storage ring . . . 51
4.2.2 Undulator . . . 51
4.2.3 Monochromatization . . . 52
4.2.4 Diagnosis utilities . . . 58

5 **Measurements** **61**
- 5.1 Experimental setup & alignment 61
- 5.2 Data reduction 65
- 5.3 Campaign 2018 67
  - 5.3.1 Electron-impact excited photon spectrum & preparation of the target 67
  - 5.3.2 Estimation of the fluorescence strength 70
  - 5.3.3 First fluorescence signal of Fe XVII 70
  - 5.3.4 Measurements 71
    - Method 1: Scanning over the transition energy range of 3C & 3D 71
    - Method 2: Measurements of the fluorescence yield on maximum 79
    - Method 3: Scanning while alternating the photon shutter 80
  - 5.3.5 Summary 82
- 5.4 Campaign 2019 84
  - 5.4.1 Preparation of the target 84
  - 5.4.2 Measurements of 3C and 3D 85
  - 5.4.3 Lorentzian linewidths 87
  - 5.4.4 Measurements on Kr XXVI 88
  - 5.4.5 Summary 89
- 5.5 Campaign 2020 90
  - 5.5.1 Iron 91
    - Preparation of the target 91
    - Measurements of 3C, 3D, B, and C 92
    - Lorentzian linewidths 96
    - Measurements of 4C and 4D 97
  - 5.5.2 Measurements on Ni XIX 98
  - 5.5.3 Summary 99

6 **Discussion** **101**
- 6.1 Measurements on Fe XVII 101
  - 6.1.1 Oscillator-strength ratio of 3C and 3D 101
    - Polarization effects 112
    - Determination of the transition energies 112
    - Final 3C/3D oscillator-strength value 113
    - Comparison with other experiments and calculations 117
  - 6.1.2 Natural linewidths of 3C and 3D 121
  - 6.1.3 Natural linewidths of B and C of Fe XVI 130
  - 6.1.4 Oscillator-strength ratio of 4C and 4D 131
- 6.2 Measurements on Ni XIX 132
  - 6.2.1 Oscillator-strength ratio of 3C and 3D 132
  - 6.2.2 Natural linewidths of 3C and 3D 134

7 **Conclusion & outlook** **137**

A List of Publications of the Author 143

Bibliography 145

Acknowledgements 159

List of Abbreviations

APPLE II	Advanced Plane Polarized Light Emitter-II
BPM	Beam position monitor
CCD	Charge-coupled device
CI	Configuration interaction
CX	Charge exchance
DESY	Deutsches Elektronensynchrotron
DR	Dielectronic recombination
EBIS	Electron beam ion source
EBIT	Electron beam ion trap
FAC	Flexible atomic code
FEL	Free electron laser
FWHM	Full width at half maximum
HCI	Highly charged ion
HF-MoMo	High frequency movement monitor
LCLS	Linac Coherent Light Source
MBPT	Many body perturbation theory
MCDHF	Multiconfiguration Dirac Hartree Fock
MCP	Multi channel plate
MPIK	Max-Planck Insitute for Nuclear Physics
P04	The Variable Polarization XUV Beamline P04
PETRA	Positron-Electron Tandem Ring Accelerator
RF	Radiofrequency
RMU	Refocusing mirror unit
ROI	Region of interest
RR	Radiative recombination
SDD	Silicon drift detector
SMU	Switching mirror unit
SNR	Signal to noise
TMP	Turbomolecular pump
ToF	Time of flight
UHV	Ultra-high vacuum
UV	Ultraviolet
VLS	Variable line spacing
XUV	Extreme ultraviolet
YAG	Yttrium aluminium garnet

Chapter 1

Introduction

As early as the third century B.C., astronomical observations recorded in star catalogs on thousands of clay tablets enabled the Babylonians to determine with surprising precision, for example, the length of the synodic month or the orbital periods of planets such as Venus and Mars [172]. While this was primarily essential for sowing seeds and gathering the harvest, astronomy took on a much more fundamental scientific character from the 16th century onwards through Nicolaus Copernicus' work. With his publication „De revolutionibus orbium coelestium“ based on astronomical observations Copernicus presented, against the prevailing opinion, his heliocentric view of the world, which Johannes Kepler and Galileo Galilei subsequently confirmed [31, 6, 61]. Especially the invention of the telescope in 1609 improved the quality of astronomical research and helped to derive Kepler's laws of planetary motion [172].

While in the early days of astronomy only positions of stars were recorded, the field was changed fundamentally by Newton in the 17th century, who observed that sunlight entering a prism is split into its color components due to dispersion [3]. Measurements by Wollaston in 1802 and Fraunhofer in 1815, who observed dark lines in the spectrum of sunlight, see figure 1.1, were the origin of what is known today as spectroscopy [135]. The dark lines, also referred to as Fraunhofer lines, were the first observations of the quantized nature of light and initially remained unexplained. The spectral analysis of various salts burned on a gas burner, introduced by Bunsen and Kirchhoff in 1861, led to the conclusion that the Fraunhofer lines correspond precisely to the emission lines of sodium, magnesium, and iron, among others [93].

If the near-continuous spectrum emitted by the sun is considered, in which the Fraunhofer lines are observed, it is noticeable that the intensity profile follows that of a black body as introduced by Max Planck, see figure 1.1 [78]. For long wavelengths, this profile could already be well described in 1900 utilizing the Rayleigh–Jeans law [77]. However, the shorter the wavelength, the stronger the law predicted the intensity. For very short wavelengths, the intensity diverged. This contradiction, often referred to as the „ultraviolet catastrophe“ could be explained by introducing a quantization of light proposed by Max Planck. Planck's resulting radiation law allowed to deduce the surface temperature of the sun as 5770 K.

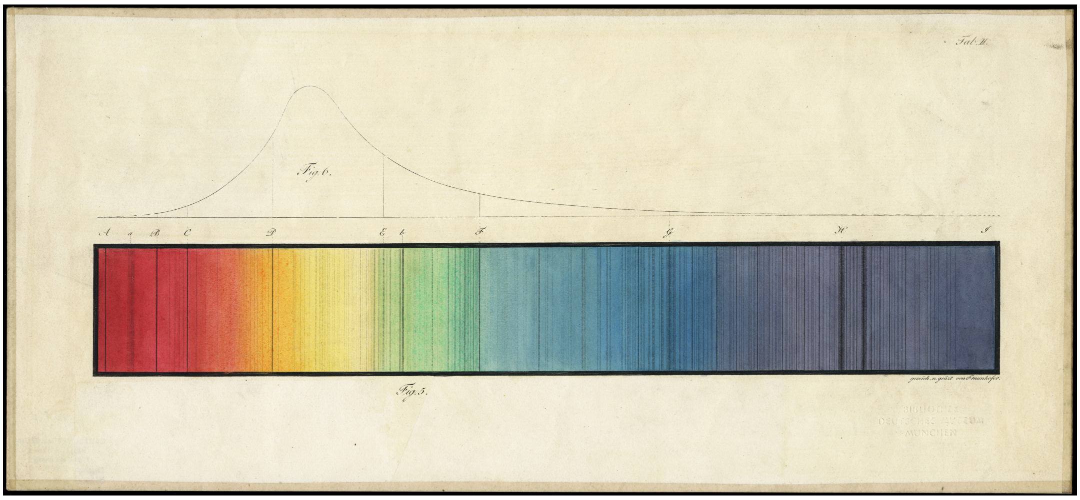

FIGURE 1.1: Picture of the sun emission spectrum published by Fraunhofer. The upper panel represents the observed intensity as a function of the individual colors. In the lower panel, the dark Fraunhofer lines are visible in the continuous spectrum emitted by the sun. Figure adopted from [48].

Today we know that the surface temperature of the sun is relatively low compared with heavier stars. Depending on the mass, surface temperatures of up to tens of thousands of Kelvin were observed for the heaviest stars exhibiting a mass larger than ten solar masses $M_\odot$. In such conditions, collisions between the atoms occur due to the high velocity at which energy is exchanged. The energy transfer is sufficient to excite electrons from one bound state to another. As the temperature rises, the exchanged energy increases and is eventually sufficient to overcome the coulomb force between the nucleus and weakly bound electrons and strip them from the shell. In extreme cases, the temperature reaches such high levels that most of the electrons are removed from the shell and hence, result in so-called highly charged ions (HCIs). The majority of visible matter in the universe, also called ordinary or baryonic matter, consists of stars, the intracluster medium and the recently found missing baryons in the warm-hot intergalactic medium, of which up to 99% occur in highly ionized states [124, 135].

Many strong transitions of HCIs are found in the ultraviolet (UV), extreme UV (XUV), soft X-ray, or hard X-ray regime [59]. Since the atmosphere of the Earth almost completely absorbs this energy range, purely terrestrial observations of various galactic source emission lines were no longer sufficient for astronomy. Therefore, first sounding rockets were launched in 1962, reaching altitudes above 100 km, and provided first X-ray observations of the extrasolar star Scorpius X-1 [20]. In the 70s sounding rockets were replaced by satellite-based observatories, such as Copernicus Observatory (1972) or Einstein Observatory (1978). Even though the spectrometers mounted on the satellites exhibited a rather poor efficiency and spatial resolution, they significantly contributed to the understanding of X-ray emission sources [114, 86, 71]. A major step was achieved in the 90s by combining X-ray observatories

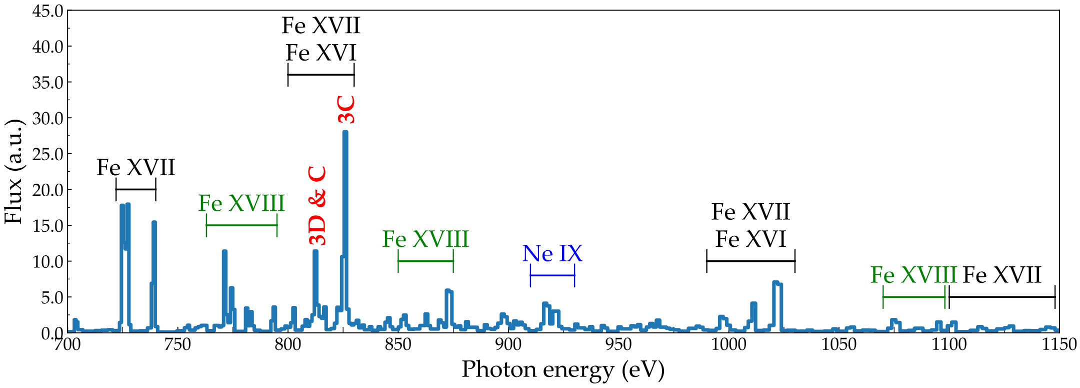

FIGURE 1.2: Soft X-ray observation of Capella using the High-Energy-Transmision Grating. The spectrum in the energy range between 700 and 1150 eV is completely dominated by transitions of highly charged iron. Observed line intensity ratio of the strong lines 3C and 3D at 825 and 812 eV, respectively, may serve as a plasma diagnosis. Additionally, strong lines of neon are also visible at roughly 920 eV. Weak, unmarked transitions arise from highly charged oxygen and nickel. Raw data adopted from [79].

and charged-coupled devices (CCDs), resulting in the still operating satellite missions XMM-Newton and Chandra [144, 87, 164, 148, 129]. The newest generation of space-based observatories, such as Hitomi (2016), XRISM (2022), and Athena (2030s) employ microcalorimeter detectors which greatly increase the resulting quality of X-ray spectral imaging [157, 158, 159, 130]. The continuous improvement of the data quality of satellite instruments places increasingly higher demands on experimental laboratory physics.

In order to keep providing reference measurements for astronomy, experimental laboratory physics is required to produce, store, and study matter in its extreme form of ionized plasma with highest accuracy. The first systematic spectral studies of HCIs were performed in the first half of the 20th century using high-voltage discharges in vacuum. The high-energy arc impinged on the material, causing it to become highly ionized and excited [160]. Further experimental developments resulted in storage rings and fusion reactors such as tokamaks, in which the ionized plasma can be stored by magnetic confinement or a combination of electrostatic and magnetic forces [4, 69]. Another compact possibility for the production and storage of HCIs are the so-called electron beam ion traps (EBITs), which play an essential role in this work [102].

Given the large number of existing lines of the various elements, each exhibiting several charge states, it is practically impossible to fill up a comprehensive reference database for astronomical observations. Therefore, one has to rely on theoretical models of physics, which have to be stringently benchmarked against experimental data. Here, laboratory measurements significantly help to improve the understanding of atomic physics and in direct comparison with theories, reveal limitations in the modeling of atoms and enable to estimate uncertainties.

A well-known example of benchmarking atomic physic theories by using laboratory measurements is found in 16-fold positively charged iron, often called neon-like iron because of the remaining ten electrons. In spectroscopy, the nomenclature starts with Fe I for neutral iron and increases the roman numeral by one for each additionally removed electron. For this reason, neon-like iron is also often referred to as Fe XVII. Owing to the large cosmic abundance of iron in combination with broad plasma temperature ranges in which Fe XVII can be found, this charge state often dominates emission spectra in the soft X-ray region between 700 and 1000 eV, see figure 1.2 [135, 8]. Here two $2p$-$3d$ transitions, namely the resonance line 3C ($[2p^6]_{J=0} \rightarrow [(2p^5)_{1/2}\, 3d_{3/2}]_{J=1}$) and the intercombination line 3D ($[2p^6]_{J=0} \rightarrow [(2p^5)_{3/2}\, 3d_{5/2}]_{J=1}$), are among the strongest lines to be observed.

Similar to the way Bunsen and Kirchhoff's measurements of the characteristic emission lines of various salts served to diagnose the elements present in the sun, the observed intensity ratio of 3C and 3D is proposed to serve as a diagnostic tool for properties of the observed plasma, such as temperature, density, or opacity [25]. However, from the beginning, the application of this diagnostic capability was limited, as even the first rocket-based measurements of the ratio in the solar spectrum in the 1970s showed a discrepancy between the observed values and the theoretical models [23]. Whereas astronomical observations gave a intensity ratio of $I_{3\mathrm{C}}/I_{3\mathrm{D}} = 2.7$, theories predicted much higher values of 4.0 and above [131]. Later, ratios of 1.8 to 3.2 were observed in spectra of the Sun and other X-ray sources by means of satellite-based missions [110, 22], which agreed with laboratory measurements using a tokamak (2.05-3.33) [11]. Systematic studies of the ratio using EBITs confirmed previous experimental results in the range of 2.77-3.04 [27, 24, 26]. In addition, the selection of the charge states present in the EBIT revealed that near the intercombination line 3D an additional strong line of sodium-like iron (Fe XVI) called C exists, which could not be resolved in the astronomical observations and the tokamak measurements. This additional line C could explain the large variance in the observed ratios since depending on the relative abundance of the Fe XVI charge state (also called charge-state distribution), the apparent intensity of 3D, and thus the 3C/3D intensity ratio, varies significantly.

Laboratory measurements using EBITs and tokamaks were based on electron-impact excitation, in which a variety of transitions are non-resonantly and simultaneously driven. Different cross sections for the excitation of 3C and 3D, nearby resonances or cascades from energetically higher electronic states excited by the electrons could have affected the measurements [34, 32, 107]. Consequently, the next step was to introduce a conceptually different measurement technique, namely laser spectroscopy, in which the ions are overlapped with photons and a transition is resonantly excited by photons with matching energy [156, 46]. By integrating the fluorescence intensity of both transitions as a function of laser energy, the amplitude ratio of 3C and 3D is obtained which is equal to the oscillator-strength ratio. It is important to note that laser spectroscopy directly measures the quantum dynamical observable of the transition probability excluding any dependence on, e.g., effective electron-excitation cross sections or cascades from higher states. Since the energies of both transitions 3C and 3D are found in the X-ray region, measurements of this kind require a photon source which offers a high photon flux intensity at the corresponding energies. Hence, first laser spectroscopy measurements of 3C and 3D were conducted utilizing a cryogenic EBIT at a so-called free-electron laser (FEL) [44, 52]. The result of these measurements showed a ratio of 2.65, which was again well below the latest state-of-the-art theoretical calculations predicting values of 3.5 and above [15, 14].

To solve the long-lasting discrepancy between experiments and theories, two explanations were introduced. First, it was postulated that the FEL intensity was sufficient to induce non-linear effects in the plasma, which could have led to a saturation of 3C and thus to a distorted result [126, 106]. Second, it was proposed that so-called population transfer mechanisms could have varied the charge-state distribution within the measurement [167]. The upper state of line C of Fe XVI exhibits a strong auto-ionizing decay channel to the ground state of 3D in Fe XVII. Since in the experiment the resolving power was insufficient to resolve the adjacent line C from 3D, both transitions were simultaneously driven by the X-ray laser. Due to the auto-ionizing nature of C, Fe XVI ions were resonantly pumped into Fe XVII and therefore increased the apparent intensity of 3D, potentially resulting in a falsified result.

In order to investigate the influence of both proposed effects and to further scrutinize the long-lasting discrepancy of the 3C/3D oscillator-strength ratio between experiments and theories, new laser spectroscopy measurements were urgently needed.

Within the scope of the this work, a transportable miniature EBIT was built based on previous work and optimized for measurements at X-ray light sources to remeasure the 3C/3D oscillator-strength ratio [119, 95]. In the experimental setup, major improvements were achieved primarily by commissioning and characterizing a novel electron gun. In contrast to conventional guns usually employed in EBITs, this so-called off-axis gun leaves the optical main axis of the experiment free of any obstacles. The resulting transparency allows to guide photon beams through the apparatus non-destructively, enabling the parasitical installation of the device at light sources.

The experiment called PolarX-EBIT, developed and built at the Max-Planck-Institut für Kernphysik in Heidelberg, was transported to the „Deutsches Elektronensynchrotron“ (DESY) in Hamburg and installed at the „Variable Polarization Soft X-Ray Beamline P04“ of the PETRA III storage ring. Compared to previous laser spectroscopy measurements at FELs, the resolving power of the experiments conducted within this work could be significantly improved, which enabled the investigation of the influence of possible population transfer mechanisms. In addition, the beamline P04 exhibited a significantly lower photon peak flux intensity compared to the FEL measurements. Therefore, the low photon flux excluded the influence of possible non-linear effects during the measurements. Beside the 3C/3D oscillator-strength ratio, the high resolution of the experiment enabled to determine the Lorentzian linewidths of the individual transitions. This offered a new testbed for benchmarking theories, since the linewidths directly probe the individual oscillator strengths and expose whether 3C, 3D or both transitions are the culprits in the available calculations that fail to model the experimental results hitherto reported.

Chapter 2

Basics

In this chapter, the basic concepts of atomic structure and fundamental collision processes of electrons and photons with ions required in this thesis will be briefly introduced. Subsequently, theoretical approaches to model atomic structure of multi-particle systems will be presented. The chapter ends with a summary of the investigated ion species Fe XVII scrutinized within this work. A more detailed elaboration of these topic beyond the scope of this thesis are found in various literature and textbooks, on whose content this chapter is based [46, 45, 70, 165, 135, 30].

2.1 Atomic structure

Schrödinger equation

In the classical picture, the hydrogen atom as the simplest assumed multi-particle system consists of a nucleus containing a proton and a neutron as well as an electron with mass m_e which moves in the central potential field around the nucleus. The nuclear charge Z in this simple example is determined by the charge of the proton, which has the same amount of positive charge as the negative elementary charge e of the electron. The classical equation of motion is given by

$$\frac{\vec{p}^2}{2m} - V\left(r\right) = E. \tag{2.1}$$

The potential field caused by the nucleus can be defined as follows

$$V\left(r\right) = -\frac{Ze^2}{4\pi\epsilon_0\left|\vec{r}\right|}, \tag{2.2}$$

where ϵ_0 corresponds to the permittivity of free space and $|\vec{r}|$ describes the distance between nucleus and electron. By replacing $\vec{p}$ and E in equation 2.1 with their quantum mechanical analogues $-i\hbar\nabla$ and $i\hbar\partial/\partial t$, respectively, the equation of motion in the Schrödinger form is obtained

$$\left[-\frac{\hbar^2}{2m}\left(\nabla^2\right) + V\left(r\right)\right]\Psi\left(\vec{r}\right) = E\Psi\left(\vec{r}\right). \tag{2.3}$$

By separating $\Psi(\vec{r})$ into a radial part $R_{nl}(r)$ and an angular part $Y_{lm}(\Theta, \Phi)$, the solution of the Schrödinger equation is be expressed as

$$\Psi(\vec{r}) = R_{nl}(r)\, Y_{lm}(\Theta, \Phi) \tag{2.4}$$

with the spherical harmonics Y_{lm} and

$$R_{nl} = D_{nl} \exp\left(-\frac{Zr}{na_0}\right)\left(\frac{2Zr}{na_0}\right)^{l} L_{n+l}^{2l+1}\left(\frac{2Zr}{na_0}\right) \tag{2.5}$$

with a normalization constant D_{nl}, the Laguerre polynomials L_{n+l}^{2l+1}, and a constant a_0 which can be interpreted as the quantum dynamical equivalent to the classic Bohr radius of the ground state.

Quantum numbers

The solution of the Schrödinger equation 2.4 of systems with one or several electrons depends on in total three quantization parameters. The principal quantum number $n = 1, 2, 3, ..., \infty$ represents the shell according to the classical atomic model by Bohr. Each shell consists of $l = 0, 1, 2, ..., (n-1)$ sub-shells, which are often referred to as the orbital quantum number. The sub-shells itself are further subdivided according to the magnetic quantum number m_l. The principle quantum numbers $n = 1, 2, 3, 4, 5, 6, ...$ are commonly labeled by capital roman letters: K, L, M, N, O, P, ... Each shell contains up to $2n^2$ electrons. If all available configurations nlm are fully occupied by electrons, the shell is often labeled as closed-shell, if vacancies are present they are commonly labeled as open-shell. The orbital quantum number are usually represented by alphabetic characters s, p, d, f, g, h, i, k, ... for $l = 0, 1, 2, 3, 4, 5, 6, 7, ...$. The total angular momentum L is expressed by similar capital characters $S, P, D, ...$. The angular momentum multiplicity of a multi-electron system is defined by $\sum_i m_i$ and exhibits $2L + 1$ possible values. In this non-relativistic approach the intrinsic spin of the electrons s is separately quantized. Similar to L, the associated spin quantum number S is defined as $S(S+1)\hbar^2$. The spin multiplicity LS of a state is given by $2S + 1$ and is labeled as singlet, doublet, triplet, ... for $LS = 1, 2, 3, ...$

Dirac equation

The wavefunction Ψ as the solution for the Schrödinger equation 2.4 holds true for non-relativistic systems with the absence of a magnetic field. The Lorentz-invariant single-particle Dirac equation extends the Schrödinger equation to describe the motion of a fermion, such as electrons, with spin $1/2$ and reads

$$\hat{H}\Psi = \left(\vec{\alpha} \cdot \vec{p}c + \beta mc^2\right)\Psi = E\Psi, \tag{2.6}$$

where $\vec{\alpha}$ and β are 4x4 matrices that fulfill the relation $\vec{\alpha}^2 = \vec{\beta}^2 = \mathbb{1}$. The resulting wavefunction Ψ becomes a four-component spinor

$$\Psi = \begin{pmatrix} \Psi_0 \\ \Psi_1 \\ \Psi_2 \\ \Psi_3 \end{pmatrix}. \tag{2.7}$$

The eigenvalues of the Hamilton operator in the Dirac equation 2.6 are given by

$$E = \pm\sqrt{c^2\vec{p} + m_0 c^4}. \tag{2.8}$$

Here, positive solutions correspond to eigenvalues of particles and negative solutions to their respective anti-particles. The Dirac equation may be modified to include external field effects and can be expressed as

$$\hat{H}\Psi = \left(\vec{\alpha}\cdot\vec{p}c + \beta mc^2 - \frac{Z\alpha}{|\vec{r}|}\right)\Psi = E\Psi, \tag{2.9}$$

with the Sommerfeld's fine-structure constant $\alpha = e^2/4\pi\epsilon_0 ch$. The Taylor expansion of equation 2.9 in terms of $Z\alpha$ results in the energy eigenvalues

$$E_{nj} = m_0 c^2 \left[1 - \frac{(Z\alpha)^2}{2n^2} - \frac{(Z\alpha)^4}{2n^3}\left(\frac{1}{j+1/2} - \frac{3}{4n}\right) + ...\right] \tag{2.10}$$

with the total angular momentum $j = l \pm 1/2$. The first term may be interpreted as the rest energy of the system. The second term represents the non-relativistic binding energy. The so-called fine structure is given by the third part of equation 2.10. The latter is caused mainly by the spin-orbit coupling j in addition to the relativistic mass changes of the electron. Further, the energy of the state must be corrected for quantum electrodynamical (QED) effects such as the Lamb shift, self energy of the electron, and vacuum polarization.

Multi-electron systems

In the case of multi-electron systems, the Coulomb interaction between the electrons must be taken into account. For neutral helium or helium-like ions, the Hamiltonian of the Schrödinger equation reads

$$\hat{H} = \frac{\hat{p}_1^2}{2m} + \frac{\hat{p}_2^2}{2m} - \frac{e^2 Z}{r_1} - \frac{e^2 Z}{r_2} + \frac{e^2}{|\vec{r}_1 - \vec{r}_2|}, \tag{2.11}$$

with the positions of the electrons $\vec{r}_i$ and the momentum operators $\hat{p}_i^2$. The multi-electron Hamiltonian for a system containing N electrons is defined as

$$\hat{H} = \sum_{i=1}^{N}\left(\frac{\hat{p}^2}{2m_e} + V(\vec{r}_i)\right) + \sum_{i<j}\frac{e^2}{|\vec{r}_i - \vec{r}_j|}. \tag{2.12}$$

Note that due to the electron-electron as well as the electron-nucleus interactions the Schrödinger equation of multi-electron systems cannot be solved analytically.

2.2 Highly charged ions

Definition of a highly charged ion

In general, an atom is ionized if bound electrons are removed from the system. With the removal of further electrons, so-called highly charged ions (HCIs) A^{q+} are produced. The limit, from which effective charge $q+$ an ion is considered as highly charged is not exactly defined to date. In common interpretations, the number of electrons to be removed varies between one and several dozen. For example, Gillaspy et al. [59] define a highly charged ion as an atom that has been stripped of a large number of electrons. Regardless of whether an ion is considered highly charged or not, the charge state of an ion can be described by different nomenclatures. A common approach denotes the charge state by the element that has the same number of electrons in its neutral state. For example, an oxygen atom that has had six electrons removed, leaving it with only two remaining bound electrons, is often referred to as helium-like oxygen. Alternatively, the same charge state can be described by the chemical element paired with the number of electrons removed O^{6+}. In spectroscopy, it is common to describe the charge state by increasing Roman numerals, with the neutral state represented by the numeral I. In this case, helium-like oxygen or O^{6+} translates to O VII.

Isoelectronic and isonuclear sequences

In general, each element with nuclear charge number Z provides a total of $Z + 1$ charge states from bare, i.e., all electrons were removed, to neutral. In principle, this results in 4278 different ion species of all elements between hydrogen Z=1 and uranium Z=92. Therefore, by considering the charge states, the periodic table of the elements is extended by another dimension. Note that if the various isotopes of the elements are also taken into consideration, the number of available systems is again drastically increased.

Since each ion consists of two charges, the positive charge of the nucleus and the negative charge of the electrons, there are two different charge dependent sequences. In the isoelectronic sequence, the number of electrons remain the same whereas the nuclear charge Z is increased [59]. In contrast, the isonuclear sequence describe a series of ions exhibiting the same nuclear charge but varying number of electrons. Both sequences are schematically represented in a plot of the full phase space for positive ions in figure 2.1.

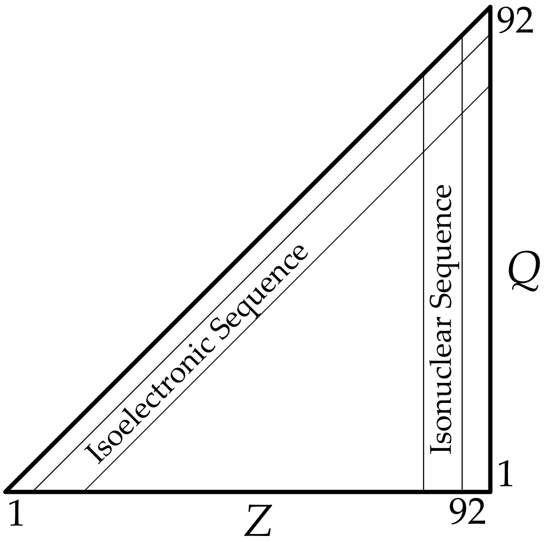

FIGURE 2.1: Schematic phase space plot of all possible positive ions with nuclear charge Z and electronic charge Q in the range between $Z = 1$ and 92. Diagonal and vertical lines represent an isoelectronic and isonuclear sequence, respectively. Figure adapted from [59].

2.3 Fundamental collision processes of electrons and photons with ions

2.3.1 Ionization

Electron-impact ionization

Electron-impact ionization is a process in which a free electron interacts with an ion by means of an inelastic collision. If the kinetic energy of the incident, free electron exceeds the binding energy of a bound electron in the atom or ion A^{q+}, it is possibly ionized by removal of the bound electron

$$\mathrm{A}^{q+} + \mathrm{e}^- \longrightarrow \mathrm{A}^{(q+1)+} + 2\mathrm{e}^-. \tag{2.13}$$

The electron-impact ionization cross section is described by the empirically determined equation published by Wolfgang Lotz [109, 108]

$$\sigma = \sum_{i=1}^{N} a_i q_i \frac{\ln \frac{E_{\mathrm{Kin}}}{E_{\mathrm{B}}}}{E_{\mathrm{Kin}} E_{\mathrm{B}}} \left(1 - b_i \exp\left[-c_i \left(\frac{E_{\mathrm{Kin}}}{E_{\mathrm{B}}} - 1\right)\right]\right), \tag{2.14}$$

where E_{Kin} represents the kinetic energy of the free electron, E_{B} the binding energy of the electrons in the $i-$th subshell, q_i the number of equivalent electrons in the i-th subshell, and a_i, b_i and c_i the constants to be determined experimentally. The ionization cross section depends primarily on the energy of the free electron. If the kinetic energy is below the ionization threshold, the cross section of an ionization of a neutral atom is zero. It increases as the kinetic energy exceeds the threshold and reaches its maximum at energy approximately three to four times the threshold [161, 59].

Photon ionization

There are different possibilities to ionize atoms or ions by means of photons. Here, a differentiation between direct and resonant photoionization processes is required. The direct and non-resonant photon ionization of an atom or ion A^{q+} is a process in which a single photon γ removes a bound electron of the investigated system by transferring its energy to the electron

$$\gamma + \mathrm{A}^{q+} \longrightarrow \mathrm{A}^{(q+1)+} + \mathrm{e}^{-}. \tag{2.15}$$

This process only occurs if the energy of the photon E_γ exceeds the binding energy of the electron E_B. The energy difference between the photon energy and the former binding energy of the removed electron is transferred to the freed electron resulting in an additional kinetic energy

$$E_\mathrm{Kin} = E_\gamma - E_\mathrm{B}. \tag{2.16}$$

If the photon energy is lower than the binding energy of the electron, multiple photons may combine their energies to remove the bound electron [47, 1]. Since the probability of such multi-photon ionization process decreases rapidly with the number of photons required, high photon densities are generally required.

In addition to direct photoionization, atoms or ions can be resonantly ionized by means of the so-called Auger decay. After an electron was resonantly photoexcited, the electron relaxes back to an energetically lower state. The released energy is simultaneously and non-radiatively transferred to a second bound electron and thereafter removed from the system. This process is illustrated in the right panel of figure 2.2.

2.3.2 Recombination

Radiative recombination

The so-called radiative recombination (RR), in which a free electron is captured by an ion and a photon simultaneously emitted, describes the inverse process of the direct photoionization

$$\mathrm{A}^{q+} + \mathrm{e}^{-} \longrightarrow \mathrm{A}^{(q-1)+} + \gamma. \tag{2.17}$$

The energy of the emitted photon is defined by

$$\mathrm{E}_\gamma = \mathrm{E}_\mathrm{Kin} - \mathrm{E}_\mathrm{B}. \tag{2.18}$$

The cross-section for the radiative recombination reads

$$\sigma_n = \frac{8\pi}{3\sqrt{3}} \frac{\alpha^5}{n^3} \frac{Z^4_{eff}}{\mathrm{E}_\mathrm{B} E_\gamma}, \tag{2.19}$$

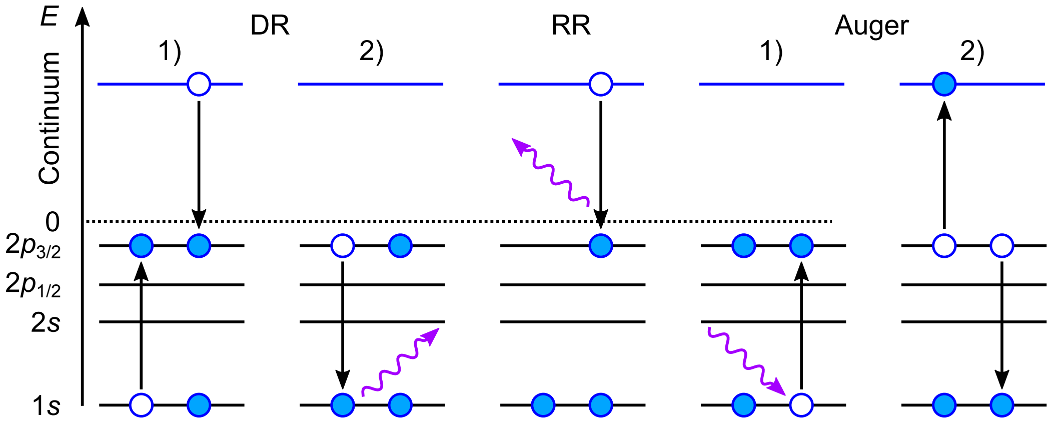

FIGURE 2.2: Representation of the dielectronic recombination (DR, left), radiative recombination (RR, center) and Auger decay (right). DR: A free electron is resonantly captured into a bound state. The energy release matches the required energy to excite another bound electron from its ground state. The excited state relaxes via emission of a photon. RR: A free electron is non-resonantly captured into a bound state. The energy excess is transferred to emitted photon. Auger: An excited state is relaxing by emitting an outer weakly bound electron. Figure adopted from [50]

where α represents the fine structure constant, n the principal quantum number, Z_{eff} the effective nuclear charge number, E_B the energy of the trapped electron and E_γ the energy of the emitted photon [92]. A schematic illustration of a radiative recombination process is shown in figure 2.2.

Dielectronic recombination

Another recombination process is given by resonant dielectronic recombinations (DR). An electron with a certain kinetic energy, captured in an ion, non-radiatively transfers the released energy to a bound electron which is thereby excited. This doubly excited state is unstable. When the excited ion relaxes to an energetically lower state, a photon is emitted, see left panel of figure 2.2. In the common nomenclature of dielectronic recombination, the two shells of the bound electron that is excited are named first. The last letter represents the shell into which the free electron was captured. Thus, KLL-DR stands for a transition of the bound electron between the K and L shells by recombining a free electron in the L shell. It holds

$$\mathrm{A}^{q+} + \mathrm{e}^- \longrightarrow \left(\mathrm{A}^{(q-1)+}\right)^{**} \longrightarrow \mathrm{A}^{(q-1)+} + \gamma, \tag{2.20}$$

whereas A^{q+} represents q-fold charged Ion in its initial state, $\left(\mathrm{A}^{(q-1)+}\right)^{**}$ the doubly excited state and $\mathrm{A}^{(q-1)+}$ the ion after the recombination in the ground state.

2.3.3 Excitation

Electron-impact excitation

In the so-called electron-impact excitation process, the ion interacts with a free electron with a kinetic energy E_{Kin}. In this process, part of the kinetic energy of the electron is transferred to the collision partner the ion. It follows

$$\mathrm{A}^{q+} + \mathrm{e}^- \longrightarrow \mathrm{A}^{(q+)*} + \mathrm{e}^-, \tag{2.21}$$

where $\mathrm{A}^{(q+)*}$ represents the excited state of the ion. The electron energy of the incident electron after the collision is defined by $E'_{\mathrm{Kin}} = E_{\mathrm{Kin}} - \Delta E_{ik}$, where ΔE_{ik} corresponds to the excitation energy, i.e., the energy difference between the final and initial states of the bound electron of the ion. The cross section of this process is approximated by the Bethe equation

$$\sigma_{\mathrm{EE}} = \frac{8\pi^2}{\sqrt{3}} \frac{I_{\mathrm{H}} a_0^2}{E_{\mathrm{Kinetic}} \left(E_{\mathrm{k}} - E_{\mathrm{i}}\right)} \cdot g f_{\mathrm{ik}}, \tag{2.22}$$

where I_{H} represents the ionization energy of hydrogen, a_0 the Bohr radius, E_{Kinetic} the kinetic energy of the free electron, and E_i and E_k the energy of the initial and excited state of the ion, respectively. The component $g f_{ij}$ is the product of the Gaunt factor, a quantum mechanical correction for this classical approach, and the oscillator-strength f.

Photon excitation

The photon excitation, also known as induced photon absorption, is a process in which a bound electron is resonantly excited by a photon

$$\mathrm{A}^{q+} + \gamma \longrightarrow \mathrm{A}^{(q+)*}. \tag{2.23}$$

Note that this process only occurs if the photon energy matches the energy difference between the upper and lower state of the bound electron

$$\mathrm{E}_{\gamma} = \mathrm{E}_{\mathrm{i}} - \mathrm{E}_{\mathrm{k}}. \tag{2.24}$$

The probability P_{12} with which this process occurs per second depends on the so-called Einstein coefficients of induced absorption B_{12} and the radiation density of the photon field ρ

$$P_{\mathrm{ik}} = B_{\mathrm{ik}} \rho. \tag{2.25}$$

This process is illustrated for a simplified two-level system in the left panel of figure 2.3.

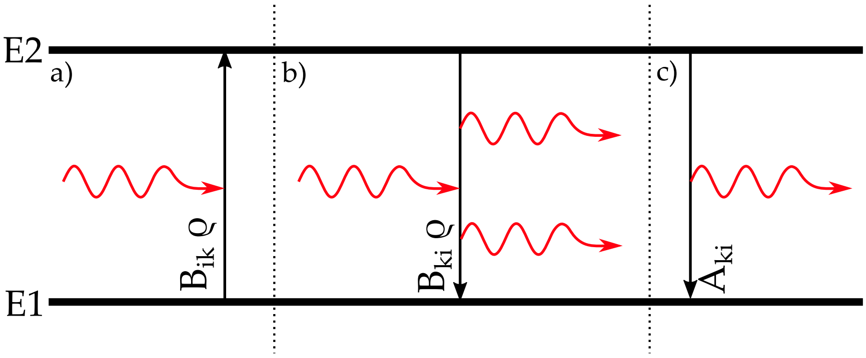

FIGURE 2.3: Illustration of a) induced absorption, b) induced emission, and c) spontaneous emission of a two-level system. While the induced processes depend on the radiation density ρ and the Einstein coefficients B, the spontaneous emission depends only on the Einstein coefficient A_{ki}. Figure adopted from [46]

2.3.4 Deexcitation

Induced & spontaneous photon emission

As previously introduced in chapter 2.3.1, a photon-excited state of a given system may result in an auto-ionizing Auger decay. Additionally, there are two further decay mechanisms. First, if the excited system is exposed to photons with matching energies, the upper state can decay back by means of an induced emission. The probability P_{ki} of such a deexcitation is described by the Einstein coefficient of induced emission B_{ki} and is equal to the probability of a resonant photon excitation, see equation 2.25

$$P_{\mathrm{ki}} = B_{\mathrm{ki}}\rho = P_{\mathrm{ik}}. \tag{2.26}$$

Second, the excited system may relax back to the ground state by spontaneous photon emission. The probability P_{ki} of this process depends only on the Einstein coefficient of spontaneous emission A_{ki}

$$P_{\mathrm{ki}} = A_{\mathrm{ki}}. \tag{2.27}$$

The Einstein coefficient A_{ki} is defined by

$$A_{\mathrm{ki}} = \frac{W^{s}_{\mathrm{ki}}}{N_{\mathrm{E}}}, \tag{2.28}$$

with W^{s}_{ki} and N_E as the total spontaneous emission rate and number of excited ions. The lifetime $\tau_{1/2}$ of a given excited state is defined as the reciprocal of the sum of all available deexcitation channels j

$$\frac{1}{\tau_{1/2}} = \sum_{\mathrm{j}} A_{\mathrm{kj}}. \tag{2.29}$$

The Einstein coefficients for the induced absorption and emission B_{ik} and B_{ki} can be expressed as

$$B_{\mathrm{ik}} = \frac{W^{i}_{\mathrm{ik}}}{\rho_{\omega} N_{\mathrm{G}}}, \tag{2.30}$$

$$B_{\mathrm{ki}} = \frac{W^{i}_{\mathrm{ki}}}{\rho_{\omega} N_{\mathrm{E}}}, \tag{2.31}$$

where ρ_{ω} is the energy density per unit angular frequency interval in the region containing N_{E} ions in the excited and N_{G} in the ground state [76]. The relation between spontaneous and induced emission is given by

$$B_{\mathrm{ki}} = \frac{\pi^2 c^3}{\hbar \omega^3_{\mathrm{ki}}} A_{\mathrm{ki}} \tag{2.32}$$

and

$$B_{\mathrm{ik}} = \frac{g_{\mathrm{E}}}{g_{\mathrm{G}}} B^{\omega}_{\mathrm{ki}}, \tag{2.33}$$

where $\hbar\omega_{\mathrm{ki}}$ represents the transition energy. g_{E} and g_{G} are often referred to as the degeneracy level of the particular states.

Oscillator strengths, line strengths & transition dipole moment

Analogous to a classical oscillator exhibiting an oscillation frequency ω_{ki}, the so-called oscillator strength f is defined which relates to the Einstein coefficient as follows

$$f_{\mathrm{ik}} = \frac{g_{\mathrm{E}}}{g_{\mathrm{G}}} \frac{2\pi\epsilon_0 m_e c^3}{\omega_{\mathrm{ki}} e^2} A_{\mathrm{ki}}. \tag{2.34}$$

For example, for an angular momentum quantum number $J_{\mathrm{E}} = 1$ and $J_{\mathrm{G}} = 0$ for the excited state and ground state, respectively, a value of $\frac{g_{\mathrm{E}}}{g_{\mathrm{G}}} = 3$ is obtained.

The measure of the ability of an atom or ion to absorb electromagnetic radiation can also be described by the so-called dipole matrix element [46, 45]. According to classical electrodynamics, the radiated power of a classical oscillator with dipole moment $p = p_0 \cos(wt)$ is defined by

$$\langle \mathrm{d}W/\mathrm{d}t \rangle = \frac{2w_0^4}{12\pi\epsilon_0 c_0^3} \langle p^2 \rangle \tag{2.35}$$

with

$$\langle p^2 \rangle = p_0^2 \langle \cos^2 wt \rangle = 0.5 p_0^2. \tag{2.36}$$

In the quantum mechanical treatment of the emission of a atom or ion, the classical dipole moment p = ex is replaced by the expectation value of the transition dipole moment

$$\vec{M}_{\mathrm{ki}} = e \int \phi_{\mathrm{k}}^{*} \vec{r} \phi_{\mathrm{i}}^{*} \mathbf{d}\tau, \tag{2.37}$$

where ϕ_{k}^{*} and ϕ_{i}^{*} represent the wavefunctions of the two involved involved states whereas $\vec{r}$ is given by the position of the electron in the system. By replacing $\langle p^2 \rangle$ in equation with $\langle \vec{M}_{\mathrm{ik}}^2 + \vec{M}_{\mathrm{ki}}^2 \rangle = 2\left|M_{\mathrm{ki}}\right|^2$, the quantum mechanical emission power of a transition obtained

$$\langle \mathrm{d}W_{\mathrm{ki}}/\mathrm{d}t \rangle = \frac{w_{\mathrm{ki}}^4}{3\pi\epsilon_0 c_0^3} \left|M_{\mathrm{ki}}\right|^2. \tag{2.38}$$

The emission power of transition also depends on the Einstein coefficient for induced photo absorption

$$\langle \mathrm{d}W_{\mathrm{ki}}/\mathrm{d}t \rangle = A_{\mathrm{ki}} h v_{\mathrm{ki}}. \tag{2.39}$$

Combining equations 2.39 and 2.38, the relation between the Einstein coefficient for induced photo absorption and the dipole matrix element is defined by

$$A_{\mathrm{ki}} = \frac{16\pi^3 v^3}{3\epsilon_0 h c_0^3} \left|M_{\mathrm{ki}}\right|^2. \tag{2.40}$$

Another way to describe the intensity of a transition is the so-called line strength S_{ki} which is based on the square of the dipole moment $\left|M_{\mathrm{ki}}\right|^2$

$$S_{\mathrm{ki}} = g_{\mathrm{E}} \left|M_{\mathrm{ki}}\right|^2 = \frac{3\epsilon_0 h c^3}{2\omega_{\mathrm{ki}}^3} g_{\mathrm{E}} A_{\mathrm{ki}}. \tag{2.41}$$

Polarization

The angular emission distribution of a photon emitted by spontaneous emission depends on the polarization of the incident photon that formerly excited the state and the total angular momentum of the energy levels involved. For a given transition

$$|\alpha_{\mathrm{i}}, J_{\mathrm{i}}\rangle + \gamma \to |\alpha_{\mathrm{j}}, J_{\mathrm{j}}\rangle \to |\alpha_{\mathrm{k}}, J_{\mathrm{k}}\rangle + \gamma, \tag{2.42}$$

consisting of an initial i, excited j and final state k with the angular momenta J and the quantum numbers α, the angular distribution of the spontaneous emission for an absorbed photon from the arbitrarily chosen direction z reads

$$W(\theta, \phi) = \frac{W_0}{4\pi} \left[1 - 3\sqrt{\frac{2\pi}{15}} \beta \sum_q \rho_{2q}^{\gamma 0} Y_{2q}(\theta, \phi) \right], \tag{2.43}$$

where $\rho_{2q}^{\gamma 0}$ corresponds to a tensor describing the polarization and Y_{lm} to the spherical surface functions [7, 154]. The anisotropy coefficient β can be represented with the so-called Wigner's 6j symbols as

$$\beta = 3(-1)^{1+J_\mathrm{i}-J_\mathrm{k}}\,(2J+1)\begin{Bmatrix} 1 & 1 & 2 \\ J_\mathrm{j} & J_\mathrm{j} & J_\mathrm{k} \end{Bmatrix}\begin{Bmatrix} 1 & 1 & 2 \\ J_\mathrm{j} & J_\mathrm{j} & J_\mathrm{i} \end{Bmatrix}. \tag{2.44}$$

In the case of fully circularly polarized light, the anisotropy coefficient is zero ($\rho^{\gamma 0}_{2q} = 0$) and equation 2.43 is reduced to

$$W\,(\theta,\phi) = \frac{W_0}{4\pi}. \tag{2.45}$$

For this reason, the angular distribution of the emission is completely independent of the angles θ and ϕ, resulting in an isotropic emission characteristic.

Energy distribution of a spontaneous emission

The energy of a spontaneously emitted photon from an excited ion is not monochromatic but follows a certain pattern or line shape and will be discussed in this section, based on the work of [46].

The spontaneous emission following the deexcitation of an excited state in an atomic system can be described as a classical harmonic oscillator. The time evolution of the oscillation amplitude is described by

$$\ddot{x} + \gamma\dot{x} + w_0^2 = 0, \tag{2.46}$$

with a damping constant γ and $w_0^2 = D/m$. Assuming $x(0) = x_0$ and $\dot{x}(0) = 0$, the real solution

$$x(t) = x_0 \mathrm{e}^{-(\gamma/2)t}[\cos wt + (\gamma/2w)\sin wt] \tag{2.47}$$

is inferred with $w = \sqrt{w_0^2 - \gamma^2/4}$. Assuming the damping factor being negligible, $w \simeq w_0 = 2\pi v_0$ is obtained, which represents the energy difference between the upper and lower state of the corresponding transition $E_\mathrm{k} - E_\mathrm{i}$. If $x(t)$ is expressed as a superposition of several amplitudes A exhibiting a frequency w

$$x(t) = \frac{1}{\sqrt{2\pi}}\int_0^\infty A(w)\mathrm{e}^{\mathrm{i}wt}\mathrm{d}w \tag{2.48}$$

one obtains

$$A(w) = \frac{1}{\sqrt{2\pi}}\int_{-\infty}^{\infty} x(t)\mathrm{e}^{-\mathrm{i}wt}\mathrm{d}t = \frac{1}{\sqrt{2\pi}}\int_0^\infty x_0\mathrm{e}^{-(\gamma/2)t}\cos(w_0 t)\mathrm{e}^{-\mathrm{i}wt}\mathrm{d}t \tag{2.49}$$

by performing a fourier transformation and assuming $x(t) = 0$ for $t < 0$. The intensity distribution of the transition is then given by $I(w) = A(w)\cdot A^*(w)$. The resulting profile is often called Lorentzian line shape or Breit-Wigner distribution and is defined as

$$I(w) = \frac{\gamma/2\pi}{(w-w_0)^2 + (\gamma/2)^2}. \tag{2.50}$$

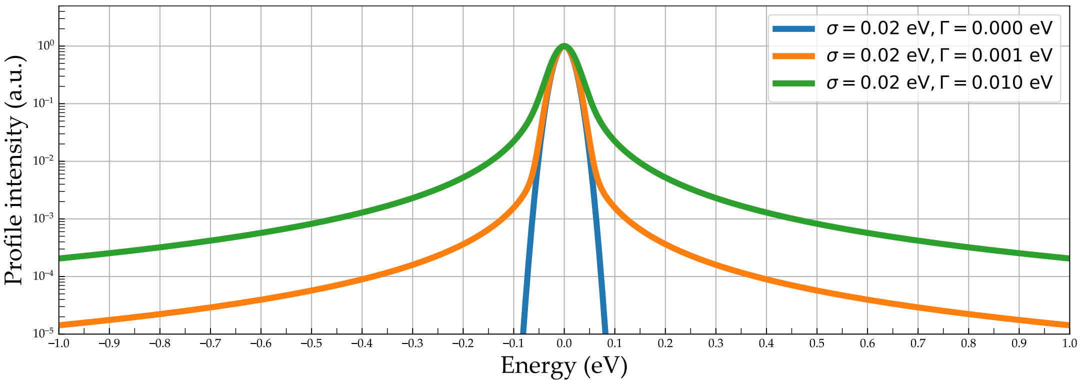

FIGURE 2.4: Comparison between a Gaussian (blue) and two Voigt (orange and green) line shapes. The intensity of a Gaussian distribution drops fast and is essentially zero for values deviating more than 3σ from the centroid. A Voigt profile exhibiting a Lorentzian width Γ much smaller than the Gaussian width σ is in the center of the line indistinguishable from a Gaussian profile with similar width (orange). In contrast to Gaussian distribution, Voigt profiles exhibit broad wing far away from the centroid of the profile.

The parameter γ represents the full width at half maximum (FWHM) of the profile and is often referred to as the natural linewidth of a transition. Based on the uncertainty principle

$$\Delta E \Delta t > \frac{\hbar}{2}, \tag{2.51}$$

the observed linewidth is proportional to the lifetime τ of the underlying transition

$$\Delta E = \frac{\gamma}{2} = \frac{\hbar}{2\tau_{1/2}}. \tag{2.52}$$

Doppler broadening and Voigt profiles

In general, the ion under investigation exhibits a temperature which results in a Doppler broading that follows a Gaussian distribution. The standard deviation σ of the Doppler broadening can be expressed as

$$\sigma = \frac{w_0}{c}\sqrt{\frac{8kTln(2)}{m}}, \tag{2.53}$$

with m and T representing the mass and temperature of the ion, respectively [46]. Experimentally, the aforementioned natural Lorentzian line shape L is often overlapped with the Gaussian distribution G induced by the ion motion and results in a convoluted line shape often referred to as Voigt line shape

$$V(x;\sigma,\gamma) = (G * L)(x) = \int G(\tau)L(x-\tau)d\tau. \tag{2.54}$$

The integral in equation 2.54 cannot be solved analytically but can be evaluated as

$$V(x;\sigma,\gamma) = \frac{\mathrm{Re}[w(z)]}{\sigma\sqrt{2\pi}}, \tag{2.55}$$

where $\mathrm{Re}[w(z)]$ is the real part of the so-called Faddeeva function

$$w(z) := e^{-z^2}\operatorname{erfc}(-iz) = \operatorname{erfcx}(-iz) = e^{-z^2}\left(1 + \frac{2i}{\sqrt{\pi}}\int_0^z e^{t^2}\mathrm{d}t\right) \tag{2.56}$$

evaluated for

$$z = \frac{x + i\gamma}{\sigma\sqrt{2}}. \tag{2.57}$$

In figure 2.4, the line shapes of various Voigt profiles with a constant Gaussian width σ and various Lorentzian widths Γ are depicted. The FWHM of the Voigt profile can be approximated with an accuracy of 0.02% by

$$f_\mathrm{V} \approx 0.5346 f_\mathrm{L} + \sqrt{0.2166 f_\mathrm{L}^2 + f_\mathrm{G}^2}. \tag{2.58}$$

Note that convolutions of Voigt profiles are invariant under convolutions, i.e., the convolution of two Voigts results again in a Voigt profile. The widths f_G and f_L of the two underlying Gaussian and Lorentzian contribution of a convolution of i Voigt profiles can be expressed as

$$f_\mathrm{G}^2 = \sum_i \left(f_{\mathrm{G_i}}^2\right) \tag{2.59}$$

and

$$f_\mathrm{L} = \sum_i \left(f_{\mathrm{L_i}}\right), \tag{2.60}$$

where $f_{\mathrm{G_i}}$ and $f_{\mathrm{L_i}}$ represent the initial widths of the convolved Voigt profiles.

2.4 Methods for the calculation of the atomic structure

2.4.1 Hartree-Fock method

One approach to approximate solutions for Schrödinger equation of a multi-electron system is given by the Hartree-Fock method [72]. The Hartree-Fock method simplifies the interactions of the particles with each other such that they no longer interact with each other in pairs, but with a so-called mean field generated by all other particles. The field still depends on the individual particles, but the solution can now be calculated stepwise. The solution of the Schrödinger equation is then given by the product of all available electronic states:

$$\Psi_{n,l,m_l,m_s} = \prod_{i=1}^{N} \Psi_{n_i,l_i,m_{l_i},m_{s_i}}. \tag{2.61}$$

However, the simple product of all wavefunction do not satisfy the general antisymmetry postulate. By including the Pauli principle which prohibits two electrons in an atom to be identical in all quantum numbers nlm, the N-electron wavefunction Ψ is represented by the so-called Slater determinant

$$\Psi = \frac{1}{\sqrt{N}} \begin{vmatrix} \psi_1(1) & \psi_1(2) & \cdots & \psi_1(N) \\ \psi_2(1) & \psi_2(2) & \cdots & \psi_2(N) \\ \vdots & \vdots & \ddots & \vdots \\ \psi_N(1) & \psi_N(2) & \cdots & \psi_N(N) \end{vmatrix}. \tag{2.62}$$

Assuming two electrons being the same, two columns and rows of the Slater determinant would be identical. Thus the resulting determinant vanishes, which fully follows Paulis principle. The eigenvalues are then obtained by the Hartree-Fock variational principle

$$\delta \langle \Psi | \hat{H} | \Psi \rangle = 0 \tag{2.63}$$

with its solution $E = E_{\text{min}}$. Note that similar to the Schrödinger equation, the Hartree-Fock approach does not include relativistic effects in its calculations. For a relativistic treatment of the system the so-called Dirac-Coulomb-Breit operator is introduced which consists of three terms:

$$\hat{H}_{\text{DCB}} = \sum_{i=1}^{N} \hat{H}_{\text{Dirac}} + \sum_{i<j} \frac{e^2}{r_{ij}} - \sum_{i<j} \hat{B}_{ij}. \tag{2.64}$$

The Dirac operator

$$\hat{H}_{\text{Dirac}} = \left(c\alpha \left(\hat{p} - \frac{e}{c}\vec{A} \right) + \beta mc^2 + e\Phi \right), \tag{2.65}$$

with the electric field described by a vector potential $\vec{A}$, a scalar potential $e\Phi$ and the Dirac matrices $\vec{\alpha}$ and β. The second term of equation 2.64 $\sum_{i<j} \frac{e^2}{r_{ij}}$ describes the

coupling of the electrons to the electric field. The third term also known as the Breit operator is defined by

$$\sum_{i<j} \hat{B}_{ij} = \frac{e^2}{2r_{ij}} \left(\vec{\alpha}_i \vec{\alpha}_j + \frac{\left(\vec{\alpha}_i r_{ij}\right) \left(\vec{\alpha}_j r_{ij}\right)}{\left|\vec{r}_j\right|^2} \right) \tag{2.66}$$

and represents the magnetic interaction between the electrons and the retardation of the magnetic and electric potential [50, 62].

2.4.2 Configuration Interaction

Another approach to find solutions to the Hamilton operator for multi-electron systems is given by configuration interaction (CI) method [150]. Here, the trial wavefunction Ψ_i is represented by a linear combination of configurations ψ_i, each weighted by a mixing coefficient c_i

$$\Psi_i = \sum_{i=1}^{n} c_i \psi_i. \tag{2.67}$$

Similar to the Hartree-Fock variational priniciple, the mixing coefficients are optimized, while the individual configurations remain the same until the total energy of the system is minimized. Many ab-initio codes to model the structure of atoms and electrons are based on CI. The accuracy of the calculated atomic structure vastly depends on the amount of configurations included in the calculation. The *Flexible Atomic Code* which is often used within the scope of this thesis is based on CI [65].

2.4.3 Multiconfiguration Dirac Hartree Fock

The Multiconfiguration Dirac Hartree Fock (MCDHF) method to model the structure of atoms is a combination of the already introduced Hartree-Fock and the configuration interaction method. Similar to CI, the wave function is represented by a set of configurations, which are represented by Slater determinants and individually weighted by mixing coefficients. In this approach both the individual mixing coefficients as well as the set of configurations are optimized. In contrast to Multiconfiguration Hartree Fock (MCHF), MCDHF does include a relativistic treatment of the electron motions. The resulting wavefunction of the system is defined by

$$\left|\Psi_{\Pi,J,M}\right\rangle = \sum_{v=1}^{N} c_{v,n} \sum_{i}^{N_v} d_i \begin{vmatrix} \psi_1\left(1\right) & \cdots & \psi_1\left(N\right) \\ \psi_2\left(1\right) & \cdots & \psi_2\left(N\right) \\ \vdots & \ddots & \vdots \\ \psi_N\left(1\right) & \cdots & \psi_N\left(N\right) \end{vmatrix} \tag{2.68}$$

2.4.4 Many Body Perturbation Theory

Another approach to solve the Schrödinger equation for a multi-electron system is based on perturbation theory (MBPT). In this approximation, the multi-particle

Hamiltonian-Dirac operator, see equation 2.11, is expressed as the sum of the single particle interactions $\hat{H}_0$ and an additional perturbation $\lambda \hat{H}_{\text{Pertub}}$

$$\hat{H} = \hat{H}_0 + \lambda \hat{H}_{\text{Pertub}}, \tag{2.69}$$

with $\lambda \in [0, 1]$. Here, the single particle Hamiltonians $\hat{H}_0$ and their respective eigenstates ψ_n^0 are already known by the semi-classical approach discussed earlier. With a series expansion in powers of the parameter λ the eigenstates ψ_n of $\hat{H}$ are approximated. The same applies to the eigenvalues E_n [57]. The first term of the expansion is given by the unperturbed eigenstates ψ_n^0 and eigenvalues E_n^0 [139]. The wave function changes of the solution of the Schrödinger equation in first order are given by

$$\psi_n^1 = \sum_{m \neq n} \frac{\langle \psi_m^0 \, |\lambda V| \, \psi_n^0 \rangle}{E_n^0 - E_m^0}. \tag{2.70}$$

Iteratively, by adding higher orders this way, the solution of the Schrödinger equation is approximated [121].

2.5 Fe XVII and Fe XVI

Iron is one of the most abundant elements in the universe. The X-ray emission spectra of many astrophysical objects, e.g., active-galactic nuclei (AGN) and stars observed by space-based spectrometers are dominated by transitions from iron [90]. The energy exchanged in collisions due to the plasma temperature of these objects often exceeds the binding energy of the weakly bound electrons of iron. The binding energy of the weakest bound electron, for example, is only 7.6 eV. The energy needed to remove further electrons from the system increases steadily. If 16 electrons are removed, the electronic shell of the ion contains no more than 10 electrons resulting in similar electronic configuration as neutral neon. Hence, the system is also often referred to as neon-like iron, Fe^{16+} or Fe XVII. The minimum energy required to produce Fe XVII is about 489 eV. Since Fe XVII exhibits closed $1s$, $2s$ and $2p$ shells, the ionization energy necessary to further remove electrons is significantly higher (1263 eV). Due to this broad energy range between the production and ionization thresholds, Fe XVII is one of the most abundant species in many medium-hot and hot plasma and is of large interest for spectroscopic analysis.

The strongest line of Fe XVII is often referred to as 3C, which is an allowed E1 transition in the soft X-ray energy regime. The intercombination line 3D, i.e., a transition that changes the spin quantum number S, is energetically close to 3C but significantly weaker. Still, 3D is one of the most intense lines observed X-ray spectra. Due to the allowed and semi-forbidden nature of 3C and 3D, respectively, it was proposed that their observed line intensity ratio, which is directly proportional to the oscillator-strength ratio, serve as a plasma density and temperature diagnostic [25].

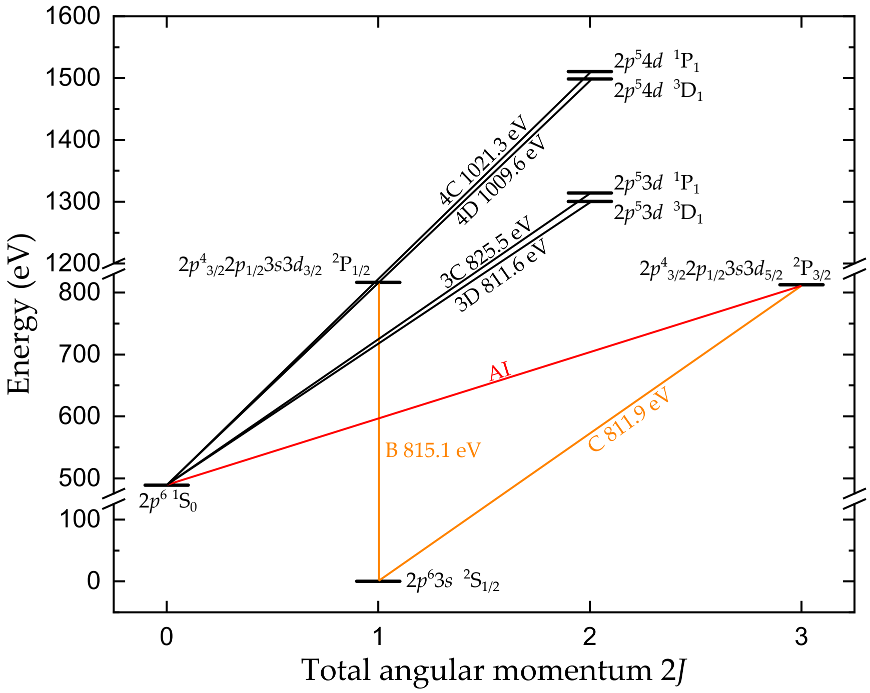

FIGURE 2.5: Grotrian diagram of Fe XVII and Fe XVI. Transitions of interest 3C, 3D, 4C, and 4D of Fe XVII are depicted by black solid lines. Orange solid lines correspond to transitions of Fe XVI. Note that the upper level of C exhibits a strong autoionizing decay channel to the ground state of Fe XVII (red solid line). Given values are based on own FAC calculations.

The transitions 4C and 4D are similar to 3C and 3D but with an increased principle quantum number and hence, higher transition energies. It is interesting to note, that all four introduced transitions of Fe XVII exclude any auto-ionizing decay channel since the energy of the upper levels are insufficient to overcome the required ionization energy of Fe XVII.

To fully understand the spectral lines investigated within the scope of this thesis, two further transitions called B and C of the next lower charge state Fe XVI are introduced. Fe XVI is often referred to as sodium-like iron as it has the same number of electrons as neutral sodium. In contrast to Fe XVII transitions, both B and C compete with auto-ionizing decay channels. Important for this work is the strong decay channel of the upper state of C, which directly decays to the ground state of Fe XVII. In figure 2.5, a selection of energy levels for Fe XVII and Fe XVI as well as the transitions introduced earlier are depicted in a Grotrian diagram. An overview of all transitions of interest including their electronic configurations, energies and Einstein coefficients is given in table 2.1. Note that all values given in figure 2.5 and table 2.1 are based on ab-initio calculations using the Flexible Atomic Code (FAC) [65]. The number of included configurations in the configuration interaction approach used here was limited, resulting in an accuracy of approximately 0.1% and 30% for the determination of transition energy and probability, respectively [64].

TABLE 2.1: Overview of Fe XVII and Fe XVI transitions treated in this thesis. $A_{Radiative}$ represents the Einstein coefficient of a transition from the upper to lower level. $A_{Rad,Alt}$ corresponds to alternative radiative decay channels from the upper state of the transition. If present, auto-ionizing channels from the upper state are listed as A_{Auger}. The sum of all coefficients resulting in A_{Total} is an important parameter for the calculation of the natural linewidth of each transition. All given values are based on ab-initio calculations using FAC performed by the author.

Transition	**Charge state**	**Lower state**	**Upper state**	**Energy (eV)**	$\mathbf{A_{Radiative}}$ **(Hz)**	$\mathbf{A_{Rad,Alt}}$ **(Hz)**	$\mathbf{A_{Auger}}$ **(Hz)**	$\mathbf{A_{Total}}$ **(Hz)**
3C	Fe XVII	$[2p^6]_{J=0}$	$[(2p^5)_{1/2}\,3d_{3/2}]_{J=1}$	825.64	2.44×10^{13}	1.2×10^{10}	./.	2.44×10^{13}
3D	Fe XVII	$[2p^6]_{J=0}$	$[(2p^5)_{3/2}\,3d_{5/2}]_{J=1}$	811.65	5.86×10^{12}	1.4×10^{10}	./.	5.86×10^{12}
4C	Fe XVII	$[2p^6]_{J=0}$	$[(2p^5)_{1/2}\,4d_{3/2}]_{J=1}$	1021.66	6.55×10^{12}	5.0×10^{11}	./.	7.05×10^{12}
4D	Fe XVII	$[2p^6]_{J=0}$	$[(2p^5)_{3/2}\,4d_{5/2}]_{J=1}$	1009.95	5.66×10^{12}	4.9×10^{11}	./.	6.15×10^{12}
B	Fe XVI	$[2p^6 3s]_{J=1/2}$	$[(2p^5)_{1/2}(3s3d)_{3/2}]_{J=1/2}$	816.23	2.58×10^{13}	5.1×10^{11}	3.8×10^{12}	3.01×10^{13}
C	Fe XVI	$[2p^6 3s]_{J=1/2}$	$[(2p^5)_{1/2}(3s3d)_{5/2}]_{J=3/2}$	812.80	1.57×10^{13}	5.0×10^{11}	3.3×10^{13}	4.92×10^{13}

Chapter 3

Electron beam ion traps

3.1 Basics

An electron beam ion trap (EBIT) is a versatile tool for the production and trapping of highly charged ions (HCIs) for spectroscopic reasons or as an ion source for other experiments. The first electron beam ion source (EBIS) was built in 1969 in Dubna, U.S.S.R. [2]. The first EBIT concept with an optical access to the ions was presented by Levine et al. from the Lawrence Livermore National Laboratory (LLNL), USA in 1988 [103]. Independent of its purpose, every EBIT or EBIS employs the same basic principle, see figure 3.1. A monoenergetic electron beam produced by an electron gun ionizes atoms by electron impacts. This process is drastically enhanced in the trap center due to the high local electron densities of the beam. This is achieved by a magnetic field that compresses the electron beam from a low density at the emission source to highest densities in the trap center.

Once the ions are produced in the trap center, they form a plasma with a diameter of a few hundred microns and a length of a few milimeter. Radially, the ions are confined in the trap by the negative space charge of the electron beam as well as the cyclotron motion due to the Lorentz force induced by the magnetic field. Axially, the ions are trapped electrostatically by a potential well formed by a set of drift

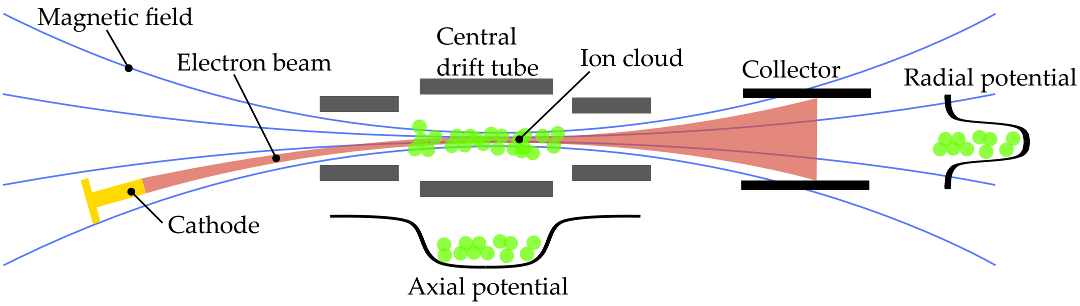

FIGURE 3.1: Basic principle of an electron beam ion trap. An electron beam (red) emitted by a cathode (yellow) is electrostatically accelerated towards the trap center. A strong magnetic field (blue lines) compresses the electron beam to high electron densities in the trap center. In the trap center, ions (green) are generated by electron impacts. Radially, the ions are confined by the negative space charge of the electron beam. Axially, a potential well induced by a set of drift tubes store the ions. After the electron beam passed the trap center, it is collected by the collector electrode.

tubes. After the electron beam passed the trap center, the electrons impinge on a so-called collector electrode. The ions in the electron beam continually interact with the electrons which results in ionizations, recombinations or excitations processes, as explained in detail in previous section.

The electron beam

Radius

The electron beam is usually produced by a cathode mounted inside an electron gun. Electrostatically, the beam is extracted from the interior of the gun towards the trap center of the EBIT. Along its path to the center, the beam is forced to follow the magnetic field lines due to the Lorentz force. In best case, the magnetic field strength increases from zero at the electron beam emission point to its maximum in the trap center. This way, maximum electron densities can be achieved according to the optical theory of thermal velocity effects in cylindrical electron beams by G. Herrmann [75]. The so-called Herrmannradius

$$r_{\mathrm{H}} = \sqrt{\frac{m_{\mathrm{e}} I}{\pi \epsilon_0 \mathrm{e} v B^2} + \sqrt{\left(\frac{m_{\mathrm{e}} I}{\pi \epsilon_0 \mathrm{e} v B^2}\right)^2 + \frac{8 k T_{\mathrm{K}} m_{\mathrm{e}}}{\mathrm{e}^2 B^2} r_{\mathrm{K}}^2 + \frac{B_{\mathrm{K}}^2}{B^2} r_{\mathrm{K}}^4}} \tag{3.1}$$

describes the radius that contains 80% of the electrons of the beam. Here, I represents the beam current, v electron velocity, B the magnetic field strength in the trap center, T_{K} the temperature of the cathode, r_{K} the radius of the cathode and B_{K} the magnetic field at the cathode. The velocity v of the electrons in the non-relativistic case is described by

$$v_{\text{classical}} = \sqrt{\frac{2eU}{m_{\mathrm{e}}}}, \tag{3.2}$$

where U represents the acceleration potential of the electrons. For velocities faster than approximately 10% of the speed of light c_0, a relativistic treatment must be applied

$$v_{\text{relativistic}} = c_0 \sqrt{1 - \frac{1}{\left(1 + \frac{qU}{m_{\mathrm{e}} c_0^2}\right)^2}}. \tag{3.3}$$

Potential

The potential induced by the electron beam in the trap center can be estimated if the electron beam is assumed being infinitely long and homogeneous and by solving the Poisson equation [13, 95]

$$\Delta \Phi_{\mathrm{e}} = -\frac{\rho}{\epsilon_0}. \tag{3.4}$$

Here, ρ corresponds to the charge density. In the case of equally distributed electrons in the beam, the Poisson equation simplifies to

$$\frac{1}{r}\frac{\partial}{\partial r}r\frac{\partial}{\partial r}\Phi_{\mathrm{e}}(r) = -\frac{\rho}{\epsilon_0}. \tag{3.5}$$

By assuming the charge density ρ to be zero outside the electron beam and constant inside, ρ is then given by

$$\rho = \frac{I}{\pi r_{\mathrm{H}}^2 v}. \tag{3.6}$$

The solution of this equation leads to the potential of the electron beam [13]

$$\Phi_{\mathrm{e}} = \begin{cases} \Phi_{\mathrm{D}} + \Phi_0\left(\left(\frac{r}{r_{\mathrm{H}}}\right)^2 + 2\ln\left(\frac{r_{\mathrm{H}}}{r_{\mathrm{D}}}\right) - 1\right) & \text{if } r \leq r_{\mathrm{H}}, \\ \Phi_{\mathrm{D}} + \Phi_0 2\ln\left(\frac{r}{r_{\mathrm{D}}}\right) & \text{else,} \end{cases} \tag{3.7}$$

where Φ_{D} represents the potential of the central drift tube and r_{D} the inner radius of the central electrode, respectively. The potential Φ_0 depends on the charge density within the electron beam and is expressed by

$$\Phi_0 = \frac{I}{4\pi\epsilon_0 c}\left(1 - \left(1 + \frac{qU}{m_{\mathrm{e}}c^2}\right)^{-2}\right)^{-\frac{1}{2}}. \tag{3.8}$$

Energy

Due to the different electrostatic potentials of the electrodes, the electron beam energy strongly depends the spatial position of the electron beam. Since only ions in the trap center are efficiently stored and observed, the beam energy outside the center is of no further interest. In the trap, the effective electron beam energy is influenced by various parameters of the machine. In general, the electron beam energy is defined by the potential difference between the origin of the electrons at the cathode -Φ_{Cathode} and the central drift tube Φ_{D}. In addition, the beam energy is affected by the Coulomb repulsion of the electrons $\Phi_{\mathrm{Electrons}}$ and attraction of the ions Φ_{Ions} in trap, respectively. The total effective electron beam energy in the interaction region is determined by

$$E_{\mathrm{Beam}} = e\left(-\Phi_{\mathrm{Cathode}} + \Phi_{\mathrm{D}} + \Phi_{\mathrm{Ions}} - \Phi_{\mathrm{Electrons}}\right) \tag{3.9}$$

3.2 The PolarX-EBIT

In this section, the PolarX electron beam ion trap (PolarX-EBIT) that was operated for the results presented in this thesis will be introduced and its components discussed in detail. In 2016, this EBIT was built and commissioned as one of three

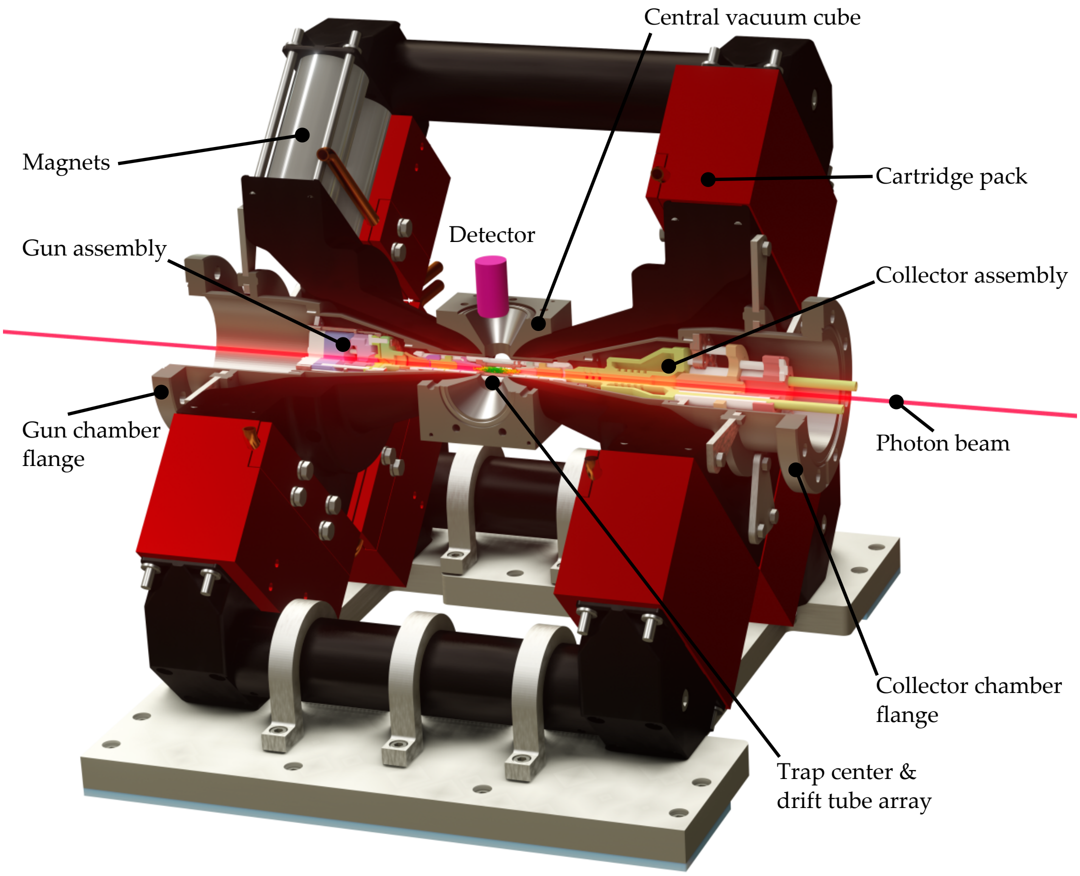

FIGURE 3.2: Sectional view of the PolarX-EBIT. The electron beam is emitted by a novel off-axis electron gun. This design allows an external photon beam to passalong the main axis of the experiment through the trap center. The magnetic field is produced by permanent magnets mounted in aluminum cartridges. Bores in the central vacuum cube allow for mounting detectors close to the trap center.

Heidelberg Compact EBITs [95, 119]. It is dedicated to the study of interactions of monochromatic X-ray photons with highly charged ions.

In contrast to superconducting EBITs, in which the magnetic field is produced by a pair of cryogenic superconducting coils in nearly Helmholtz configuration, the PolarX-EBIT utilizes a magnetic system based on permanent magnets at room temperature. Furthermore, the magnetic system enables a more compact footprint. Hence, vital components, such as electron gun, drift tube array, collector, and detection system are designed to much smaller dimensions compared to superconducting EBITs. The frame, on which the EBIT is mounted, exhibits a length of 120 cm and a width of 44 cm, which allows for convenient transportation. The compact dimensions combined with the advantage of the room temperature and free-of-maintenance magnetic system based on permanent magnets enables quick deployment after transportation.

Furthermore, the PolarX-EBIT features a novel off-axis electron gun leaving the longitudinal axis of the experiment free from obstacles. The free main axis allows to introduce an external photon beam to the trap region from both sides through the collector as well as gun, allowing for a parasitic use of the EBIT at beamlines of various light sources with another experimental setups downstream. In figure 3.2 a sectional overview of the central parts of the PolarX-EBIT is shown.

3.2.1 Magnetic system

The magnetic field in the PolarX-EBIT is generated by a set of permanent magnets arranged in an assembly to maximize the electron current density in the trap center. For this purpose, the cathode is positioned at nearly zero-magnetic field. The electrons, emitted there, propagate along the field lines with increasing flux density towards the trap center, where the strongest compression of the electron beam is achieved. The magnetic system consists of 72 permanent neodymium magnets with a diameter of 45 mm and height of 30 mm each. The magnets have an adhesion force of approximately 700 N m and can be heated up to 80 °C without losing their magnetization. The Curie temperature at which the magnets are entirely demagnetized is at 310 °C [113]. The magnets are arranged in eight cartridge packs in a four-fold symmetry with respect to the electron beam axis. Four cartridge packs are mounted on both sides of the EBIT, each containing three columns of three magnets each. Radially, the inner cartridges of each stack are mounted on one of two rectangular soft-iron yoke parts which pass into conical pole pieces tapering towards the trap center. The axially opposing outer pairs of cartridges are connected by cylindrical soft-iron bars, see figure 3.3. Figure 3.4 depicts finite element method (FEM) simulations as well as measurements of the magnetic field strength along and perpendicular to the main axis of the setup. Measurements revealed a maximal magnetic field strength in the trap center of approximately 860 mT, well above the simulated field strength [119, 38].

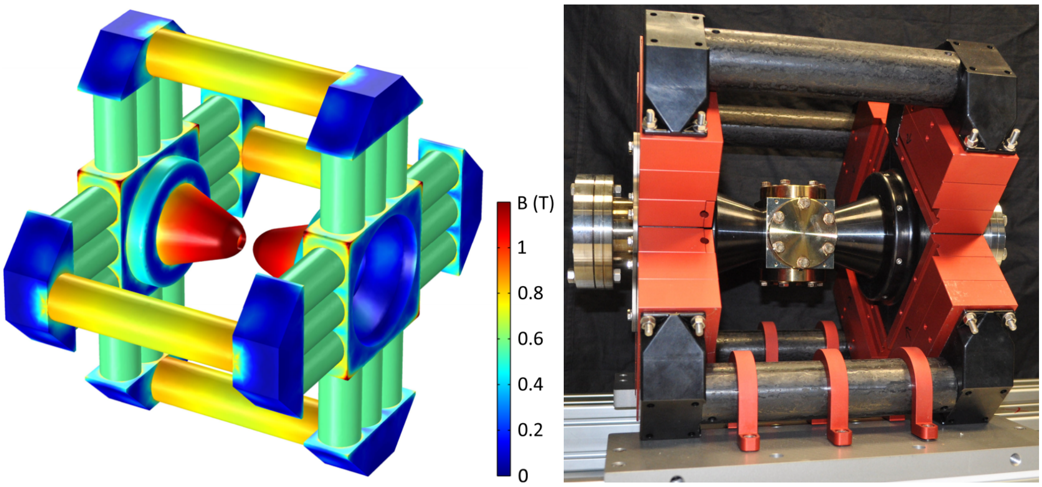

FIGURE 3.3: Left: Finite element method (FEM) simulation of the magnetic field strength using COMSOL. Highest magnetic field strengths are obtained at the tips of the yoke (red). Right: Photograph of the magnetic system of the PolarX-EBIT. On each side 36 magnets are mounted inside the four red cartridges. Figure adopted from [119].

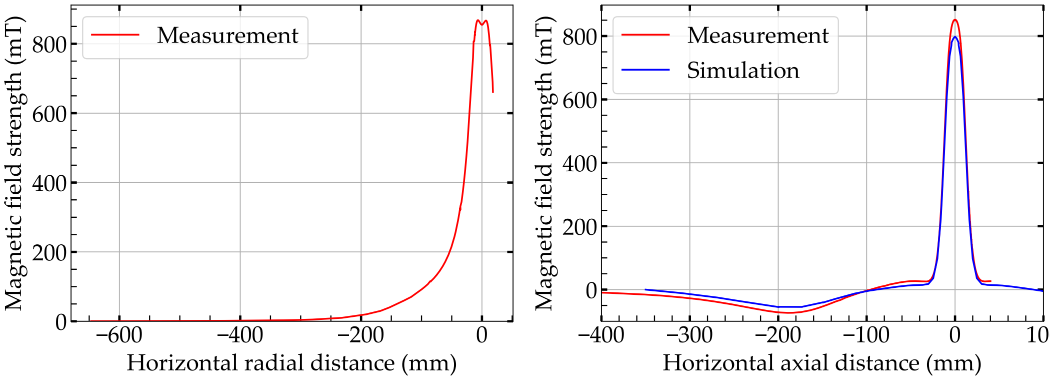

FIGURE 3.4: Measurement and simulation of the magnetic field strength of the PolarX-EBIT in the axial and radial direction as a function of distance to the trap center. Data adopted from [38].

3.2.2 Vacuum system

The vacuum system of the PolarX-EBIT consists of four different sections, namely the gun, trap, collector, and injections. Each section consists of a recipient which is pumped by several turbomolecular pumps (TMP) to reach the required pressures in the order of 1×10^{-9} mbar. The vacuum chambers of the gun and collector are directly connected to the central, cubic recipient, in which the trap components are mounted, see figure 3.2. Inner parts of the recipient were electropolished to reduce the surface area and thereby minimizing the outgassing rate of the walls resulting in a lower pressure. Each TMP is connected to the pre-vacuum system consisting of another TMP combined with a roughing pump. This two-stage pumping system ensures that ultra-high vacuum (UHV) conditions are maintained and components of the experiment sensitive to humidity are protected in case of a malfunction of one of the TMP.

3.2.3 Off-axis electron gun

The electron gun generating the electron beam consists of three distinct parts, a cathode, a focus electrode, and an anode. The thermionic cathode emits electrons which are accelerated inside the gun by the potential difference between cathode and anode. The focus electrode which is mounted between cathode and anode focuses the electron beam. In the PolarX-EBIT a novel gun design was employed in which the cathode is mounted off-axis, see figure 3.5. The design keeps the optical main axis of the experiment free, allowing for an external photon beam to pass through the gun unperturbed. In the first part of this section, details of the prototype off-axis gun will be presented. In the second part, a revised version of the gun addressing the limitations of the prototype will be introduced.

Prototype gun

Cathode

In an electron gun, the electrons are emitted by a cathode. In order to reach high electron beam currents, a cathode exhibiting a low work function is necessary. Here, a commercial barium dispenser cathode is employed. The tip of the dispenser cathode consists of a porous tungsten matrix in which barium oxide is dispersed. A monoatomic layer of barium is generated by heating the cathode to temperatures between 850 °C and 1200 °C [41, 81] to lower the work function. Additional osmium and ruthenium coatings (M-type coatings) on the tip of the cathode lower the required operation temperatures, prolonging the lifetime of the cathode [80].

Heating of the cathode is achieved by applying a voltage across the cathode housing and its filament inducing the heat [82]. The voltage applied to the filament must be negative with respect to the cathode housing since tungsten ions forming on the hot filament wire surface may react with oxygen in the alumina potting and

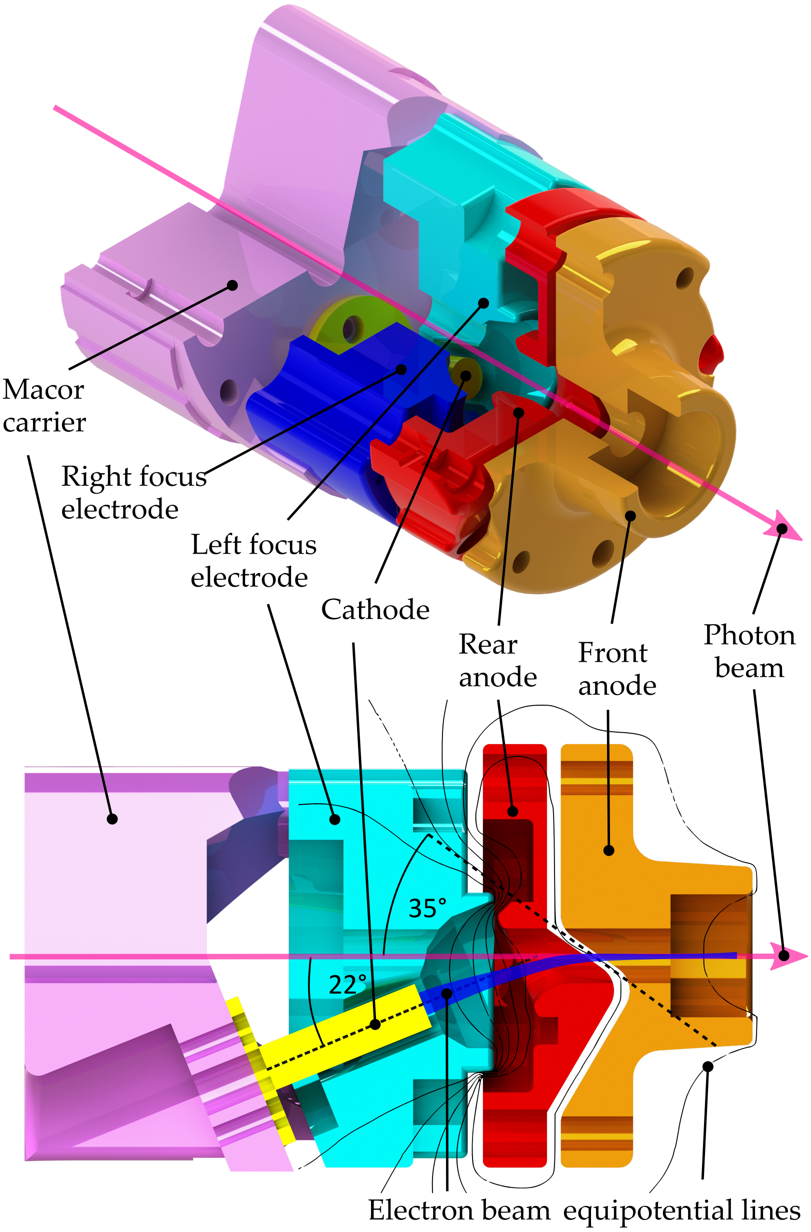

FIGURE 3.5: Cross-sectional views of the prototype off-axis electron gun. The cathode (yellow) is tilted by an angle of 22° to the trap axis to allow an external photon beam to pass through an unobstructed central bore. The mirror-symmetric focus electrodes compensate for a drift of the electron beam due to the Lorentz force. Bending of the electron beam onto the trap axis is realized by splitting the anode into a rear (red) and a front (orange) electrode, cut by a 35° plane with respect to the horizontal. Simulated electrostatic potential lines (black) and electron beam trajectories (blue) are also shown. Figure adopted from [119].

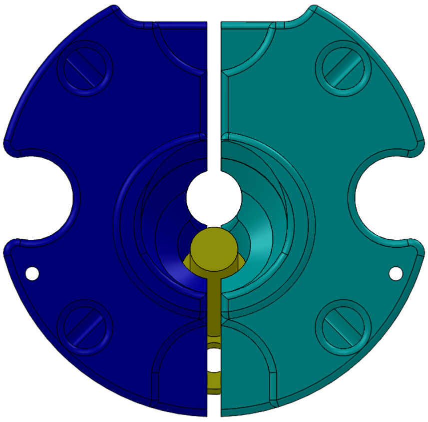

FIGURE 3.6: Front view of the focus electrodes of the off-axis gun along longitudinal axis. The tilted cathode is shown in yellow, the two focus electrodes in turquoise and blue. To compensate for the Lorentz force acting on the electron beam due to the magnetic field, individual voltages can be applied to the two focus electrods. Figure adopted from [95].

form $Al_2(WO_4)_3$, potentially damaging the cathode [83]. Before the first operation, an activation is necessary which is accomplished by slowly heating the cathode. By slowly increasing the current, the cathode heats up until a temperature between 1000 and 1200 °C is achieved. The resistance of the cathode increases as the temperature rises from approximately one to a few ohms.

In order to prevent poisoning of the cathode, the heat-up process must be conducted slowly and at UHV conditions ($p < 1.0 \times 10^{-7}$ mbar) at any time. If the temperature increases at high rates, moisture inside the substrate cannot escape, especially at 400 °C, where the temperature breaks down the hydrates formed with the barium-calcium aluminates, and at 900 °C, where W_2O_5 breaks down and allows the reduction to clean tungsten [84]. Both processes may lead to blisters on the cathode surface, drastically reducing its lifetime and performance capabilities. Once the cathode cathode is activated, it is very sensitive to oxygen and humidity. Therefore, exposure to air requires a subsequent reactivation of the cathode.

Focus electrodes

The focus electrode is mounted between the cathode and the anode to electrostatically focus the electron beam. Since the distance to the hot cathode is short, focus electrodes are made of molybdenum to sustain the high heat load.

In contrast to regular electron guns [19, 119], the cathode of the off-axis gun emits the electron beam at an angle of 22° with respect to the main axis, see figure 3.5. Thus, the electron beam propagates with an angle to the magnetic field lines, resulting in an additional deflecting Lorentz force. In order to compensate for this effect, the focus electrode is split into two parts, see figure 3.6. By applying a voltage across the focus electrodes, the electron beam can be steered in the opposite direction of the deflecting Lorentz force and compensate for it.

Additionally, the two electrodes focus the electron beam together inside the electron gun for a stable beam extraction. In order to establish an appropriate focusing effect, the electrodes are both operated at slightly more negative voltages than the cathode. Without the focusing, the electron beam hits the backside of the anode and no stable beam extraction would be feasible.

Furthermore, the potential difference between the cathode and focus electrodes actively stabilizes the current of the emitted electron beam. In general, the lower the potential difference, the higher the electron emission. This effect can be used for a closed-loop electron beam current control.

Note that if the cathode voltage is altered, it is required to change the focus voltages accordingly to sustain the electron current as well as to ensure proper electron beam deflection.

Anodes

In an conventional on-axis electron gun, the anode is mounted downstream the focus electrode. It is used to accelerate the electron beam towards the trap center as well as to adjust the electron beam current level. However, in an off-axis gun, the anode is required to bend the electron beam onto the main axis. Thus, the anode is split into two electrodes along a plane at 35° with respect to the horizontal plane, see figure 3.5. Similar to the focus electrodes, the rear anode controls the current emitted by the cathode, while the front anode accomplishes the deflection onto the main axis. Simulations agree with experimental results that the positive front anode voltage should be approximately half the rear anode voltage.

Carrier and housing

High voltages are required to bias the individual electrodes. Since cathode and anode have opposing polarity, potential differences of up to 6 keV may be encountered. Hence, sufficient spacing and creepage distances are required. The off-axis gun prototype design consists of a carrier mount made of Macor, providing excellent insulator properties. The cathode and focus electrodes are directly mounted onto the carrier, while the anodes are stacked onto the focus electrodes using ceramic insulators. The distance between the anodes is maintained by small insulator washers. An aluminum housing around the gun electrodes exerts force longitudinally between the anode front and the carrier backside to fix all components of the gun, see left panel of figure 3.7.

Next generation gun

The operation and performance of the off-axis electron gun prototype described in the previous chapters was excessively tested during the preparation and execution of various measurement campaigns. Cathode voltages up to $-2000\,\mathrm{V}$ and electron beam currents up to $25\,\mathrm{mA}$ were successfully operated. However, short distances

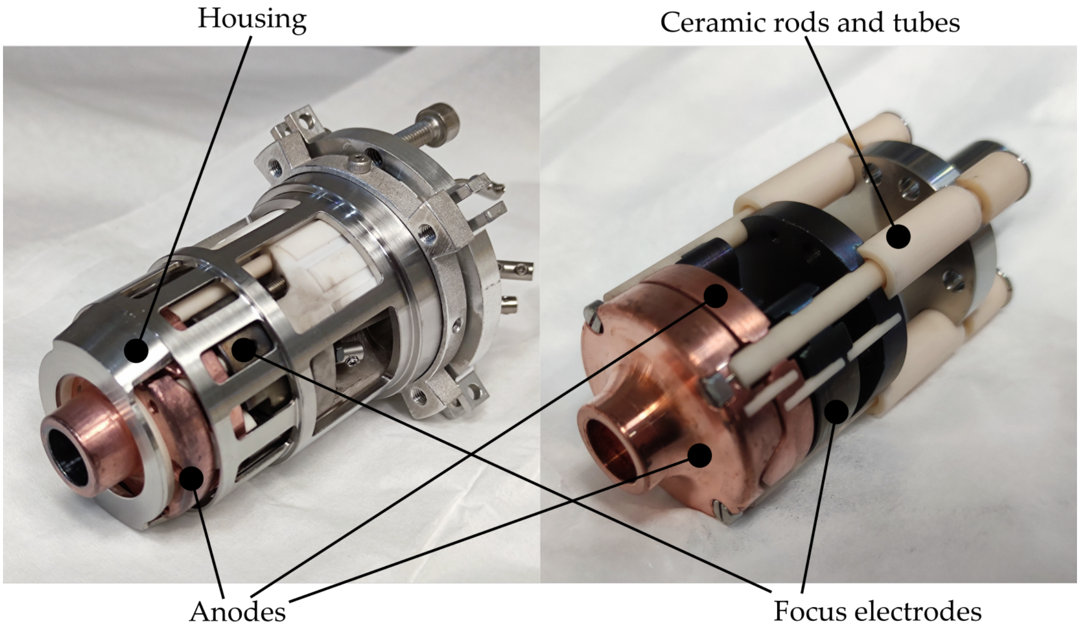

FIGURE 3.7: Comparison of the prototype (left) and the next generation (right) off-axis gun. In the revised design, the electrodes are kept in place by four ceramic rods instead of an aluminum housing. The creeping distance between the electrodes is enlarged by small ceramic rods.

between the individual electrodes have limited the maximum applicable voltages. Furthermore, the prototype electron gun is held together by a cylindrical aluminum housing surrounding the electrodes, which drastically reduced the pumping cross section towards the gun interior. In the former design, the cathode is the central part that needs to be installed first during assembly. The exposure of the cathode to atmospheric conditions should be reduce to prevent poisoning. Thus, the electron gun needed to be assembled in an inert gas atmosphere and subsequently mounted in the experiment. In the case of occurring shorts during high voltage tests, the gun was required to be disassembled again, potentially harming the cathode.

The next generation off-axis gun design addresses the problems mentioned above. Instead of stacking one electrode on top of another, all electrodes now share a carcass of four insulating ceramic rods, which increases the overall stability and allows for the removal of the aluminum housing, which drastically enhances the pumping cross section of the whole assembly. In order to improve the dielectric strength between the electrodes, the creepage distance was increased to at least 5 mm between two adjacent electrodes. Finally, the geometry was changed such that the cathode is now the last part installed during assembly. This allows for testing of the electric connections and dielectric strength in the final assembly and for mounting the cathode after the tests were successful.

The geometry of the electrodes inside the gun remained unchanged to ensure similar performance. First tests revealed a reduced leakage current compared to the prototype, allowing to apply higher voltages to the electrodes resulting in higher beam currents and energies. The electron beam loss inside the gun, e.g., electrons

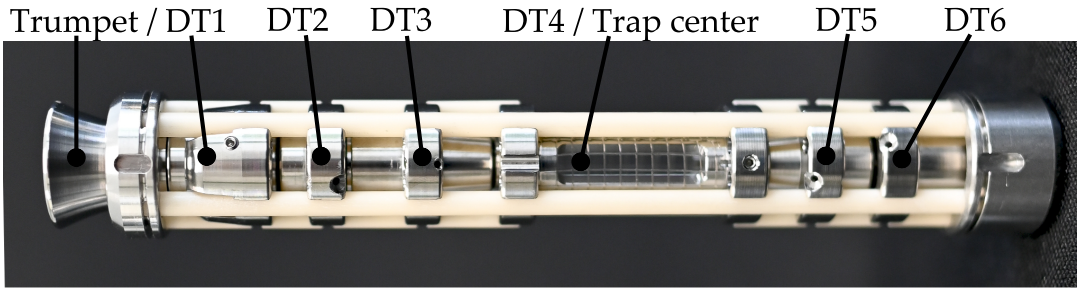

FIGURE 3.8: Picture of the drift tube (DT) assembly. The optical access to the trap center is enabled by the cut-outs in the central electrode. The trumpet on the left hand side is oriented toward the electron gun and improves the guidance of the electron beam into the trap center.

hitting the anode, could be optimized to nearly 0%. Pictures of the prototype and the revised design are shown in figure 3.7.

3.2.4 Drift tubes

In an EBIT, ions are produced by electron impact ionization. In order to confine the ions axially, an electrostatic potential well is established by a set of cylindrical drift tubes. Additionally, the drift tubes are employed to guide the electron beam through the trap center and towards the collector.

The drift tube assembly of the PolarX-EBIT consists of six hollow cylindrical titanium electrodes placed at the center of the magnetic system, see figure 3.8. The first drift tube points towards the electron gun and has a trumpet-shaped extension for threading in the electron beam. The first and second electrodes are used to minimize electron losses inside the assembly. The third, fourth, and fifth electrodes form the axial trap. The sixth and last drift tube is used for further electron beam steering and is typically operated close to ground potential.

The potential confining the ions at the trap center is formed by applying a potential difference between the fourth and its adjacent electrodes. The potential difference is referred to as the axial trap depth and affects the ion cloud temperature, trap conditions, and the total number of stored ions. The potential difference between to the central drift tube and the cathode defines the electron beam energy at the trap center. Furthermore, the central drift tube provides optical access to the ion cloud by four 16 mm long and 2.5 mm broad cut-outs. To mitigate fringe effects, the cut-outs are covered by a stainless-steel mesh. The drift tubes in the PolarX-EBIT are high-voltage proven up to 6 kV. Similar setups have been operated up to voltages of 8 kV [147].

3.2.5 Collector

The collector assembly. see figure 3.9, is mounted on the opposite side of the electron gun and consists of three electrodes. Its primary purpose is to dump the electron beam on an electrically isolated electrode after passing through the trap center. The collecting electrode is connected to the ground of the cathode which allows to measure the number of electrons impinging on the collector. Since the cathode is biased with respect to the collector, the impinging electrons dissipate heat

$$P = \kappa \cdot U_{\mathrm{Cath}} \cdot I_{\mathrm{Cath}}, \tag{3.10}$$

where U_{Cath} and I_{Cath} represent the bias voltage of the cathode and the emission current, respectively. The dimensionless parameter κ describes the transmission, e.g., the fraction of emitted electrons arriving at the collector. The dissipated heat can reach values up to tens of watt resulting in the need of water cooling to maintain ultra-high vacuum conditions. In order to prevent local melting of the collecting electrode, maximal heat flow is required and achieved by high-purity copper. In this setup, the electrode is connected to a passive chiller employing electrically insulating fluid feed-throughs.

Two additional extractor electrodes are located downstream the collector electrode and are biased negative with respect to the cathode to prevent the electron beam from passing through the collector electrode. If the EBIT is operated as an ion source, by ejected the trap content through the collector the two extractor electrodes are also utilized to focus the ion beam [137].

3.2.6 Injection system

The residual gas of the apparatus is dominated by hydrogen, oxygen, nitrogen, water, and hydrocarbons desorbing from the vacuum chamber surfaces. If ions of other elements are desired, appropriate neutral atoms or molecules can be injected into the apparatus through a differentiallypumped injection system. It employs a TMP, a pressure gauge, and a needle valve and is attached to the central vacuum chamber of the experiment through a 5 mm-diameter aperture, see figure 3.10. The needle valve allows to precisely regulate the flow between the injection system and the gas inlet. On the backside of the needle valve, gaseous, liquid or solid substances can be attached. However, liquids and solids are required to exhibit a relatively high vapor pressure to evaporate or sublimate into the vacuum.

A full range pressure gauge provides a quantitative diagnostic of how much gas is injected. Furthermore, the gauge indicates variations of the pressure due to temperature changes and depletion in the source reservoir attached to the backside of the needle valve.

A gate valve is used to stop the injection for diagnostic reasons or to maintain UHV-conditions in the trap center while the injection system pressure is high, for example, during the exchange of the source or maintenance of the injection system.

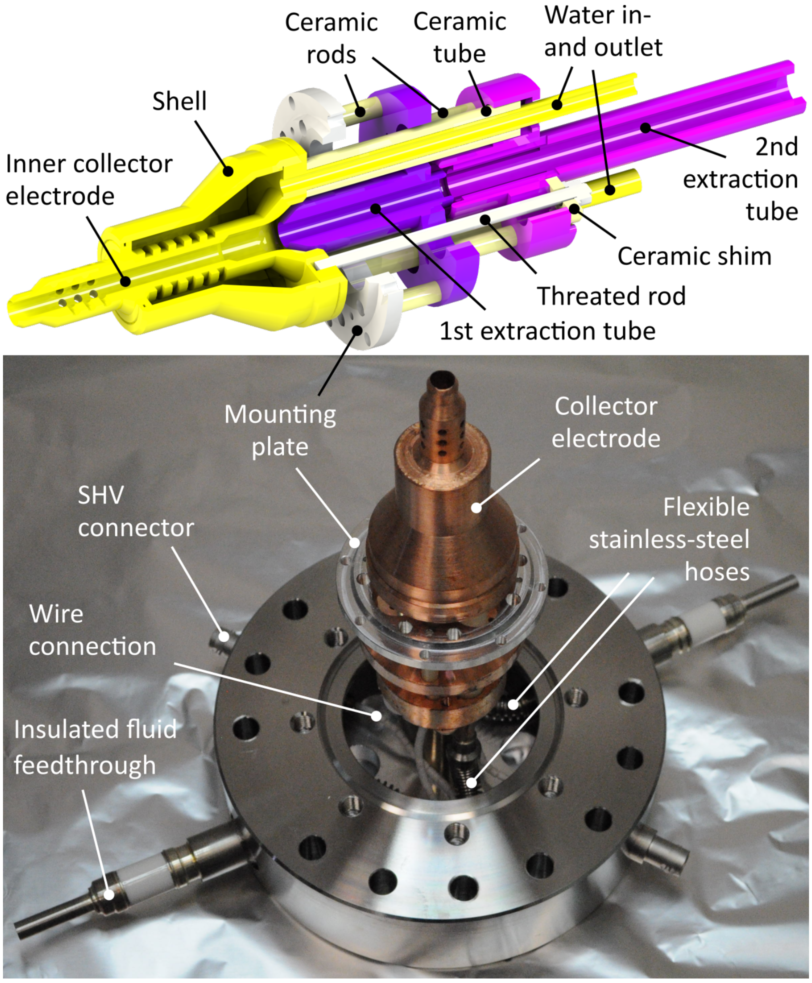

FIGURE 3.9: Top panel: Schematic drawing of the collector assembly. Bottom panel: Picture of the assembly including the mounting flange and the electrical and water cooling connection. Picture adopted from [119].

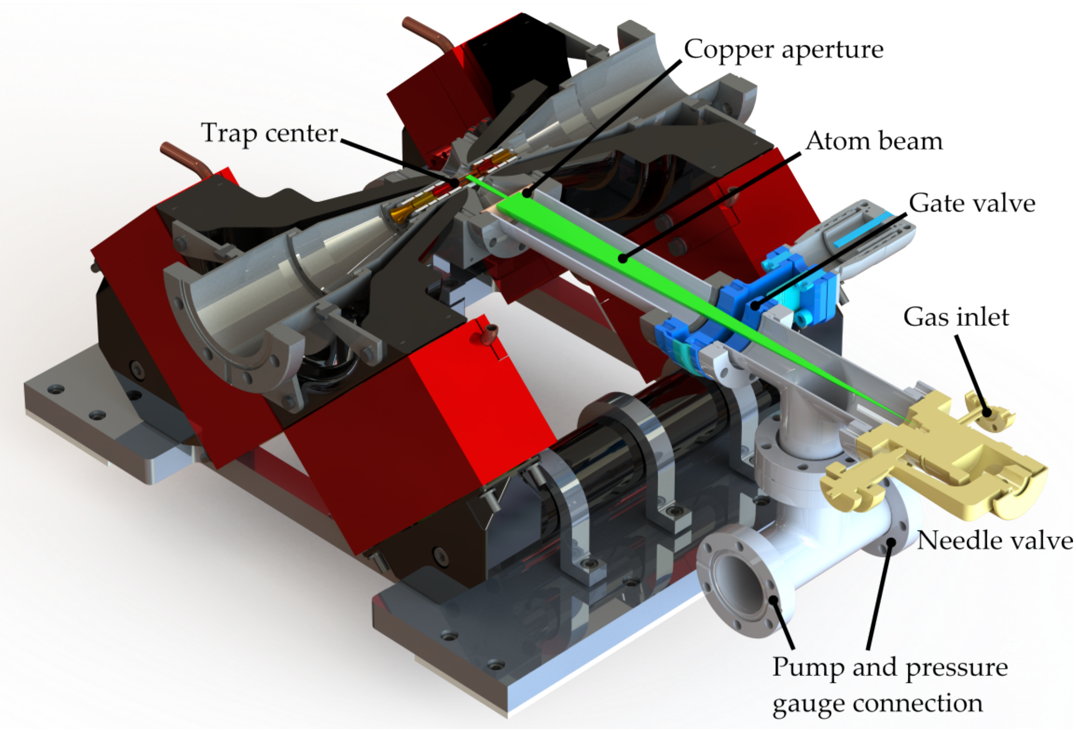

FIGURE 3.10: Cross section through the EBIT and injection system. The needle valve (yellow) regulates the injected gas quantity. Only the central part of the injected particle beam (green) enters the trap. A gate valve (blue) can be closed to separate the injection system from the EBIT.

3.2.7 Detection of X-ray photons

The ions stored in the trap center of the EBIT continuously emit photons. In order to acquire the emitted spectrum, suitable detectors are attached to the central cube of the EBIT. This setup employs a silicon drift detector (SDD), which offers a large photon acceptance from soft to hard X-rays. In this section, the working principle of a SDD is briefly explained. Deeper insights beyond the scope of this thesis may be found in the sources used [99, 100, 42, 58].

A SDD consists of a cylindrical n-doped silicon substrate with a thickness of only a few hundred microns, see figure 3.11. The back side of the detection area is covered by a p-doped layer, while on the front side separate concentric rings of p-doped material are distributed and equally spaced. Close to the center of the front side, an electron collecting anode is located. This concentric design minimizes the anode size, drastically reducing its capacity. A n-channel junction-gate field-effect transistor (JFET) is directly integrated on the front side close to the anode. A potential difference between the back and front plate is applied, fully depleting the substrate. The concentric field strips on the front plate exhibit increasing negative voltage biases with respect to the anode, applied by a set of voltage dividers. The maximum negative voltage of approximately two times the back plate voltage is applied to the outermost ring.

An X-ray photon entering the detection volume from the back side causes an

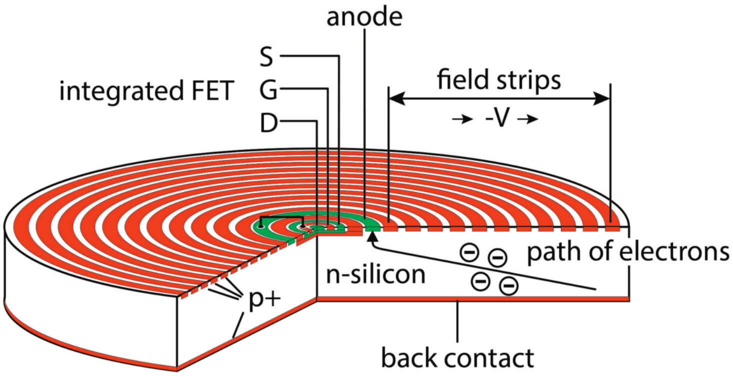

FIGURE 3.11: Schematic of a silicon drift detector. X-ray photons entering the substrate from the backside produce an electron-hole pair. Electrons drift towards the anode on the front plate resulting in a charge increase in the connected capacitor, which is proportional to the photon energy. Figure adopted from [42].

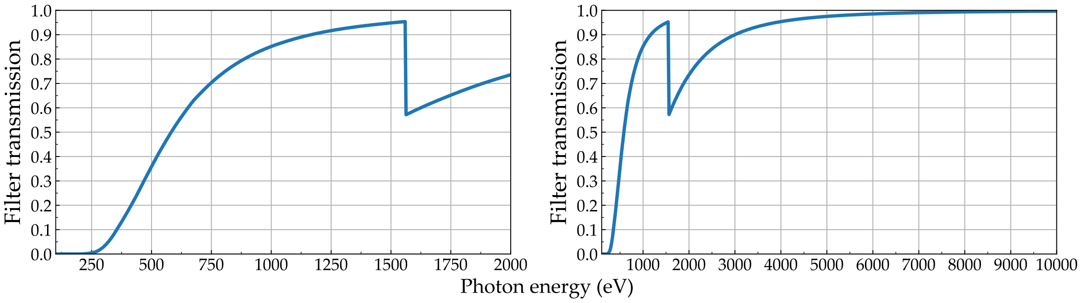

FIGURE 3.12: Left panel: Tansmission curve of the 500 nm thick aluminum filter in the XUV energy regime is shown. Right panel: Extented energy range from 100 eV to 10 000 eV. Data adopted from [74].

electron-hole pair in the substrate. While the electron holes drift to the back contact, electrons are forced towards the collecting anode by the potential of the p+ strips on the front plate as well as the potential difference between the front and back plate. Each arriving electron charges a capacitor, which is connected to the anode. The deposited charge is proportional to the energy of the detected X-ray photon. Besides the signal charges, leakage currents also charge the capacitor. Once the charge in the capacitor exceeds a certain threshold, the capacitor is cleared again by a reset pulse. This leads to a sawtooth-like signal, where positive voltage steps correspond to the energy of the detected photon, while the falling edges correspond to the negative reset pulses. The pre-amplified signal is fed into a commercial spectroscopy amplifier Ortec 672 [127]. Due to the opposing polarity of the photon signal and the reset pulses, they are separated by processing the derivative of the signal. Internally, the spectroscopy amplifier converts the step-like signal of the incoming photons to a Gaussian shape, where the area under the Gaussian corresponds to the detected photon energy.

The analog signal is digitized using a commercial analog-to-digital converter (ADC) „FastComTec Multiparameter Multichannel Analyzer“ [55]. The area of the Gaussian signal is assigned to one of up to 8192 digital channels, each corresponding to a certain photon energy. Thresholds and discriminators of the ADC are used to suppress noise induced by the leakage current in the substrate of the detector.

Compared to cryogenic EBITs [53, 19], the compact design of PolarX-EBIT allows for mounting the detector only a few millimeters from the ion cloud, resulting in a large solid angle of approximately 1.0 sr. The SDD is sensitive to visible and ultraviolet photons emitted as black body radiation by the hot cathode and pressure gauges. The large number of photons in this low energy regime is sufficient to fully saturate the detector. Hence, a filter in front of the detector is employed to block the visible and ultraviolet light. Here, a 500 nm thick aluminum filter was mounted between the ion cloud and the sensor. The transmission efficiency of the employed filter is depicted in figure 3.12.

Chapter 4

Synchrotron radiation

In this chapter, the concept and historical background of synchrotron radiation will be introduced. With these fundamentals, the synchrotron facility PETRA III in Hamburg and especially the XUV beamline P04 with its components relevant for this work will be discussed.

4.1 Basics

In 1944 Iwanenko et al. [85] predicted an upper limit for the attainable energy in a betatron. Since in a betatron electrons move in a magnetic field, they are continuously accelerated and radiate photons in accordance with classical electrodynamics. In 1947 this effect was observed for the first time as a loss mechanism of a particle accelerator (synchrotron) at General Electrics. This loss mechanism is the foundation for synchrotron radiation, which is nowadays well understood and will be introduced in this section.

Emission of synchrotron radiation

The power emitted by an electron undergoing an acceleration due to the conservation of energy E is given by the Larmor formula [98]

$$I = \frac{2e^2 E^2}{3c_0^3}, \tag{4.1}$$

where e and c_0 represent the elementary charge and speed of light, respectively [39]. Since the electrons in a synchrotron are usually moving approximately with almost the speed of light, the relativistic form of the equation must be employed

$$I = \frac{2e^2 E^2}{3m^2 c^3} \left(\left(\frac{\mathrm{d}\,(\gamma p)}{\mathrm{d}\tau} \right)^2 - \frac{1}{c^2} \left(\frac{\mathrm{d}E}{\mathrm{d}\tau} \right)^2 \right), \tag{4.2}$$

where $\mathrm{d}\tau = (1/\gamma)\,\mathrm{d}t$ and

$$\gamma = \left(1 - \left(\frac{v}{c} \right)^2 \right)^{1/2} = \frac{m_0 c^2}{E}. \tag{4.3}$$

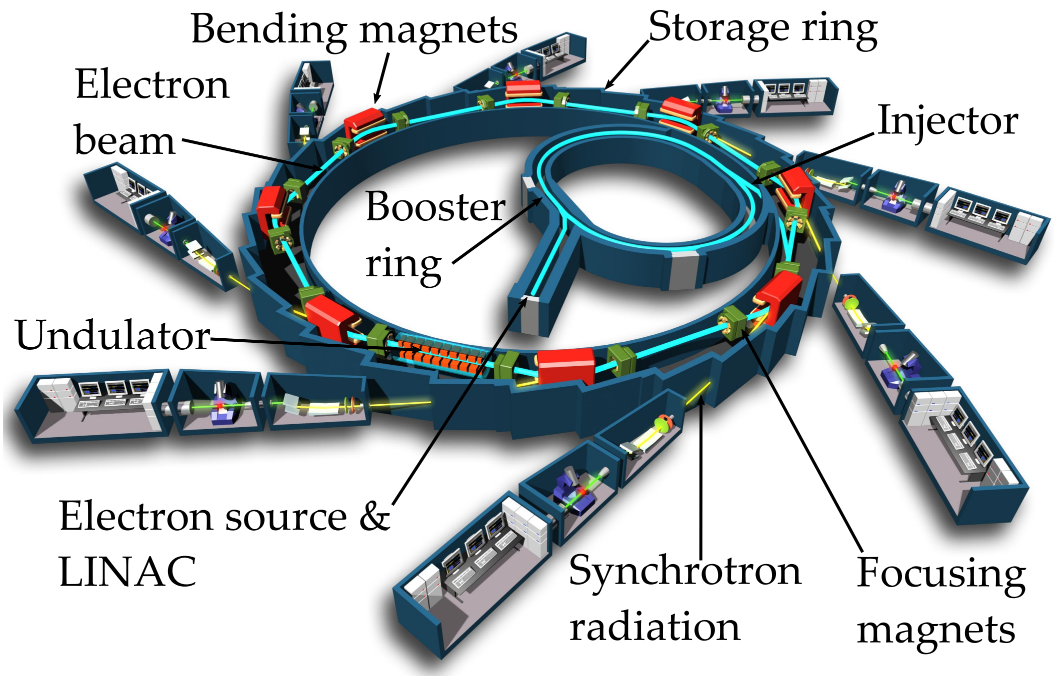

FIGURE 4.1: Overview scheme of a synchrotron. An electron beam is emitted by an electron source, accelerated by means of a two-stage system (LINAC and Booster) and injected into the main storage ring. In the ring, bending magnets force the electrons onto their cylindrical trajectories. Several quadrupole magnets refocuse the beam inbetween insertion devices, in which either a wiggler or undulator may be placed to produce photons. Figure adopted from [54].

Here, $m_0 c_0^2$ is the rest mass of the electron and τ is the proper time. According to Lienard et al. [105, 39] the rate of momentum change is larger than the rate of energy change E. Thus, by neglecting the second term of equation 4.2, the so-called Schwinger equation is obtained

$$I \simeq \frac{2e^2 c}{2R^2} \left(\frac{E}{m_0 c^2} \right)^4 , \tag{4.4}$$

where R represents the orbital radius of the electron. The total energy radiated per revolution is given by

$$\Delta E = \frac{2\pi I R}{c} \simeq \frac{88.5 E^4}{1 \cdot 10^{33} R}. \tag{4.5}$$

In the laboratory, synchrotron radiation is commonly produced by circular accelerators, where bending magnets are employed to force the electrons to follow a circular path, see figure 4.1. First, the free electrons are generated in a suitable source and pre-accelerated using a linear accelerator (LINAC) up to kinetic energies of several MeV. Subsequently, the electrons enter a booster ring, where the electron energy is steadily increased from MeV to GeV energies. Once the energy of the electrons in the booster ring matches that of the electrons in the storage ring, they are deflected by the injector into the main storage ring. In the ring, the electrons lose energy due to

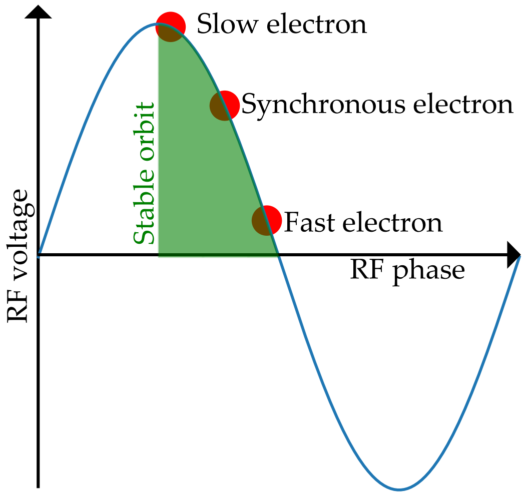

FIGURE 4.2: The sinusoidal shape of the RF voltage accelerates and decelerates electrons (red dots) that are too slow and fast respectively. Synchronous electrons gain exactly the energy lost in the last revolution. Only electrons arriving within the area marked in green are on a stable orbit. Figure adapted from [120].

the emission of the synchrotron radiation. The energy loss is compensated by radio-frequency (RF) cavities. Note that the sinusoidal shape of the RF phase demands the electrons to arrive at a certain point in time and space, see figure 4.2. If a electron is perfectly synchronous to the RF field, it will gain exactly the amount of energy lost during the last turn. On one hand, if an electron is too fast, it will arrive earlier compared to synchronous particles and the total energy transfer will be reduced. On the other hand, if it is too slow it meets the RF field at a higher voltage amplitude resulting in a disproportionately high energy transfer. This effect of the deceleration of fast and acceleration of slow electrons leads to the bunch structure of the electron beam in the storage ring. Note that only a quarter of the RF phase (green shaded area in figure 4.2) can be used for the energy replenishment and the following bunching process. Electrons completely out of phase are not on a stable orbit and will be lost quickly. Thus, the radio frequency is an important parameter of a synchrotron machine limiting the number of allowed stable electron bunches which also determines the bunch separation in space and time.

In a synchrotron, various techniques can be employed to generate photons. The first generation is based on the parasitic use of the radiation emitted by electrons in bending magnets of particle accelerator in the late 1960s. As a next step, dedicated synchrotron facilities of the second generation were built which employed wiggler insertion devices, see figure 4.3. In the wiggler, electrons are periodically deflected by alternating dipole magnets resulting in sinusoidal-like trajectories with N periods of length λ_u. The emitted radiation is the incoherent sum of each individual turn inside the wiggler, which drastically improve the quantity and quality of the photon beam compared to bending magnets.

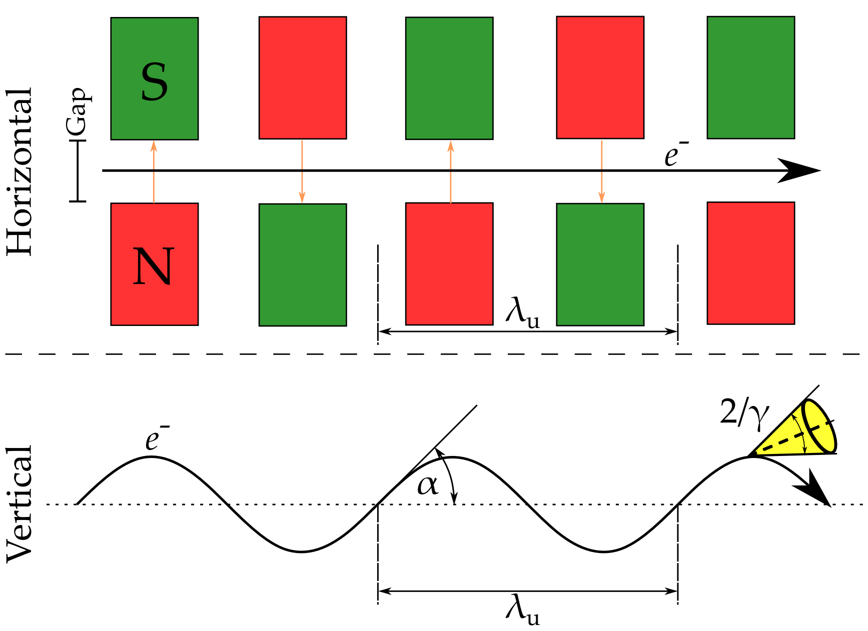

FIGURE 4.3: Sectional view of an electron trajectory in a wiggler in the horizontal plane (top) and vertical plane (bottom). In the horizontal plane, the distances between magnet elements longitudinally (λ_u) and transversal (gap) are depicted. Unlike λ_u, the gap distance is variable and determines the photon energy spectrum. In the vertical plane, α and γ are shown which characterize the angle of the electron oscillation and the natural angular aperture of the emitted synchrotron radiation respectively. Figure adapted from [53, 120].

The dimensionless parameter K is given by the ratio between the wiggling angle α and the natural angular aperture of the synchrotron radiation $1/\gamma$ [120]

$$K = \alpha\gamma. \tag{4.6}$$

In case of an electron moving in a magnetic field on a sinusoidal trajectory, K is simplifed to [120]

$$K = \frac{e}{2\pi mc}\lambda_u B = 0.934\lambda_u[\text{cm}]B[\text{T}]. \tag{4.7}$$

The amplitude of the electron trajectory in a wiggler is usually much larger than the emission angle of the synchrotron radiation and no interference between the light emitted from the different periods occurs. In other words, in a wiggler K is usually large ($K \gg 1$).

In third generation synchrotrons, undulators were introduced, which are based on the same basic principle as wigglers. In contrast, in an undulator the K value is below 1, meaning that the wiggling angle of the electron is smaller than the angle of the photon emission cone. In this regime, the electron bunches are able to constructively interfere with photons produced at different positions in the undulator. The wavelength for which the interference condition is met reads

$$\lambda = \frac{\lambda_u}{2\gamma^2}\left(1 + \frac{K^2}{2} + \gamma^2 + \theta^2\right), \tag{4.8}$$

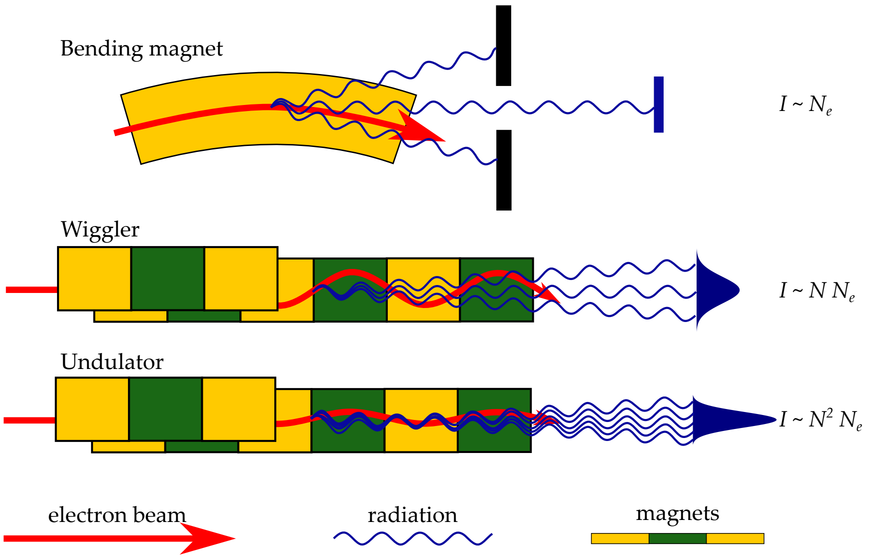

FIGURE 4.4: Overview of the photon production for the three different generation of synchrotron facilities. In the first, radiation emitted in the bending magnets was used parasitically. In the second and third generation, two different insertion devices were employed. In a wiggler (second generation) the electron beam is forced onto a sinusoidal trajectory with a large amplitude with respect to the emission angle of the photons. In undulators, the amplitude of the electrons are reduced until interference between the electrons and photons occur. The photon intensity I depends on the number of electrons in the beam N_e and the number of periods in the magnetic field N. Figure adapted from [171].

where θ describes the angle of observation with respect to the main axis of the undulator [120]. Due to interference, higher harmonics of shorter wavelength than λ are present. Note that for emission along the center axis ($\theta = 0$), only odd harmonics appear. According to equation 4.8, the resonance energy is tunable by changing either λ_u or K^2. λ_u is a fixed undulator design parameter of the distance between the magnetic poles longitudinally and cannot be changed. In contrast, K^2 depends on the magnetic field strength inside the undulator, which is easily adjustable by varying the gap between the magnetic yokes perpendicular to the direction of the photon beam. An overview of the different synchrotron generations is shown in figure 4.4.

For the sake of completeness, one should also mention synchrotron light sources of the fourth generation, also called free electron laser (FEL). Here, either the length of the undulator is extended or several subsequent undulators are employed. In the undulator, electrons form a substructure within a single bunch with a separation corresponding half of the wavelength of the resonance energy. This so-called micro bunching effect drastically increases coherence and brilliance of the photon beam. More information beyond the scope of this thesis may be found in [44, 52, 145].

A common quantity used to compare the quality of the produced photon beam is brightness, also called brilliance. It is defined by

$$\Psi_{\text{Brightness}} = \frac{n_{\text{Photons}}}{A\sigma\lambda}, \tag{4.9}$$

where n_{Photons} represents the number of photons per second, A the source area, ω

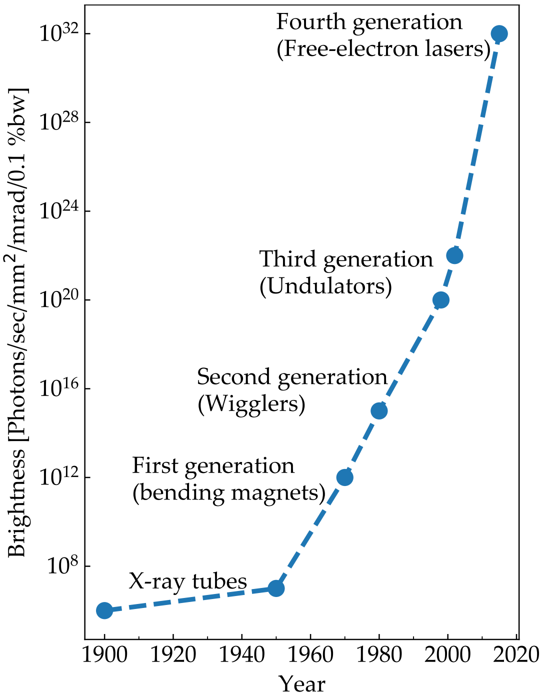

FIGURE 4.5: Semi-logarithmic plot of the evolution of the synchrotron radiation brightness. Note that for sources of the fourth generation, the peak brightness is given instead of the average brightness. Data adopted from [16]

the source divergence and λ the bandwidth, respectively. Figure 4.5 depicts the historical development of the brightness of different X-ray sources.

In principle, the light generated by synchrotrons is polarized. Whether the light is linearly, circularly or eliptically polarized depends on the trajectory of the electrons in the bending magnet, wiggler or undulator. In the most common setup, the insertion device employs alternating poles leading to linearly polarized photons, see figure 4.3. In more sophisticated setups, each side of the undulator is split into two retractable yoke sets, which can be arbitrarily shifted among each other longitudinally. By changing the shifts on both side of the undulator, circular and eliptical polarization can be achieved.

4.2 The variable polarization XUV beamline P04

The Variable Polarization XUV Beamline, also known as P04, is the only soft X-ray beamline of the third generation synchrotron light source PETRA III located in Hamburg, Germany. The acronym PETRA stands for „Positron-Elektron-Tandem-Ring-Anlage“, which translates to „Positron Electron Tandem Ring Facility“ and describes its former purpose when built in the 70s. Positron-electron collision experiments performed in 1979 provided first clear and direct observational evidence of the gluon existence and thus confirmed crucial predictions of quantum chromodynamics [152]. Later the collider was used as a pre-accelerator for the injection into the larger particle accelerator HERA, in which electron-proton collisions were intensively studied

[154]. After HERA was decommissioned in 2007, PETRA converted to its current state as a pure synchrotron facility. In order to distinguish between the different phases of the ring, the extension „III“ was added as a name suffix. Since the first user operation in 2009, the facility steadily increased the number of beamlines in its portfolio. Beside the oldest experimental hall „Max-Von-Laue“, which offers 35 endstations distributed over 15 beamlines (P01-P14), two additional halls were built to accommodate the high demand for synchrotron radiation. Once fully commissioned, PETRA III will provide 26 beamlines operating in parallel [133].

4.2.1 Storage ring

Strictly speaking, PETRA III is not a synchrotron but a storage ring since it is fed with electrons already exhibiting the desired kinetic energy of approximately 6 GeV by a combination of a linear pre-accelerator and the synchrotron DESY. Once injected, the storage ring itself only compensates for the electron energy losses due to radiation emission. The half-life of an injected electron beam is in the order of 10 h. In order to compensate for the electron losses, new electrons are re-injected into the storage ring every few minutes.

PETRA III mainly operates in two different modes. In the so-called „multi-bunch mode“, the ring is filled with 480 equidistant electron bunches resulting in a total beam current of 120 mA. Due to its circumference of 2304 m, the bunch separation in the time domain is 16 ns, which leads to a photon bunch rate of ≈62.5 MHz. In contrast, in the „timing mode“, the number of bunches simultaneously stored in the ring is reduced to only 40, which increases the bunch separation in the time domain to 192 ns and decreases the photon bunch rate to 5.2 MHz. Since in the timing mode the total charge per bunch is increased, the maximum available beam current in the ring is limited to 100 mA, resulting in a slightly decreased maximum photon flux at the endstations. The bunch length in both operation modes is in the order of 100 ps.

In principle, the enlarged bunch separation in the time mode enables coincidence measurements, in which only a fraction of the fluorescence is accepted by the detector as demonstrated in [15, 53]. Depending on the processing time of the detection system, the background of fluorescence signal can be vastly reduced utilizing this technique. In multi-bunch mode, the time separation between two bunches is usually too short for such measurements. Unfortunately, the pulse processing period of the employed silicon drift detector is in the order of several hundreds of ns, preventing coincidence measurements in both modes.

4.2.2 Undulator

P04 employs an APPLE-II-type undulator which stands for „Advanced Planar Polarized Light Emitter“. It consists of in total four magnetic arrays that produce a spatially oscillating magnetic field [146], see figure 4.6. The APPLE-II undulator exhibits a period length, e.g., a distance between two adjacent magnets of $\lambda_\mathrm{u} = 65.6\,\mathrm{mm}$ and in total 72 periods, which results in a total length of ≈5 m [162]. Due to its characteristic period length, the undulator is often referred to as U65.

As described by equation 4.8, the primary energy of the produced photons in the undulator depends on the magnetic field strength. The field strength depends longitudinally on the gap distance, e.g., the distance between the upper and lower magnet arrays perpendicular to the photon emission direction and transversely on the period length λ_u. Since in an APPLE-II undulator λ_u is a fixed parameter, the magnetic field strength can be easily tuned by adjusting the gap. The highest available photon energy is achieved for a minimum gap distance of only 6 mm. At PETRA III, the APPLE-II undulator covers an energy range from 245 up to 2500 eV in the first harmonic while providing a high degree of polarization throughout the entire energy range [5]. A brilliance and energy coverage comparison of the different undulator employed at the PETRA III synchrotron is depicted in figure 4.7.

The polarization of the produced synchrotron radiation depends on the shift of the individual magnetic arrays against each other, see figure 4.6. The geometry depicted in the upper panel results in shift of zero and hence, in a maximum magnetic field strength and linear polarization. In its current state, only shifts of a quarter of the period length are available, for which circular polarization can be obtained.

4.2.3 Monochromatization

The photon beam produced by the undulator exhibits a rather broad energy distribution covering approximately $1/N$ of the primary energy, where $N = 72$ represents the number of periods in the undulator. For a desired energy of, for example, 800 eV, photons in the range from 790 eV up to 810 eV are typically generated. Since this distribution is too broad to probe individual transitions of highly charged ions, further monochromatization is required.

P04 consists of two identical branches each employing an own monochromator. This enables to (dis-)assemble an experiment on the platform of one branch while at the other branch, experiments can be conducted. Since both branches share the same undulator, only one monochromator is provided with photons at a time. To switch between the branches, a switching-mirrors unit (SMU) is located between the undulator and the two branches. Furthermore, several collimators and apertures are installed between the undulator and the monochromators. The apertures enable to clip photons produced off-center of the main axis in the undulator, which would result in a defocused or asymmetric line shape. Since the unmonochromatized photon beam introduces a considerable heat load to those apertures, they require water cooling.

The core of a monochromator utilized at P04 consists of a diffraction grating combined with an exit slit, see figure 4.8. The photon beam produced in the undulator impinges on the grating at a flat angle (also called grazing incidence) and is dispersed according to the individual photon energies. Only a fraction of the dispersed light passes through the exit slit. The exit slit width is variable from a few microns

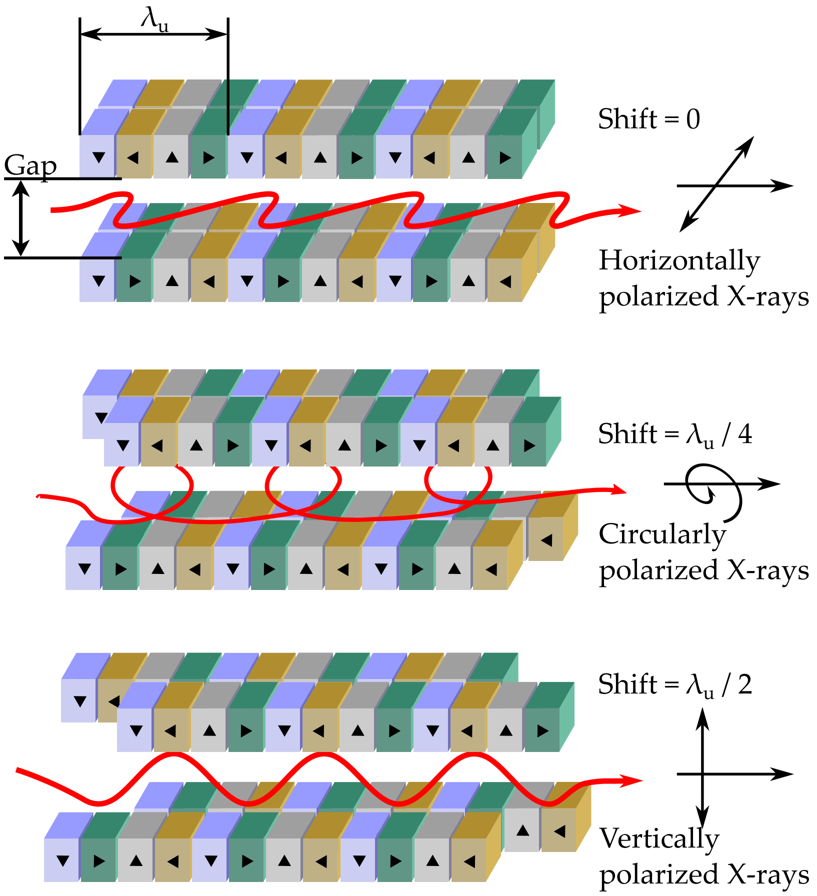

FIGURE 4.6: Design of an APPLE-II-type undulator as employed at P04. Synchrotron radiation is produced by periodically forcing the electron bunch to change its direction of motion. The energy of the produced photons depends on the fixed period length λ_U and the variable distance between the upper and lower magnetic arrays, also called gap. By sliding the magnetic arrays against each other, different types of linear and circular polarization can be obtained. Figure adapted from [142].

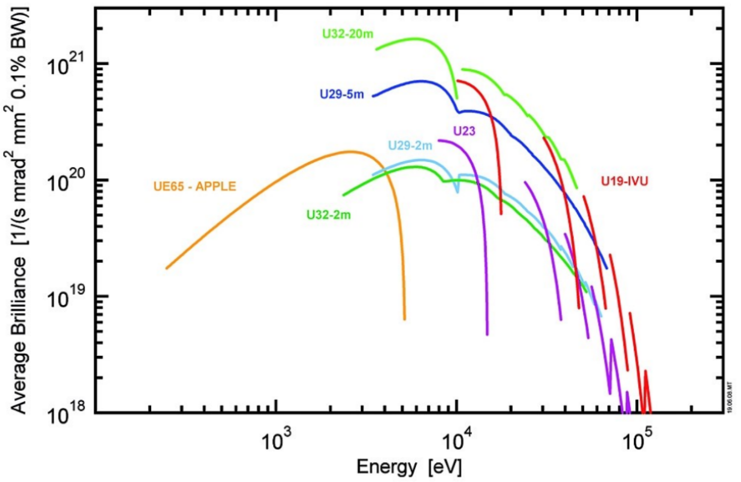

FIGURE 4.7: Average brilliance as a function of photon energy for a selection of available undulators at the PETRA III. The APPLE-II-type undulator (U65) employed at the XUV beamline P04 covers the lowest energy range from 245 eV up to 2500 eV. Note that for U65 only the first harmonic is depicted. Figure adopted from [146].

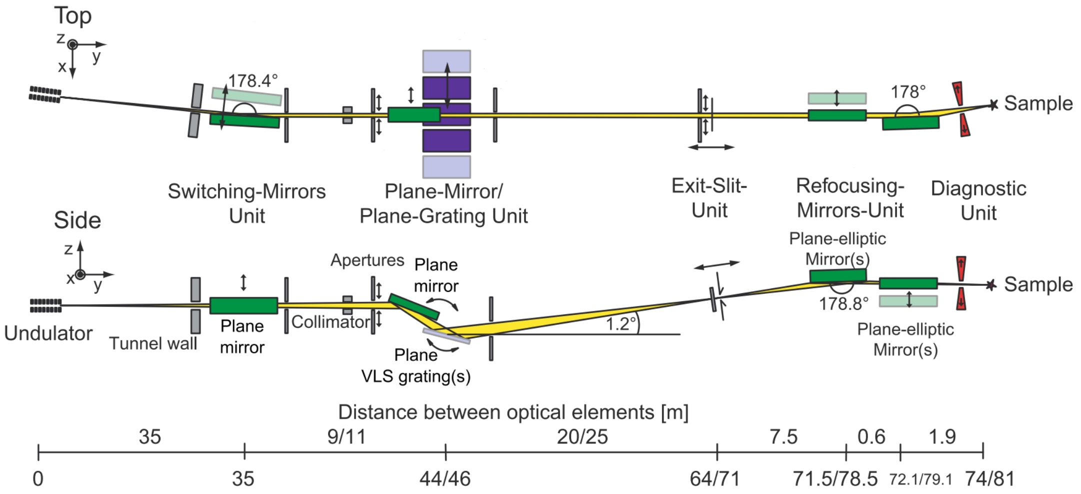

FIGURE 4.8: Layout of one of the two branches at P04. After the photon beam is produced in the undulator, it is either directed into branch 1 or 2 by moving the switching mirror unit (SMU). A combination of a plain mirror and plain grating disperses the light. An exit slit selects only a fraction of the dispersed light and monochromatizes the photon beam. The refocusing mirror unit (RMU) focuses the divergent photon beam onto the sample. Figure adopted from [162].

up to 2 mm, which consequently affects the on-sample photon flux as well as the energetic width of the photon beam, also called resolving power. The P04 design is further based on the so-called Peters mount, which adds a plane mirror in front of the diffraction grating to provide the „variable-included-angle“ capability [132]. In this configuration, the so-called constant fixed-focus value

$$c_{ff} = \frac{\cos\beta}{\cos\alpha} \tag{4.10}$$

is introduced, where α and β represent the angle of the normal incidence to the grating and the angle of diffraction, respectively, see figure 4.9 [136]. For a given c_{ff}-value, the exit focal distance r_B depends on the entrance focal distance r_A

$$r_\mathrm{B} = -c_{ff}^2 r_\mathrm{A}. \tag{4.11}$$

If c_{ff} is kept constant, the photon beam focus is virtual but remains at the same position along the direction of propagation [136]. A downstream mounted concave mirror images the virtual focus onto the sample spot.

Each monochromator employed at P04 exhibits five bays for the installation of various gratings. In its current state, each monochromator features gratings with 400 and 1200 L mm^{-1} spacing. Here, so-called variable spacing gratings (VLS) are employed, which exhibit an increasing groove density along the grating. VLS gratings allow for defocus, coma, and spherical aberration corrections and additionally improve the resolving power across the entire energy range. In contrast to plain gratings, VLS gratings also exhibit an additional focusing effect. Calculations of the maximum achievable resolving power for the 1200 L mm^{-1} grating are shown in

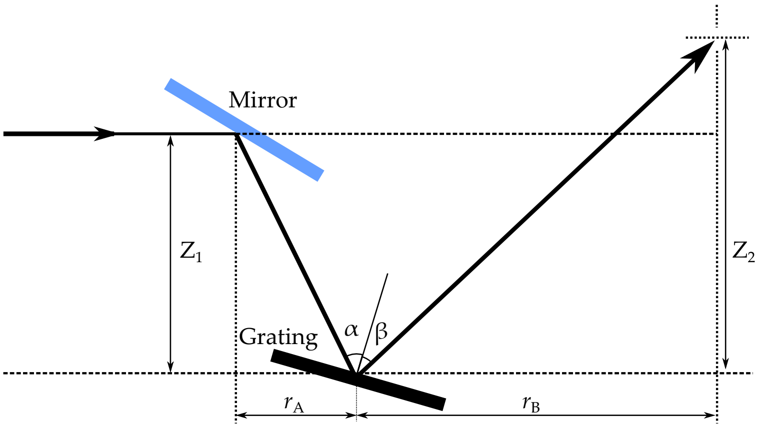

FIGURE 4.9: Sketch of the Peters mount configuration consisting of a plain mirror (blue) and a plain grating monochromator (black). The c_{ff}-value is defined as the quotient of the cosine of β and α. Given a constant c_{ff}, the focus remains at the same position of the exit slit. Figure adopted from [43].

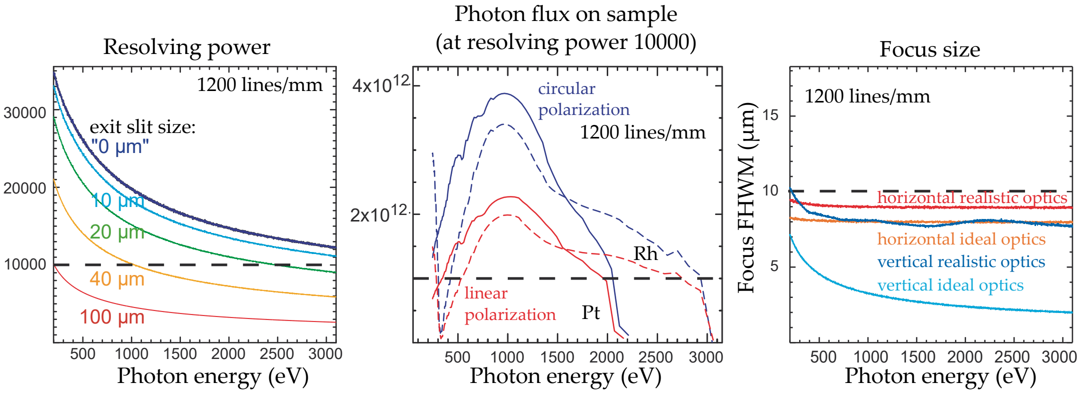

FIGURE 4.10: Left Panel: The simulated achievable resolving power of the beamline using the 1200 lines/mm grating for different exit slit configurations. Center panel: Calculations of the photon flux on sample for the two different available grating and mirror coatings rhodium and platinum. Dashed lines represent the flux utilizing Rh coatings. Pt coatings are depicted by solid lines. Right panel: Simulation of the spot size on sample using the refocusing mirror unit for ideal and realistic optics. The black dashed lines represent the designed minimum values to be achieved. Figure adapted from [128].

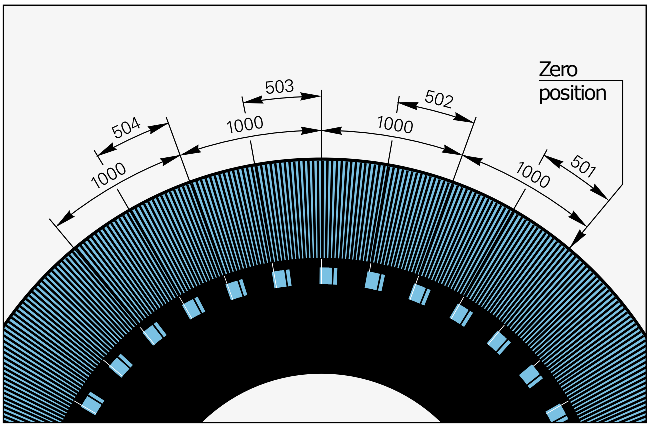

FIGURE 4.11: A disk as employed in the angular encoders. On the disk, a very fine grid structure with increasing µm spacing is etched. One disk employs in total 36000 lines which serve as an absolute angular reference. Figure adopted from [73].

figure 4.10.

Angular encoder interpolation

At P04, the monochromatized photon energy is set by adjusting the angles of the grating and mirror in front of the grating to the corresponding values. A closed-loop controller continually monitors the angles and, if necessary, corrects for, e.g., drifts or low-frequency vibrations. The controller relies on the feedback of two angular encoders, which track the positions of the grating and mirror. Two units of the commercially available Heidenhain RON 905 angular encoder are mounted on the main axis of the grating and mirror. The angular encoders consist of several disks on which a very fine grid structure with increasing spacing is etched, see figure 4.11. The encoders employed here exhibit 36000 lines per disk, leading to 36000 increments at values of of 0.01°, which can be measured precisely.

Since for small energy steps the movements of the grating and mirror are significantly smaller than 0.01°, interpolation between two absolute reference points is required. Therefore an LED light source is installed on one side of a disk and two photodiodes on the opposite side, see figure 4.12. If the measurement axis of the angular encoder is moving, the light intensity registered by the photodiodes changes depending on the angle, see lower panel of figure 4.12. Utilizing look-up tables containing the light intensity courses in between of two absolute references, the position of the angular encoder is obtained with a relative uncertainty of 10^{-6} and better [73].

Refocusing mirror unit

To maximize the resolution, the exit slit should be positioned in the focal point of the grating. By nature, the photon beam spatially diverges after passing through the exit slit. The so-called „Refocusing Mirror Unit“ (RMU) consists of a set of two mirrors downstream of the monochromator exit slit to refocus the photon beam onto the

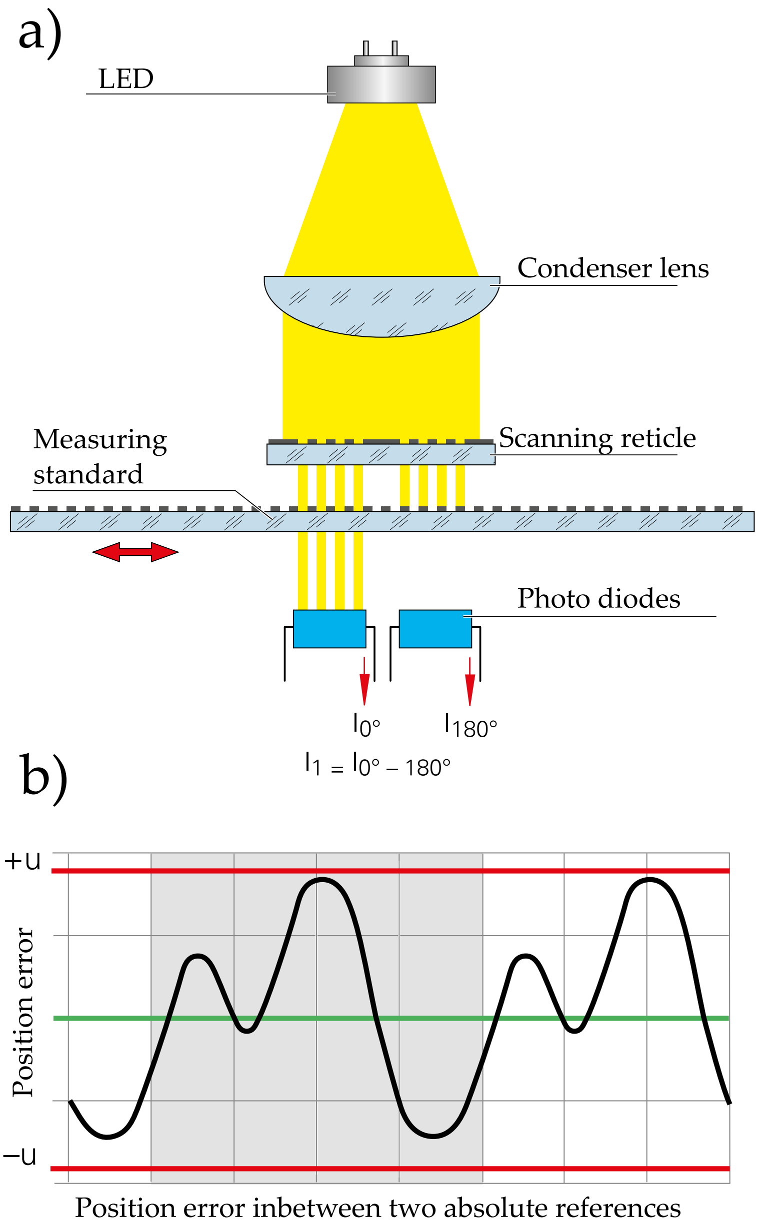

FIGURE 4.12: a): Principle of the photoelectric interpolation scanning method. A scanning reticle is overlapped with a measuring standard. An LED illuminates the reticle from one side. Two diodes are mounted opposite of the LED. As the measuring standard moves, the intensity observed by the diodes changes. In a calibration process, the intensity changes in between two absolute references are registered by the diodes as the measuring standard is rotated by 360° with constant speed, see b). In inverse of the observed intensity course is stored in look-up correction tables and enables accurate position interpolation of small rotations. Figure adapted from [73].

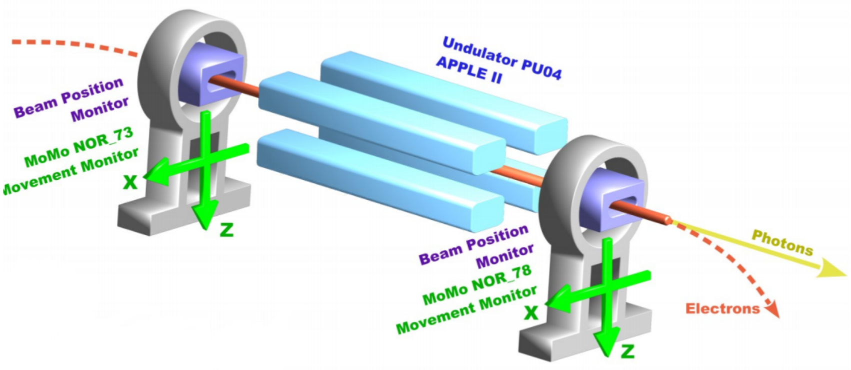

FIGURE 4.13: Commercial beam position monitors (BPM) are mounted on movement monitors, which track movements of the setup with respect to ground on the µm-scale. The BPM offers a nm-scale determination of the electron beam position. Figure adopted from [28].

experimental platform, see figure 4.8. According to the work of P. Kirkpatrick and A. V. Baez [94], an X-ray photon beam is focused if reflected at grazing incidence off a curved surface, resulting in a much higher efficiency compared to focusing by compound refractive lenses. Hence, a pair of perpendicular, curved mirrors are often named Kirkpatrick/Baez-optic or KB-optic. At P04, two mirrors in a KB-optic configuration are mounted on commercial hexapods provided by FMB Oxford. The hexapods offer an angular resolution down to 40 nrad. The translational resolution is specified to be 1 µm. Simulations resulted in a focal spot size below 10 µm FWHM, see figure 4.10.

Coatings

In order to increase the photon flux transmission of P04, mirrors and gratings are coated by a tens-of-nm thick layer of various heavy metals. Since P04 offers an extensive photon beam energy range from 245 to 2500 eV, no coating material covers the entire energy range without any absorption edges. This calls for at least two different coatings to bridge efficiency gaps. At P04, every optical element is installed twice, whereas one is coated with a thin layer of rhodium (Rh), and one is coated with a mixture of gold and platinum (Au/Pt). In the lower energy range up to 1500 eV, the Au/Pt coating is preferred. For higher energies up to 2500 eV, Rh is favorable. The photon fluxes as a function of photon energy for both coatings are shown in figure 4.10.

4.2.4 Diagnosis utilities

Beam monitors

Due to the length between the undulator and the experimental platform of 75 m, a slight variation of the photon emission point or angle inside the undulator can result in immediate photon beam loss, misalignment, or optical scattering effects. Using two commercial electron beam monitors, one upstream and one downstream

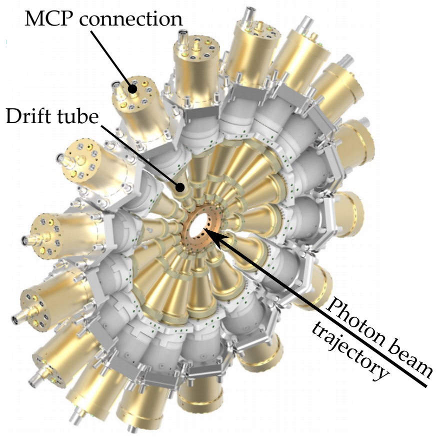

FIGURE 4.14: Scheme of the Cookiebox containing 16 drift tubes circularly mounted around the photon beam. Various gaseous target are be injected by means of a needle valve. Figure adopted from [28].

of the undulator of P04 (see figure 4.13), the electron beam position is recorded with a 1-σ resolution of 150 nm by means of pick-up electrodes [166]. Hence, short-scale variations of the electron beam positions, e.g., due to imperfections of the magnetic fields in the storage ring are registered and can be compensated in the order of nm. Long-term drifts of the whole assembly, due to, e.g., thermal expansion, is compensated by so-called high-frequency movement monitors (HF-MoMo), which track the locations with respect to the girder with a resolution below 1 μm.

Cookiebox

The Cookiebox is a time-of-flight polarimeter and spectrometer which offers various diagnostic tools and enables fundamental polarimetry and photo ionization measurements [111]. The Cookiebox employs 16 drift tubes equiangular distributed perpendicular to the photon beam trajectory in the radial plane, see figure 4.14. At the end of each drift tube, a biased fast-rising multi-channel plate (MCP) detects impinging electrons. Due to its large diameter in the center, the Cookiebox can be installed parasitically in the beamline without interfering with the photon beam or decreasing its photon flux. A gaseous target can be injected into the center by means of a needle valve. If the photon beam interacts with the target, photoelectrons produced by non-resonant photoionizations are emitted and detected by the MCPs after a certain time of flight. The arrival time t of the photoelectrons depends on the incident photon beam energy E_γ, the former binding energy of the released electron E_B and the distance s between the interaction point and the MCP

$$t = \frac{s}{\sqrt{\frac{2e(E_\gamma - E_\mathrm{B})}{m_e}}}. \tag{4.12}$$

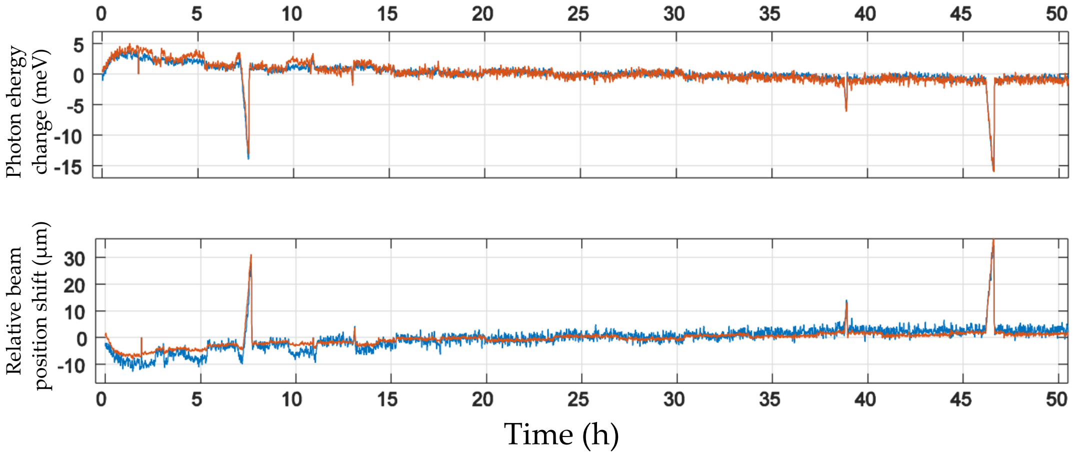

FIGURE 4.15: Top panel: measurement of the photon energy drift in the horizontal (blue) and vertical (red) plane using the Cookiebox without changing the requested monochromator energy over a period of 50 hours. Lower panel: Photon beam position shifts in the horizontal (blue) and vertical (red) plane observed simultaneously to the photon energy drifts. Both observable show a steady drift on the timescale of hours. Short-scale spikes, e.g. after 7 and 47 hours originated from instabilities of the electron beam in the storage ring. Parallel to the two spikes, the electron refill failed resulting in a electron beam current drop in the ring from 100 to 80 mA (not shown here). Figure adopted from [28].

By following the observed time-of-flight changes, the energy drifts of the incident photon beam can be inferred. However, if solely the time-of-flights of a single drift tube is inspected, it is impossible to distinguish between photon beam energy drifts and spatial movements of the photon beam, since both change the time of flight. To compensate for this, the acquired time of flights of two opposed MCPs are usually averaged to determine a photon energy drifts. Vice versa, photon beam pointing changes are tracked by subtracting the time of flights of two opposite MCPs. Such proof-of-principle measurements are depicted in figure 4.15.

Besides its diagnostic utility for photon beam energy and position drifts, the Cookiebox also offers to measure resonant photo ionization processes of neutral gases as demonstrated in [101, 122]. Instead of measuring the non-resonant photoelectrons, the Auger electrons are observed, which exhibit different kinetic energies and thus arrive at different times at the MCPs. Due to its resonant nature, the count rates of Auger electrons usually exceed those of non-resonant photoelectrons.

Chapter 5

Measurements

In total three measurement campaigns, also called beamtimes, aiming at the determination of the Fe XVII 3C/3D oscillator-strength ratio were conducted within the scope of this thesis. The employed measurement technique of laser spectroscopy allows to resonantly excite an individual transition of an highly charged ion (HCI) and detect the following relaxation by means of a photon emission. The PolarX-EBIT, built and commissioned at the Max-Planck-Institute for Nuclear Physics in Heidelberg, was transported to the PETRA III synchrotron located in Hamburg. On site, the EBIT was connected to XUV beamline P04, which provided a monochromatic and high-intensity photon beam in the required soft X-ray energy regime.

In the beginning of this chapter, the alignment of the experimental setup at P04 is explained in details. Subsequently, the measurement scheme and the data reduction is briefly introduced. In chapters 5.3, 5.4, and 5.5, the three measurement campaigns conducted in 2018, 2019, and 2020 are presented, respectively. At the end of each section, the results of the beamtimes are shortly summarized.

5.1 Experimental setup & alignment

After the combination of resonant photon excitation of HCI using soft X-rays has been successfully demonstrated using cryogenic EBITs [53], the measurement method was steadily improved and extended to the hard X-ray range at various synchrotron facilities [138, 155, 15].

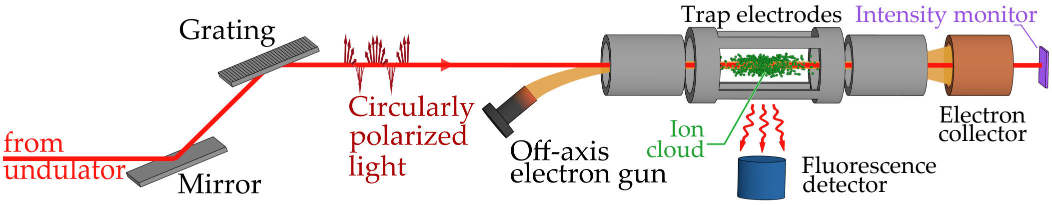

FIGURE 5.1: Experimental setup: an electron beam (orange) aimed at the trap center produces highly charged ions, which are then resonantly excited by a monochromatic photon beam (red) provided by beamline P04. Subsequent X-ray fluorescence is registered by a silicon drift detector. The intensity of the photon beam is registered using an X-ray sensitive diode downstream of the experimental setup. Figure adopted from [96].

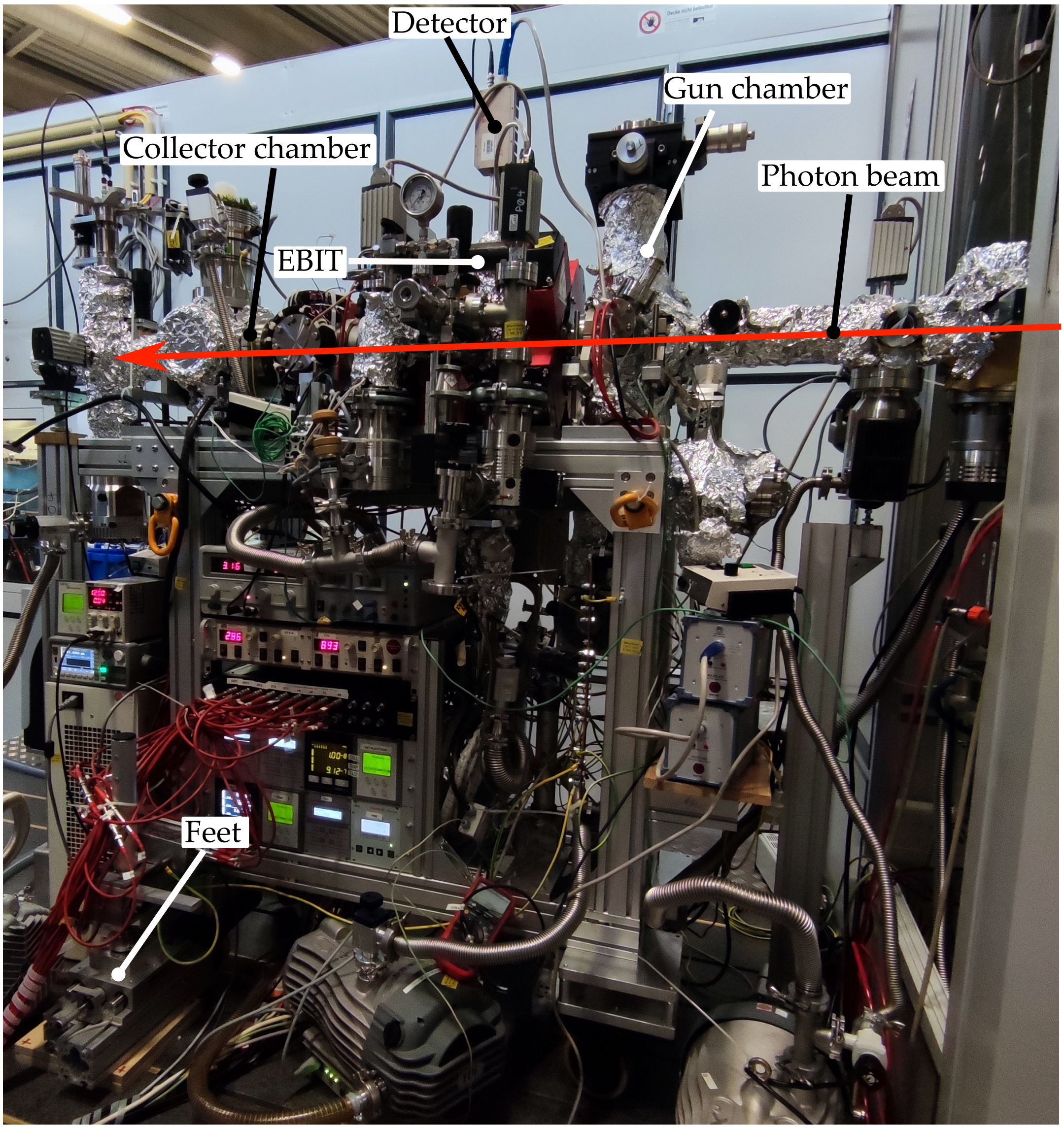

FIGURE 5.2: Photograph of the PolarX EBIT as an endstation at beamline P04 of the PETRA III synchrotron in Hamburg.

In every previously conducted laser spectroscopy experiment utilizing EBITs, the external photon beam was guided through the hollow collector of the experimental setup into the trap center. After passing through the trap center, the photon beam hit components of the electron gun, which was mounted on the main axis of the experimental setup. Here, the arrangement of the novel off-axis gun developed within this work allowed the photon beam to enter and exit the trap center from both sides. This has not only simplified the initial alignment but also allowed the photon beam to be provided for further experiments or to install diagnostic devices such as an intensity monitor downstream of the experimental setup. A schematic representation of the laser spectroscopy setup employing the PolarX-EBIT at beamline P04 is depicted in figure 5.1. A photograph of the Polar-X EBIT at P04 is shown in figure 5.2.

FIGURE 5.3: The laser level (red) are overlapped with the white synchrotron light produced in the bending magnets of the storage ring.

Alignment

The first crucial step of an X-ray laser spectroscopy measurement at a synchrotron facility is overlapping the incident photon beam provided by the beamline with the stored ion cloud in the EBIT. Since both, the photon beam and the ion cloud, exhibit small dimensions of only hundreds of microns in diameter, this process is challenging. The procedure of how to efficiently and quickly overlap the photons with the ion cloud is described in this section. This may be adapted to different beamlines as well but is essentially optimized for the XUV beamline P04.

First, the height as well as the pointing of the photon beam needs to be determined. Since XUV photons are absorbed by air under atmospheric conditions, either an X-ray sensitive and retractable yttrium-aluminium-garnet (YAG) screen under vacuum conditions [151] or the so-called white light is used to follow the path of the photons. The white light is part of the low energy synchrotron radiation produced in the bending magnets of the storage ring PETRA III and is easily perceivable by the human eye. Since white light is emitted by the same electron bunches that produce the X-ray light in the undulator, both are sufficiently well aligned to each other. However, white light is usually dispersed by the grating and does not pass the exit slit of the monochromator. In order to provide white light at the experimental platform of the beamline, the grating angle inside the monochromator is set such that the grating acts as a non-dispersive mirror.

It is beneficial to mark the white light prior to the beamtime and before installing the EBIT on the experimental platform if possible, for example, during a machine studies day of the storage ring the week before the measurement campaign. This enables to coarsely align the EBIT without spending shifts of the actual allocated and limited beamtime and ensures that the experimental setup is connected to the vacuum system of the beamline as early as possible to reach UHV conditions.

Several laser level beside and above the platform are aligned with the white light marks, see figure 5.3. Subsequently, the EBIT is moved into the beamline and aligned using the laser level. The EBIT frame is mounted on four wheels, which are used for transportation and the coarse alignment on the experimental platform. Once coarsely aligned, the wheels are substituted by three feet connected to stepper motors, one upstream below the gun and two downstream below the collector. The feet allow to tilt, rotate and alternate the height of the experimental setup.

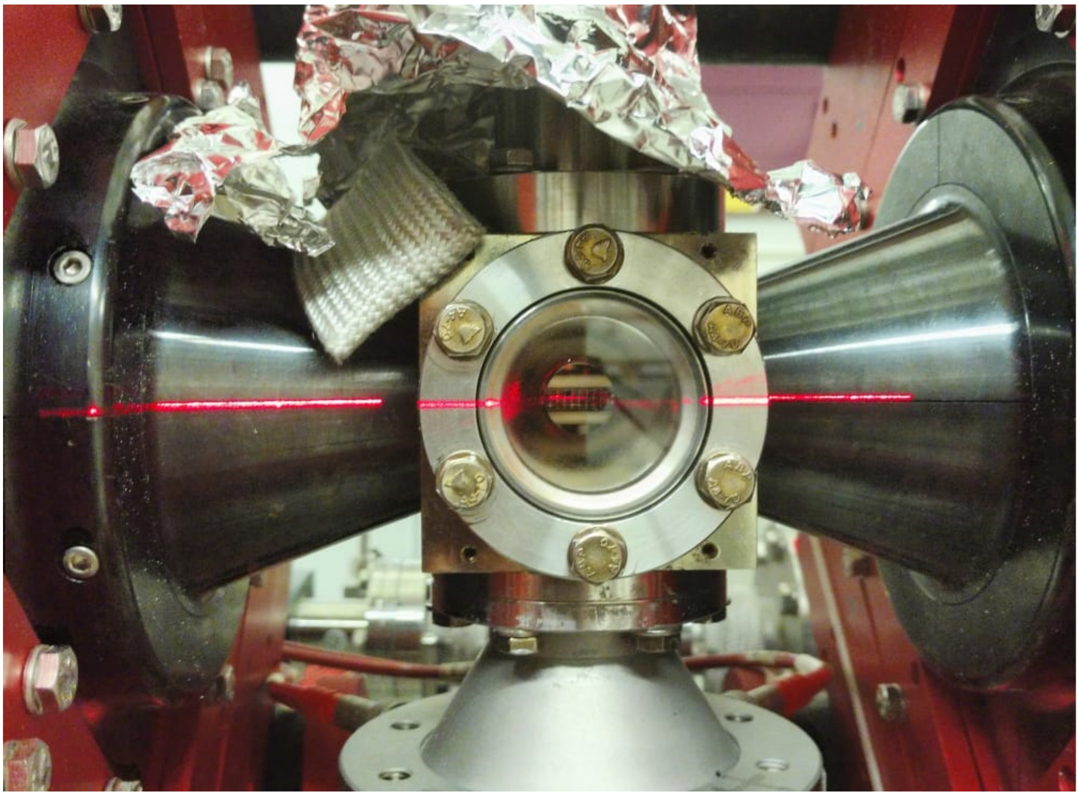

FIGURE 5.4: Using the red laser level which is aligned with the trajectory of the synchrotron radiation the final position of the EBIT is coarsely defined. The optical access to the trap center eases the determination of the correct tilt and height.

Once the experimental setup is vertically in place, the frame is lifted by approximately 20 cm to reach the photon beam height of 142 cm at beamline P04. Due to the small dimensions of the PolarX-EBIT and the optical access to the trap center, the horizontal alignment and height of the trap center are easily verified, see figure 5.4. Additionally, the coarse alignment can be once again verified by observing the white light beam behind the EBIT.

By moving the grating of the monochromator to the first dispersive order, the white light is substituted by X-ray photons. Using either a YAG-screen or a photon diode, the alignment of the EBIT with the X-ray beam is once again confirmed, see picture 5.5.

For further adjustments, a photon beam intensity reference value is measured upstream of the EBIT using the built-in photon intensity diode of P04. By comparing the photon intensity behind the experimental setup with the reference value, the position of the EBIT is optimized until no intensity loss is noticeable. Subsequently, the coarse alignment of the experimental setup is accomplished, i.e., the vertical tilt and the horizontal rotation are both aligned more precise than one degree with respect to the photon beam.

After, the incident photon beam energy is tuned to a well known and strong transition. In the XUV energy range, the strongest K_α line $1s^2$ ($^1S_0$) $\rightarrow$ 1s2p ($^1P_1$), also called w of He-like oxygen (O VII) at 574 eV or He-like neon (Ne IX) at 922 eV is

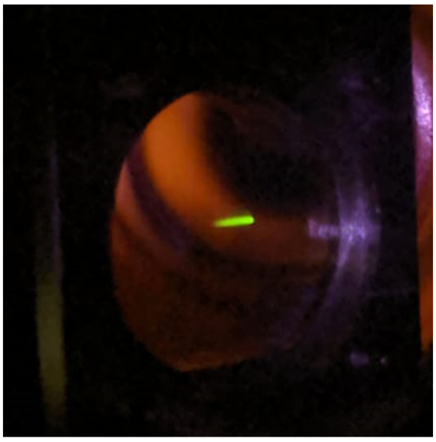

FIGURE 5.5: After the white light was guided through the EBIT, the beamline is set to produce X-ray photons. A YAG-screen behind the EBIT shows the size of the X-ray photon beam (green fluorescence). Here, the EBIT is already well aligned and the exit slit width is set to 50 µm resulting in a narrow vertical spatial width. Horizontally, the strong divergence of beam is visible and reveals a size of a few millimeter approximately one meter behind the trap center.

favorable. In order to finally overlap the photon beam with the ion target, the exit slit is completely opened. Opening the exit slit increases both, the vertial spatial size as well as the energetic width of the photon beam. The latter is beneficial to account for minor miscalibrations of the monochromator by covering a broader photon energy range. While observing the count rate on the O VII or Ne IX w line, the whole experimental setup is now slightly moved in all directions. Since the background should be essentially zero, even a weak fluorescence signal is detectable. Once the fluorescence signal is maximized, the exit slit width of the monochromator is reduced resulting in a smaller vertical photon spot size as well as a narrower energetic width. After, the fluorescence yield is once again optimized by moving the EBIT position. This procedure is repeated until the desired exit slit width is achieved. Since the accuracy and reproducibility of the EBIT feet position are limited, further optimization is accomplished by moving the mirrors of the refocusing mirrors unit (RMU) of the beamline. By adjusting the angles and positions of the two mirrors inside the RMU, the fluorescence signal is maximized. Subsequently, the overlap between the ion cloud and the photon beam is established with an accuracy in the order of tens of microns.

5.2 Data reduction

Once the ion cloud is overlapped with the photon beam and the element of interest is injected into the EBIT, the monochromator energy is typically varied stepwise in the expected energy range of the transitions of interest. For each monochromator energy, the ion cloud is exposed to the photon beam for several seconds, while the SDD acquires the photon spectrum emitted by the ion cloud. Such a single, one-dimensional photon energy spectrum is depicted in figure 5.6. The resolution of the

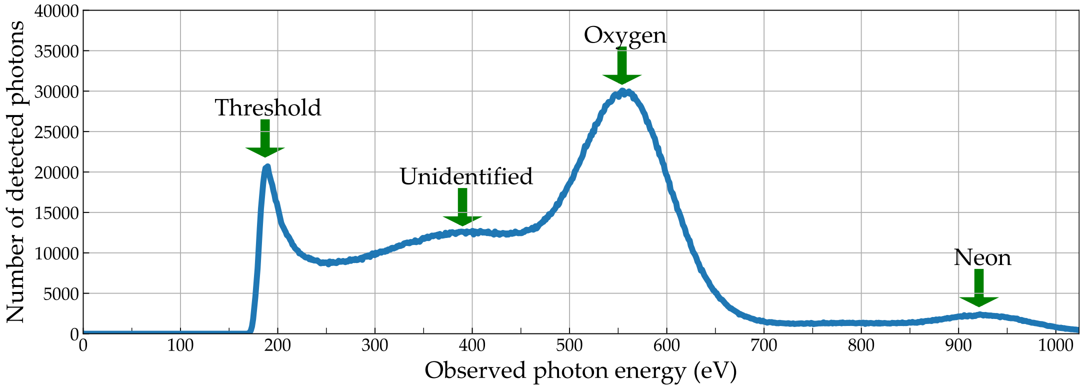

FIGURE 5.6: A single spectrum acquired by the silicon drift detector. Due to the limited resolution of the detector (FWHM 100 eV), the complex of an element consisting of many transitions, e.g., oxygen or neon, remains unresolved.

detector exhibits a FWHM of approximately 100 eV and is thus by far insufficient to resolve individual transitions with similar energies. However, the resolution is sufficient to coarsely identify the different element complexes, e.g., neon or oxygen.

If the one-dimensional detector spectra are plotted as a function of the incident photon beam energy, a two-dimensional spectrum is obtained, in which the resonance is often directly visible, see top panel of figure 5.7. To extract the fluorescence signal of a single transition, the number of events within a suitable ROI are summed as a function of monochromator energy, see bottom panel of figure 5.7. For many applications, e.g., the precise determination of the transitions amplitude, the selection of the ROI is vital. In most cases, the ROI should be chosen such that the SNR is maximized.

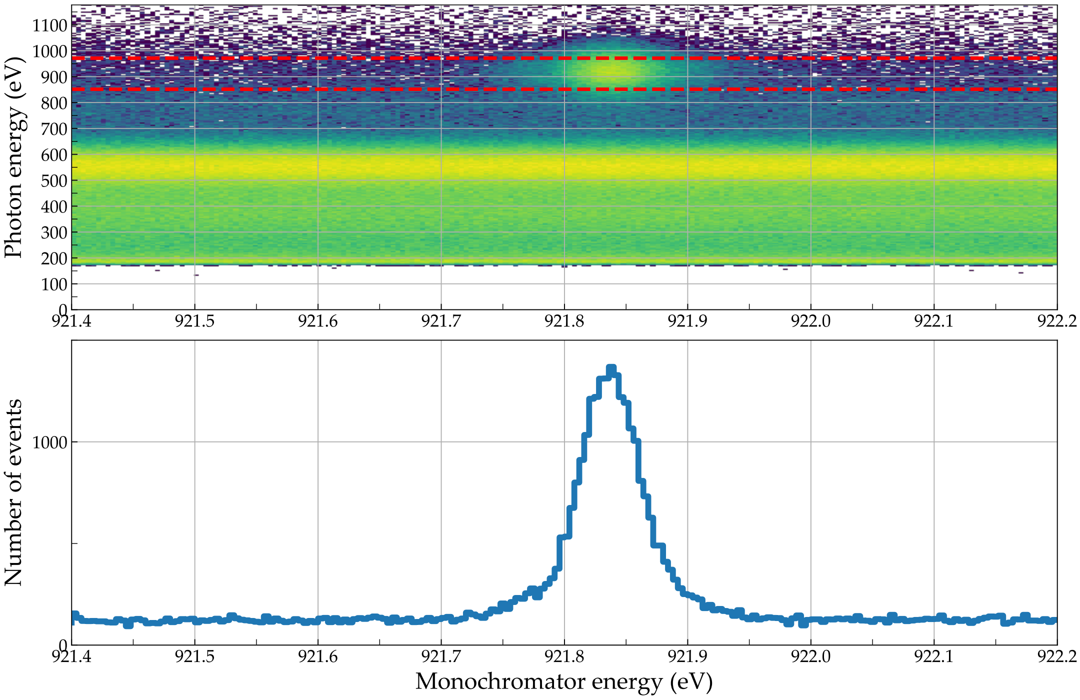

FIGURE 5.7: Top panel: The individual one-dimensional detector spectra, see figure 5.6, are plotted against the monochromator energy, resulting in a two-dimensional plot. The resonance w of Ne IX appears strong and well above the background produced by electron impacts. Lower panel: The number of events in the energy region in which the detector observes photons emitted by neon ions (red-dashed lines in the top panel) is summed and depicted as a function of monochromator energy.

5.3 Campaign 2018

The first measurements of the 3C/3D oscillator-strength ratio of Fe XVII in this work were conducted in December 2018. In the beginning of this section, the ion target preparation, the expected fluorescence rate, as well as the optimization of the first fluorescence signal from Fe XVII ions will be discussed. After, first results from regular scans across both lines, 3C and 3D, along with the systematical limitations will be presented. In order to overcome those systematical limitations, two novel measurement schemes will be introduced to solidify the insights of the first presented measurement method. At the end of this chapter, the individual measurement results of the three methods will be summarized and the uncertainties estimated.

5.3.1 Electron-impact excited photon spectrum & preparation of the target

In a laser spectroscopy experiment, the ion cloud as a target is generated by means of electron-impact ionizations and confined in the trap center. Subsequently, the incident monochromatic photon beam is overlapped with the ion cloud and resonantly drives a transition of interest resulting in a fluorescence signal. Apart from photon excitations, the electron beam simultaneously interacts with the ion cloud resulting in an electron beam driven photon emission spectrum. Such a photon emission spectrum is dominated by three processes, the non-resonant processes of electron-impact

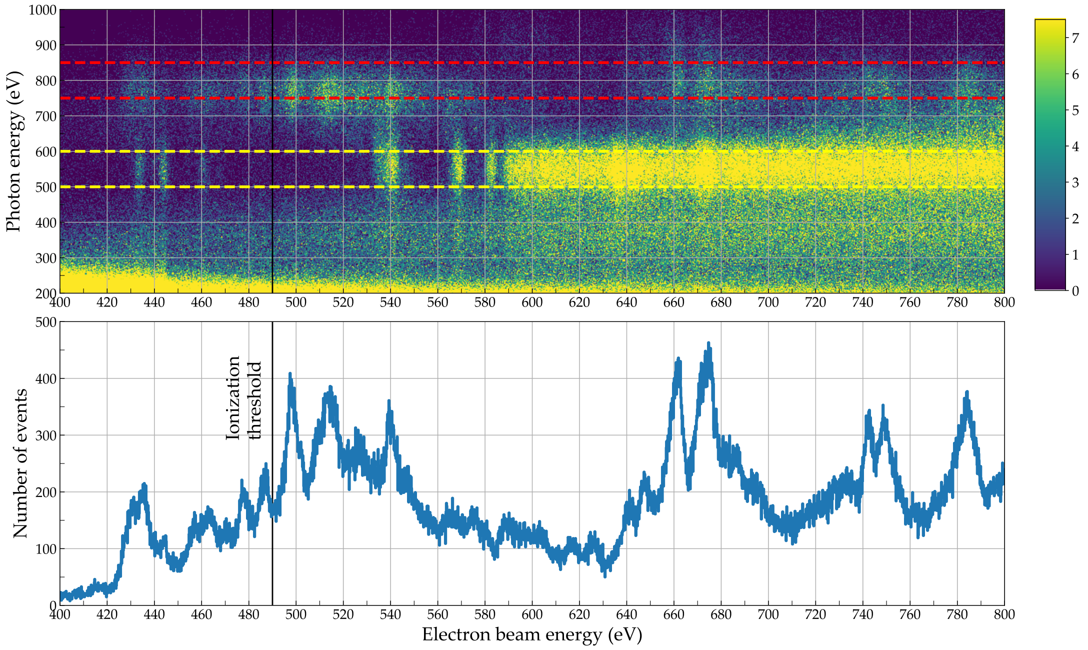

FIGURE 5.8: Dielectronic recombination measurement of highly charged iron. Top panel: The detected photon emission spectrum as a function of electron beam energy. Bottom panel: The projection of the region of interest (red dotted lines) in which the fluorescence of 3C and 3D is expected. By scanning the electron beam energy from 400 eV to 800 eV, resonant DR processes of iron are observed. Black vertical line: Production threshold of Fe XVI. The yellow dotted lines indicate the region of resonances of the co-produced He- and Li-like oxygen.

excitation and radiative recombination as well as the resonant process of dielectronic recombination, see chapter 2.3.2 for more details and illustrations. In order to maximize the SNR of the fluorescence signal, a mitigation of recombination processes that result in a photon emission with similar photon energy as the fluorescence photons is desirable.

The dominating non-resonant process is given by electron-impact excitations in which part of the kinetic energy of a free electron is transferred to an ion resulting in an excited state that decays by emission of a photon. The cross section of this process is approximated by the Bethe equation, see equation 2.22, and is inversely proportional to the kinetic energy of the incident electron, i.e., the higher the kinetic energy of the free electron, the lower the resulting photon emission strength. Note that this process only occurs if the kinetic energy of the free electron exceeds the energy of the transition.

In the second non-resonant process labelled radiative recombination, a free electron is captured by an ion in a bound state of the system by a simultaneous emission of a photon. The photon emission energy is given by the sum of kinetic energy of the free electron and the binding energy of the captured electron after recombination. In contrast to electron-impact excitations, in which the resulting photon energy never exceeds the kinetic energy of the free electron, the resulting photon energy of a radiative recombination is always higher than the kinetic energy of the free electron.

Compared to electron-impact excitation, the cross section of radiative recombinations is marginal for low and medium nuclear charges Z, see also equation 2.19.

The third process, the dielectronic recombination (DR) is given by a free electron resonantly captured in a bound state of an ion while a second bound electron of the ion is excited. Similar to the radiative recombination, the energy of the resulting photon emission exceeds the kinetic energy of the free electron. The cross section of a dielectronic recombination is significantly stronger compared to the non-resonant processes mentioned above. Since DRs only occur for distinct free electron energies for which the resonance condition is met, a strong photon emission can be prevented by setting the electron beam energy well below or above a DR resonance energy.

In the specific case of this measurement campaign, a minimum electron beam energy of approximately 490 eV was required to remove 16 electrons from a neutral iron atom and to produce the required charge state Fe XVII. The ionization cross section slightly above the production threshold is low and increases for higher electron beam energies until the maximum at approximately two to three times the production threshold energy is reached. In order to avoid non-resonant electron-impact excitations of the transitions of interest, the electron beam energy should be set well below the transition energies of 3D and 3C at 812 and 825 eV, respectively. Hence, only a small electron beam energy range between 490 and 800 eV is in principle available for background free measurements. Unfortunately, this energy range is also covered with many strong L-shell DRs of iron, i.e., resulting in strong photon emission background.

In order to identify electron beam energies for which the photon emission is minimized, the electron beam energy was scanned stepwise in the energy range between 400 and 800 eV while the photon beam shutter of the beamline was shut. For each electron beam energy, the resulting photon emission was registered by the detector and depicted as a two-dimensional plot, see upper panel of figure 5.8. The ROI in which the fluorescence of 3C and 3D is expected is marked with red dashed lines. The sum of the number of events in this ROI as a function of electron beam energy is shown in the lower panel of the same figure. Lowest count rates were observed for electron beam energies below 420 eV. However, this energy region is below the production threshold and therefore unable to produce the required charge state Fe XVII. Above the threshold, lowest count rates were observed for electron beam energies of approximately 630, 710, and 765 eV.

Apart from minimizing the background count rate, DR measurements as presented in figure 5.8 also provide an excellent diagnostic tool for the charge states present in the trap, as each charge state exhibits a characteristic resonance spectrum. Unfortunately, resonances of the required charge state Fe XVII occur at electron beam energies between 300 and 420 eV, well below the production threshold of Fe XVII at 490 eV. Thus, a direct proof of the Fe XVII presence was unfeasible due to the comparably slow electron beam energy scan of only $0.25\,\mathrm{V\,s^{-1}}$ and short lifetime of Fe XVII in the order of approximately hundreds of ms below the production threshold.

5.3.2 Estimation of the fluorescence strength

The number of observed fluorescence photons of line 3C per second can be estimated in a semi-classical approach using

$$N_{\text{Fluorescence}} = \frac{N_{\text{Ions}}}{A_{\text{eff}}} \kappa \int_{-\infty}^{\infty} N_{\gamma}(w) \sigma(w) \mathrm{d}w \tag{5.1}$$

with the number of stored ions N_{Ions} within an effective area A_{eff} exposed to the photon beam [46]. The detection efficiency κ of the experiment due to a finite detection area and a limited filter transmission is assumed as 0.5%. In this estimation, the spectral intensity $N_{\gamma}(w)$ on resonance of line 3C is represented by a Gaussian profile centered at 825 eV with a width of $\sigma = 100\,\text{meV}$ FWHM which covers both, the Doppler broadening due to the ion target movement as well as the resolving power of the monochromator. Here, $N_{\gamma}(w)$ was normalized to a total photon flux of 1×10^{12} photons/s as specified by the beamline datasheet. The absorption cross section $\sigma(w)$ is described by

$$\sigma(w) = \frac{\pi e^2}{2\epsilon_0 m_e c_0} \frac{\gamma/2\pi}{(w_0 - w)^2 + \gamma^2/4}, \tag{5.2}$$

where γ represents the natural linewidth of the investigated transition $\gamma_{3\text{C}} \approx 14\,\text{meV}$ FWHM. Assuming an effective area $A_{\text{eff}} \approx 1 \times 10^{-8}\,\text{m}^2$ based on the focus size of the beamline and $N_{\text{Ions}} = 1 \times 10^6$, a fluorescence rate of

$$N_{\text{Fluorescence}} = 60\,\text{photons/s} \tag{5.3}$$

is estimated.

5.3.3 First fluorescence signal of Fe XVII

In order to register a first fluorescence signal from highly charged iron, several electron beam settings were tested. For each electron beam energy, a monochromator energy scan in the expected range of 3C was performed. The exit slit of the beamline was opened to a width of 500 µm to increase the photon flux on sample. First, electron beam energies of 400 eV, well below the production threshold of Fe XVII, and 630 eV, for which the background induced by resonant DRs was low, were tested. Since no fluorescence signal was found, several trap depths ranging from shallow up to very deep potentials of several hundred volts were applied. For neither of the two electron beam energies, a resonance signal of 3C was found. Subsequently, several transitions of Fe XVII with the same ground but energetically higher excited state, also known as 4C and 5C, were scanned. For these transitions, the observed fluorescence was expected at energies well above the observed background. Since no signal of 4C or 5C was found, several strong transitions of lower charge states, e.g., Fe XVI and Fe XV, were unsuccessfully probed. The absence of any fluorescence signal hinted towards the lack of highly charged iron or loss of overlap between the

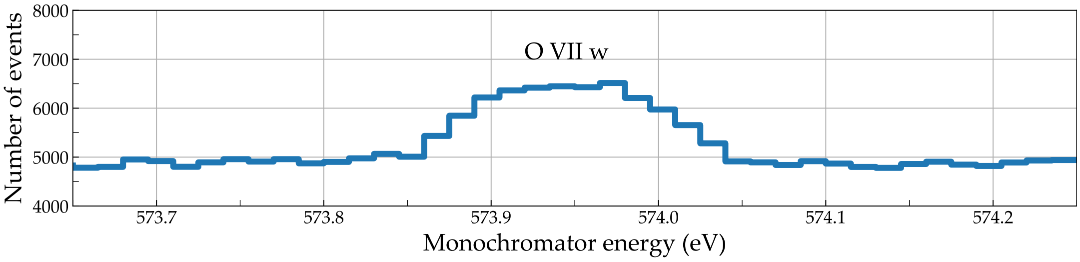

FIGURE 5.9: Fluorescence signal of the transition *w* of O VII. Since no transitions of iron could be found, the overlap between the incident photon beam and the plasma was once again verified using the strongest line of O VII, which is always co-injected into the trap as a part of the compound iron pentacarbonyl. Note the increased background due to impact excitation of the electron beam.

incident photon beam and the trapped plasma. In order to exclude the latter, the transition *w* of O VII, which was also used to align the experimental setup, was once again scanned without changing the electron beam properties or varying the injection pressure. Since oxygen is a major part of the compound iron pentacarbonyl $Fe(CO)_5$ which was used to inject iron into the setup, highly charged oxygen was always co-produced and confined within the EBIT plasma. Furthermore unlike Fe XVII, the presence of O VII could be easily verified utilizing DR measurements. The signature of strong DR resonances of O VII are marked in figure 5.8. Despite the high background in the ROI due to electron excitations ($E_{\mathrm{beam}} > 600\,\mathrm{eV}$), a clear fluorescence signal was obtained on top of the background, although the SNR decreased from usually a few hundred to 0.3, see figure 5.9.

After the overlap was once again verified using oxygen, the electron beam energy was changed to 1600 eV to increase the amount of higher charge states of iron. The electron beam current remained at 6 mA, whereas the trapping potential was lowered to a shallow trap of only 20 V. Employing these settings, the first fluorescence signal of the resonance line 3C was observed, see figure 5.10. Since the electron beam energy was well above the 3C transition energy of 825 eV, the measurement signal was dominated by a background in the order of 60 Hz due to electron-impact excitations. On resonance, the fluorescence showed a rate of approximately 5 Hz resulting in a low SNR below 0.10. After the first signal of 3C was registered, the fluorescence yield was maximized by setting the monochromator energy to the centroid of 3C and optimizing the iron injection pressure.

5.3.4 Measurements

Three different measurement methods were applied to systematically measure the 3C/3D oscillator-strength ratio of Fe XVII.

Method 1: Scanning over the transition energy range of 3C & 3D

After the centroid of line 3C was found, the expected energy range of line 3D was scanned. As presented in previous work [15, 10, 25] and described in chapter 2.5,

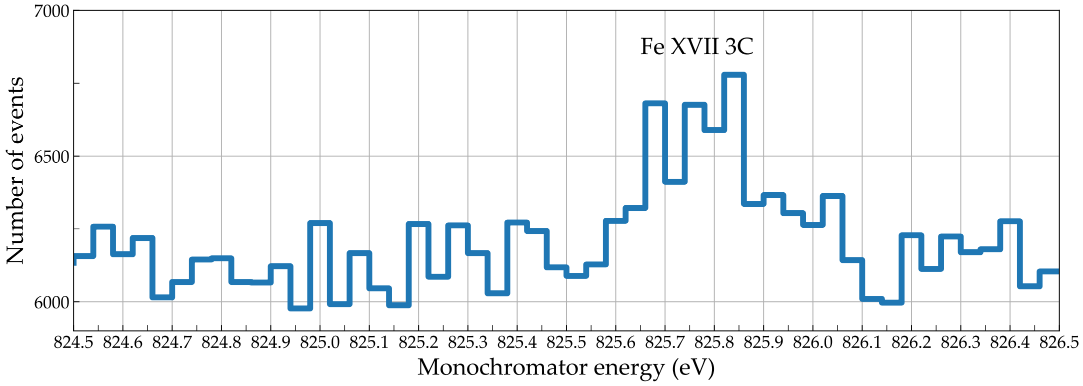

FIGURE 5.10: First fluorescence signal of the transition 3C of Fe XVII, after drastically increasing the electron beam energy. Note the high background count rate due to collisional excitations of the electron beam. The SNR was comparably low and exhibited a value below 0.10.

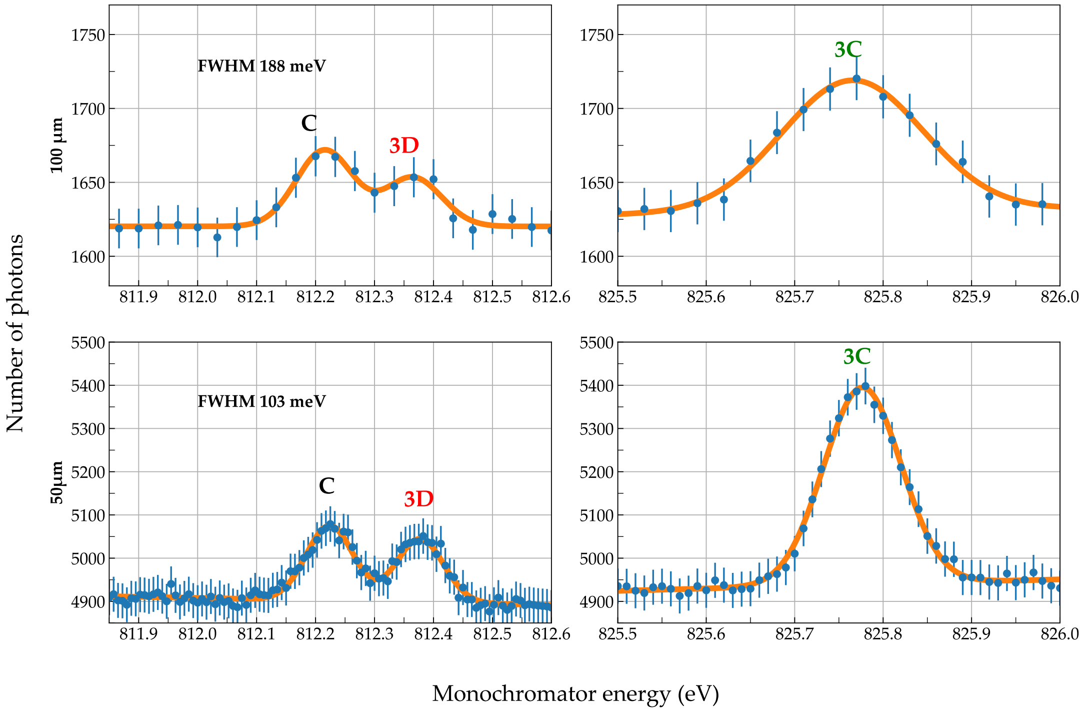

FIGURE 5.11: Projections of the three measured lines 3C, 3D, and C. Top panel: Sum of measurements using an exit slit width of 100 µm. Bottom panel: Sum of projections utilizing a narrowed slit width of 50 µm, resulting in a higher resolution.

an additional line C of Fe XVI is energetically close to 3D ($E_{3D} - E_C = \approx 150\,\mathrm{meV}$). In order to directly infer the fluorescence yield of 3D, it was necessary to resolve the 3D from C. Hence, the exit slit of the monochromator which controlled the resolving power of the incident photon beam was required to be narrowed until a satisfying resolving power was achieved, see chapter 4.2.3.
After closing the exit slit width to 100 µm, the complex consisting of 3D and C was scanned by changing the monochromator energy equidistantly in 45 steps from 811.5 eV to 813.0 eV. Scans of the 3C contained 50 steps covering the energy range from 825.2 eV to 826.2 eV. For each monochromator setting, the photon emission of the ion cloud was acquired for 20 s. In the top panel of figure 5.11, the sum of the in total 17 scans of each line is depicted. The achieved resolving power of $\frac{E}{\Delta E} = 4500$ was barely sufficient to resolve 3D from C. Hence, it was required to further increase the resolution by closing the exit slit to a remaining width of only 50 µm, see bottom panel of figure 5.11. As expected, the resolving power increased by almost a factor of two ($\frac{E}{\Delta E} = 8250$), whereas the total incident photon flux decreased by the same factor. In order to compensate for the lower flux, the upstream mounted mesh, which served as a photon flux monitor but also absorbed a vast part of the photon beam, was retracted from the photon beam path. Hence, a photon flux correction of the fluorescence strength using the intensity signal provided by the mesh was no longer possible, since a second diode downstream of the EBIT was not available during this beamtime. Employing the smaller slit width of 50 µm, the resolution was sufficient to resolve 3D from C and to reliably fit two Gaussian models to the 3D and C transition complex.

Determination of the region of interest

The 3C/3D oscillator-strength ratio is given by the ratio of the respective fluorescence yields. The fluorescence yields were inferred by the areas under the Gaussian profiles applied to the acquired data. Since the resulting areas crucially depended on the ROIs that were used to extract the one-dimensional projections from the two-dimensional acquired spectra, see figure 5.7, the ROI center and width must be chosen carefully and should be precisely in the center of the detector channels in which the fluorescence signal of both lines are registered. If the ROI center was chosen too low, less signal of 3C was taken into account compared to 3D, since 3D is energetically lower, and vise versa, if the center was chosen too high. For a visualization of this effect, the observed 3C/3D oscillator-strength ratio is plotted as a function of ROI centroid in figure 5.12.

In the upper panel of figure 5.13, the summed two-dimensional spectrum of all 3C measurements is shown. In order to accurately determine the detector channels in which the fluorescence of 3C is registered, the photon emission spectrum observed by detector on resonance of 3C (blue) and off resonance (green) is depicted in the lower left panel of 5.13. By subtracting the emission spectrum off resonance from the one on resonance, the pure fluorescence signal was extracted. The same

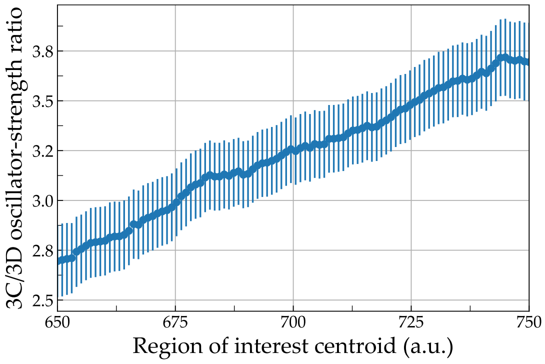

FIGURE 5.12: The 3C/3D oscillator-strength ratios are plotted for several ROI centroids using a ROI width of 120 detector channels. The lower the centroid was chosen, the less counts from 3C were taken into account resulting in a reduced ratio. For higher centroids, the contribution from 3D was suppressed, resulting in higher observed ratios.

procedure was repeated for line 3D. By applying Gaussian fits to the pure fluorescence signals, the centroid detector channel between 3C and 3D was determined as 710. Optimizations of the SNR resulted in a narrow ROI width of 80 channels, which corresponded approximately to the FWHM of the detector signal. Note that all values are given in arbitrary detector channel units and are thus independent of any detector calibration.

Using the optimal ROI center and width determined in the section above, the projections of all stable measurements were extracted and are depicted in figures 5.14 and 5.15 for 3C and 3D, respectively. Gaussians were fitted to the fluorescence signal where area, centroid, and width were treated as free parameters. A linear function was necessary to correctly model the fluctuating background. The observed FWHM of the fluorescence of 3C and 3D differed due to the the broader underlying natural linewidths of 3C, see chapter 2.3.4. Note that Voigt fits, which account for different natural linewidths, were unfeasible due to low statistics and lack of resolving power.

Both the ratio of the areas as well as the Gaussian FWHMs are depicted in figure 5.16. The 3C/3D oscillator-strength ratio value was inferred by averaging the individual measurement results weighted by their respective uncertainties.

Systematical uncertainties of method 1

As depicted in figure 5.12, the resulting oscillator-strength ratio depends on the selection of the ROI. In order to estimate how significant the systematical error contribution of this effect is, Gaussian fits were repeated for several projections using different ROI center and widths. The center of the alternatively selected ROIs were shifted by up to five channels in each direction, which corresponded to a 5-σ deviation from the determined optimal center. The resulted ratio varied by only 1% which will be taken into the error budget accordingly. By varying the ROI width by a factor of two, the resulting ratio changed up to additional 1.5%.

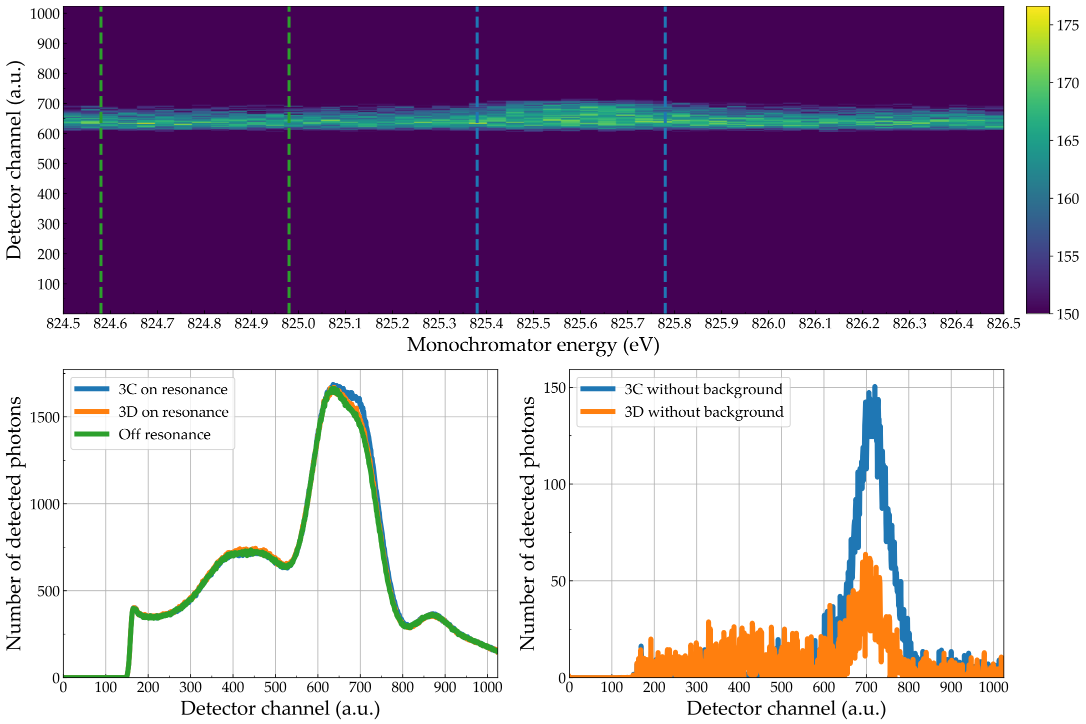

FIGURE 5.13: Upper panel: Summed two-dimensional spectrum of all 3C scans. Blue and green dashed lines indicate the regions that were summed for the one-dimensional spectra on and off resonance of 3C depicted in the lower left panel, respectively. In order to visualize the fluorescence signal, the two-dimensional spectrum ranges only from 150 to 180 number of detected photons, see also colorbar on the right hand side of the spectrum. Lower left panel: The observed emission spectrum on resonance of 3C (blue), 3D (orange) and off resonance (green). Lower right panel: The emission spectrum off resonance is subtracted from the spectra on resonance of 3C and 3D, respectively, resulting in the pure fluorescence signal. Note that the detector channels are given in uncalibrated arbitrary units.

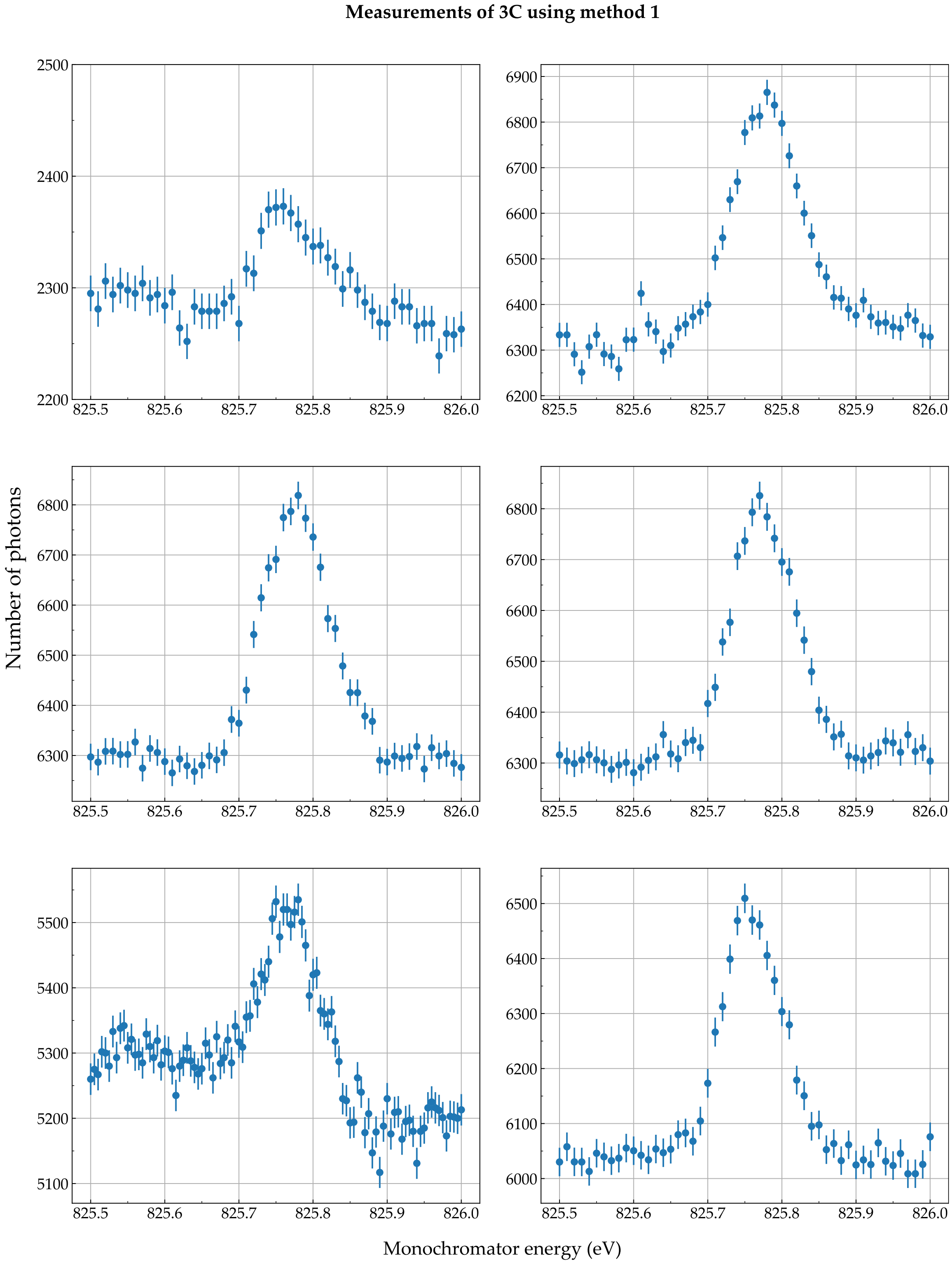

FIGURE 5.14: Projections of the six 3C measurements. These measurements were performed using method 1 described in the previous section.

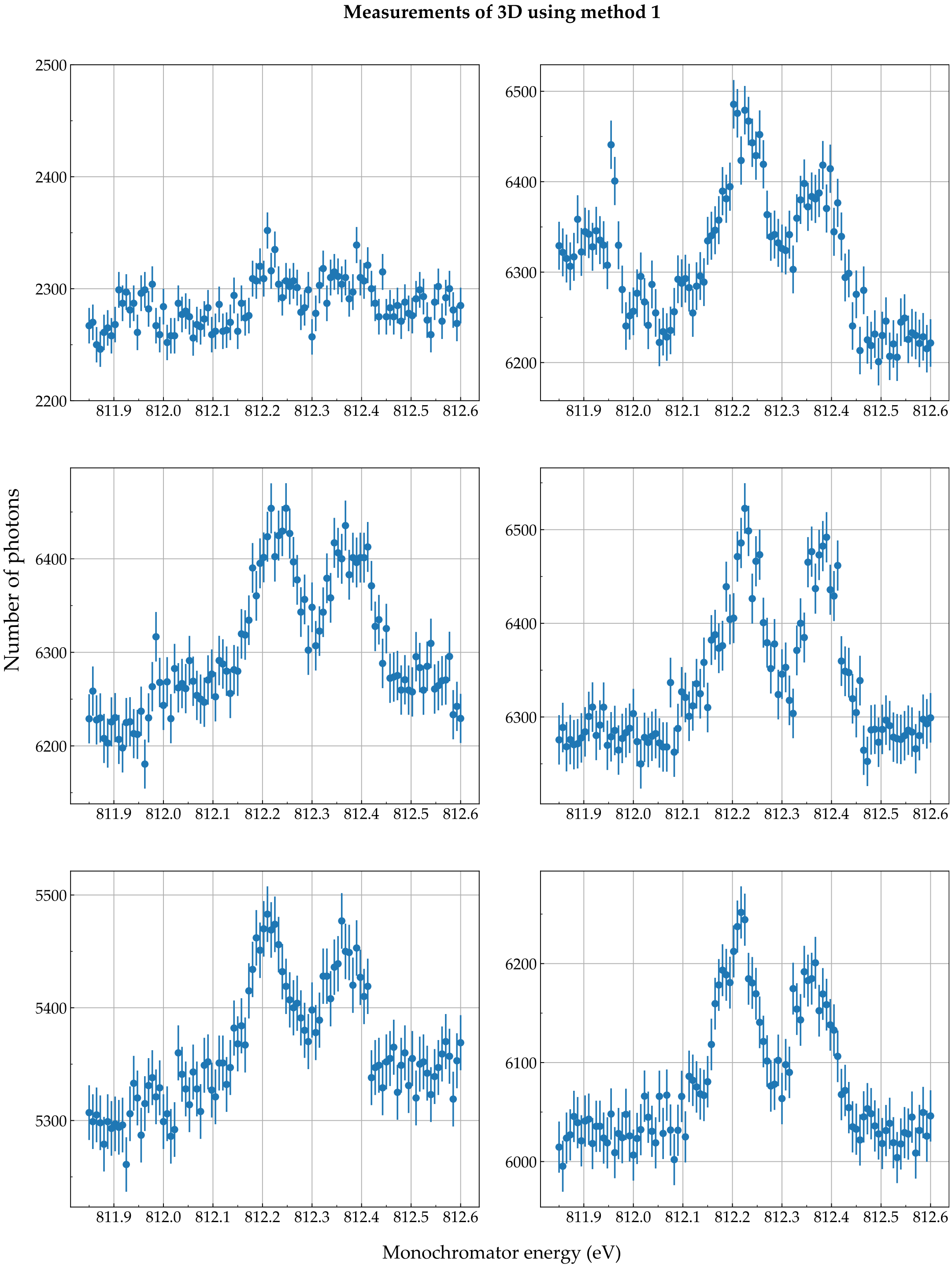

FIGURE 5.15: Projections of the six 3D measurements. These measurements were performed using method 1 described in the previous section.

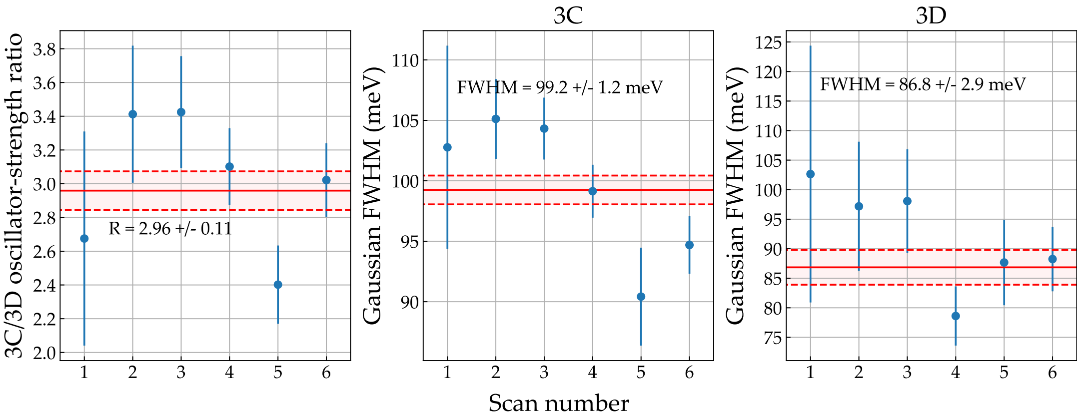

FIGURE 5.16: Left panel: The ratio of the obtained areas from the individual 3C and 3D scans resulting in the oscillator-strength ratio. Center and right panel: The observed Gaussian FWHMs for 3C and 3D are depicted, respectively. Red solid lines indicate the weighted average value combined with the 1-σ statistical uncertainty (red dashed lines).

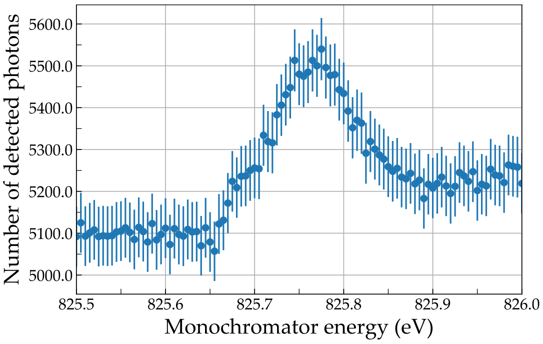

FIGURE 5.17: A discarded scan of 3C. While the background emitted by the plasma in the EBIT was stable on the lower photon energy half of the resonance, it suddenly increased at higher photon energies. Those fluctuations most likely arose from electron beam instabilities or injection pressure variations.

The advantage of this measurement scheme was that Gaussian models were directly fitted to the acquired datasets. The resulting areas were then proportional to the oscillator-strengths of the underlying transitions. The scan duration of 15 to 20 min was short compared to the often observed long-time energy drifts of the beamline on the timescale of hours and thus did not disturb the measurements. However, a scan was much slower than the background fluctuations that arose from electron beam instabilities and predominantly from injection pressure fluctuations on the timescale of minutes. In order to demonstrate the latter, a scan that needed to be discarded is depicted in figure 5.17, during which the background was suddenly increasing after being stable for half of the scan duration. Combined with the low SNR, slow scans as employed in this method were very sensitive to background variations.

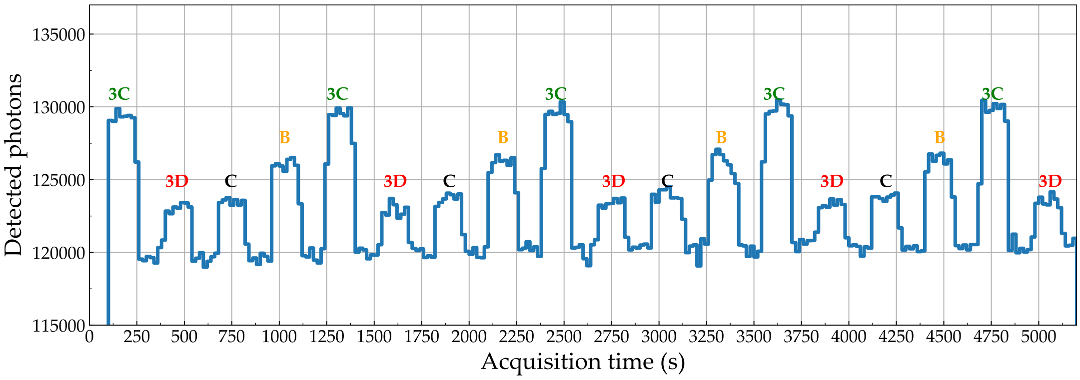

FIGURE 5.18: Measurement of the photon yield on the centroids of the resonances 3C, 3D of Fe XVII and C, B of Fe XVI. Each transition was observed for 120 s per cycle, with an background measurement of 20 s in between each line to observe possible drifts.

Method 2: Measurements of the fluorescence yield on maximum

In the second method, the limitations arising from fluctuating background in the first method were addressed. Instead of regularly scanning the photon beam energy, the monochromator energy was set to the maxima of the transitions. On the maxima, photons were acquired for 120 s, see figure 5.18. In order to distinguish the fluorescence from background photons, the background was measured by closing the photon beam shutter for 20 s in between each monochromator energy. Prior to the measurement, regular scans were performed to determine the individual energy centroids of the transitions. Since the monochromator energy calibration usually drifted on the timescale of hours, the newly determined centroids ensured that the fluorescence yields were correctly measured on the maximum of each transition.

The observed number of events on each resonance was time-normalized to obtain the centroid yields including the background. The bare fluorescence rate was determined by subtracting the time-normalized background acquired before and after the actual resonance measurement. The areas of the transitions, which were required to determine the oscillator-strength ratio, were inferred by multiplying the observed centroid fluorescence yields with the corresponding Gaussian widths obtained from method 1. Using this measurement scheme, the centroid fluorescence yield of the lines 3C and 3D, as well as C and B of Fe XVI, were consecutively measured twelve times. The observed heights, the resulting oscillator-strength ratios, and the weighted average are shown in figure 5.19.

Systematical uncertainty of method 2

Compared to method 1, the total amount of registered fluorescence events were increased by orders of magnitude, which positively affected the statistical accuracy. Besides, the background variations were under control by regularly acquiring the background emission. However, the second method also introduced new possible systematical errors. First, if the monochromator unexpectedly shifted its energy during the measurement, the observed photon yield might have corresponded to the

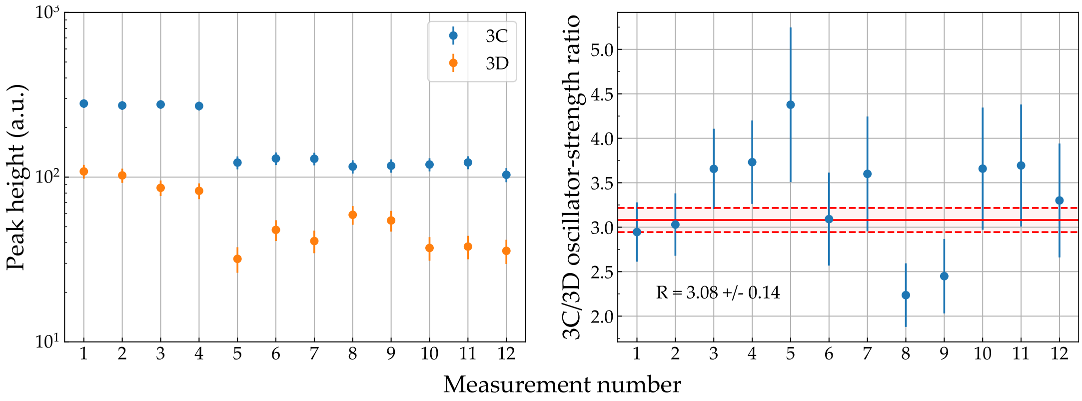

FIGURE 5.19: Left panel: The individual peak height values of method 2 which were used to infer the oscillator-strength ratio by multiplying the heights with the corresponding widths obtained in method 1. Right panel: The individual values of the 3C/3D oscillator-strength ratio measurements using the second method. The red bar indicate the weighted average including the 1-σ uncertainty.

rising or falling edge of the Gaussian line shape of the fluorescence and not to its maximum. Based on the experiences from method 1, a maximal monochromator energy drift of less than 10 meV h^{-1} was estimated. Since the length of the measurements was in the order of one hour, the energy drift could be limited, accordingly. By applying the possible energy drift of 10 meV to the typical line shapes acquired in method 1, the flux deviation from the maximum flux on centroid was estimated to be 0.3% or less. Secondly, the widths obtained from method 1, which were required to infer the transition areas, also exhibited an uncertainty between 1 to 3%, which affected influenced the uncertainty for the final result of method 2 accordingly.

Method 3: Scanning while alternating the photon shutter

The third method combined the advantages of methods 1 and 2. While scanning across the lines as in method 1 and exposing the ion cloud for 30 s to the incident photon beam, the background was measured for another 30 s in between each monochromator step by repeatedly closing the photon beam shutter. Since this scheme was very time consuming and the available measurement time limited, only a fraction of the monochromator energy range scanned in the first method could be probed in this method.

The sum of the background-subtracted signal of eleven scans is depicted in figure 5.20. The individually obtained 3C/3D oscillator-strength ratios of the eleven scans are depicted in figure 5.21. Unfortunately, the scan range was insufficient to reliably fit Gaussian models to the data without any further constraints. Especially, the width as well as the background were not adequately modeled by the fit routine. Hence, the linewidths obtained in method 1 were included as fixed parameters in the fit routine and contributed to the final systematic uncertainty. Assuming the background being completely removed, the baseline was fixed to zero.

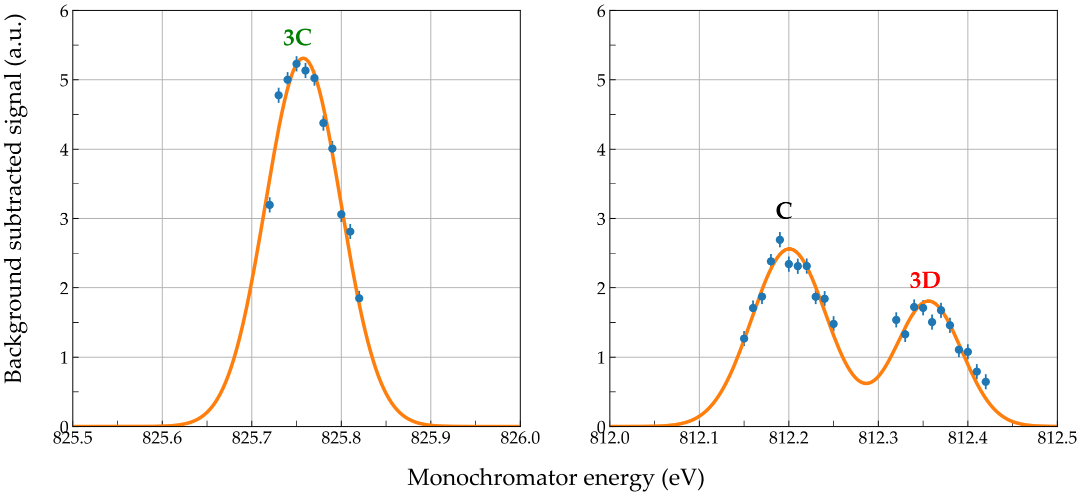

FIGURE 5.20: Sum of the background subtracted spectra obtained using method 3. Due to the limited available measurement time, only a fraction of the line was scanned. The widths of the fit were constrained by the values observed using method 1.

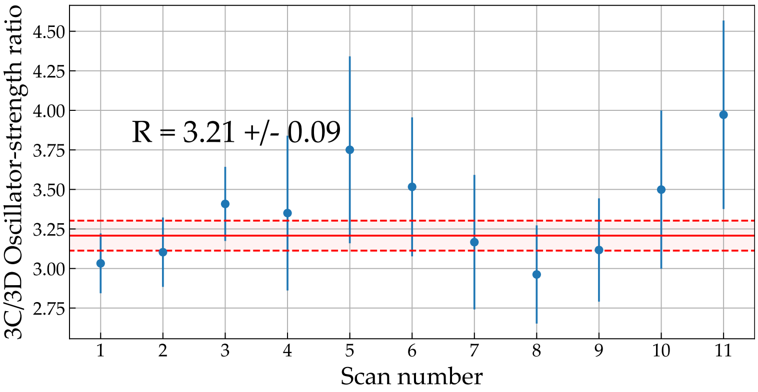

FIGURE 5.21: The individual 3C/3D oscillator-strength ratios measurements using the third method. The red bar indicate the weighted average including 1σ uncertainty.

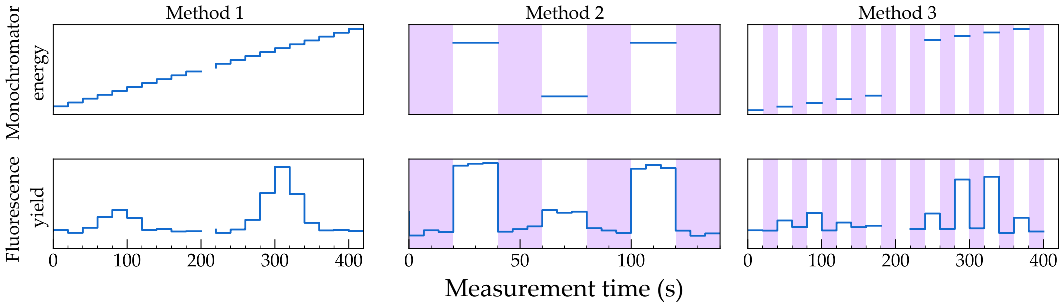

FIGURE 5.22: Overview scheme of the three performed measurement methods. The top panel represents the monochromator energy for each step. The lower panel shows the resulting fluorescence yield. Purple shaded areas indicate phases in which the photon beam shutter was closed for background measurements. Figure adopted from [96].

5.3.5 Summary

The X-ray laser spectroscopy beamtime in 2018 focused on measurements of the oscillator-strength ratio of the prominent resonance line 3C and the intercombination transition 3D of Fe XVII. The unprecedented achieved resolving power of approximately $\frac{E}{\Delta E} = 8250$ allowed for the first time to separate the adjacent line C of Fe XVI from line 3D. Thus, the 3C/3D oscillator-strength ratio could be directly determined by fitting Gaussian profiles to the lines and dividing the observed areas of 3C by the areas of 3D. However, the electron beam instabilities and the varying injection pressure hampered the accuracy of regularly performed scans in method 1, as demonstrated in figure 5.17. To resolve these instabilities, two additional methods to measure the oscillator-strength ratio were introduced. A schematic overview of the three different measurement routines is presented in figure 5.22.

The individual systematical uncertainties of each method were estimated and explained in detail. Independent of the method, an additional uncertainty needed to be taken into account. The synchrotron was operated in the so-called „top-up mode“, which means that once the electron beam current in the storage ring dropped below a certain threshold, new electron bunches were injected. During this beamtime, the electron beam was refilled by 1 mA once the current dropped below 99 mA. In a first-order assumption, the photon beam intensity was linear to the storage ring current. Since the flux registering mesh was removed during the measurements, a direct compensation of the flux deviations was inaccessible. Thus, an additional uncertainty of 2% was added to the error budget.

Each individual measured 3C/3D oscillator-strength-ratio value separated by the employed method as well as the weighted average value for each method is depicted in figure 5.23. The final 3C/3D oscillator-strength value of this beamtime of $f_{3C}/f_{3C} = 3.09(10)$ including the statistical uncertainty and the systematical error budget are listed in table 5.1.

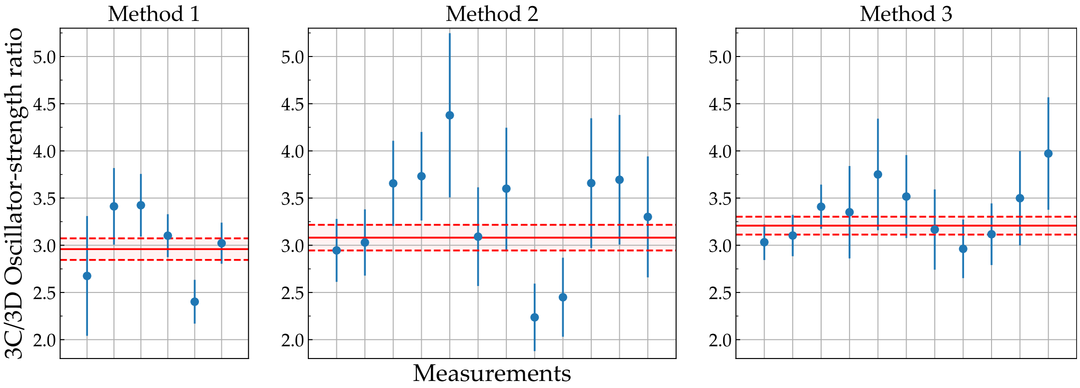

FIGURE 5.23: The individual 3C/3D oscillator-strength ratio values including the statistical and systematical uncertainties separated by the three applied measurement techniques. Red bars indicate the corresponding weighted average and 1σ deviations.

TABLE 5.1: $3C/3D$ oscillator-strength ratios obtained from three diffferent measurement methods and their statistical and systematic uncertainties. Table adopted from [96].

	Method 1	Method 2	Method 3
$3C/3D$ oscillator-strength ratio	2.960	3.080	3.210
Uncertainty Budget			
Statistical	0.106	0.140	0.095
Systematics due to:			
(1) ROI width selection on 2D histogram	0.030		
(2) ROI centroid selection on 2D histogram	0.044		
(3) Time-dependent background variation due to the electron-impact excitation	0.036		
(4) Monochromator shifts		0.092	
(5) Linewidth constraints in fits			0.048
Total systematic uncertainty	0.071	0.097	0.058
Total (statistical + systematic) uncertainties	0.127	0.170	0.111
Common systematics for all three methods: Flux variation of the incident photon beam at P04/PETRA III		0.0618	
Final $3C/3D$ **oscillator-strength ratio**		$\mathbf{3.09} \pm \mathbf{0.08}_{\text{stat.}} \pm \mathbf{0.06}_{\text{sys.}}$	

5.4 Campaign 2019

After the 3C/3D oscillator-strength ratio was remeasured in 2018, the subsequent beamtime in September 2019 aimed at increasing the resolving power as well as the signal strengths in order to determine the natural linewidths of the transitions. In the beginning of this section, the preparation of the target will be discussed, followed by the introduction of a novel measurement scheme that was used to measure the 3C/3D oscillator-strength ratio of iron as well as krypton. Finally, the measurement campaign will be summarized.

5.4.1 Preparation of the target

As presented in chapter 5.3.1, dielectronic recombination (DR) measurements provide a diagnostic utility of the charge-state distribution present in the trap. The L-shell DRs of Fe XVII occur at lower electron beam energies than required to produce this particular charge state. In the previous beamtime 2018, the presence of Fe XVII using DRs could not be directly proven, as the employed power supplies that drove the voltages applied to the electrodes and hence, defined the electron beam energy, did not exhibit the required slew rates to produce enough Fe XVII at high electron beam energies and probe the resonances below the production threshold. During this beamtime, a fast power supply with load-free slew rates larger than $300\,\mathrm{V}\,\mu\mathrm{s}^{-1}$ was employed. The fast power supply enabled the production of Fe XVII at sufficiently high electron beam energies and subsequently ramped the energy down to the range of Fe XVII DRs. The high slew rate of the power supply ensured that the voltage ramp-down process was faster than the recombination rate of Fe XVII below the production threshold in the order of milliseconds.

As for the preparation of the beamtime, such a DR measurement was performed. The obtained results are depicted in figure 5.24. The abundance of Fe XVII ions were proven by observing Fe XVII resonances below 340 eV for times shorter than 200 ms after ramping down the electron beam energy. Within 200 ms, Fe XVII completely recombined to Fe XVI and subsequently to Fe XV by means of radiative recombinations, dielectronic recombinations, and charge exchange, see chapter 2.3.2. After 2 s, a new charge-state equilibrium was established dominated by Fe XV and Fe XIV ions. Note that once the electron beam energy was low to probe DR resonances, the energy was insufficient to further reproduce Fe XVII. Since DRs recombine a given charge state into the next lower charge state, e.g., Fe XVII into Fe XVI, the higher charge states were resonantly depleted during the DR measurement. Hence, the actual Fe XVII lifetime off resonance might exceed the observed lifetime inferred from the DR measurements depicted in figure 5.24.

The achieved electron beam energy resolution of 3.5 eV FWHM significantly improved the quality of available experimental data of Fe L-shell DRs measured in an EBIT and is treated and published in detail in [149, 63].

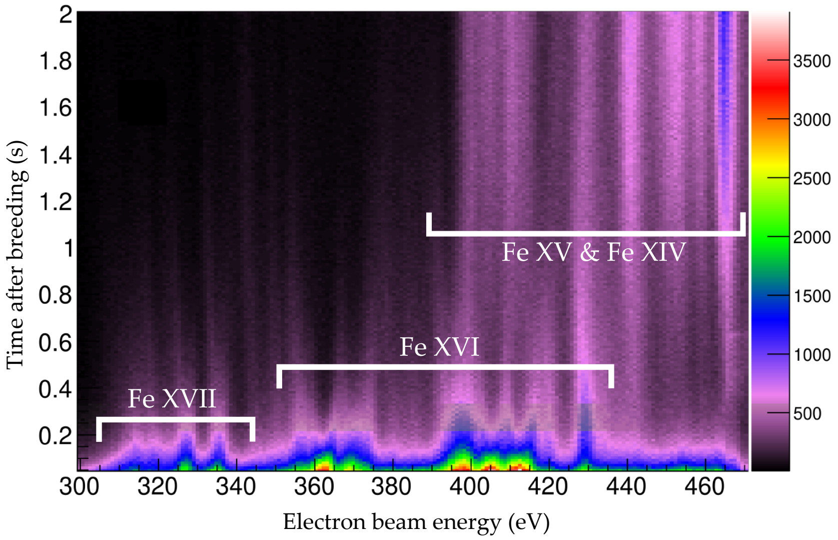

FIGURE 5.24: The observed intensity of dielectronic recombinations as a function of time after breeding (ordinate) and electron beam energy (abscissa). After the ion cloud was bred at high electron beam energies to produce the desired charge state Fe XVII (not shown here), the beam was ramped down to a constant beam energy between 300 eV and 470 eV. Once ramped down, the time-dependent photon emission of the ion cloud was observed for 2 s. Higher charge states such as Fe XVII recombined within a few milliseconds, where lower charge states (Fe XV & Fe XIV) started to emit photons once the higher charge states were completely recombined. Figure adopted from [63].

5.4.2 Measurements of 3C and 3D

Similar to the first measurement campaign in 2018, the experimental setup was aligned, e.g., the ion cloud was overlapped with the incident photon beam using strong transitions of light elements like oxygen and neon. Once the alignment was accomplished, the lines 3C and 3D of Fe XVII were scanned.

Based on the experiences gained during the first campaign, the experimental measurement scheme was completely revised. In 2018, the electron beam energy was set at values of approximately three times the Fe XVII production threshold to produce a sufficient amount of the desired charge state. Due to the high electron beam energy, transitions were non-resonantly driven by the electron-impact excitation process, resulting in a high background.

In this campaign, instead of continually producing the ions at high electron beam energies, the measurement scheme was divided into a breeding and a probing phase, see figure 5.25. During the breeding phase, a sufficient amount of Fe XVII was produced by the electron beam exhibiting an energy similar to the energies employed during the first measurement campaign. Subsequently, the electron beam energy was reduced to only 260 eV within ms to mitigate the background induced by electron impacts. In the probing phase, the electron beam was unable to produce a strong background signal in the photon energy region above 800 eV. However, the ions still recombined due to radiative recombination and charge exchange. The beam energy during the probing phase was selected such that resonant dielectronic

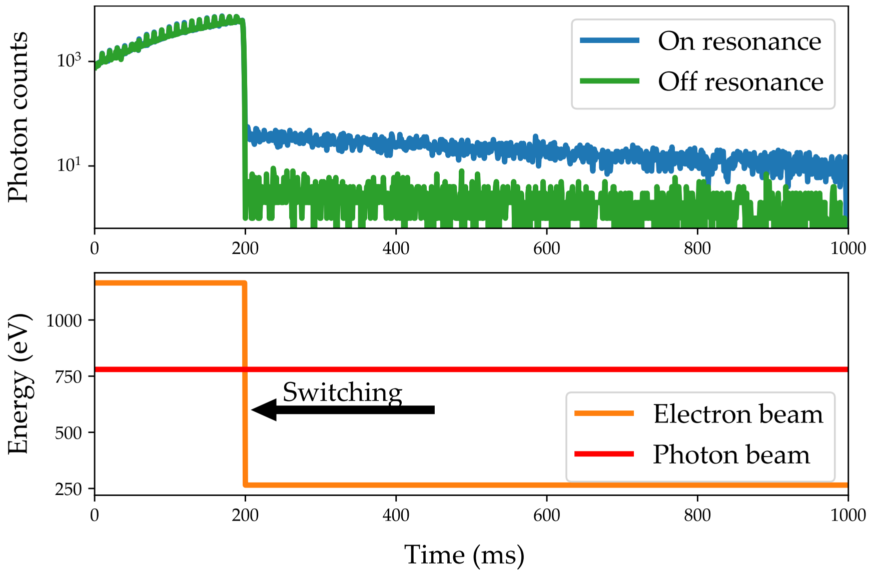

FIGURE 5.25: Photon yield (top panel) as well as electron and photon beam energy (bottom panel) as a function of time in a measurement cycle. While the photon energy remained constant, the electron beam energy was alternating between a high and a low value. The background during the probing phase ($t > 200$ ms) was reduced by orders of magnitudes compared to the breeding phase ($t < 200$ ms), while the resonance signal was clearly separated from the background signal.

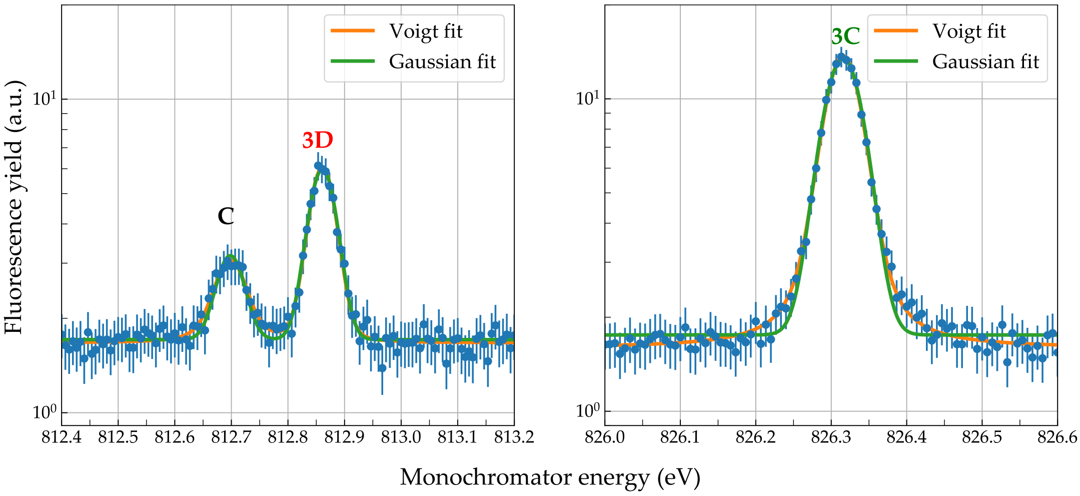

FIGURE 5.26: The summed fluorescence yield of seven consecutive scans of 3C and 3D. The increased resolving power $E/\Delta E = 14000$ required and enabled to model the transitions with Voigt (orange) instead of Gaussian (green) line profiles.

recombinations, which have large cross sections compared to radiative recombinations, could be neglected. Due to the constant loss and lack of any reproduction channels of Fe XVII, the ion population depleted exponentially. After Fe XVII almost entirely recombined, the cycle started over and new ions were bred at high electron beam energies. During the breeding, usually hundreds of ms were required to produce Fe XVII. The lifetime of Fe XVII in the probing phase depended on many parameters such as electron beam current, injection pressure, residual gas pressure, or potential auto-ionizing transitions driven by the photon beam and was usually in the order of tens to hundreds of ms. Using the so-called „Magnetic-Trapping Mode", e.g., completely turning off the electron beam and radially confine the ion cloud purely by the magnetic field as demonstrated in [12, 112], was unfeasible in the PolarX-EBIT.

Utilizing this scheme, the SNR could be improved by two orders of magnitude compared to the previous beamtime. The strengthened fluorescence signal allowed to further close the exit slit, resulting in an improved resolving power of the experiment. The sum of seven consecutive scans of 3C and 3D is depicted in figure 5.26.

The resolving power achieved during beamtime 2019 was in the order of $E/\Delta E = 14000$, an improvement by at least a factor of two compared to the previous beamtime. Hence, the resolving power was sufficient to observe a Voigt line shape which consists of the convolution of the Gaussian instrumental profile with the Lorentzian natural line shape of the individual transitions, see chapter 2.3.4 for detailed information about Voigt profiles. In order to illustrate the difference, a Voigt and Gaussian model were fitted to the data, see figure 5.26. As expected, Gaussian line shapes were unable to replicate the acquired dataset.

In total, 74 scans of 3C and 3D each were acquired and grouped in 5 datasets. Each scan covered an energy range of approximately 0.6 eV across the line centroids in equidistant steps of 6.7 meV. The observed amplitudes of the datasets were averaged weighted by their uncertainties. The resulting 3C/3D oscillator-strength ratios are depicted in figure 5.27. Even though the individual datasets partially reached statistical uncertainties well below 1%, the obtained ratios appeared to vary non-statistically. The non-statistical distribution of the oscillator-strength ratios most likely arose from fluctuations of the charge-state balance in the trap induced by instabilities of the injection pressure which were observed during the measurements. Note that systematical effects such as ROI determination and photon flux differences were excluded in this beamtime, since the SNR was vastly improved and an additional photon intensity diode was installed behind the experimental setup.

5.4.3 Lorentzian linewidths

Due to the excellent resolving power achieved in this beamtime, the quality of the data allowed to fit Voigt profiles to the observed fluorescence yield. Hence, Lorentzian widths of the Voigt profile were measured for the first time, which in principal allow to infer the individual natural linewidths of the investigated transitions. Compared

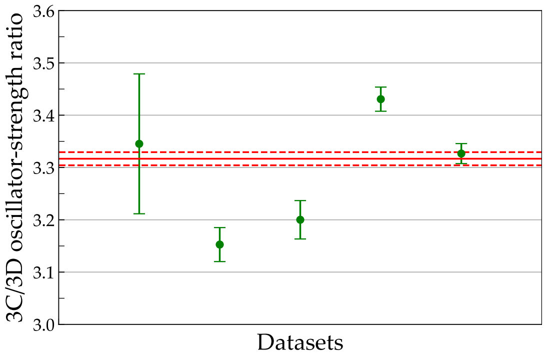

FIGURE 5.27: The observed 3C/3D oscillator-strength ratio for the available datasets. Each dataset contains several scans for which the experimental conditions seemed to be stable. The individual results seem to non-statistically deviate. Red line: Weighted average including 1-σ uncertainty (dashed lines).

to oscillator-strength ratios, a linewidth is less vulnerable to systematical uncertainties such as ROI selection and photon flux correction and should deliver more robust experimental results. The observed Lorentzian linewidths Γ'_{3C} and Γ'_{3D} of line 3C and 3D, respectively, were determined by summing up all measurements and fitting Voigt models to the summed dataset:

$$\Gamma'_{3C} = 22.06(76)\,\text{meV},$$
$$\Gamma'_{3D} = 12.49(106)\,\text{meV}.$$

5.4.4 Measurements on Kr XXVI

An additional element other than iron was measured during the beamtime to scrutinize if the discrepancy of the oscillator-strength ratios between experimental and theoretical work is persistent over an extensive range of various elements [24]. Neon-like Krypton (also written as Kr XXVI) features an increased nuclear charge $Z = 36$ while the number of electrons as well as the electronic structure remains the same compared to Fe XVI. Since the required electron beam energy to produce Kr XXVI is significantly higher compared to Fe XVII, the EBIT parameter settings needed to be adjusted accordingly. Due to the higher effective charge state of krypton, a relatively long breeding time of 1 s was required to remove 26 electrons and to produce a decent amount of Kr XXVI. The long breeding time drastically reduced the duty cycle and the effective measurement time compared to iron.

As expected, the transition energies of 3C and 3D scale with Z^2, resulting in values of 1851 and 1802 eV, respectively. For such high photon beam energies, the transmission efficiency of the employed optical elements of the beamline coated with a platinum layers was vastly reduced, see chapter 4.2.3. In future measurements, employing rhodium coatings that exhibit higher transmission efficiencies for photon energies above 1500 eV compared to Pt coatings are desirable. Since switching optical elements of the beamline requires a realignment of the experimental setup, the

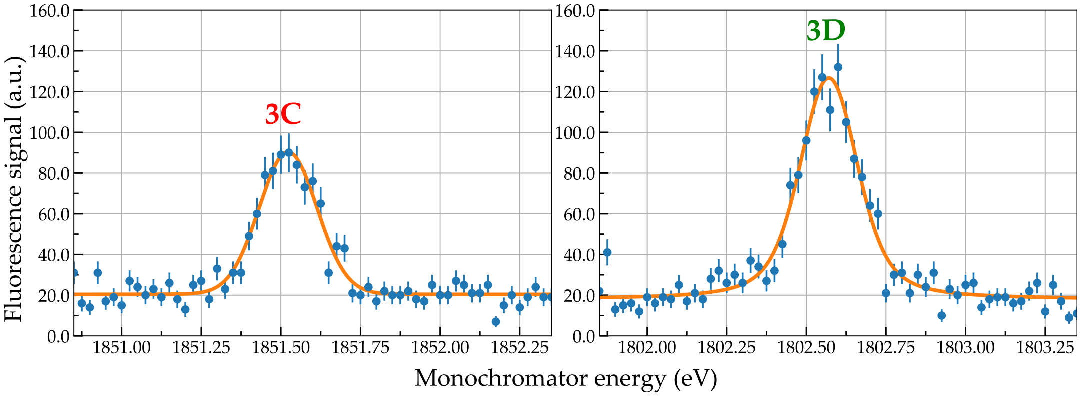

FIGURE 5.28: Sum of eleven consecutive 3C/3D scans of Kr XXVI. Due to the increased amount of electrons to be removed, the breeding time needed to be prolonged. Hence, the duty cycle and the effective fluorescence rate is reduced.

same optical elements as for iron were employed resulting in a reduced photon flux.

Despite the reduced duty cycle due to increased breeding time and lower photon flux, a clear fluorescence signal for both 3C and 3D of Kr XXVI was obtained. In figure 5.28, the sum of eleven 3C and 3D scans are depicted. Unfortunately, the data files that recorded the effective photon flux on sample were corrupted for these particular measurements, which hampered the accurate determination of the individual observed amplitudes for the oscillator-strength ratio. However, the measurements demonstrate that even for higher Z such as Kr, both the EBIT and the beamline were able to acquire the fluorescence of the respective 3C and 3D lines.

5.4.5 Summary

The second beamtime performed in 2019 also focused on the two prominent lines 3C and 3D of Fe XVII. In contrast to the first beamtime, the measurement scheme was fundamentally changed, which improved the SNR by several orders of magnitude. The increased SNR allowed to further close the exit slit which influenced the resolving power of the experiment but also decreased the photon flux. The improvement in resolving power allowed to observe the Lorentzian width of Voigt-like fluorescence shape of the two lines for the first time. Despite the improved measurement procedure, strong fluctuations of the observed fluorescence intensities were also observed. Simultaneously, the pressure in the injection system varied. For this reason, a conclusive determination of the 3C/3D oscillator-strength ratio was not possible. However, it was shown that the statistical accuracy of the single measurement of the oscillator-strength ratio was significantly improved compared to the measurement campaign in 2018.

5.5 Campaign 2020

Prior to the third and last beamtime presented in this thesis, the PolarX-EBIT was extensively modified. Based on the experiences gained during the measurement campaigns at synchrotron facilities, several vital components of the EBIT were replaced or improved. During the first and second beamtime, the residual gas pressure in the experimental setup was limited to the lower 1×10^{-8} mbar regime. Hence, additional pumps were installed and in the central cube, in which the drift tubes were mounted, four additional pumping holes were milled, which significantly increased the pumping cross section in the trap center and especially in the detector chambers attached to it. Furthermore, it was suspected that the electron collector had a micro leak and was therefore replaced with a new exemplar.

The prototype off-axis electron gun was replaced with a next-generation off-axis electron gun, see also chapter 3.2.3. This modification increased the maximum applicable voltages and thus, enabled higher electron beam energies and currents compared to the previous setup.

In order to further increase the amount of detected photons, the filter mount which prevents visible light from saturating the detector was redesigned such that the detector was mounted closer to the ion cloud. Additionally, a second detector with a larger detection area was mounted on a free optical port to the trap center. Both detectors combined offered a solid angle of approximately 3% of 4π, an increase of at least a factor of three compared to previous setup.

The main systematic uncertainty during the two previous beamtimes arose from instabilities of the injection pressure that affected the charge-state balance and the fluorescence strength. Hence, the injection system was extented by a second stage which were separated by a gate valve. Additional differential pumping barriers in between the stages further increased the pressure difference between the stages. The diameter of the aperture separating the final stage from the trap center was also vastly reduced, see figure 3.10. This allowed to increase the pressure in the injection system by two orders of magnitude while keeping the injection quantity into the trap at the minimal required level. The employed needle valve in combination with the liquid compound $Fe(CO)_5$ exhibited much more stable conditions if the partial pressure in the first stage was higher. During the preparation of the experiment, a stable injection pressure over hours was demonstrated.

An ion extraction beamline consisting of an electrostatic bender, an Einzel lens and a channeltron as an ion detector was attached to the EBIT, see figure 5.29. As presented in [137], this enabled to extract the confined ion cloud towards the collector side of the EBIT. Subsequently, the ions were separated due to the different kinetic energies according to the individual charge-to-mass ratios q/m. By measuring the time between ejecting the ions and the time of arrival on the channeltron, the individual charge states that were present in the trap were identified.

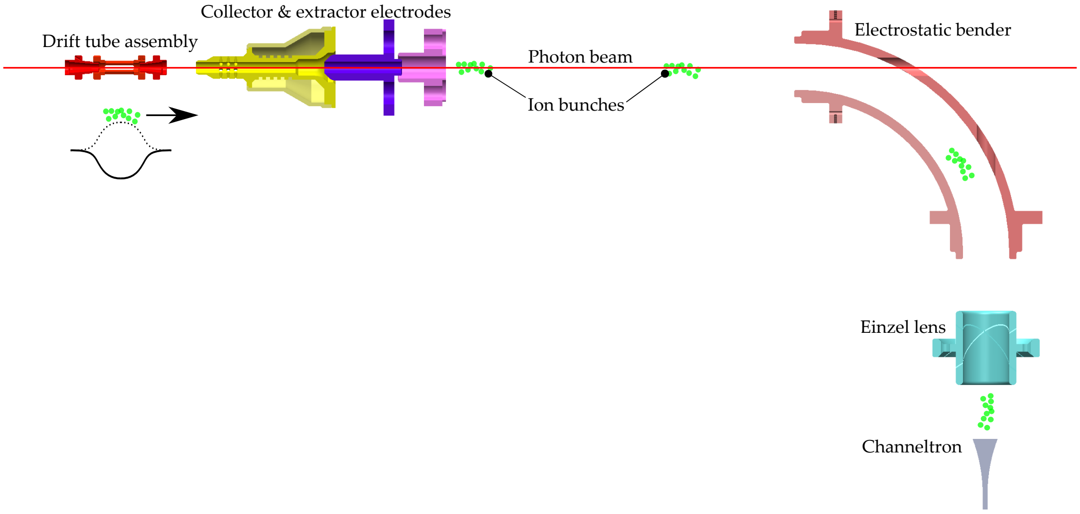

FIGURE 5.29: Schematic of the ion extraction beamline. The potential induced by the drift tube assembly (red) is inverted for tens of nanoseconds in order to extract the produced ions (green) towards the collector (yellow) and the subsequent extractor electrodes (purple and pink). The various ion species are separated according to their charge-to-mass ratio. An electrostatic bender deflects the ion bunches towards the channeltron. An Einzel lens in between refocusses the ion beam onto the channeltron. A cutout in the outer bender electrode allows the synchrotron photon beam to pass the experimental setup.

5.5.1 Iron

Preparation of the target

In contrast to previous beamtimes, the ion extraction beamline enabled to directly analyze the trap content. Hence, the presence of Fe XVII could be verified independent of DR measurements as performed as a target preparation prior to the measurement campaigns 2018 and 2019. In figure 5.30, a typical time-of-flight spectrum generated by the ions impinging on the channeltron is depicted. The strongest peaks arose from the dominant isotope of iron exhibiting charge states between $^{56}\mathrm{Fe}^{3+}$ and $^{56}\mathrm{Fe}^{13+}$. Additionally, weaker peaks from the less abundant isotope $^{54}\mathrm{Fe}$ as well as

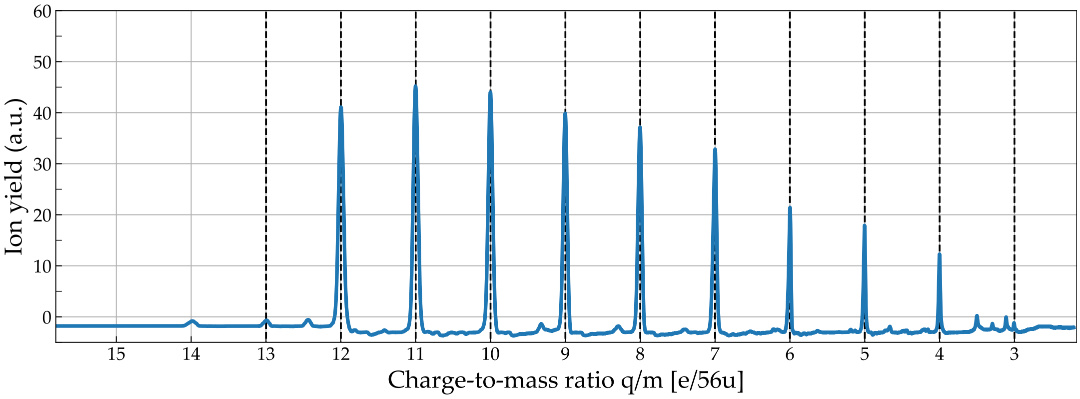

FIGURE 5.30: Ion yield as a function of the charge-to-mass ratio q/m. Apart from $^{56}\mathrm{Fe}$, indicated by dashed vertical lines, peaks from $^{56}\mathrm{Fe}$, carbon as well as oxygen could be identified, elements which are part of the injected compound $\mathrm{Fe(CO)_5}$.

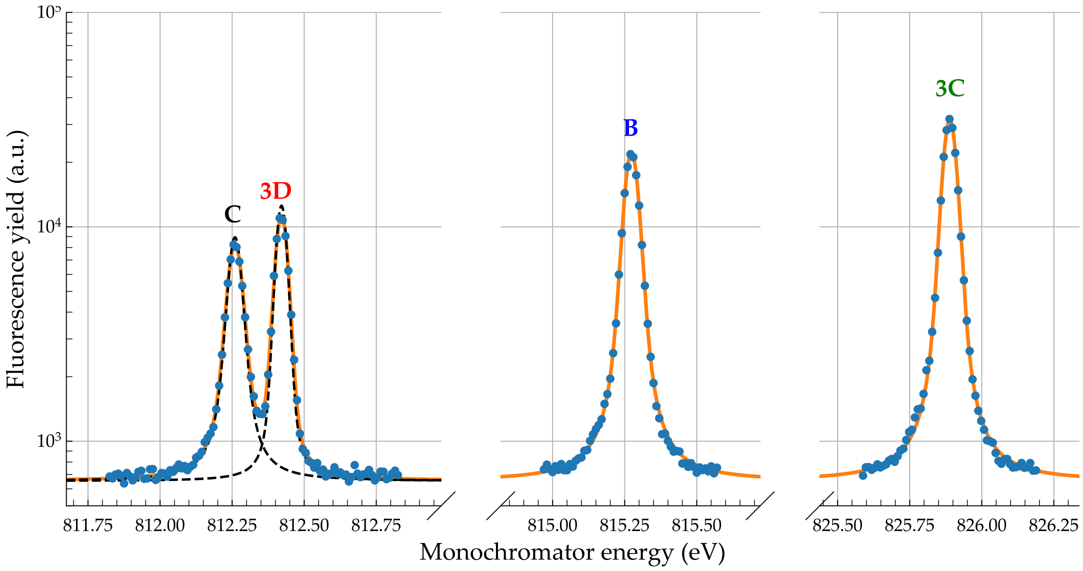

FIGURE 5.31: Sum of 20 consecutive scans of 3C and 3D of Fe XVII and B and C of Fe XVI. The orange line represents the result of the applied fit. All transitions share a minor asymmetry exhibiting a small excess on the lower energy edge side of each transition. In the left panel, the individual contributions of 3D and C to the complex are represented by black dashed lines.

oxygen and carbon, which were also trapped, were detected. It is evident that the experimental parameters that resulted in the time-of-flight spectrum depicted in 5.30 were insufficient to produce the required charge state Fe XVII. Hence, the EBIT parameters such as injection pressure, trap depth, electron beam energy, and current were optimized by means of repetitively ejecting the ions and inspecting the trap content until the Fe XVII yield was maximized.

Measurements of 3C, 3D, B, and C

Similar to the second beamtime in 2019, the measurement scheme was divided in a breeding and probing phase, see figure 5.25. At high electron beam energies, the ions were bred for 250 ms and probed at low energies well below the L-shell DR complex of iron for another 50 ms. In contrast to the cycle in 2019 which used a sharp step-like function, here, a smoothened sigmoid-like function was applied to alternate between the breeding and probing phase. Empirically, it was found that the number of ions getting lost during the ramp-down process of the electron beam was reduced if the ramp was smoothened.

Additional to 3C and the complex consisting of 3D and C, a fourth, well separated line B of Fe XVI was measured in between 3C and 3D scans. Due to its high intensity and the lack of strong auto-ionizing channels, line B provided a solid diagnosis of the Fe XVI abundance during the experiment. For each line, the monochromator energy was increased by equidistant 10 meV steps in a 0.6 eV broad energy range across the line centroids. The sum of 20 performed scans of the lines 3C, 3D, C, and B transitions are depicted in figure 5.31. In order to properly model the data,

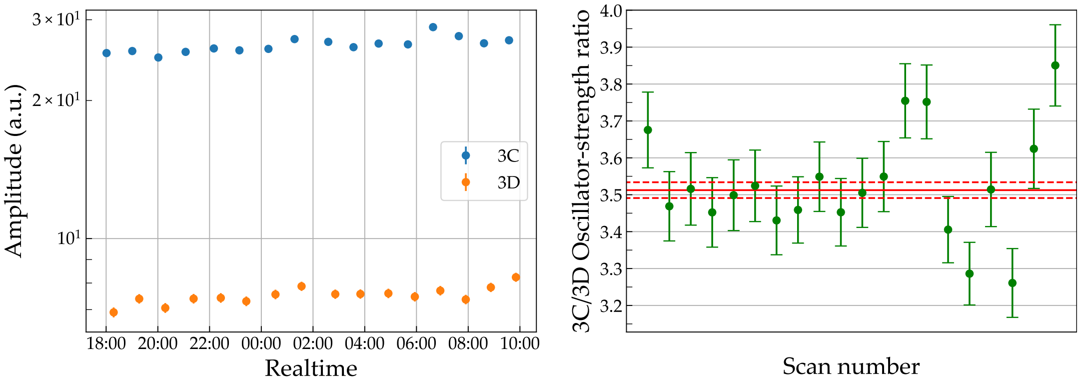

FIGURE 5.32: Left panel: The observed amplitudes for 3C and 3D as a function of the measurement time. Right panel: The inferred 3C/3D amplitude ratio for two consecutive scans at a time. The red solid and dashed lines indicate the weighted average and the statistical uncertainty.

a global fit utilizing multiple Voigt profiles was performed with free parameters for the amplitudes, centroids, offsets as well as Lorentzian and Gaussian widths for each individual scan. The centroids of C were determined by a shared energy difference to the individually determined centroids of 3D, since the energy drifts of the monochromator within one scan across a small energy range of only 160 meV were assumed to be negligible.

The resolving power achieved in the third campaign exceeded previous measurements and reached values of up to $\frac{E}{\Delta E} = 20000$. The increased detector solid angle of the setup enabled to record count rates of up to 1000 Hz on resonance of 3C. Besides, the background was also significantly reduced to a count rate slightly above 20 Hz. However, the instrument profile of the monochromator showed a minor asymmetry, which was revealed by a slightly stronger fluorescence rate on the low-energy side of each transition, see figure 5.31.

In the left panel of figure 5.32, the resulting amplitudes for 3C and 3D are depicted as a function of time. Compared to previous beamtimes, the amplitude signal was much more stable even on large timescales. During the measurements, the injection pressure also remained stable for hours. Within a single scan, no variation of the background emission which could also have hinted towards injection pressure or electron beam instabilities were observed. The right panel of figure 5.32 shows the inferred 3C/3D oscillator-strength ratios of two consecutive scans by dividing the obtained Voigt area of 3C by the area of 3D. As expected, the fluctuations of the ratios are statistically distributed. The obtained amplitudes were corrected for photon flux differences of P04 between line 3C and 3D measured by a well-calibrated XUV-sensitive photon diode mounted downstream of the EBIT. Additionally, a compensation factor accounting for the different detector filter transmissions of 3C and 3D was applied to the results. Combined, both corrections increased the oscillator-strength ratio by 0.5%. The weighted average of the performed scans yielded a 3C/3D oscillator-strength ratio of

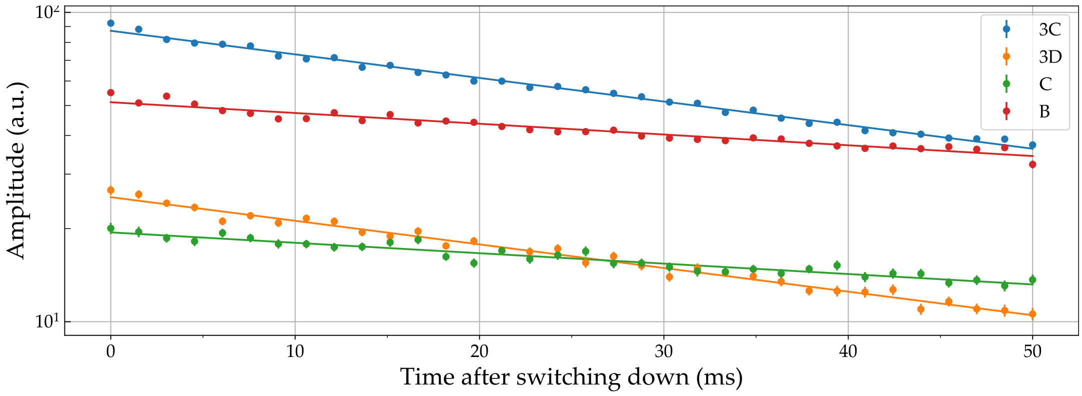

FIGURE 5.33: The amplitude of 3C, 3D, C and B as a function of time after ramping down the electron beam energy. Solid lines represent best fit results for an exponential decay model.

$$\frac{f_{3C}}{f_{3D}} = 3.51(2)_{\text{stat}}.$$

Note that similar to beamtime in 2019, the determination of ROI which were used to extract the projections did not result in an additional systematical uncertainty.

Half-life of the ion population

After the ions were bred, the electron beam energy was lowered to a fraction of the upper value to suppress background. Thereby, the lower electron beam energy of 265 eV was no longer sufficient to produce the investigated charge states Fe XVI and Fe XVII. Due to recombination caused by interactions with the electron beam (radiative recombinations) as well as with neutral residual gas (charge exchange), the number of highly charged ions continuously depleted. In figure 5.33, the amplitudes as a function of time after switching down the electron beam energy is depicted. The depletion of Fe XVII and Fe XVI ions could be well modeled with an exponential decay. The half-lifes and initial amplitudes obtained of the exponential decay model are summarized in table 5.2. As expected the lifetimes of 3C and 3D were identical within the statistical accuracy achieved. The half-lifes of the lines B and C of Fe XVI were more than twice as long compared to the half-lifes of 3C and 3D. In principle, the recombination rates of both charge states Fe XVII and Fe XVI were expected to exhibit similar strengths, but since Fe XVII recombined into Fe XVI, the latter was continuously fed resulting in a vastly prolonged lifetime. Since Fe XVII was the highest possible charge state, Fe XVII was not fed by higher charge states. Additionally, even though not statistically significant, it seems that C exhibited a longer lifetime than B. The reason for this lifetime difference is most likely found in the strong auto-ionization channel of C, resonantly pumping fractions of Fe XVI back into Fe XVII again.

In principle, the determined ratio of the initial amplitudes of the exponential decay model used to fit the data depicted in figure 5.33 represents the oscillator-strength ratio of the two transitions. In the case of 3C and 3D, a value of

TABLE 5.2: Half-lifes and initial amplitudes of the exponential decay model fitted to the fluorescence of 3C, 3D, C, and B after switching down the electron beam energy into the probing phase.

Transition	**Half-life (ms)**	**Initial Amplitude (a.u.)**
3C	56.97(89)	87.20(63)
3D	56.88(137)	25.27(28)
B	124.84(552)	51.23(53)
C	129.03(680)	19.45(22)

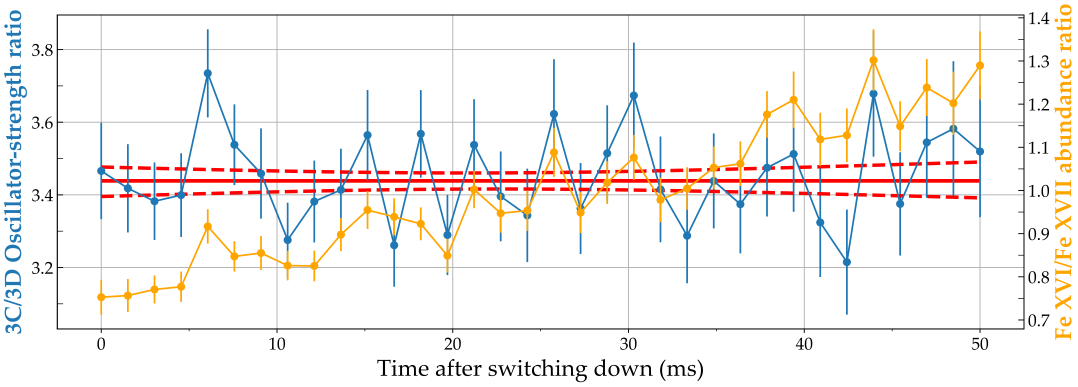

FIGURE 5.34: The observed 3C/3D oscillator-strength ratios (blue, left axis) and the Fe XVI/Fe XVII abundance ratio (orange, right axis) as a function of time after switching down the electron beam. Red solid line shows the result of a linear function fitted to the oscillator-strength ratios. Dashed lines indicate the 1-σ uncertainty.

$$\frac{f_{3C}}{f_{3D}} = 3.45(5)_{\text{stat}}.$$

was obtained, which is in good agreement with the value determined by using the conventional Voigt profile fit procedure as described earlier.

Time evolution of the oscillator-strength ratio

Similar to the individual amplitudes in the previous section, the time evolution of the 3C/3D oscillator-strength ratio in the probing phase was examined. Hence, the probing phase was divided into equidistant time sections and the respective amplitudes of both lines were divided by each other. Additionally, the evolution of the Fe XVI/Fe XVII abundance ratio during the probing phase was obtained by comparing the areas of the line C and 3D.

In figure 5.34 the time evolution of both, the Fe XVI/Fe XVII abundance as well as the 3C/3D intensity ratio is depicted. Even though the relative abundance of Fe XVI almost doubled, the 3C/3D oscillator-strength ratio remained stable. In order to verify that the observed 3C/3D oscillator-strength ratio was constant and thus independent of the Fe XVI/Fe XVII abundance ratio, a linear model was fitted to the oscillator-strength ratio evolution. As expected the linear model resulted in a slope

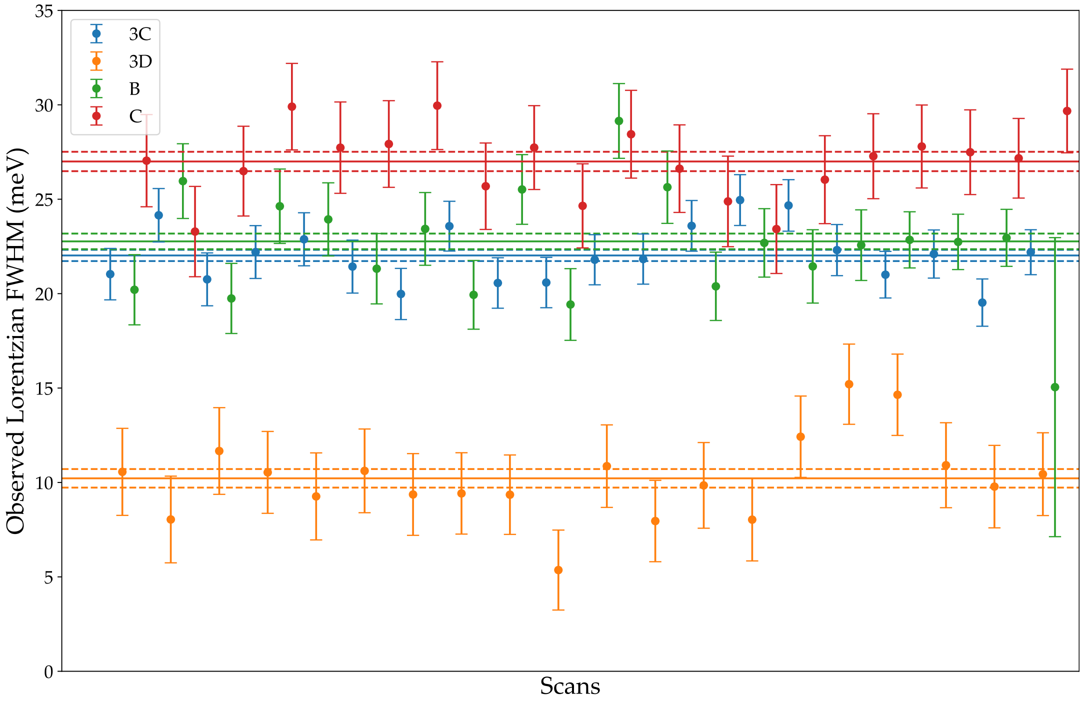

FIGURE 5.35: The observed Lorentzian linewidths of the Voigt profiles applied to the measured fluorescence of the lines 3C (blue), 3D (orange), B (green), and C (red). The solid line represent the weighted average of all measured linewidths of a given transition including the 1-σ deviation (dashed lines).

of zero. Hence, the 3C/3D oscillator-strength ratio was independent of Fe XVI/Fe XVII abundance ratio.

Lorentzian linewidths

The large SNR of the fluorescence signal and the excellent resolving power of the experiment offered to observe and model the Lorentzian linewidths of the Voigt-like line shape of all four investigated lines 3C, 3D, B, and C with unprecedented relative statistical uncertainties well below 10% for a single scan. The individual observed Lorentzian linewidths Γ' for the lines in each scan is depicted in figure 5.35. Similar to the distribution of the observed oscillator-strength ratio, all Lorentzian linewidth values appear to be statistically distributed. The values for the observed Lorentzian linewidths

$$\Gamma'_{3C} = 22.02(30)\,\text{meV},$$

$$\Gamma'_{3D} = 10.22(49)\,\text{meV},$$

$$\Gamma'_{B} = 22.77(41)\,\text{meV},$$

and

$$\Gamma'_{C} = 27.00(51)\,\text{meV},$$

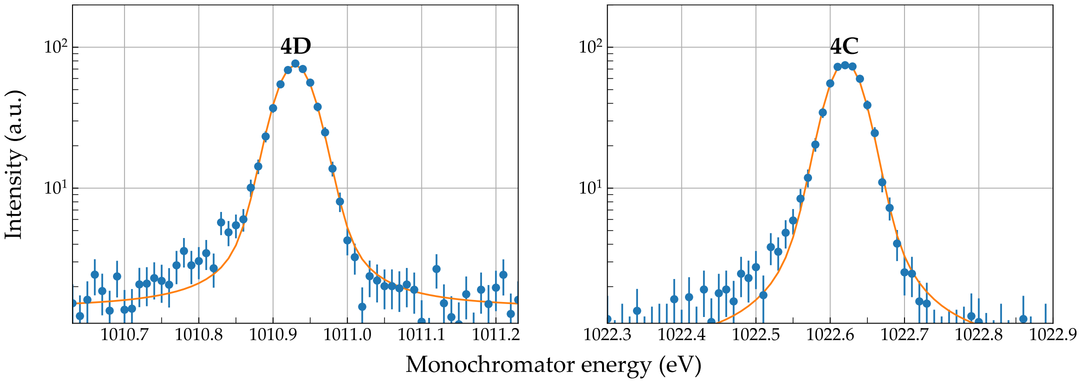

FIGURE 5.36: Sum of four measurements of 4C and 4D of Fe XVII. Since those transition are energetically distant to the optimized range of 3C and 3D, strong asymmetries were visible on the lower energy side of the transitions.

were obtained by the average of the individual measurements weighted by their uncertainty.

Measurements of 4C and 4D

Additional to 3C and 3D, two further lines of Fe XVII, namely 4C and 4D, with transition energies of 1022 and 1010 eV, respectively, were measured. Compared to 3C and 3D, those lines differ by their principle number n, but exhibit similar electronic configurations, see chapter 2.5. Additionally, neither of the two lines exhibit an adjacent line that could interfere with the measurements, such as in the case of C and 3D. Hence, the 4C/4D oscillator-strength ratio offers a supplemental benchmark of theoretical predictions.

In contrast to 3C and 3D, 4C and 4D feature several decay channels from their upper states. Thus, the observed intensities need to be corrected for the branching ratio provided by calculations to obtain the oscillator-strength ratio. The branching ratio describes the fraction of the upper state that directly decay back to the ground state compared to all possible decay channels. Ab initio FAC calculations showed branching ratios for the main decay channel of 95% for 4C and 92% for 4D. In the experiment, decays other than the main channel remained undetected, since the employed X-ray detector was unable to register photons in the expected energy. Note that neither 4C nor 4D exhibit any additional auto ionizing decay channel to higher charge states.

Due to finite available measurement time, each line was scanned only four times. The sum of the scans are depicted in figure 5.36. During the beamtime, the beamline optics were optimized to minimize asymmetries across the energy ranges of 3C and 3D. Since 4C and 4D are energetically distant, major asymmetries are visible on the lower energy side of the transitions, which resulted in a larger amplitude determination uncertainty. A re-optimization of the higher energy range was unfeasible due to limited time. By fitting Voigt profiles to the data, the observed 4C/4D line intensity ratio was determined as

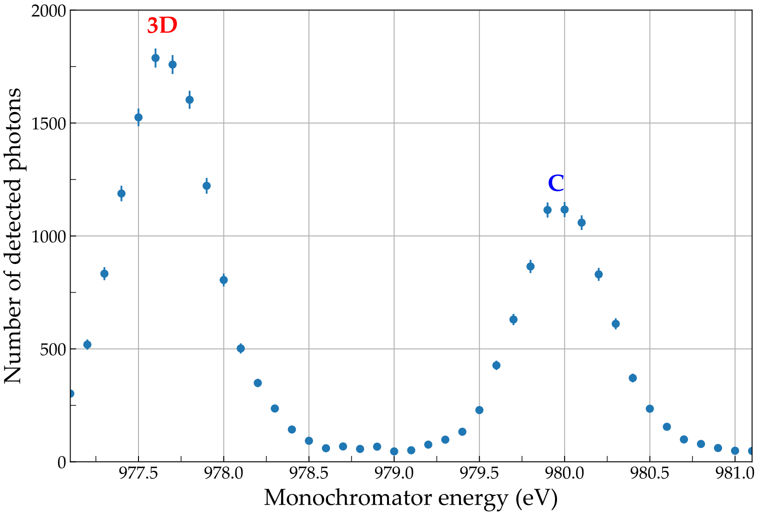

FIGURE 5.37: Fluorescence yield across the energy range of 3D (left) and C (right) of Ni XIX and Ni XVIII, respectively, using a wide exit slit width of 100 µm.

$$\frac{I_{4\mathrm{C}}}{I_{4\mathrm{D}}} = 1.019(35)_{\mathrm{stat}}.$$

Additionally, to compensate for the strong asymmetry of the lines, the intensity ratio was also determined by integrating the background subtracted signal. This approach resulted in similar values compared to the determination of the areas using Voigt profiles. Furthermore, a reliable estimation of the individual natural linewidths was also inaccessible due to the lack of statistics and strong asymmetric line shapes.

5.5.2 Measurements on Ni XIX

Similar to the measurements performed on iron, the 3C/3D oscillator-strength ratio of the element nickel ($Z = 28$) was determined. Nickel was injected into the trap by means of the organometallic compound nickelocene $C_{10}H_{10}Ni$. Despite its solid state form, the compound exhibit a high vapor pressure and evaporated without any external heating in the high-vacuum condition of the injection system. As demonstrated for iron in greater detail, the presence of nickel in the trap was verified using DR measurements as well as time-of-flight identification utilizing the ion extraction beamline of the EBIT.

Using a larger exit slit of 100 µm, resulting in a higher photon flux on sample, both transitions 3C and 3D of Ni XIX were scanned. The energy range of the 3D scan was extended to fully observe the adjacent transition C of Ni XVIII, see figure 5.37. The energy separation between 3D and C in nickel of $\Delta E = 2.36$ eV was sufficient to exclude any interfering effects among them.

Once the centroids of 3C and 3D were determined, both lines were alternately scanned 20 times using a smaller exit slit width of 25 µm. The sum of the performed scans is depicted in figure 5.38. Voigt profiles were fitted to the fluorescence signal

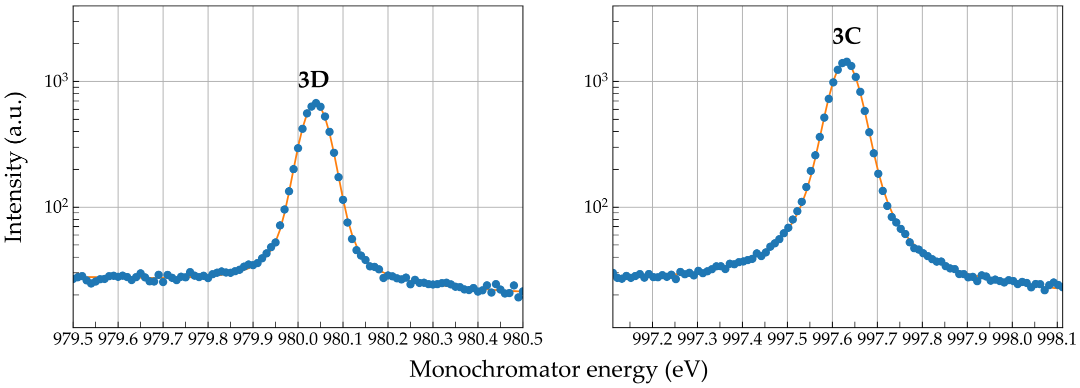

FIGURE 5.38: Summed projection of 20 performed scans of 3C and 3D of Ni XIX. Orange lines represent the best fit results utilizing Voigt profiles with a linear function for modeling the background.

whereas the background was modeled by a linear function. The obtained amplitudes for 3C and 3D were corrected for their flux variation observed by the diode downstream of the experiment and the individual transmission of the filter mounted in front of the detector. By calculating the weighted average of all amplitude quotients, the 3C/3D oscillator-strength ratio of nickel was inferred as

$$\frac{f_{3C}}{f_{3D}} = 2.48(2)_{\text{stat}}.$$

The observed Lorentzian linewidths of 3C and 3D were determined to be

$$\Gamma'_{3C} = 30.15(37)\,\text{meV},$$

$$\Gamma'_{3D} = 17.96(55)\,\text{meV}.$$

5.5.3 Summary

The third and last beamtime presented in this work addressed the oscillator-strength ratios of several transitions of Fe XVII, Fe XVI, and Ni XIX. In preparation of the measurement campaign, the experimental setup was thoroughly modified. As a result, the count rate, the SNR, and the spectral resolution were significantly improved. Beside the 3C/3D oscillator-strength ratio of Fe XVII, the ratio of the equivalent lines in Ni were measured. The statistical uncertainty of the oscillator-strength ratio determination in the order of 0.5% achieved in this measurement campaign was again significantly compared to previous beamtimes.

Additional to the oscillator-strength ratios, the high resolving power allowed to extract the Lorentzian linewidths of the Voigt profile of the fluorescence signal. The statistical uncertainty of the averaged values vary between 1 and 2%, a significant improvement compared to the measurement campaign in 2019.

Chapter 6

Discussion

6.1 Measurements on Fe XVII

6.1.1 Oscillator-strength ratio of 3C and 3D

For more than four decades, experimentalists, astronomers, as well as theoretical physicists have been scrutinizing the emission behaviors of the resonance line 3C and the intercombination line 3D of Fe XVII. It was proposed to use the observed intensity ratio of these two lines as an astrophysical plasma diagnostic instrument [25]. Using comprehensive laboratory measurements and theoretical modeling as references, the observed intensity ratio emitted by the source under investigation can be used to determine, for example, its density [8]. However, a discrepancy of the intensity ratios between existing models and experimental or observed values is persistent ever since [23].

In first experiments, the intensity ratio was measured by analyzing the emission of electron-impact excited plasmas in tokamaks and EBITs. Usually, electron impacts non-resonantly drive a variety of transitions, if the kinetic energy of the impinging electron is sufficient. The effective cross section of such a process can be approached using the Bethe approximation and is proportional to the kinetic energy of the free electron as well as the oscillator-strength and energy of a given transition, see equation 2.22. Therefore, the observed intensities were potentially affected by different electron-impact excitation cross sections. Additionally, cascades from energetically higher states than the upper levels of 3C or 3D excited by the electrons may have interfered with the measurements. Furthermore, the resolution of these measurements was insufficient to resolve the energetically close transition C of Fe XVI from 3D. Hence, if Fe XVI was present in the investigated plasma, the observed intensity of 3D was potentially affected by an unknown contamination from C, resulting in a falsified 3C/3D intensity ratio.

In an attempt to solve this long-standing enigma, the 3C/3D oscillator-strength ratio was re-measured utilizing the laser spectroscopy technique, in the early 2010s. A portable cryogenic EBIT was transported to the free-electron laser (FEL) LCLS in Stanford and similar to this work, the confined ions were overlapped with the photon beam and resonantly excited [15, 14]. In contrast to electron-impact excitations, laser spectroscopy directly samples the oscillator strength of a single transition and thus categorically excludes any dependence on effective cross sections or cascades. Unfortunately, the resolution of the LCLS measurements was also insufficient to resolve C from 3D. Hence, a contamination of C was mixed with the intensity measurements of 3D. However, by careful subtractions using reference measurements, the intensity of 3D could be separated from C and the 3C/3D oscillator-strength ratio determined. The result of these measurements again confirmed the discrepancy between theory and experiment, excluding the previously mentioned effects due to electron-impact excitations in earlier measurements.

In order to explain the deepened discrepancy between the LCLS results and theory, two unregistered systematical effects that could have affected the LCLS measurements were postulated by various groups. On one hand, it was argued that the photon peak intensity of the FEL was sufficient to cause non-linear effects in the plasma [126, 106]. This would have led to a saturation of the stronger transition 3C and thus, resulting in a reduced observed oscillator-strength ratio. On the other hand, it was suggested that due to insufficient resolution, the observed intensity of 3D may have been falsified by line C in a so-called population transfer mechanism [167]. New laser spectroscopy measurements were urgently needed to investigate these two effects. In contrast to the LCLS measurements, it was necessary to improve the resolution of the measurement as well as to significantly attenuate the photon peak intensity. Both of these requirements could be fulfilled at the beamline P04 of the PETRA III storage ring, where in total three such measurement campaigns were carried out within the scope of this thesis. In the beginning of this chapter, systematical effects that may have affected the measurements will be investigated. After, the results of the various campaigns as presented in chapter 5 including the final error budgets will be revisited. Finally, those results are put in context of other available experimental and theoretical works.

Systematical uncertainty analysis

Determination of the line intensity using Gaussian and Voigt profiles

The oscillator-strength ratios obtained within this work were inferred from the areas under Gaussian and Voigt profiles fitted to the acquired data. Modeling the data was necessary to separate the background of the measurement from the actual fluorescence signal. In addition, this way the intensity contamination from the adjacent line C was subtracted from the signal of line 3D. Due to background fluctuations and lack of resolving power, the data acquired in 2018 were fitted with Gaussians, whereas the resolving powers of subsequent measurement campaigns in 2019 and 2020 were sufficient to enable fits of Voigt profiles. In contrast to Gaussians, Voigt profiles account for the different natural line shapes of the individual transitions under investigation.

Using synthetic Gaussian and Voigt profiles, it was investigated whether Gaussians are sufficient to correctly determine the intensities of the individual lines for

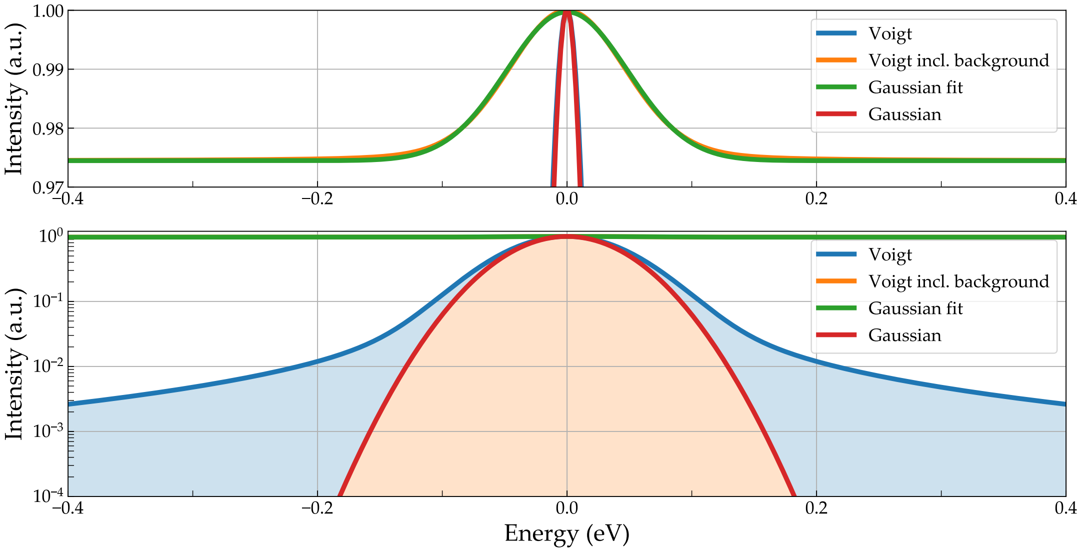

FIGURE 6.1: Linear (top panel) and logarithmic (bottom panel) representation of a synthetic spectrum consisting of a Gaussian (red) and a Voigt profile (blue). Both lines exhibit a Gaussian FWHM of 100 meV, while the Voigt profile features a Lorentzian width of 20 meV. A constant, high background was added to another Voigt profile (orange) to simulate the experimental conditions of the first beamtime. A Gaussian fit (green) was successfully fitted to the synthetic Voigt profile exhibiting a background. Blue and red shaded areas in the lower panel represent the area difference between a Gaussian and Voigt profile exhibiting similar widths.

similar experimental conditions as achieved during the 2018 beamtime. Figure 6.1 depicts a Gaussian profile (red) exhibiting a FWHM of 100 meV as well as a Voigt profile (blue) with a Gaussian FWHM of 100 meV and a Lorentzian FWHM of 20 meV. Additionally, a background was added to another Voigt profile with the same widths (orange), resulting in a SNR of 0.05, similar to the condition found during the measurement campaign 2018. Subsequently, a Gaussian model (green) was fitted to the synthetic Voigt profile including the background. In direct comparison of the courses of the synthetic Voigt (orange) and the best Gaussian fit results depicted in the upper panel of 6.1, the Gaussian profile is able to describe the Voigt profile under the given conditions. However, if comparing the areas, the Gaussian fit resulted in an area which is by several percent smaller than the initial input area of the Voigt profile. The area difference between a Gaussian and Lorentzian profile exhibiting the same Gaussian widths is illustrated by red and blue shaded areas in the lower panel of figure 6.1. In order to systematically investigate this effect, several synthetic 3C and 3D Voigt profiles exhibiting a Gaussian FWHM ranging from 10 to 1000 meV were generated. The input parameter of the amplitude ratio corresponded to 3.55. A noise-free background was applied to the spectra such that the SNR of line 3C was approximately 5%. Subsequently, Gaussian profiles were fitted to the synthetic spectra. In figure 6.2, the determined oscillator-strength ratios are depicted as a function of Gaussian width. It shows that for very broad Gaussian profiles, i.e., very poor resolving powers, the obtained values match well with the initial parameters. However, the narrower the widths, the worse the synthetic spectra are properly modeled

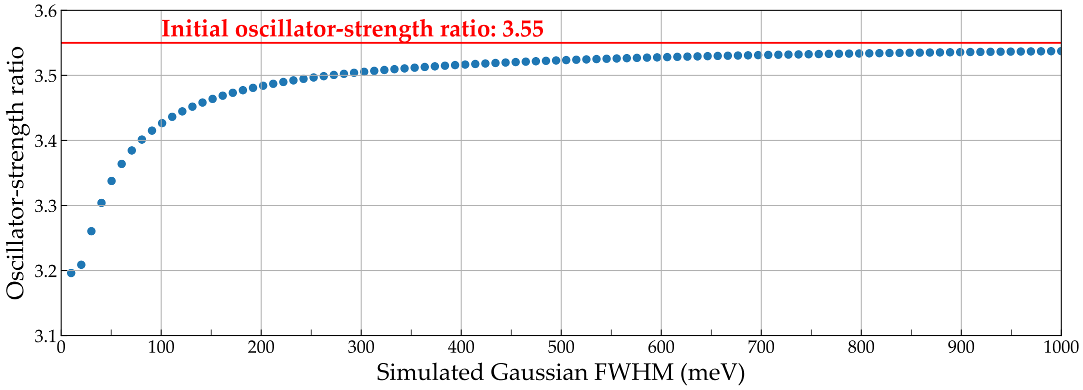

FIGURE 6.2: Several 3C and 3D Voigt profiles exhibiting an amplitude ratio (or oscillator-strength ratio) of 3.55 were produced for various Gaussian widths ranging from 10 to 1000 meV FWHM. Subsequently, Gaussian models were fitted to the synthetic spectra consisting of Voigts and the obtained amplitude ratio compared with the initial value. For Voigt profiles exhibiting a broad Gaussian width, the simulated difference between the initial and resulting oscillator-strength ratio is negligible. The smaller the Gaussian widths, the larger is the systematic shift towards an underestimated oscillator-strength ratio.

by Gaussians, resulting in a strong reduction of the observed oscillator-strength ratios. Therefore, it is inevitable to fit high-resolution measurements with more correct Voigt models. The simulation performed for the quantification of the systematic underestimation of the determined areas was based on profiles with no statistical variation or noise. Hence, in the case of more realistic data such as obtained during the first beamtime 2018, this effect is generously assumed to be enhanced. However, fitting Voigt profiles to the data of the first beamtime in 2018 was not feasible due to the weak fluorescence signal, high background, and especially due to the strong background fluctuations. For this reason, a systematic shift of the observed oscillator-strength ratios towards lower values during the measurement campaign 2018 cannot be excluded. For the achieved resolution of 100 meV FWHM, the simulation showed a reduction of the ratio of almost 4% from 3.55 to 3.42.

Population transfer mechanism

Apart from determining the area and thus the intensities of the transitions, modeling the data with Gaussian and Voigt profiles also allowed to estimate the impact of possible population transfer mechanisms as proposed by Wu et al. [167]. In figure 6.3, this process is illustrated by a simplified level schematic. Electrons are excited from the ground state of Fe XVI to the upper state of transition C by the photon beam. From this upper level, two channels dominate the decay of the state. Approximately 40% of the electrons return to the initial ground state of Fe XVI by emission of a photon. Alternatively, the state decays via an Auger decay by emission of an electron, ending up in the ground state of Fe XVII. The energy difference of 3D and C is predicted to be in the range of several hundreds of meV. Measurements revealed an energy difference of about 160 meV. If the experimental resolution is insufficient, both lines 3D and C are simultaneously excited by the photon beam. It was therefore

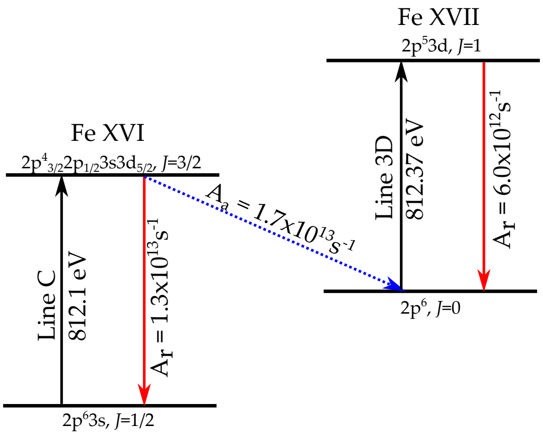

FIGURE 6.3: An energetically broad photon beam is able to drive both transitions, C of Fe XVI and 3D of Fe XVII, which are only separated by hundreds of meV, simultaneously. Since the upper state of C exhibits a strong decay channel to the ground state of Fe XVII (blue, dashed arrow), the number of Fe XVII ions could have been increased and the observed 3D intensity might be falsified. Figure adopted from: [167].

postulated that due to the strong Auger decay of line C, the charge-state equilibrium in the trap would change during the measurement. Compared to 3C, which is completely free of adjacent transitions, the number of Fe XVII ions would increase on the resonance complex consisting of 3D and C. Thus, the apparent intensity of 3D might be enhanced compared to 3C and the resulting oscillator-strength ratio would decrease accordingly.

The impact of such a population transfer from Fe XVI to Fe XVII was investigated based on an estimation of the number of stored ions and the observed fluorescence strength on resonance C during the beamtime 2020. Due to a finite detection area, the detector only registers a fraction of the fluorescence signal which is additionally attenuated by the aluminum filter in between. In order to calculate the number of isotropically emitted fluorescence photons of C, a solid angle of the detector of 3% of 4π and a filter transmission of 75% are assumed. On average, within one probing cycle, 12.6 photons on resonance centroid of C were registered. Combined with the solid angle and filter transmission correction, this results in a total number of 560 photons per cycle. The branching ratios, i.e., the fraction of excited states decaying via a particular transition is calculated by theories. From the upper state of C, approximately 40% decay back to the initial ground state of Fe XVI and 60% decay to the ground state of Fe XVII by emission of an electron [167]. Since the total number of emitted photons n_{Photons} was estimated and the branching ratios predicted, the number of transferred ions n_{Ions} from Fe XVI to Fe XVII can be calculated

$$n_{\text{Ions}} = \frac{\frac{A_{\text{a}}}{A_{\text{total}}}}{\frac{A_{\text{r}}}{A_{\text{total}}}} n_{\text{Photons}} = \frac{0.6}{0.4} \cdot 560 = 840, \tag{6.1}$$

where A_{r}, A_{a}, and A_{total} represent the Einstein coefficients for a decay back to the ground state of Fe XVI, to the ground state of Fe XVII, and the sum of all possible decays, respectively. Hence, the number of Fe XVI ions transferred to Fe XVII per

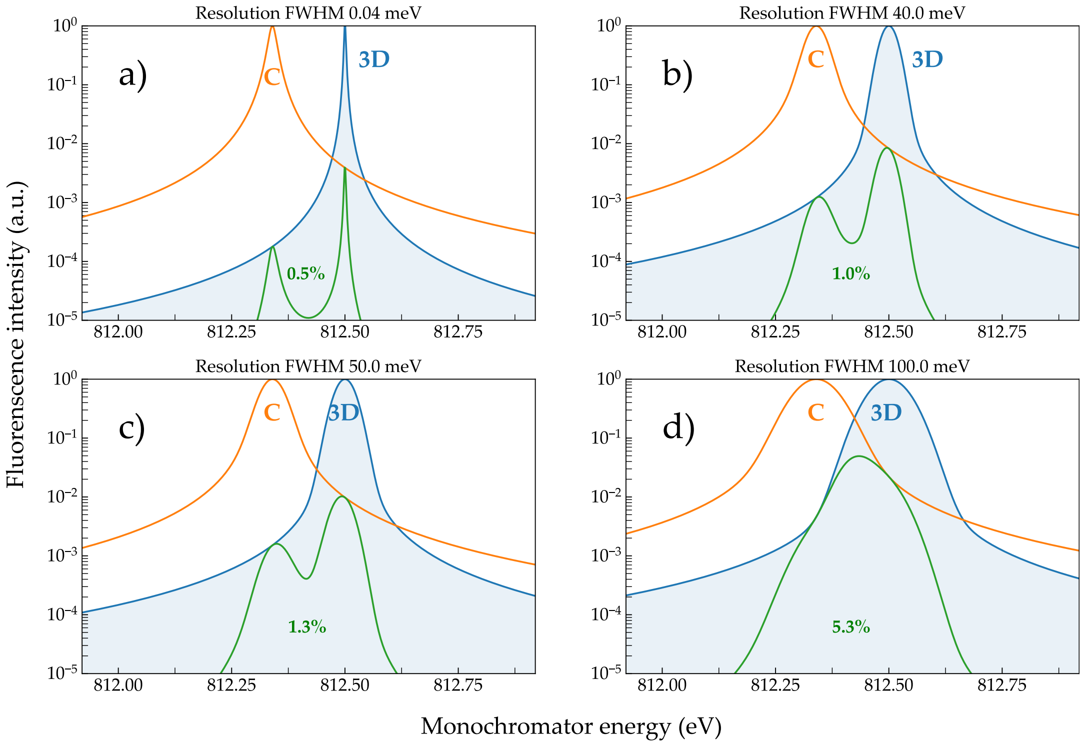

FIGURE 6.4: Simulation of the overlap between lines C and 3D. The two normalized Voigt profiles separated by 160 meV exhibit similar intensities and individual Lorentzian widths of 20 and 4 meV for C and 3D, respectively. Green shaded areas represent the overlap for in total four different resolutions ranging from a) ideal experimental conditions to the resolutions achieved during the beamtimes b) 2020, c) 2019, and d) 2018.

cycle is estimated as 840.

In order to evaluate this value, an estimation of the total number of Fe XVII ions based on the total negative charge in the trap induced by the electron beam is required. The charge in the trap is defined as

$$Q = It, \tag{6.2}$$

where I and t represent the electron beam current and the duration of a single electron in the trap center, respectively. The latter can be calculated based on the spatial length of the trap electrode $s = 16\,\mathrm{mm}$ and the kinetic energy of electrons in the trap center of $\frac{1}{2}m_e v^2 = qU = 265\,\mathrm{eV}$

$$t = \frac{m_e}{2qU}s. \tag{6.3}$$

For the employed electron beam current of $I = 3\,\mathrm{mA}$, a total negative charge of $Q = -30 \times 10^6\,e$ is generated by the electron beam inside the trap. In the trap center, ions are radially confined by the negative space charge of the electron beam. Hence, the total negative charge forms an upper limitation for the maximum number of ions that can be stored. Previous dielectronic recombination measurements revealed that approximately 50% of the negative charge was compensated by the positively charged ion cloud [95]. Hence, a total positive charge in the trap of $Q = 15 \times 10^6\,e$

is estimated. Assuming an even distribution of all ions among the four highest possible charge states of iron (Fe XVII, XVI, XV, and XIV), the number of ions in each charge state is about 260000. On centroid of C, approximately 840 of the 260000 or 0.3% of the Fe XVI ions are resonantly ionized to Fe XVII per cycle. It is important to note that after each probing cycle, the trap content was emptied and refilled by the production of new ions. Hence, a gradual transfer from Fe XVI to Fe XVII over several cycles was impossible.

To estimate the effect on the observed line intensity of 3D, the overlap factor of both lines, which crucially depends on the resolving power of the experiment, is required. The overlap factor of C and 3D is defined as the area under the product of two normalized Voigt profiles exhibiting a energy difference and Lorentzian linewidths as observed in the measurements divided by the area under line 3D. This overlap factor was simulated for various resolving powers and is shown in figure 6.4. For the resolution achieved during beamtime 2020, an overlap of approximately 1% is estimated. Hence, the increase of the observed 3D signal induced by population transfers from Fe XVI is determined in the order of 0.003%. Even if the number of Fe XVII ions were overestimated by one to two orders of magnitude, the 3D intensity increase due to population transfers of up to 0.3% would still be negligible.

A second completely independent approach to investigate possible population transfer mechanisms is based on the measured time evolution of the 3C/3D oscillator-strength ratio after switching down the electron beam energy to the probing phase. In figure 5.34 presented in the previous chapter, a Fe XVI/Fe XVII abundance ratio increase of about a factor of two during the probing phase is visible. Assuming that line C had a significant effect on the intensity of 3D by means of population transfers, the effect should be visible in the time evolution of the 3C/3D oscillator-strength ratio. As the relative abundance of Fe XVI increases compared to Fe XVII ions, the 3C/3D oscillator-strength ratio is expected to decrease simultaneously if the population was transferred. However, a linear model fitted to the evolution of the 3C/3D oscillator-strength ratio reveals a slope of zero, showing that the 3C/3D oscillator-strength ratio was completely independent of the Fe XVI/Fe XVII abundance ratio. Hence, population transfer mechanisms during the measurements presented in this work can be excluded.

Non-linear effects

In order to explain the unexpectedly low value of the 3C/3D oscillator-strength ratio measured at LCLS, non-linear effects due to the high photon flux peak intensity of the FEL were proposed [125, 106]. The radiative lifetimes of 3C and 3D are predicted to be 163 and 45 fs, respectively, and are thus in the same order of magnitude as typical X-ray pulse envelope lengths of LCLS between 200 and 2000 fs [106]. It was hence proposed that the high flux of the laser was sufficient to populate the upper level of 3C and 3D at different rates within the short laser pulse. This effect is shown for different radiation field densities in the left panel of figure 6.5. The non-linear

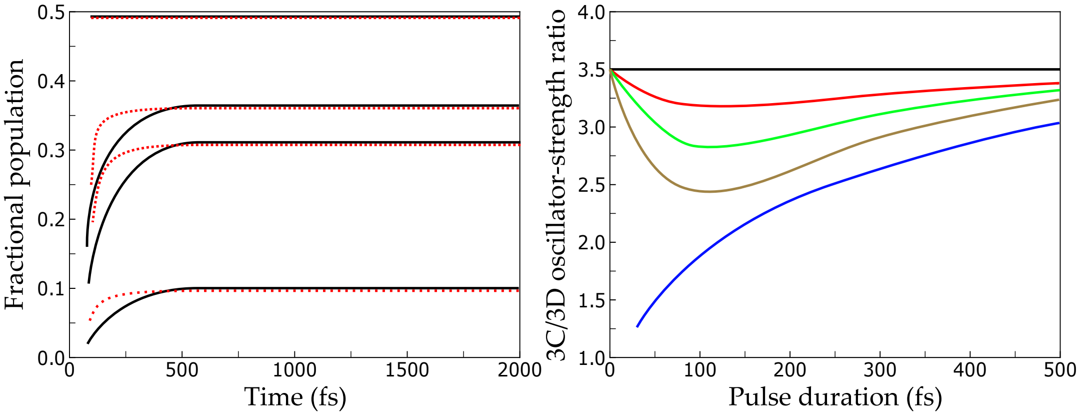

FIGURE 6.5: Left panel: Schematic representation of fractional population as a function of laser exposure time. The population evolutions of the transitions 3C and 3D are depicted as dashed red and solid black lines, respectively. The four datasets correspond for different radiation field densities ranging from $\rho = 1 \times 10^{-7}$, 1×10^{-6}, 1×10^{-5}, and $1 \times 10^{-4}\,\mathrm{J\,m^{-3}\,Hz^{-1}}$ from bottom to top, respectively. Right panel: The 3C/3D line intensity ratio as a function of the pulse duration for given radiation field densities: $\rho = 1 \times 10^{-8}$, 1×10^{-7}, 1×10^{-6}, and $1 \times 10^{-5}\,\mathrm{J\,m^{-3}\,Hz^{-1}}$ from top to bottom. Figures adopted from [106].

population increase of the upper level could have potentially lowered the observed ratio, see right panel of figure 6.5.

According to Oreshkina et al. [125], a peak flux density of at least $1 \times 10^{12}\,\mathrm{W\,cm^{-2}}$ or more is required to observe such non-linear effects during the measurement. The photon peak intensity at the synchrotron beamline P04 is estimated based on the number of photons registered by the calibrated diode downstream of the experimental setup

$$\Psi_{\mathrm{Beam}} = 4 \times 10^{11}\,\mathrm{photons/s}. \tag{6.4}$$

Given the employed monochromator energy of

$$E = 825\,\mathrm{eV} = 1.32 \times 10^{-16}\,\mathrm{J}, \tag{6.5}$$

an average power of

$$P_{\mathrm{average}} = 5.28 \times 10^{-5}\,\mathrm{W} \tag{6.6}$$

is obtained. During the third beamtime, from which the photon flux was obtained, PETRA III operated in timing-mode, resulting in a photon bunch repetition rate of 5.21×10^{6} pulses/s. Combined with a minimal possible focal spot size of $1 \times 10^{-10}\,\mathrm{cm}^2$ and a typical photon bunch length of 44 ps, a peak flux density of

$$\rho \approx 2.3 \times 10^{9}\,\mathrm{W\,cm^{-2}} \tag{6.7}$$

is obtained, which is orders of magnitude below the required value predicted by theories. It is interesting to note, that the duration between two photon pulses of 192 ns was sufficiently long for the excited states of 3C and 3D, exhibiting lifetimes of tens

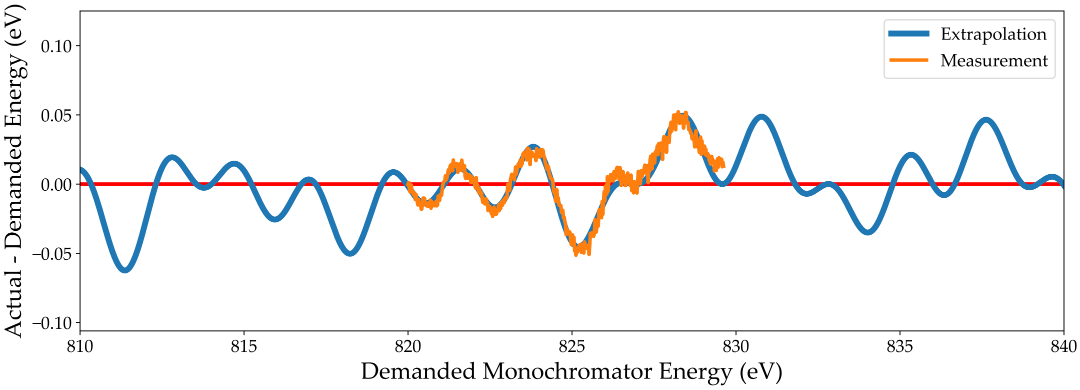

FIGURE 6.6: Orange: measured difference between the actual and the demanded monochromator energy utilizing the ASPHERE photoelectron spectrometer. Blue: The acquired dataset is modeled and extrapolated using a combination of four sinusoidal waveforms. Raw data adopted from [29].

to hundreds of fs, to relax back to the ground states before the next photon pulse arrived. Due to the determined photon peak flux and the long photon pulse separation, non-linear effects of any kind, even for the most conservative assumptions of a minimal focus spot size and minimal bunch lengths, can be explicitly excluded for the measurements presented within this work.

Encoder interpolation errors

For each requested monochromator energy, the required angles of the mirror and grating inside the monochromator are calculated and changed accordingly. These angles are registered by two angular encoders and actively stabilized by a closed-loop controller. For small photon energy steps as usually employed during the measurements, tiny angle changes are required. For example, a 10 meV energy step is achieved by rotating the grating and mirror by an angle of approximately 0.000 04°. Since these angle changes are significantly smaller than the absolute reference marks of the angular encoders every 0.01°, the positions are interpolated by using so-called correction tables, see chapter 4.2.3 for more information about the interpolation correction. In the course of a similar measurement campaign as presented here, the assumption arose that the available correction tables might be incorrect. This could result in a vastly reduced grating position determination accuracy, well below the one specified. In order to confirm this conjecture, the relative photon energy changes were measured as a function of the demanded monochromator energies using a photoelectron spectrometer independently of the measurement campaigns of this work [29]. The utilized apparatus labeled as ASPHERE is capable of measuring relative energy changes of the incident photon beam with an accuracy of about 1 meV. In this proof-of-principle test, the demanded photon energy was scanned over the range from 820 to 830 eV. For each requested equidistant monochromator energy step, the actual photon energy change was registered by the photoelectron spectrometer. The result of this measurement is shown in figure 6.6. A periodic deviation of the actual

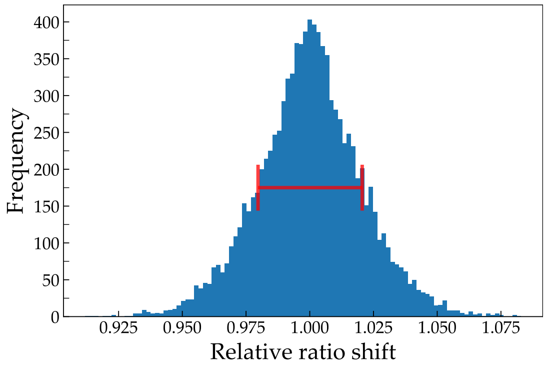

FIGURE 6.7: Histogram of simulated relative shifts of the 3C/3D intensity ratio. Two synthetic Voigt lines were disturbed by simulated interpolation errors of the monochromator. The amplitudes of the disturbed lines were analyzed and compared with the initial parameters. The 1-σ standard deviation is represented by red bars.

photon energy from the requested photon energy can be clearly observed. This deviation can be well described by a combination of four sinusoidal waveforms. Since improperly maintained compensation tables could lead to an oscillation behavior as observed, the origin of the energy deviations is most likely found in inaccurate compensation tables of the angular encoders.

Unfortunately, correction measurements as presented in figure 6.6 were unfeasible in parallel to the 3C/3D oscillator-strength measurements. Therefore, the influence of the periodic deviations on the oscillator-strength ratio was investigated by simulations. For this purpose, a synthetic periodic deviation of the photon energy consisting of the product of four sinusoidal waveforms was simulated, which in shape, amplitude and periodicity approximately corresponded to the observed oscillations. Two synthetic Voigt profiles corresponding to the energies, amplitudes and linewidths of 3C and 3D, respectively, were generated. Subsequently, each energy for which the intensities of the Voigt profiles were calculated were shifted by the simulated energy deviation. The shifted profiles were then analyzed using the same algorithms used for the analysis of the actual data. The best fit results were compared with the initial input parameters of the synthetic lines. In order to obtain an estimate of the distribution of the parameter changes, this simulation was performed 10000 times.

The relative change of the amplitude ratio due to simulated interpolation errors is depicted in figure 6.7. The simulation shows a distribution of the relative ratio shifts that is similar to a normal distribution centered at 1.0. Hence, on average the ratio shift induced by incorrect energy interpolations is expected to be negligible. However, the periodic oscillations are assumed to be constant throughout the measurements for similar operating parameters, unless the correction tables are changed. Hence, measurements of the same energy range will always result in the same oscillating deviation between the actual and the demanded photon energy. In order to assess this effect, the 1-σ standard deviation of the simulation result of approximately 2% is added to the error budget of the final 3C/3D oscillator-strength

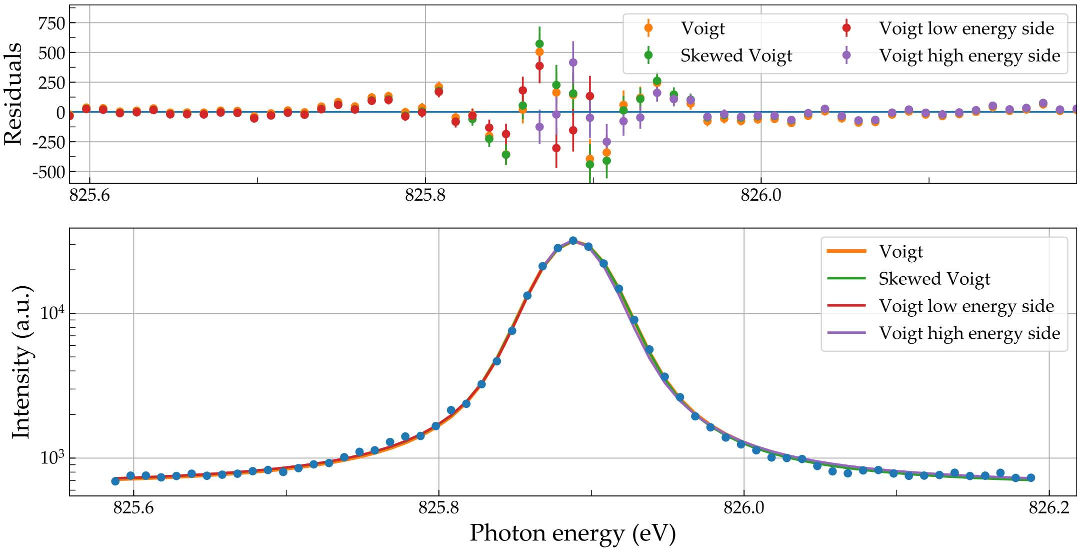

FIGURE 6.8: The sum of all measurements of 3C acquired during the measurement campaign 2020 (blue dots). In total four models were fitted to data to investigate systematical effects of line asymmetries. Comparing the amplitudes of the skewed Voigt (green) with conventional Voigt (orange) resulted in a negligible difference. Fitting conventional Voigts to the either the lower or higher energy half of the profile resulted in variations of the observed amplitude from -0.8% up to 2%.

value.

Detection efficiency uncertainties

As explained in detail in chapter 3, the detection system employed a 500 nm thick aluminum filter to prevent visible light from saturating the silicon drift detector. Since 3C and 3D exhibit distinct energies, the filter transmission is different for each transition. The observed intensities were corrected for the respective transmissions based on literature values [74]. However, the thickness tolerance of the aluminum filter was specified within +/- 10%. This results in an uncertainty of the transmission correction based on the literature values for 450 and 550 nm thick filters of approximately 0.13% and is therefore neglected in the final error budget.

Asymmetric line shape

During the measurement campaign 2020, small asymmetries in the instrumental profile were observed. In order to investigate the influence of the observed asymmetries on the oscillator-strength ratio two approaches were introduced. For both, all available 3C scans were summed up and the resulting profile was fitted once with a conventional Voigt and once with a so-called skewed Voigt profile. In contrast to the conventional Voigt fits, skewed Voigt fits allow for a non-zero skewness and therefore should consider possible asymmetries and their effects on the resulting amplitude ratio, accordingly. In figure 6.8, best fit results including the residuals of both models are plotted along with the measured data. In the residuals, it is visible that the best fit results of both models slightly differ in shape. However, a comparison of the corresponding amplitudes shows a difference of only 0.0035%. This indicates that either the asymmetry plays a negligible role or that the skewed Voigt model does also not correctly reproduce the experimental data. In order to investigate the latter assumption, the observed line profile of 3C was split into two regions separated by the line centroid. Subsequently, each half of the profile was individually fitted with Voigt models, see also figure 6.8. The resulting amplitudes varied from -2% to +0.8% compared to the values obtained using a conventional Voigt profile to the entire dataset. However, if applying the same method to the line profile of 3D, the variation of the observed amplitude were identical. Hence, by taking the ratio of the 3C/3D amplitudes, the uncertainty arising from a possible asymmetric line shape cancels out completely. It is therefore assumed that line asymmetries have only minor impact on the obtained oscillator-strength ratio and hence, will be neglected in the final error budget.

Polarization effects

As introduced in chapter 2.3.4, the angular photon emission distribution of a photo-excited state depends on the polarization of the incident photon beam. However, the emission distribution is isotropic in the plane perpendicular to the photon propagation direction if the photon beam is circularly polarized. Since the detectors were mounted in that plane and the synchrotron light at P04 was fully circularly polarized, no fluorescence intensity corrections for 3C and 3D were required. Even if the polarization consisted of partial linear component, the emission distribution of both lines 3C and 3D are identical since both exhibit the same total angular momenta, see also chapter 2.5.

Determination of the transition energies

In addition to oscillator strengths, the observed energy of a transition is also a vital parameter for benchmarking theory. Furthermore, precise knowledge of transition energies helps to identify lines in raw astrophysical spectra. Especially the accuracy with which the velocity of objects relative to the Earth can be determined using the Doppler shift is increased. To date, the most accurate measurements of the transition energies of 3C and 3D with a relative accuracy of $\Delta E/E = 10^{-5}$ were obtained by Brown et al. in 1998 [27]. Laser spectroscopy measurements at LCLS were able to confirm the results of Brown et al. but could not further lower the uncertainty due to monochromator energy variations, insufficient spectral resolution, and a lack of statistics.

Individual measurements within this work showed a relative statistical uncertainty of $\Delta E/E = 10^{-7}$ in the determination of the transition energies, which is two orders of magnitude better than previous measurements. Nevertheless, an accurate determination of the absolute transition energies was unfeasible. The current photon energy of the beamline at any point in time is calculated based on the measured grating angle and the given geometry. These calculations usually result in absolute energy accuracies in the order of $\Delta E/E = 10^{-3}$.

To calibrate the monochromator, external references are required. In the soft X-ray regime, absorption lines of neutral gases, such as O_2, N_2, CO_2 or SF_6 are commonly used. However, the accuracies of those references are even in the best case limited to $\Delta E/E = 10^{-5}$. Another approach is based on calibrating the beamline by using well-known transitions of HCIs trapped in the EBIT. In contrast to absorption lines of neutral molecules, transitions of HCIs are by orders of magnitude narrower and can be calculated by state-of-the-art atomic structure codes with an uncertainty below $\Delta E/E = 10^{-6}$. This technique was successfully demonstrated in a similar measurement, in which the monochromator of a soft X-ray beamline of the BESSY II synchrotron in Berlin was calibrated with relative accuracies of $\Delta E/E = 10^{-6}$ [101].

However, even if the monochromator of this measurement would have been accurately calibrated as discussed, measurements utilizing a photoelectron spectrometer revealed an oscillating deviation of the actual from the requested photon beam energy in the order of up to 50 meV peak-to-peak, see figure 6.6. Without measuring the relative photon energy changes in parallel, the achievable accuracy is therefore limited to $\Delta E/E = 10^{-4}$. Hence, no further attention was paid to the redefinition of the transition energies in the scope of this work. However, future measurements with appropriate effort will in principle be able to improve the accuracy of the literature values by 1 to 2 orders of magnitude.

Final 3C/3D oscillator-strength value

Based on the results of the in total three beamtimes and the estimation of all relevant systematical error contributions, the final value of the 3C/3D oscillator-strength ratio of Fe XVII will be determined in this section. First, the individual features of each measurement campaign will be revisited.

The first beamtime conducted in 2018 was based on a measurement procedure featuring a constant electron beam energy high enough to produce the required charge state Fe XVII. This resulted in a dominant background and a low SNR by direct electron-impact excitation. In addition, the fluorescence signal was also affected by a varying charge-state equilibrium induced by an unstable injection pressure and electron beam. In order to increase the statistical accuracy, two additional measurement methods were introduced in which the fluorescence signal with background and the background alone were alternatingly registered by regularly closing a photon shutter. Due to the weak fluorescence signal, the achieved resolving power was limited to 6500 which was nevertheless sufficient to separate line 3D from line C for the first time. However, the limited resolution and fluctuating background allowed only Gaussian profiles to be fitted to the acquired data. A simulation which reproduced the measurement conditions indicated a systematic underestimation of the oscillator-strength ratio by at least 4% if Gaussian models were fitted to initially Voigt shaped profiles. Given the fact that the simulation was based on perfect profiles without any statistical or systematical background variations, it can be generously assumed that this effect could have an impact even larger than 4%. Further strong systematics of the first measurement campaign are based on uncertainties of the ROI determination and the lack of a photon flux correction, as discussed in chapter 5.3.

In the subsequent beamtime 2019, the resolving power was significantly increased by introducing a novel measurement method separating the ion production and probing phases of the experiment. In contrast to 2018, systematical errors induced by inaccurate ROI determinations and photon flux variations played no longer a role due to the increased SNR and an additionally installed diode measuring the photon flux behind the experiment. Also, the achieved resolving power of $E/\Delta E = 14000$ was sufficient to fit Voigt profiles to the data for the first time. Unfortunately, it was still not possible to draw a clear conclusion regarding the observed oscillator-strength ratio due to significantly fluctuating values between 3.1 and 3.5. These fluctuations probably originated from instabilities of the injection pressure. However, it was apparent that the observed ratios tended to higher values than previously observed in any experiment.

Prior to the third beamtime conducted in 2020, the setup was fundamentally overhauled and the injection system was extended by an additional stage. By fine-tuning the measurement cycle and mounting additional detectors, both the SNR and the resolving power could again be significantly increased. The intensities were measured over a period of 14h and showed no non-statistical variation or systematical instabilities of any kind. Using Voigt profiles, the oscillator-strength ratio was determined as 3.51. The achieved relative statistical uncertainty of 0.5% outperformed all previous measurement campaigns.

Additionally, all three beamtimes were found to be affected by energy interpolation errors of the monochromator. These energy interpolation errors arose from incorrect position interpolation tables of the angular encoder of the monochromator and dominate the final error budget of especially the beamtimes 2019 and 2020 with an additional relative uncertainty of 2%.

In table 6.1 the conditions of the various measurements, their results and the individual systematic error budgets are listed. For a comparison of the data quality, the summed measurements of 3C and 3D of each campaign are depicted in figure 6.9. Additionally, the results of the measurement at LCLS as well as a typical observation of the star Capella recorded by the satellite Chandra are included. The improvement of the resolution by a factor of up to 40 between LCLS and the measurements presented here is noticeable.

Due to the low resolution and the consequent inaccuracies due to Gaussian fits, the results of the first beam time will be neglected for further consideration in this

TABLE 6.1: Comparison of 3C/3D oscillator-strength ratio results including error budgets of the beamtimes conducted within this work. Note that the final value of the measurement campaign 2019 represents the average value of the large range of observed ratios.

Campaign	**2018**	**2019**	**2020**
Number of scans	6 + 11	74	60
Resolving Power $E/\Delta E$ (FWHM)	8250	14000	20000
Signal-to-noise ratio	≈ 0.05	≈ 8.5	≈ 45
Model used	Gaussian	Voigt	Voigt
3C/3D oscillator-strength ratio	3.09	3.1-3.5	3.51
Statistical uncertainty	±2.58%	±1.00%	±0.57%
Systematical uncertainties			
ROI selection	±1.8%	X	X
Background instabilities	±1.0%	X	X
Photon flux variation	±2.0%	X	X
Area underestimation of Gaussian profiles fitted to Voigt lines	+4%	X	X
Detection efficiency uncertainty	±0.13%	±0.13%	±0.13%
Asymmetric line shape	X	X	±0.003%
Monochromator interpolation errors	±2.0%	±2.0%	±2.0%
Charge-state equilibrium changes	X	X	X
Final 3C/3D oscillator-strength ratio	$3.09^{+0.18}_{-0.13}$	3.3(2)	3.51(7)

thesis. Although for beamtime 2019 the statistical uncertainty of a single measurement was sufficiently improved compared to the previous measurements, these results are also left out due to the inconclusively fluctuating values between 3.1 to 3.5. The most recent beam time with the lowest statistical uncertainty, best resolution, and highest SNR was used to determine the final value of the 3C/3D oscillator strength ratio to be

$$\frac{f_{3\mathrm{C}}}{f_{3\mathrm{D}}} = 3.51(7).$$

It should be emphasized here that the final error is dominated by systematical interpolation errors of the monochromator. In addition, proposed effects of a population transfer mechanism as well as non-linear excitation are explicitly excluded.

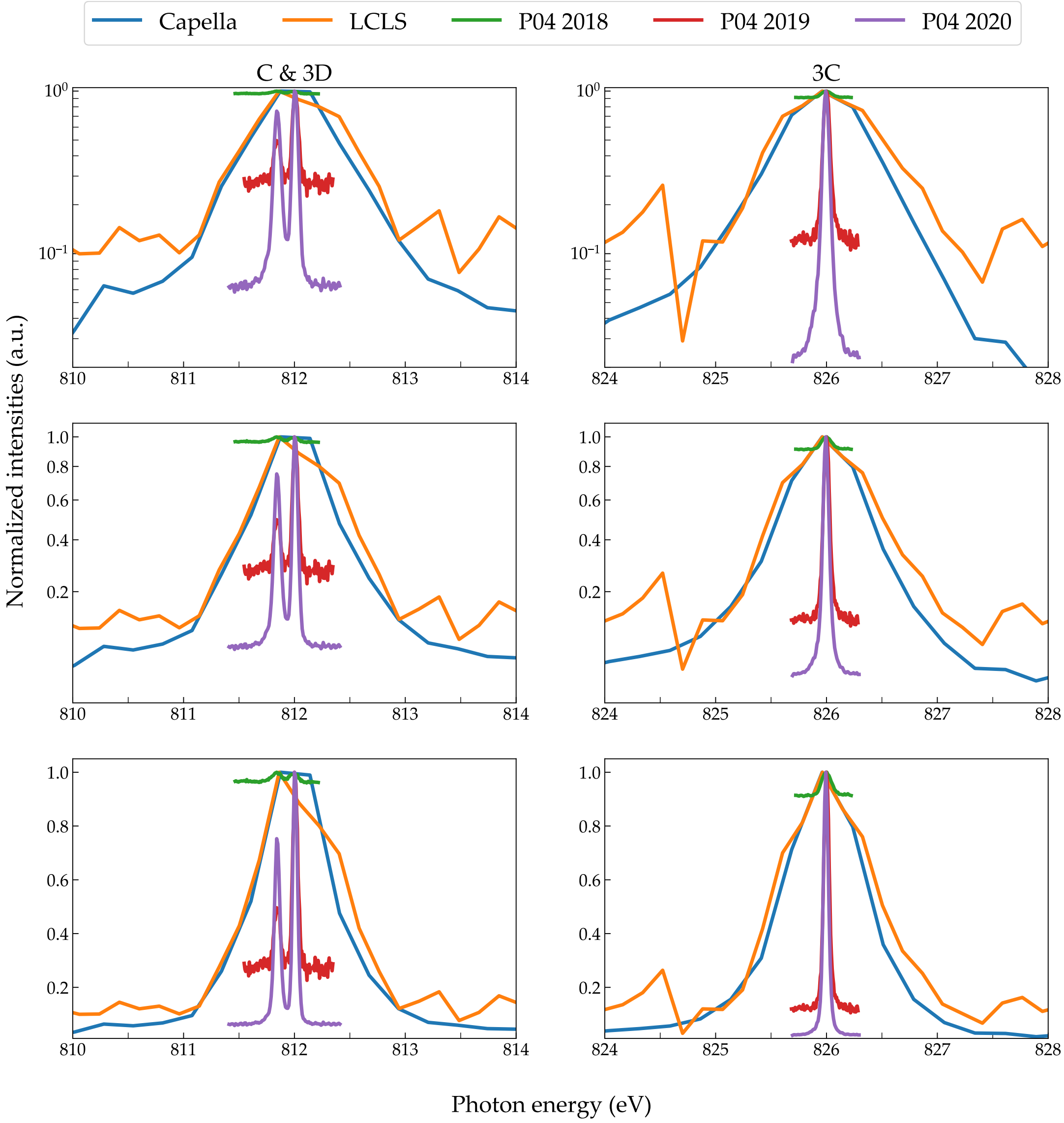

FIGURE 6.9: Logarithmic (top panel), square root (center panel), and linear (bottom panel) representation of the normalized 3C and 3D line profiles obtained by astrophysical observations (blue), the FEL measurement at LCLS (orange), and the three campaigns at P04 conducted within this work (green, red, purple). Note that the complex of C and 3D is unresolved in the measurements and observations of LCLS and Capella, respectively.

Comparison with other experiments and calculations

In this section, the obtained 3C/3D oscillator-strength ratio $f_{3C}/f_{3D} = 3.51(7)$ will be put in context of experimental values, astrophysical observations and calculations, see table 6.2 and figure 6.10. In comparison with other experiments, only one previous measurement directly measured the ratio of the quantum mechanical transition probabilities based on X-ray laser spectroscopy, which was performed at the LCLS. The oscillator-strength ratio value obtained in the LCLS measurement $f_{3C}/f_{3D} = 2.61(23)$ deviates almost four standard deviations from the value found within this work. The large discrepancy is a strong indication that the LCLS measurements were indeed affected by non-linear effects and charge-state population transfers as proposed by several research groups mentioned earlier, effects which are clearly excluded in this work.

Earlier measurements of the 3C/3D intensity ratio using EBITs and tokamaks were based on electron-impact excitation and observations of the emission strengths using suitable grating spectrometer [25, 26, 60, 10]. However, according to the Bethe approximation, see equation 2.22, the observed intensity is proportional to the product of the quantum mechanical Gaunt factor and oscillator strength gf as well as the electron-impact excitation cross section for a given transition. Hence, the observed intensity ratio induced by electron impact-excitation is only equal to the oscillator-strength ratio if the cross sections for 3C and 3D are assumed to be similar. Apart from different cross sections, the observed intensity ratio can also be affected by electron cascades from higher energy levels or a non-Maxwellian electron distribution in the EBIT or tokamak [107, 32]. Also, the polarization of the electron beam influences the emission characteristic of the ion cloud and needs to be corrected for.

In addition, in many EBIT measurements a contamination by line C of Fe XVI could not be explicitly excluded, since the resolving power of up to $E/\Delta E \approx 575$ was by far insufficient to separate C from 3D and the charge state distribution was often unknown. Lowest intensity ratios of 1.90(11), 2.04(42), and 1.96(14) were observed in measurements in which Fe XVI was present. Highest intensity ratios of 3.04(12), 2.98(30) and 2.78(11), and thus values closest to the results presented here, were obtained by measurements using the Livermore EBIT in combination with a so-called „Metal Vapour Vacuum Arc“ (MeVVA) as injection source. The MeVVA system with its pulsed injection enabled the generation of a pure Fe XVII plasma. The absence of the strong and isolated resonance line B of Fe XVI verified the plasma to contain only Fe XVII ions. The broad range of measured ratios between 1.90 and 3.04 is a strong indication that many of the experiments were indeed falsified by a contamination of C to the apparent intensity of 3D. However, even the highest observed values still significantly deviate from the findings obtained in this work.

The electron beam energy of the measurements employing the MeVVA system varied between 850 and 1300 eV. Chen et al. [33] performed simulations of the

TABLE 6.2: Comparison of the 3C/3D intensity ratio between this work, available experimental datasets, astrophysical observations and theoretical predictions. Note that Ness et al. [123] presented a review of in total 50 observations of the ratio. For the sake of clarity, the listed value consists of the calculated mean and the standard deviation. An asterisk (*) represents methods for which a probable contamination of the adjacent line C of Fe XVI was not or only partially taken into consideration. Note that the validity of theory based on a Breit-Pauli configuration interaction approach published by Mendoza et al. † has been disputed [163]. Table extended on the work of [14].

Source	**Method/Object**	**3C/3D Intensity Ratio**
This work (2020)	EBIT, Laser spectroscopy	3.51(7)
This work (2019)	EBIT, Laser spectroscopy	3.3(2)
This work (2018) [96]	EBIT, Laser spectroscopy	$3.09^{+0.18}_{-0.13}$
Brown (2001) [25]	EBIT, Electron Excitation*	1.90(11) - 3.04(12)
Beiersdorfer (2004) [9]	Tokamak*	2.04(42) - 3.33(56)
Brown (2006) [26]	EBIT, Electron Excitation*	2.98(30)
Gillaspy (2011) [60]	EBIT, Electron Excitation*	1.96(14) - 2.78(11)
Bernitt (2012) [15]	EBIT, Laser spectroscopy	2.61(23)
Blake (1965) [18]	Sun*	1.63
McKenzie (1980) [115]	Sun*	2.75
Mewe (2001) [117]	Capella*	2.42
Behar (2001) [8]	Capella*	3.02
Xu (2002) [168]	NGC4636*	2.31(18)
Ness (2003) [123]	Astrophysical Observations*	2.73(57)
Zhang (1989) [169]	Distorted Wave	4.15
Bhatia & Doschek (1992) [17]	R-Matrix	3.74
Cornille (1994) [40]	Distorted Wave	4.52
Kaastra (1996) [91]	R-Matrix	3.84
Safronova (2001) [140]	MBPT	3.43
Dong (2003) [51]	MCDF	4.26
Loch (2005) [107]	Configuration Interaction	3.91
Chen (2007) [32]	Dirac-R-Matrix, converged	3.43
Gu (2009) [66]	Distorted Wave	4.03
Gu (2009) [66]	MBPT + Distorted Wave	3.50
Harman (2012) [15, 14]	MCDF	3.49
Jönsson (2014) [89]	Configuration Interaction	3.56
Santana (2015) [141]	Configuration Interaction	3.68 - 3.96
Santana (2015) [141]	MBPT	3.44
Oreshkina (2016) [126]	Configuration Interaction	3.55
Mendoza (2017) [116]	BP-CI†	2.82
Wu (2019) [167]	MCDF	3.48
Wu (2019) [167]	MCDF incl. Breit-Interaction	3.56
Harman (2020) [96]	MCDHF	3.55(5)
Safronova (2020) [96]	Configuration Interaction	3.55(5)
Berengut (2020) [96]	AMBiT	3.59(5)
Gu (2021) [64]	Configuration Interaction	3.49
Safronova (2021) [36, 37]	MCDHF	3.55(2)

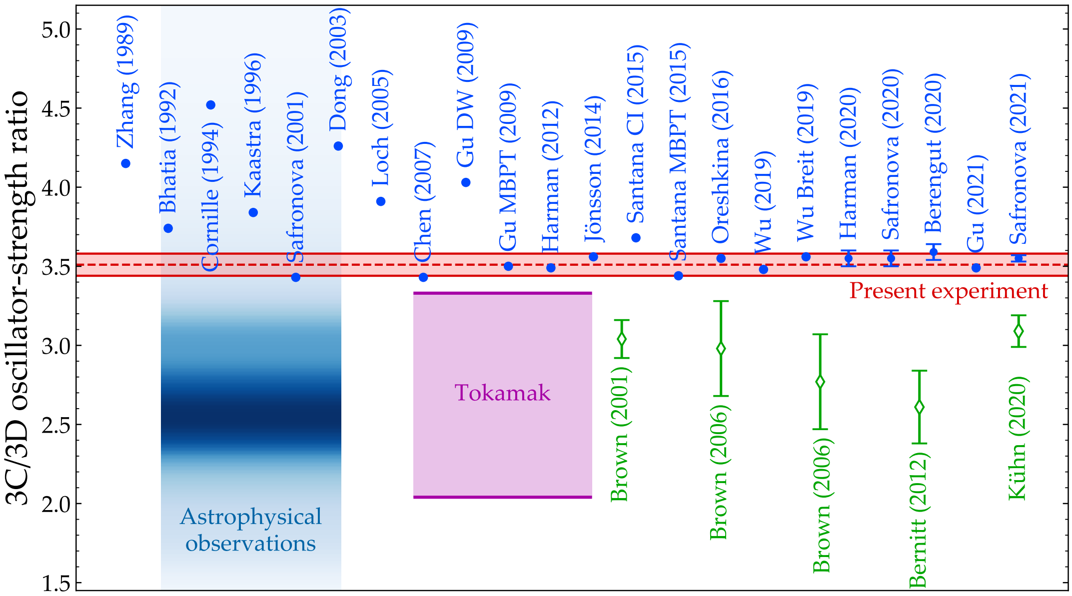

FIGURE 6.10: Present experimental 3C/3D ratios compared with previous predictions and experiments. Red band: result of the this work. Blue circles: Theoretical predictions. Blue band: observed line ratios in astrophysical sources, with color shades coding the distribution of values weighted by their reported accuracies. Purple band: spread of tokamak results. Open green diamonds: previous EBIT results. Note that the spread seen in various astrophysical sources, EBITs, and tokamak in part arises from insufficient removal of Fe XVI line C contamination of Fe XVII line 3D, at varying Fe XVI/Fe XVII abundance ratios.

intensity ratio including cascades, resonant excitation, polarization effects, and population transfer mechanisms as a function of electron beam energy. The simulations revealed that for low electron beam energies as employed in the EBIT experiments mentioned above, the observed intensity ratio might be drastically lowered compared to the oscillator-strength ratio. According to [60], experiments based on electron-impact excitation require electron beam energies higher than 2000 eV to observe an unperturbed intensity ratio of approximately 3.5. Experimentally such conditions were unfeasible since electron beam energies above 2000 eV are sufficient to produce charge states up to Fe XXV. Hence, Fe XVII ions are usually completely ionized to higher charge states.

The result obtained in this work is in excellent agreement with the predicted unperturbed intensity ratio of simulations that were able to reproduce the results of electron-impact excitation measurements for low electron beam energies. This clearly hints towards a systematical reduction of the observed intensity ratio induced by different cross sections, cascades, resonant excitation, and polarization effects for 3C and 3D in previous EBIT and tokamak measurements based on electron-impact excitation.

Looking at astrophysical observations, it is also noticeable that the observed intensity ratios between 1.63 and 3.02 significantly deviate from the result of this work.

A possible explanation for this, similar to the one discussed for laboratory measurements, is found in unknown contaminations of C or different electron-impact excitation cross sections for 3C and 3D. In addition, while in an EBIT the plasma is considered to be optically thin, in some astrophysical sources this may not necessarily hold true. Hence, the observed 3C/3D intensity ratios may have been partially affected and reduced by the plasma density, which is the same effect proposed to use as plasma density diagnostic utility.

A systematic underestimation of the observed intensities due to modeling the signal with Gaussian profiles, as for example during the first beamtime of this work, is unlikely in the laboratory measurements as well as in the astrophysical observations. Figure 6.2 shows that this effect is particularly strong when high resolution is obtained but the data quality does not allow modeling with Voigt profiles. The resolution of all comparison measurements and observations exhibited values of 1 eV FWHM and broader. Hence, this effect should only have a minor impact on the observed intensity ratios. Behar et al. [8], for example, determined the line intensities in the emission spectrum of Chandra by the areas of Gaussians fitted the observed spectrum as well as by summing up the number of events within a 275 meV broad energy bin. Both approaches deliver similar results.

Older theoretical works on the 3C/3D oscillator-strength ratio from the 1980s and 1990s were based on the so-called R-matrix and distorted wave (DW) approaches. The theoretically determined ratios of these calculations in the range from 3.74 to 4.52 are all well above the experimental results. A significant step towards lower values was achieved in the 2000s by, for example, the introduction of many body perturbation theory (MBPT) calculations and relativistic treatment of the R-matrix approach, resulting in values between 3.43 and 3.54, respectively [140, 32]. Note that after the validity of a calculation similar to the one presented here based on a Dirac-R-Matrix approach was questioned by Zhang et al. [170], Chen et al. found several small errors and „bugs“ in the code used [35]. Unfortunately, it remains unclear to date whether the oscillator-strength ratio value of 3.43 reported by Chen et al. based on the same code were also affected by these errors [32]. In 2005, first configuration interaction (CI) calculations resulted in a ratio of 3.91 [107], which is also significantly higher than the experimental result of this work. For the CI approach as well as for multiconfiguration Dirac Fock (MCDF) calculations, the output heavily depends on the number of configurations involved. The high value of 3.91 is possibly due to the limitated computing power at that time and the resulting limitation on the number of involved electronic configurations to 139. The effect of the number of configurations involved can be exemplified by the MCDF calculations presented in [14]. For 96 configurations involved, the calculation resulted in a value of approximately 4.0. Adding more configurations to a total of 152000 configurations decreased the oscillator-strength ratio to 3.5. However, even this large number of configurations was not sufficient to achieve a fully converged result. In

2017, Mendoza et al. [116] presented a 3C/3D oscillator-strength ratio of 2.82 which was in good agreement with the LCLS measurements and claimed theoretical confirmation of the experimental results. However, this approach based on Breit-Pauli configuration interaction paired with a fine-tuning of the relativistic coupling has been disputed by Wang et al. [163].

Parallel to this work, further calculations of the 3C/3D oscillator-strength ratio were conducted by three research groups based on different approaches and codes. The nowadays drastically increased computational power allowed a total of 1.2 million configurations to be added in a multiconfiguration Dirac Hartree Fock (MCDHF) approach by Harman et al. [96]. Other calculations based on CI and a combination of particle-hole CI with MBPT with 230000 and 1000000 configurations performed by Safronova et al. and Berengut et al., respectively, are in excellent agreement with the MCDHF calculations [96]. The fully converged results cover a range between 3.55 and 3.59 and include all known quantum mechanical effects. In direct comparison with the obtained experimental ratio, these very-large scale calculations are in excellent agreement.

It was shown that previous EBIT measurements of the 3C/3D oscillator-strength ratio based on electron-impact excitation resulted in values in the range of 1.90 to 3.04. The large discrepancy with the present result of 3.51 suggests that electron-impact excitation cross sections may have had a greater influence on the observed intensity ratios than hitherto assumed. This is also supported by simulations predicting lower values for the experimental conditions of these measurements. First laser spectroscopy measurements at the free electron laser LCLS revealed independently of effective cross sections an oscillator-strength ratio of 2.61 well below all available theoretical predictions. Subsequently, non-linear effects and population transfer mechanisms were proposed to explain the discrepancy between experiment and theory. The measurements conducted within this thesis explicitly excluded both effects and resulted in an excellent agreement with newest state-of-the-art calculations. The continuously increasing computational power and the steadily improved quality of experimental data finally resulted in a convergence of the predicted 3C/3D oscillator-strength ratio towards the measured value. Therefore, the long-lasting discrepancy appears to be finally resolved and the diagnostic utility for astrophysical plasmas may now be fully applied.

6.1.2 Natural linewidths of 3C and 3D

Generally, the fluorescence profile $G_i(E)$ of an observed transition i consists of the natural Lorentzian line profile $\gamma_i(E)$ convolved with the instrumental profile $g_{\mathrm{Instrument}}(E)$

$$G_i(E) = (\gamma_i * g_{\mathrm{Instrument}})(E) := \int \gamma_i(\tau) g_{\mathrm{Instrument}}(E-\tau)\mathrm{d}\tau. \tag{6.8}$$

The linewidth Γ_i of the natural Lorentzian line profile γ_i is proportional to the Einstein coefficient A_i for a given transition

$$\Gamma_i = \hbar A_i, \tag{6.9}$$

with the Planck constant $\hbar = 6.582\,119\,569 \times 10^{-16}\,\text{eV s}$ and hence, offers an excellent testbed for benchmarking calculated transition probabilities independently of ratios or effective cross sections, as demonstrated in [138].

In many cases, the instrumental profile $g_{\text{Instrument}}(E)$ is the convolution of several Gaussian profiles but in principle can be arbitrarily shaped. Gaussian profiles arise, e.g., from the intrinsic velocity distribution of the ion cloud and the resulting Doppler broadening or from the energy distribution of the incident photon beam. The convolution of one or several Gaussian profiles with a Lorentzian profile arising from the natural line broadening of a transition results in a Voigt profile, see also chapter 2.3.4.

In measurements exhibiting a broad Gaussian component compared to the natural linewidth, as for example during the beamtime in 2018, this Gaussian component completely dominates the observed Voigt profile. Hence, a determination of the Einstein coefficients by measuring the Lorentzian linewidth is unfeasible.

In order to resolve the Lorentzian component of a Voigt profile, an instrumental profile with a FWHM in the same order of magnitude as the Lorentzian width or narrower is required. For example, the spectral resolution $E/\Delta E$ of the second and third beamtimes being 14000 and 20000, respectively, was sufficient to determine the width of the Lorentzian component with an statistical uncertainty on the percent level.

In general, the ratio of the oscillator strengths $\frac{f_1}{f_2}$ and natural linewidths $\frac{\Gamma_1}{\Gamma_2}$ of two transitions are related. It is

$$\frac{\Gamma_1}{\Gamma_2} = \frac{f_1}{f_2} \cdot \left(\frac{E_1}{E_2}\right)^2, \tag{6.10}$$

where $\left(\frac{E_1}{E_2}\right)^2$ is the squared ratio of the transition energies. Since in the specific case of 3C and 3D of Fe XVII, the transition energies and thus, the squared energy ratio $\left(\frac{E_{3C}}{E_{3D}}\right)^2 = 1.032$ are well known [27], the expected ratio of the natural linewidths of 3C and 3D is

$$\frac{\Gamma_{3C}}{\Gamma_{3D}} = \frac{f_{3C}}{f_{3D}} \cdot \left(\frac{E_{3C}}{E_{3D}}\right)^2 = 3.51 \cdot 1.032 = 3.62 \tag{6.11}$$

when using the measured 3C/3D oscillator-strength ratio $\frac{f_{3C}}{f_{3D}} = 3.51$ determined in the previous chapter. However, the measured Lorentzian linewidths Γ'_{3C} and Γ'_{3D} obtained during the beamtime 2020 result in a ratio of

$$\frac{\Gamma'_{3C}}{\Gamma_{3D}} = \frac{22.02\,\text{meV}}{10.22\,\text{meV}} = 2.15 \tag{6.12}$$

which is irreconcilable with the expected value based on the oscillator-strength ratio. As stated in the beginning of this chapter, the instrumental profile $g_{\text{Instrument}}(E)$ was expected to consist of the convolution of several Gaussian distributions. Here, it would seem that $g_{\text{Instrument}}(E)$ also contained an additional non-Gaussian contribution that could be well modeled by a Lorentzian profile. Hence, all Lorentzian linewidths Γ'_i measured during the campaigns appear to be falsified.

The analysis of measurements of well-known transitions of He-like systems, for which the natural linewidths are well known, confirmed this conjecture. For this reason, it was impossible to directly infer the Einstein coefficients from the measurements of the Lorentzian widths.

Universally, Lorentzian profiles are invariant under convolutions, that is, the width $\Gamma_{\text{Convolved}}$ of two convolved Lorentzian profiles results in

$$\Gamma_{\text{Convolved}} = \Gamma_1 + \Gamma_2, \tag{6.13}$$

where Γ_1 and Γ_2 are the linewidths of the individual Lorentzian distributions. Hence, the apparent Lorentzian linewidths $\Gamma'_{3\text{C}}$ and $\Gamma'_{3\text{D}}$ can be expressed as

$$\Gamma'_{3\text{C}} = \Gamma_{3\text{C}} + \Gamma_{\text{Beamline}} \tag{6.14}$$

and

$$\Gamma'_{3\text{D}} = \Gamma_{3\text{D}} + \Gamma_{\text{Beamline}}, \tag{6.15}$$

where $\Gamma_{3\text{C}}, \Gamma_{3\text{D}}$ and Γ_{Beamline} correspond to the natural linewidths of 3C, 3D as well as the offset given by the beamline, respectively. Furthermore, the difference of the natural linewidths of 3C and 3D is defined as

$$\Delta\Gamma_{3\text{C}-3\text{D}} = \Gamma_{3\text{C}} - \Gamma_{3\text{D}}. \tag{6.16}$$

Equations 6.14, 6.15 and 6.16 result in

$$\Delta\Gamma_{3\text{C}-3\text{D}} = \Gamma_{3\text{C}} - \Gamma_{3\text{D}} = \Gamma'_{3\text{C}} - \Gamma_{\text{Beamline}} - \left(\Gamma'_{3\text{D}} - \Gamma_{\text{Beamline}}\right) = \Gamma'_{3\text{C}} - \Gamma'_{3\text{D}}. \tag{6.17}$$

This shows that $\Gamma_{3\text{C}} - \Gamma_{3\text{D}}$ is equal to the difference of the observed Lorentzian linewidths $\Gamma'_{3\text{C}} - \Gamma'_{3\text{D}}$. However, this only holds true, if the Lorentzian contribution of the instrumental profile of the beamline Γ_{Beamline} is assumed being constant. The true origin of Γ_{Beamline} remained unexplained but is most likely found in scattering effects, imperfections of the employed optical elements, and misalignment of the photon beam. Similar instrumental profiles at the diffraction limit are a common phenomenon observed at several soft X-ray beamlines [88, 56]. Since for the measurements of 3C and 3D as well as B and C, only the angles of the grating and mirror were changed by approximately 0.01°, while all other components of the beamline, such as slits and the mirrors in the refocusing mirror unit remained in their positions, the additional Lorentzian contribution is assumed to be constant over the relevant

TABLE 6.3: Obtained linewidth differences between 3D of Fe XVII and various lines of Fe XVII as well as Fe XVI. In total up to three values were given, one obtained during beamtime 2019 and two during beamtime 2020. In the latter, two fit approaches provided varying results, the final value covers the whole range of the fit results. Note that the value from 2019 was disregarded due to large statistical uncertainty. All linewidth differences are given in meV FWHM.

Line	**2019**	**2020**	**2020 (Convolution)**	**Final value**
$\Gamma_{3C} - \Gamma_{3D}$	9.57(130)(48)	11.84(59)(59)	9.72(26)(49)	10.92(175)
$\Gamma_{C} - \Gamma_{3D}$	X	16.75(60)(84)	15.68(36)(78)	16.30(148)
$\Gamma_{B} - \Gamma_{3D}$	X	12.26(80)(61)	11.75(21)(59)	12.20(107)

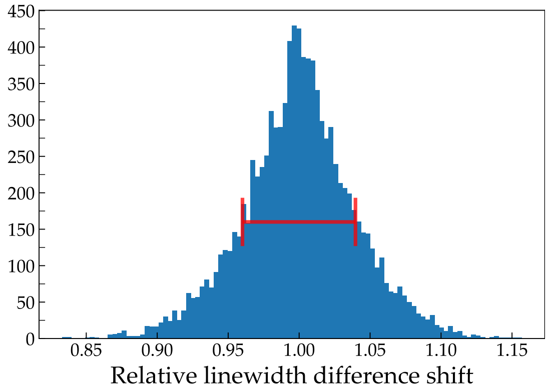

FIGURE 6.11: Simulated relative shifts of the linewidth difference between 3C and 3D. Two synthetic Voigt lines were disturbed by a simulated interpolation error of the monochromator. The linewidth differences of the disturbed lines were analyzed and compared with the initial parameters. Red bars indicate the corresponding 1-σ deviations.

energy range. Hence, the natural linewidth differences of 3C, 3D, B, and C could be inferred from the Lorentzian linewidths obtained during the beamtimes in 2019 and 2020 and are listed in table 6.3.

Monochromator energy interpolation errors dominated the final error budget of the 3C/3D oscillator-strength ratio in the previous chapters. In order to scrutinize if these interpolation errors also affected the determined linewidth differences, simulations of non-equidistant energy steps similar to the ones described in previous chapter regarding the oscillator-strength ratio were conducted resulting in a systematical uncertainty of approximately 5%, see figure 6.11.

Additional to the Lorentzian component, the instrumental profile of the measurement campaign in 2020 possessed a minor asymmetry on the lower energy side of each transition. Simulations to systematically investigate the impact of the asymmetry on the observed oscillator-strength ratio performed in the previous chapter also showed that the observed Lorentzian linewidth differences remained constant if a skewed Voigt model was applied or if only the upper or lower energy half of a transition was fitted by conventional Voigt models. However, the asymmetry itself leads to the question whether the instrumental profile can be described by a Voigt profile and to which degree equation 6.17 holds true, even for an asymmetric line shape.

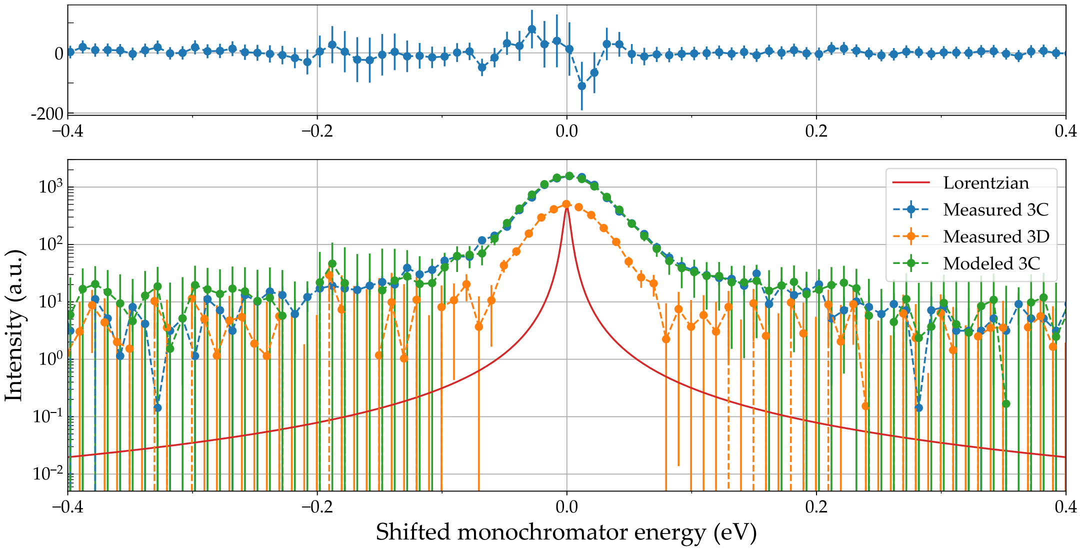

FIGURE 6.12: Example of a convolution fit of a measured line profile of 3D (orange) with a Lorentzian line shape (red) resulting in a modeled line 3C which was fitted to the measured profile of 3C. Top panel shows the residuum of the performed fit. Note that the line C was subtracted from the 3D spectrum resulting in larger uncertainties in the former energy range of C.

For this reason a second approach to determine the natural linewidth differences was introduced. Since the Lorentzian part of a given transition profile $G_2(E)$ is invariant under convolutions, $G_2(E)$ can be expressed as a convolution of another transition $G_1(E)$ with an additional Lorentzian profile $\gamma_{2-1}\left(A_{2/1}, \Gamma_{2-1}, E\right)$ without loss of generality

$$G_2(E) = (\gamma_{2-1} * G_1)(E). \tag{6.18}$$

Here, the parameters $A_{2/1}$ and Γ_{2-1} of the Lorentzian profile γ_{2-1} correspond to the amplitude ratio as well as the linewidth difference of the two transitions G_2 and G_1. Note that equation 6.18 only holds true if $\Gamma_2 \geq \Gamma_1$.

In the specific case of the measurements in this thesis, this means that the observed line shape of 3D can be convolved with a suitable Lorentzian profile γ_{3C-3D} in order to describe the line shape of 3C. Hence, independent of the instrumental profile $g_{\text{Instrument}}(E)$, the amplitude ratio $A_{3C/3D}$ as well as the natural linewidth difference Γ_{3C-3D} can be determined. Note that this still only holds true if the instrumental profile is constant.

In a least-squares fit routine, the free parameters $A_{3C/3D}$ and Γ_{3C-3D} were optimized such that the convolution of the measured line shape of 3D with the Lorentzian distribution $\gamma_{3C-3D}(A_{3C/3D}, \Gamma_{3C-3D}, E)$ replicated the measured line shape of 3C. The result of such a fit is depicted in figure 6.12. Note that the contribution of line C was subtracted from the complex consisting of line 3D and C prior to the fit. The fit was repeated for the available 20 consecutive scans of 3C and 3D obtained during beamtime 2020. Note that the SNR achieved in beamtime 2019 was insufficient to apply the convolution fit method to the data. The same method was also applied to extract the linewidth differences $\Gamma_{\mathrm{C-3D}}$ and $\Gamma_{\mathrm{B-3D}}$. The obtained 3C/3D oscillator-strength ratio of $f_{3\mathrm{C}}/f_{3\mathrm{D}} = 3.46(6)$ is in good agreement with the results obtained using conventional Voigt fits described in the previous chapter. The weighted averages of the natural linewidth differences using the convolution fit method are listed in table 6.3. Note that the 5% relative systematical uncertainty due to monochromator energy interpolation errors is included in the listed uncertainties.

Since the results of the two approaches of using conventional Voigt and convolution fits differ, it is ambiguous to deduce which approach is more accurate. Hence, the final values were conservatively chosen as the mean of the two values which are also listed in table 6.3. The uncertainty was defined as the lowest and the highest obtained value including 1-σ uncertainty. Note that the determined linewidth difference of 3C and 3D from 2019 beamtime was disregarded due to large statistical uncertainty

Even though a direct determination of the individual natural linewidths was unattainable due to the instrumental profile, the natural linewidths of the transitions could be analytically calculated by combining the measured natural linewidth difference and oscillator-strength ratio. From 6.11 follows

$$\Gamma_{3\mathrm{C}} = \frac{f(3\mathrm{C})}{f(3\mathrm{D})} \cdot \left(\frac{E_{3\mathrm{C}}}{E_{3\mathrm{D}}}\right)^2 \Gamma_{3\mathrm{D}} \tag{6.19}$$

and

$$\Gamma_{3\mathrm{D}} = \frac{\Gamma_{3\mathrm{C}}}{\frac{f(3\mathrm{C})}{f(3\mathrm{D})} \cdot \left(\frac{E_{3\mathrm{C}}}{E_{3\mathrm{D}}}\right)^2}. \tag{6.20}$$

By combining equations 6.19 and 6.20 with equation 6.16, the natural linewidths of 3C and 3D are expressible as

$$\Gamma_{3\mathrm{C}} = \frac{\Delta\Gamma_{3\mathrm{C-3D}}}{1 - \frac{1}{\frac{f(3\mathrm{C})}{f(3\mathrm{D})} \cdot \left(\frac{E_{3\mathrm{C}}}{E_{3\mathrm{D}}}\right)^2}} \tag{6.21}$$

and

$$\Gamma_{3\mathrm{D}} = \frac{\Delta\Gamma_{3\mathrm{C-3D}}}{\frac{f(3\mathrm{C})}{f(3\mathrm{D})} \cdot \left(\frac{E_{3\mathrm{C}}}{E_{3\mathrm{D}}}\right)^2 - 1}. \tag{6.22}$$

In such a way, the individual natural linewidths of 3C and 3D are calculated using the experimental results for both the oscillator-strength ratio and the Lorentzian linewidth difference. The results are listed in table 6.4. Also listed are the natural linewidths of B and C, which were determined by adding the measured linewidth differences $\Gamma_{\mathrm{B-3D}}$ and $\Gamma_{\mathrm{C-3D}}$ to the value of $\Gamma_{3\mathrm{D}}$.

TABLE 6.4: Natural linewidths of various lines of Fe XVII and Fe XVI deduced in this work. The linewidths of 3C and 3D were determined by combining the observed 3C/3D oscillator-strength ratio, the linewidth difference $\Gamma_{3C} - \Gamma_{3D}$ and equations 6.21 or 6.22. Linewidths of B and C were determined by adding the linewidth differences listed in table 6.3 to the obtained value of Γ_{3D} .

Transition	Natural linewidth (meV) FWHM	Relative uncertainty (%)
3C	15.27(247)	16.2
3D	4.22(68)	16.1
C	20.52(380)	18.5
B	16.42(301)	18.3

Comparison with theory

Here, the measured natural linewidth difference between 3C and 3D as well as their individual calculated linewidths will be put in context of the available theoretical work. For decades, theories were continuously benchmarked by comparing predicted 3C/3D intensity ratios with measurements. Measuring an individual line strength, i.e., the Einstein coefficient of either 3C or any other line in the Fe XVII system was not possible, since even the highest available resolving powers of approximately $E/\Delta E \approx 600$ utilizing crystal spectrometers were by far insufficient. One disadvantage of comparing only ratios is that for example for a measured 3C/3D intensity ratio of 3.5, a theory that predicts natural linewidths of 350 and 100 meV for 3C and 3D, respectively, performs equally well as a possibly much more accurate theory that predicts linewidths of 35 and 10 meV. Hence, comparing individual linewidths provides much more stringent tests of the theoretical predictions.

In figure 6.13 the experimental result for the natural linewidth difference Γ_{3C-3D} and a selection of available theoretical values are depicted. The same values are also listed in table 6.5. It is noticeable that, with a few exceptions, the calculations are in good 1-σ agreement with the measurements of this work. In addition, it is evident that more recent calculations deviate less from the experimental result compared to older calculations based on distorted wave or R-matrix approaches by Cornille et al. and Kaastra et al., respectively [40, 91]. Calculations made in parallel to this work (Harman et al., Safronova et al., and Berengut et al. [96]) are in excellent agreement and deviate by only about 0.1σ from the experimental value.

Additionally to the natural linewidth difference, the individual natural linewidths of 3C, 3D, B, and C were deduced which allows for the direct comparison of Einstein coefficients instead of oscillator-strength ratios. It should be emphasized that the obtained natural linewidths are dependent on the observed 3C/3D oscillator-strength

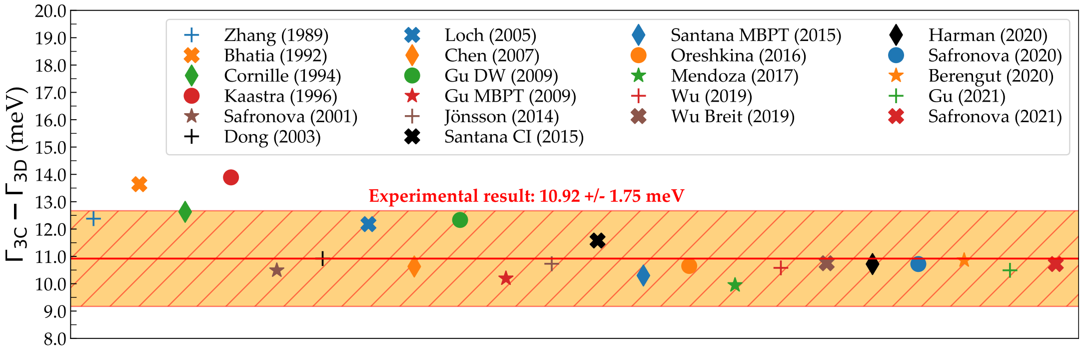

FIGURE 6.13: Comparison of the experimentally obtained natural linewidth difference of 3C and 3D in this work with available theories listed in table 6.5

ratio and therefore do not provide a completely independent benchmark for theories. The relative accuracies achieved are limited to 16-18% due to monochromator interpolation errors and inconclusive results of two different fit approaches described earlier. Although the accuracy is limited and the linewidths were not measured independently of the oscillator-strength ratio, the values still allow to broadly compare calculations and the experiment.

In table 6.5 the natural linewidths for 3C and 3D as well as theoretical predictions are listed. Theories based on R-matrix and distorted wave approaches calculated natural linewidths for 3C between 16 and 17.7 meV and for 3D between 3.4 and 3.8 meV, respectively. Results of newest state-of-the-art calculations (Harman et al. and Safronova et al., 2020) show natural linewidths of 14.74 for 3C and 4.02 meV for 3D, and hence, deviate by only 0.2 and 0.26σ from the experimental result of this work.

In figure 6.14, predicted natural linewidth differences between 3C and 3D are depicted as a function of the 3C/3D natural linewidth ratio for a selection of available theoretical works. For direct comparison, the experimental result of this thesis including its 1 and 2-σ uncertainties is added to the plot. Note that the experimental linewidth ratio was inferred by using equation 6.11 with the measured 3C/3D oscillator-strength ratio and the transition energy measurements of Brown et al. [27]. In comparison with theory, it seems that the majority of values calculated with codes based on CI and MCHDF are in excellent 1-σ agreement with the present experimental results. The deviation of the predicted values by Santana et al. [141] and Loch et al. [107] which both are also based on CI is most likely rooted in not fully converged calculations, due to a too small number of included configurations of 816 and 189, respectively.

The measurements of the natural linewidths of lines 3C and 3D, which were originally intended to determine which of the two lines were incorrectly predicted by theory, reveal, consistent with the measurements of the oscillator-strength ratio, that no discrepancy between experiment and theory is found.

TABLE 6.5: Comparison of the natural linewidths of 3C and 3D between this work and a selection of theoretical predictions. If available, n_{Config} corresponds the number of included configurations in the calculation. Additionally, the employed method of each calculation is given: DW - distorted wave, RM - R-Matrix, MBPT - many body perturbation theory, MCDF - multi-configuration Dirac Fock, CI - configuration interaction, BP-CI - Breit-Pauli configuration interaction. Note that the validity of theory published by Mendoza et al. has been disputed [163]. All linewidths and linewidth differences are given in meV FWHM.

	Method	Γ_{3C-3D}	Γ_{3C}	Γ_{3D}	n_{Config}
This work	EBIT	10.92(175)	15.27(247)	4.22(68)	
Zhang (1989) [169]	DW	12.38	16.15	3.77	./.
Bhatia (1992) [17]	RM	13.64	17.38	3.74	37
Cornille (1994) [40]	DW	12.63	16.07	3.44	65
Kaastra (1996) [91]	RM	13.89	17.73	3.84	./.
Safronova (2001) [140]	MBPT	10.49	14.63	4.14	36
Dong (2003) [51]	MCDF	10.92	15.18	4.26	20257
Loch (2005) [107]	CI	12.18	16.19	4.01	189
Chen (2007) [32]	DRM	10.63	14.81	4.18	./.
Gu (2009) [66]	DW	12.33	16.23	3.90	./.
Gu (2009) [66]	MBPT	10.19	14.09	3.90	./.
Jönsson (2014) [89]	CI	10.73	14.74	4.01	700000
Santana (2015) [141]	CI	11.58	15.71	4.13	816
Santana (2015) [141]	MBPT	10.30	14.34	4.04	7
Oreshkina (2016) [126]	CI	10.65	14.61	3.96	100000
Mendoza (2017) [116]	BP-CI	9.95	15.14	5.19	./.
Wu (2019) [167]	MCDF	10.58	14.66	4.08	3.7×10^6
Wu (2019) [167]	MCDF+B	10.75	14.76	4.01	3.7×10^6
Harman (2020) [96]	MCDHF	10.72	14.74(3)	4.02(6)	1.2×10^6
Safronova (2020) [96]	CI	10.72	14.74(3)	4.02(5)	230000
Berengut (2020) [96]	AMBiT	10.86	14.90	4.04	1×10^6
Gu (2021) [64]	CI	10.50	14.52	4.02	./.
Safronova (2021) [36, 37]	CI	10.72	14.74(2)	4.02(2)	795907

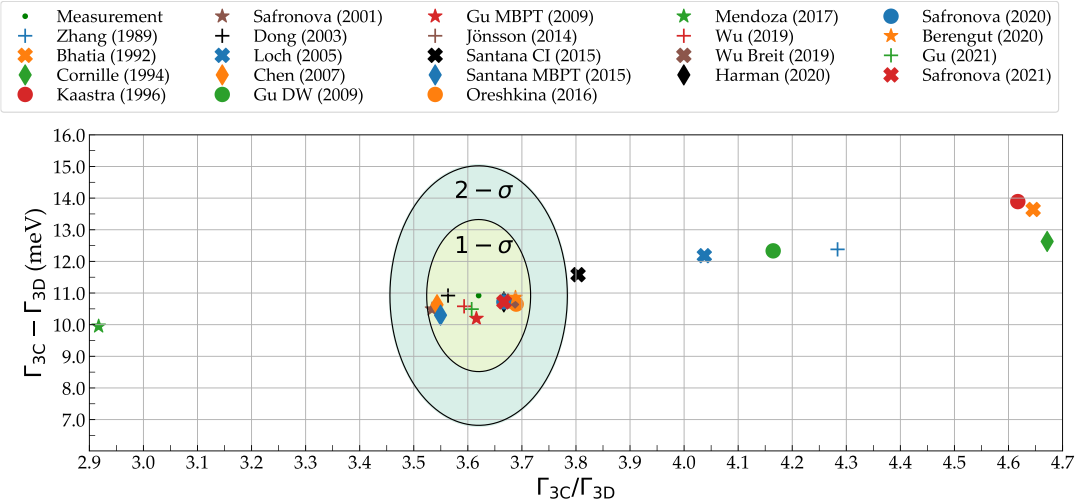

FIGURE 6.14: Colored symbols: Predicted natural linewidth difference between 3C and 3D as a function of the 3C/3D natural linewidth ratio for a selection of available theoretical work. A green dot represents the experimental values of this work, including the 1 and 2-σ ellipses of the measurement uncertainties (green shaded areas). All the values depicted here are also listed in table 6.5.

6.1.3 Natural linewidths of B and C of Fe XVI

Two additional lines, B and C of Fe XVI, were also measured as part of this work. These lines of the sodium-like system are particularly interesting since the additional electron in the 3s shell in principal enables strong auto-ionization decay channels. Thus, the natural linewidths provide unique references in benchmarking theories, since the models are required to calculate the strengths of one or more radiative channels as well as the Auger rates.

In contrast to 3C and 3D of Fe XVII, significantly fewer theoretical predictions for the lines B and C were published. In table 6.6, the experimental results as well as theoretical predictions are listed. If available, the Lorentzian linewidth arising from the sum of all radiative decays $\Gamma_{\mathrm{Radiative}}$ as well as the sum of all Auger decays Γ_{Auger} are listed for each theory. Regarding line B, it is interesting to note that calculations performed by Gu et al. and Diaz et al. [67, 49] predict a negligible Auger contribution, whereas calculations by Wu et al. [167] resulted in an Auger contribution of almost 8% of the total natural linewidth. If comparing only the predicted linewidths of radiative decays, all theories result in similar values. The total natural linewidth value predicted by Wu et al. is slightly larger due to the additional Auger contribution. In direct comparison with this work, all predictions are in good agreement with the experimental result.

In contrast to B, line C is expected to exhibit a significantly stronger Auger decay. Since Diaz et al. did not include Auger decays in the calculations, that value is only partially comparable. The theoretical works of Gu et al. and Wu et al. included all possible Auger decay channels but result in different linewidths. While the radiative decays are predicted with similar strengths for all three available theories, the Auger decay strength of Gu et al. is predicted approximately 25% higher compared to Wu

TABLE 6.6: Comparison of natural linewidths of B and C of Fe XVI between this experimental work and available theoretical predictions. Note that Diaz et al. only calculated the radiative channels.

Source	$\Gamma_{\text{Radiative}}$ (meV)	Γ_{Auger} (meV)	Γ_{Total} (meV)
B			
This work			16.42(301)
Gu (2006) [67]	15.66	0.001	15.66
Diaz (2013) [49]	15.59	0.0	15.59
Wu (2019) [167]	16.13	1.38	17.53
C			
This work			20.52(380)
Gu (2006) [67]	9.28	13.89	23.17
Diaz (2013) [49]	9.41	0.0	9.41
Wu (2019) [167]	8.69	10.94	19.63

et al. Both theories that included Auger decays in their calculations are in a solid agreement with the experimental results. However, the value given by Wu et al. is significantly closer to the experimental results than the value of Gu et al.

6.1.4 Oscillator-strength ratio of 4C and 4D

Additionally to the oscillator-strength ratio of 3C and 3D, the ratio of 4C and 4D of Fe XVII was measured during beamtime 2020. In contrast to 3C and 3D, neither 4C nor 4D exhibit any adjacent lines in the ion species trapped during the measurement that could have adulterated the measurements. Hence, an agreement of experimental results for the 4C/4D oscillator-strength ratio combined with a persistent disagreement for 3C/3D could have hinted towards the presence of a systematic population transfer induced by C during the measurements of 3D as has been proposed.

Due to the higher principle quantum number, the transition energies ($E_{4\mathrm{C}} = 1022\,\mathrm{eV}$ and $E_{4\mathrm{D}} = 1010\,\mathrm{eV}$) are well above those of 3C and 3D and additionally exhibit several decay channels which remained undetected in the experiment. If benchmarking theory with the obtained experimental results, the theoretical values are required to be corrected for the predicted branching ratios of the transitions.

Experimentally, an uncorrected 4C/4D intensity ratio of $I_{4\mathrm{C}}/I_{4\mathrm{D}} = 1.019$ was found. The relative statistical uncertainty of the result was 3.5%. Similar to the measurements of 3C and 3D, 4C and 4D were most likely affected by systematical uncertainties originating from monochromator energy interpolation errors of approximately 2%. Hence, the final value for the 4C/4D intensity ratio amounts to

$$I_{4\mathrm{C}}/I_{4\mathrm{D}} = 1.019(40).$$

Compared to 3C and 3D, fewer reference data from measurements, astrophysical observations or theoretical calculations are available for lines 4C and 4D. A selection

TABLE 6.7: Comparison of the 4C/4D intensity ratio between this work, astrophysical observations and theoretical predictions. Note that the experimental value doesn't include corrections for the undetected branching ratios. An asterisk (*) represents for which a probable disturbance of the adjacent line Ly_{α} of Ne X was not taken into consideration or unable to resolve. Note that for the theoretical work, the uncorrected, pure oscillator-strength ratio as well as the for the branching ratio corrected value are listed.

Source	**Method/Object**	**4C/4D Intensity Ratio**
This work	EBIT, Laserspectroscopy	1.019(40)
McKenzie (1980) [115]	Sun*	0.865
Mewe (2001) [117]	Capella*	2.49
Behar (2001) [8]	Capella*	1.97
Gu (2021) [64]	MBPT, uncorrected	1.055
Gu (2021) [64]	MBPT, corrected	1.063
Safronova (2021) [36, 37]	MCDHF, uncorrected	1.085
Safronova (2021) [36, 37]	MCDHF, corrected	1.096
Liang (2010) [104]	R-Matrix, uncorrected	1.146
Landi (2006) [97]	Distorted Wave, uncorrected	1.160
Loch (2005) [107]	R-Matrix, uncorrected	1.168

of literature values is listed in table 6.7. If available, the oscillator-strength ratio of 4C and 4D was corrected for the branching ratio. The obtained 4C/4D intensity ratio is in good 1-σ agreement with newest state-of-the-art predictions by Gu [64] based on a MBPT approach. Compared to MCDHF calculations performed by Safronova et al. [36, 37], a deviation of 2σ is present. Older theories based on R-Matrix and DW depart by almost 4σ from the experimental results. Additionally, R-Matrix and DW calculations are both uncorrected for branching ratios, which in principle should increase the calculated value and further deepen the discrepancy.

Astrophysical observations of the 4C/4D intensity ratio listed in table 6.7 might have been contaminated by the strong line Ly_{α} of Ne X exhibiting an energy separation of less than 1 eV from 4C, which is unresolvable by common space-based spectrometers. Hence, a direct comparison of the result of this work with astrophysical observations is not expedient. However, future space-based observatories mounting high-resolution microcalorimeters might isolate 4C and provide more reliable reference data.

6.2 Measurements on Ni XIX

6.2.1 Oscillator-strength ratio of 3C and 3D

Similar as for iron, the 3C/3D oscillator-strength ratio of Ni XIX was measured during beamtime 2020 with unprecedented spectral resolution. The measurements provide first results of an oscillator-strength ratio based on X-ray laser spectroscopy apart from iron. Since 3C as well as 3D of Ni XIX are free of any adjacent lines, such

TABLE 6.8: Comparison of the 3C/3D oscillator-strength ratio of Ni XIX between this work and a selection of experiments, astrophysical observations and theoretical predictions. Methods used: DW - distorted wave, MBPT - many body perturbation theory, MCDF - multi-configuration Dirac Fock, CI - configuration interaction.

Source	**Method**	**3C/3D Intensity Ratio**
This work	EBIT, Laserspectroscopy	2.48(8)
Brown (2001) [24]	Electron excitation	2.30(16)
Gu (2004) [68]	Electron excitation	1.90(18) - 2.35(21)
McKenzie (1980) [115]	Sun	2.12
Mewe (2001) [117]	Capella	2.42
Behar (2001) [8]	Capella	2.19
Zhang (1989) [169]	DW	3.00
Safronova (2001) [140]	MBPT	2.36
Dong (2003) [51]	MCDF	2.59
Jönsson (2014) [89]	CI	2.65
Santana (2015) [141]	CI	2.73
Santana (2015) [141]	MBPT	2.59
Safronova (2021) [36, 37]	CI	2.65
Gu (2021) [64]	CI	2.61

as C of Ni XVIII, population transfer mechanisms are excluded. This system therefore forms an excellent testbed for benchmarking theory. Additionally, measuring the 3C/3D oscillator-strength ratio of multiple neon-like ion species enables studies of the dependency on the nuclear charge Z [25].

The obtained value of $f_{3C}/f_{3D} = 2.48$ with a relative statistical uncertainty of approximately 0.8% was also possibly influenced by systematical effects induced by monochromator interpolation errors in the order of 2%. Hence the final value is given as

$$f_{3C}/f_{3D} = 2.48(8).$$

Comparison with other experiments and theories

In contrast to the 3C/3D oscillator-strength ratio of iron, the ratio of the the same transitions in nickel is much less prominent in the scientific literature. This originates mainly in the reduced abundance of nickel compared to iron in most of the stars of interest and the consequent reduced line intensity in the observed spectra [21]. Hence, more attention was paid to the oscillator-strength ratio of iron experimentally as well as theoretically. The final result of this work and a selection of experiments, astrophysical observations and theoretical predictions are listed in table 6.8.

Two laboratory measurements of the 3C/3D intensity ratio of nickel based on electron-impact excitation have been reported [24, 68]. The values of both experiments, ranging between 1.9 and 2.35, are below the value found within this work. The large spread arose from various electron beam energies that were used to excite the transitions. This once again emphasizes the inferiority of measuring intensity ratios based on electron excitation instead of photo excitation which are independent of cross sections and directly probe the oscillator strengths. However, the largest observed ratios are in a good 0.6-σ agreement with the result of this work. In the case of iron, the closest value obtained in EBIT measurements based on electron excitation departed by 4σ. Since for iron the deviation is significantly larger, this could indicate that the the influence of C in the iron measurements was still underestimated in the hitherto reported measurements. During the nickel measurements such an effect was ruled out since C was fully resolved.

Astrophysical observations resulted in 3C/3D intensity ratios between 2.12 and 2.42. In case of the star Capella, depending on which spatial region was observed and analyzed, the recorded ratios vary between 2.19 and 2.42. This large spread can be attributed to different densities of the emitting plasma. The larger of the two values is in good agreement with the experimental results of this work.

In comparison with theoretical work, the experimental results are in a fair agreement and deviate by approximately 2σ from large-scale calculations performed by Santana et al., Safronova et al., and Gu et al. [141, 36, 64]. The origin of the larger deviation is maybe found in an underestimation of the systematical uncertainty of the monochromator interpolation error, which was estimated based on a photoelectron measurement in the energy range of 3C of iron. Since the transition energies of 3C and 3D in nickel is approximately 25% higher compared to iron, the employed angles of the mirror and grating in the monochromator were vastly differed. Hence, the estimated systematical uncertainty of 2% is probably too low.

6.2.2 Natural linewidths of 3C and 3D

Similar as for iron, the natural linewidth difference between 3C and 3D of nickel was determined using conventional fits of Voigt profiles applied to the data

$$\Gamma_{3C} - \Gamma_{3D} = \Gamma'_{3C} - \Gamma'_{3D} = 30.15(37) - 17.96(55)\,\text{meV} = 12.19(66)\,\text{meV}. \tag{6.23}$$

Additionally, a systematical uncertainty of 5% was added due to possible monochromator interpolation errors, resulting in a final value of

$$\Gamma_{3C} - \Gamma_{3D} = 12.19(90)\,\text{meV}. \tag{6.24}$$

Applying the convolution fit method as introduced for the iron measurements to account for instrumental profile asymmetries was unfeasible since the background during the nickel measurements was not as stable as for iron. The individual natural linewidths of 3C and 3D were calculated using equations 6.21 and 6.22

$$\Gamma_{3C} = 19.94(161)\,\text{meV}, \Gamma_{3D} = 7.75(62)\,\text{meV}.$$

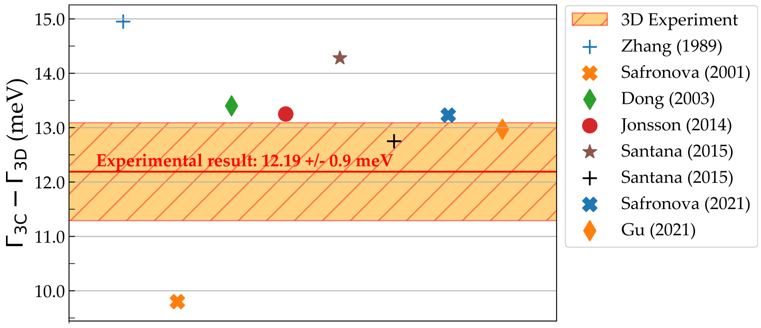

FIGURE 6.15: Comparison of the experimentally obtained natural linewidth difference of 3C and 3D in Ni XIX in this work with available theories listed in table 6.9.

Comparison with other experiments and theories

In this section the natural linewidth difference Γ_{3C-3D} of 3C and 3D in Ni XIX as well as the individual linewidths Γ_{3C} and Γ_{3D} will be put in context of available theoretical predictions, see also figure 6.15 and table 6.9. It is noticeable that the work of Zhang et al. [169] based on a distorted wave approach resulted in a natural linewidth difference that significantly departs from the experimental value by more than 4σ. Further, it is interesting to note that calculations performed by Safronova et al. in 2001 [140] resulted in a natural linewidth difference that is significantly below the experimental value. Linewidth difference values closest to the experimental reference were achieved by newest state-of-the-art calculations performed with CI and MBPT approaches performed by Gu et al., Safronova et al. (2021), and Santana et al., which only deviate by approximately 1σ.

If comparing the predicted linewidths of 3D among theories, it is evident that all available calculations result in a 3D linewidth between 7.27 and 7.96 and are in excellent agreement with the experimental work. However, the two theories of Zhang et al. and Safronova et al. (2001) for which the predicted linewidth difference departed from the experimental result show a significantly larger and lower natural linewidth for 3C, respectively. If comparing the linewidth of 3C between experiment and theory a solid agreement for most of the theories is found. Natural linewidth calculations performed by Safronova et al. (2021) and Gu et al. are in excellent agreement with the experiment and deviate by less than 0.5σ.

TABLE 6.9: Comparison of the 3C/3D intensity ratio between this work and theoretical predictions. Additionally, the employed method of each calculation is given: DW - distorted wave, MBPT - many body perturbation theory, MCDF - multi-configuration Dirac Fock, CI - configuration interaction. All linewidths and linewidth differences are given in meV FWHM.

Source	**Method**	Γ_{3C-3D}	Γ_{3C}	Γ_{3D}
This work	EBIT	12.19(90)	19.94(161)	7.75(62)
Zhang (1989) [169]	DW	15.38	22.65	7.27
Safronova (2001) [140]	MBPT	9.80	17.51	7.71
Dong (2003) [51]	MCDF	13.40	21.36	7.96
Jönsson (2014) [89]	CI	13.25	20.81	7.56
Santana (2015) [141]	CI	14.28	22.08	7.80
Santana (2015) [141]	MBPT	13.23	20.80	7.57
Safronova (2021) [36, 37]	CI	13.23	20.80	7.57
Gu (2021) [64]	CI	12.97	20.55	7.58

Chapter 7

Conclusion & outlook

Within the scope of this thesis, the emission behaviors of the resonance line 3C and the intercombination line 3D of Fe XVII which are among the strongest soft X-ray lines observed in many astrophysical sources were investigated. For this reason, a transportable room-temperature EBIT, dedicated to the research of the resonant interaction of highly charged ions and X-ray photons, was developed and successfully commissioned within this work. The EBIT, built at the Max Planck Institute for Nuclear Physics in Heidelberg, was transported to the synchrotron facility PETRA III located in Hamburg and attached to the soft X-ray photon beamline P04.

Due to the prominence of the two aforementioned lines 3C and 3D, it was proposed to employ the intensities observed in astrophysical spectra as a diagnostic tool to probe, for example, the plasma density or opacity of the respective emission source. However, the diagnostic utility was hampered by a persistent disagreement of the 3C/3D intensity ratio between models and laboratory measurements as well as astrophysical observations since 1974.

First laboratory results were gained by analyzing the emission spectra of electron-impact excited plasmas confined in an EBIT acquired by grating spectrometers. However, those measurements were most likely influenced by an at that moment unknown contamination by the unresolved strong line C of Fe XVI and by different electron-impact excitation cross sections for 3C and 3D, respectively. Therefore, first laser spectroscopy measurements, which were independent of collisional cross sections and probe individual transitions, were conducted by means of a free electron laser (FEL). The result of these measurements once again confirmed the discrepancy between experiments and models. Subsequently, systematical effects induced by insufficient spectral resolution and a high peak flux of the FEL lowering the observed ratio were proposed. Hence, new high-precision measurements were urgently needed to solve this astrophysical puzzle.

In this work, the 3C/3D oscillator-strength ratio of Fe XVII was remeasured three times. An excellent resolving power paired with a by orders of magnitude attenuated peak photon flux excluded the aforementioned systematical effects that could have affected the FEL measurements. The first measurement campaign conducted within this work resulted in a ratio that was in excellent agreement with previous experimental references and therefore exacerbated the long-lasting discrepancy [96]. This hinted towards serious problems even in newest state-of-the-art calculations, including more than one million configurations, which failed to properly model systems that contain only ten electrons in exclusively closed shells.

In order to further investigate this deepened controversy, two additional measurement campaigns were carried out to measure the individual linewidths of 3C and 3D which are directly proportional to the Einstein coefficients. In contrast to the intensity ratio, the individual linewidths provide much more stringent tests and allow to identify whether the strengths of 3C, 3D or both lines were insufficiently predicted by theory. To measure the natural linewidths, a significant increase in resolving power compared to the first campaign was required. By using a novel measurement scheme, an improvement in resolving power by a factor of almost three and an approximately 1000-fold better signal-to-noise ratio was achieved. Compared to the best available resolutions hitherto reported in measurements and observations, this resulted in an at least twenty-fold improvement. This allowed to model the fluorescence signal with Voigt profiles. Surprisingly, the second measurement campaign showed oscillator-strength values higher than previously reported. However, due to instabilities, the second campaign remained inconclusive. The last beamtime addressed the instabilities by an overhaul of the experimental setup and resulted in a relative statistical uncertainty well below 1%. The uncertainties of the results of this campaign were dominated by systematical effects introduced by energy interpolation errors of the monochromator, which increased the total uncertainty to approximately 2%. The measured 3C/3D oscillator-strength ratio significantly deviated from the results of the first measurement campaign of this thesis by approximately 15%.

The large ratio difference between the first and the last measurement campaign is most likely found in a systematical underestimation of the oscillator-strength ratio by using Gaussian profiles to model the data. The final result of this thesis based on the measurements of the most recent beamtime is in an excellent agreement with newest theories and seems to finally resolve the astrophysical enigma.

The individual widths of the lines which were the primary aim of the second and third campaign were found to be disturbed by an Lorentzian shaped contamination induced by the instrumental energy profile of the monochromator. Hence, a precise determination of individual oscillator strengths of 3C and 3D was unfeasible. However, under the assumption of a constant instrumental profile, the difference of the natural linewidth of 3C and 3D was extracted using Voigt fits. Additionally, the instrumental profile also exhibited a slight asymmetry. Therefore, a second approach was introduced which determined the linewidth difference independently of the shape of the instrumental profile. Since the two methods resulted in contradicting values for the obtained linewidth difference, it was ambiguous which approach was more accurate. Therefore, the final value for the natural linewidth difference covers the range of both approaches resulting in a large relative uncertainty of 16%.

The obtained linewidth difference is in excellent agreement with state-of-the-art calculations. By combining the measured natural linewidth difference and oscillator-strength ratio, the individual linewidths were inferred, which also agree with newest theoretical work.

Apart from 3C and 3D of Fe XVII, further transitions such as 4C and 4D of the same system as well as 3C and 3D of nickel and krypton were investigated. The observed intensity ratio of 4C and 4D showed a 1-σ agreement with theories. Unfortunately, the data for krypton were corrupted and hence disregarded but nevertheless showed the feasibility of measuring significantly heavier elements than iron using the setup presented.

The results of the nickel measurements allowed to scrutinize the oscillator-strength ratio as well as individual linewidths of a system that is certainly not affected by possible perturbations by the adjacent line C. A persistent disagreement of the 3C/3D oscillator-strength ratio in iron, while observing an agreement in nickel could have hinted towards disturbing effects due to line C in the iron measurements. However, since the measured ratio in iron is in agreement with calculations, the nickel measurement served as a supplemental testbed for benchmarking the oscillator-strength ratio as a function of the nuclear charge Z. The obtained ratio in nickel deviate from state-of-the-art theories by up to 2σ. The larger deviation could originate in an underestimated systematical uncertainty caused by the monochromator energy interpolation error. The estimation of this error was based on measurements in the energy regime of 3C and 3D of iron and was extrapolated to the range of nickel which is approximately 20% higher.

The measurements conducted within the scope of this thesis significantly improved the laboratory reference data exhibiting an outstanding quality for the prominent 3C/3D oscillator-strength ratios of iron and nickel and provided first results on the individual linewidths and therefore Einstein coefficients. The obtained value of the 3C/3D oscillator-strength ratio of Fe XVII is in excellent agreement with state-of-the-art calculations and finally closes the gap between experiments and theories that was persistent for almost 50 years. Additionally, the result support several hypotheses that earlier EBIT measurements based on electron-impact excitation were falsified by varying cross sections and that previous laser spectroscopy measurements were indeed affected by non-linear effects and population transfers due to high peak photon flux and insufficient resolving power. With the new results obtained in this work, the proposed diagnostic utility of the 3C/3D intensity ratio is now able to take full effect.

It should be emphasized that Fe XVII is one of the most intensively studied multi-electron ion, both experimentally as well as theoretically. As stated in the introduction of this thesis, it is impossible to fill a comprehensive reference database with experimental values due to the amount of available systems to the same extent as for

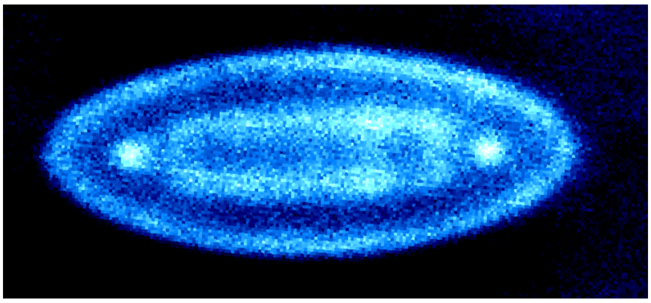

FIGURE 7.1: Picture of laser cooled Be^{+} ions confined in a Paul trap. Below a certain temperature a Coulomb crystal is formed by the Be^{+} ions. In such a crystal, highly charged ions produced in an EBIT can be re-trapped and sympathetically cooled from MK to mK temperatures. Figure adopted from [153]

Fe XVII. Hence, the findings of this work are particularly important for the calculation of other systems than Fe XVII using theories that have been successfully benchmarked. However, larger deviations of the 3C/3D oscillator-strength ratio of nickel between the present work and theories as well as large uncertainties of the linewidth results call for further investigations. Since the statistical uncertainties are on the per mill level, improvements of the systematical uncertainties are required. Hence, future measurements need accurate determinations of the actual monochromator energies, e.g., by means of a photoelectron or electron time-of-flight spectrometer in parallel to the experiment. In principle, this will reduce the remaining uncertainties of linewidth determinations by at least one order of magnitude. Additionally, this would also enable accurate measurements of transition energies, urgently needed for red and blue shift corrections in astrophysical spectra, which could be improved by one to two orders of magnitude compared to current literature values.

The measurement principle in this work was based on the simultaneous production and storage of the ion species of interest in an EBIT. Due to the continuous collisions of the ions with the electrons, the plasma exhibited a rather high temperature. The resulting Doppler broadening played a significant role in the instrument profile of the experimental setup. In order to reduce the ion temperature in future experiments, the ions could be produced in an EBIT, extracted and decelerated by means of an ion extraction beamline. Subsequently, the ions could be re-trapped in a so-called Paul trap, in which Be^{+} ions are laser cooled such that a Coulomb crystal is formed, see figure 7.1. By sympathetic cooling, the temperature of the re-trapped highly charged ions could be reduced from the MK in the EBIT to the mK regime in the Paul trap. This cooling principle has been successfully demonstrated for Ar^{13+} ions [118, 143, 153].

While this extension of the experimental setup with a cryogenic Paul trap would significantly reduce the temperature of the target and the resulting Doppler broadening, it is also necessary to improve the monochromaticity of the synchrotron laser. Here, it would be conceivable to employ a grating with 3600 lines/mm instead of the commonly used 1200 lines/mm. However, the efficiency of such gratings is reduced. For this reason, an increased number of photons produced in the undulator would be favorable. This could be achieved, for example, during the conversion of the PETRA III storage ring to the next generation PETRA IV, which is scheduled for completion within this decade. It is planned, for example, to increase the electron beam current in the storage ring by a factor of two [134]. This would increase the effective photon flux by a factor of approximately four. In addition, a selection of beamlines of PETRA IV are planned to be equipped with two underlators. If this were the case for the soft X-ray beamline P04, the effective photon flux would be increased by almost an order of magnitude. Hence, the use of a higher resolution grating would be feasible.

Both, experimental development which will result in a reduced temperature of the ion target as well as the improvement of synchrotron light sources will substantially increase the data quality obtained from laser spectroscopy measurements on highly charged ions in the soft and hard X-ray regime. Resolving powers well above $E/\Delta E = 100000$ will allow to measure transition energies and strengths with a precision hitherto impossible.

The methods developed and the results achieved in this work are leading the way for future high-precision measurements of transitions in highly charged ions in the soft as well as hard X-ray energy regime. Only by such laboratory reference measurements, beneficial improvement of literature values can be established, which enable to benchmark atomic models and thus, substantially increase the scientific harvest of upcoming satellite missions such as XRISM and Athena that will demand a significant increase of reference data quality.

Appendix A

List of Publications of the Author

1. **S. Kühn**, C. Shah, J. R. Crespo López-Urrutia, K. Fujii, R. Steinbrügge, J. Stierhof, M. Togawa, Z. Harman, N. S. Oreshkina, C. Cheung, M. G. Kozlov, . G. Porsev, M. S. Safronova, J. C. Berengut, M. Rosner, M. Bissinger, R. Ballhausen, N. Hell, S. Park, M. Chung, M. Hoesch, J. Seltmann, A. S. Surzhykov, V. A. Yerokhin, J. Wilms, F. S. Porter, T. Stöhlker, C. H. Keitel, T. Pfeifer, G. V. Brown, M. A. Leutenegger, and S. Bernitt. „High Resolution Photoexcitation Measurements Exacerbate the Long-Standing Fe XVII Oscillator Strength Problem“. In *Physical Review Letters*, 2020.
   Editors' Suggestion. Featured in the online magazine *Physics* of the American Physical Society.
   `https://doi.org/10.1103/PhysRevLett.124.225001`

2. M. A. Leutenegger, **S. Kühn**, P. Micke, R. Steinbrügge, J. Stierhof, C. Shah, N. Hell, M. Bissinger, M. Hirsch, R. Ballhausen, M. Lang, C. Gräfe, S. Wipf, R. Cumbee, G. L. Betancourt-Martinez, S. Park, V. A. Yerokhin, A. Surzhykov, W. C. Stolte, J. Niskansen, M. Chung, F. S. Porter, T. Stöhlker, T. Pfeifer, J. Wilms, G. V. Brown, J. R. Crespo López-Urrutia, and S. Bernitt. „High-Precision Determination of Oxygen K_α Transition Energy Excludes Incongruent Motion of Interstellar Oxygen“. In *Physical Review Letters*, 2020.
   `https://doi.org/10.1103/PhysRevLett.125.243001`

3. M. Togawa, **S. Kühn**, C. Shah, P. Amaro, R. Steinbrügge, J. Stierhof, N. Hell, M. Rosner, K. Fujii, M. Bissinger, R. Ballhausen, M. Hoesch, J. Seltmann, S. Park, F. Grilo, F. S. Porter, J. P. Santos, M. Chung, T. Stöhlker, J. Wilms, T. Pfeifer, G. V. Brown, M. A. Leutenegger, S. Bernitt, and J. R. Crespo López-Urrutia „Observation of strong two-electron–one-photon transitions in few-electron ions“. In *Physical Review A*, 2020.
   `https://doi.org/10.1103/PhysRevA.102.052831`

4. P. Micke, **S. Kühn**, L. Buchauer, J. R. Harries, T. M. Bücking, K. Blaum, A. Cieluch, A. Egl, D. Hollain, S. Kraemer, T. Pfeifer, P. O. Schmidt, R. X. Schüssler, Ch. Schweiger, T. Stöhlker, S. Sturm, R. N. Wolf, S. Bernitt, and J. R. Crespo López-Urrutia „The Heidelberg compact electron beam ion traps“. In *Review*

of Scientific Instruments, 2018. Featured.
https://doi.org/10.1063/1.5026961

5. F. Grilo, C. Shah, **S. Kühn**, R. Steinbrügge, K. Fujii, J. Marques, M. F. Gu, J. P. Santos, J. R. Crespo López-Urrutia, and P. Amaro. „Comprehensive laboratory measurements resolving the LMM dielectronic recombination satellite lines in Ne-like Fe XVII ions“. Accepted in *The Astrophysical Journal*, 2020.

6. J. Stark, C. Warnecke, S. Bogen, S. Chen, E. A. Dijck, **S. Kühn**, M. K. Rosner, A. Graf, J. Nauta, J.-H. Oelmann, L. Schmöger, M. Schwarz, D. Liebert, L. J. Spieß, S. A. King, T. Leopold, P. Micke, P. O. Schmidt, T. Pfeifer, J. R. Crespo López-Urrutia „An ultralow-noise superconducting radio-frequency ion trap for frequency metrology with highly charged ions“. Submitted to *Review of Scientific Instruments*, 2021.
https://arxiv.org/abs/2102.02793

7. G. Brenner, S. Bernitt, S. Dobrodey, R. Steinbrügge, M. Blessenohl, A. Cieluch, Z. Hockenbery, **S. Kühn**, J. Nauta, M.-A. Sanchez, S. W. Epp, and J. R. Crespo López-Urrutia „Benchmarking quantum-electrodynamic calculations in lithiumlike Kr^{33+} ions by soft-x-ray laser spectroscopy“. Submitted to *Physical Review A*, 2019.

8. **S. Kühn**, et al. „Lifetime measurements of the prominent transitions 3C and 3D of Fe XVII resolve the long-lasting oscillator-strength conundrum “. *In preparation*, 2021.

9. M. Togawa, et al. „High-resolution measurements of Auger decays in Fe XIV ions“. *In preparation*, 2021.

10. R. Steinbrügge, **S. Kühn**, et al. „Resonant photo excitation of metastable states in boron-like neon and iron“. *In preparation*, 2021.

Bibliography

[1] Pierre Agostini et al. “Free-free transitions following six-photon ionization of xenon atoms”. In: *Physical Review Letters* 42.17 (1979), p. 1127. DOI: `10.1103/PhysRevLett.42.1127`.

[2] E. D. Donets et al. “Ultrahigh vacuum electron beam source of highly stripped ions”. In: *Premiere Conference Internationale sur les Sources d'Ions* (1970).

[3] R. de Andrade Martins and C.C. Silva. “Newton and colour: the complex interplay of theory and experiment”. In: *Science Education and Culture*. Springer, 2001, pp. 273–291. DOI: `https://doi.org/10.1007/978-94-010-0730-6_18`.

[4] L.A. Artsimovich. “Tokamak devices”. In: *Nuclear Fusion* 12.2 (1972), p. 215.

[5] J. Bahrdt et al. “Apple undulator for PETRA III”. In: *Proc. EPAC08* 2219 (2008).

[6] D. Baker. *"Galileo Galilei: Views of the universe"*. Viewed on 12.04.2021. URL: `http://sitemaps.bighistoryschool.org/wp/wp-content/uploads/2018/07/1.2.3-Galileo-900L.pdf`.

[7] V. Balashov, A.N. Grum-Grzhimailo, and N.M. Kabachnik. *Polarization and correlation phenomena in atomic collisions: a practical theory course*. Springer Science & Business Media, 2013. DOI: `10.1007/978-1-4757-3228-3`.

[8] E. Behar, J. Cottam, and S. Kahn. “The Chandra iron-L X-ray line spectrum of Capella”. In: *The Astrophysical Journal* 548.2 (2001), p. 966. DOI: `10.1086/318999`.

[9] P. Beiersdorfer et al. “Laboratory measurements of the Fe XVII 2p-3s and 2p-3d transitions and comparison with solar and astrophysical observations”. In: *The Astrophysical Journal* 610.1 (2004), p. 616. DOI: `10.1086/421512`.

[10] P. Beiersdorfer et al. “Laboratory Measurements of the Relative Intensity of the 3s→2p and 3d→2p Transitions in Fe XVII”. In: *The Astrophysical Journal Letters* 576.2 (2002), p. L169. DOI: `10.1086/343785`.

[11] P. Beiersdorfer et al. “Measurement of the 3 d→ 2 p resonance to intercombination line-intensity ratio in neonlike Fe XVII, Ge XXIII, and Se XXV”. In: *Physical Review A* 64.3 (2001), p. 032705. DOI: `10.1103/PhysRevA.64.032705`.

[12] P Beiersdorfer et al. “X-ray emission following low-energy charge exchange collisions of highly charged ions”. In: *Physical Review Letters* 85.24 (2000), p. 5090. DOI: `10.1103/PhysRevLett.85.5090`.

[13] S. Bernitt. “Optimierung der Ladungszustandsverteilung in einer EBIT durch resonante Photorekombination”. In: *Universität Heidelberg & Max-Planck-Institut für Kernphysik, Diplomarbeit* (2009).

[14] S. Bernitt. “Resonante Anregung astrophysikalischer Röntgen-Übergänge in hochgeladenen Eisenionen mit dem Freie-Elektronen-Laser LCLS”. PhD thesis. 2013.

[15] S. Bernitt et al. “An unexpectedly low oscillator strength as the origin of the Fe XVII emission problem”. In: *Nature* 492.7428 (2012), pp. 225–228. DOI: `10.1038/nature11627`.

[16] A. Bharti and N. Goyal. “Fundamental of Synchrotron Radiations”. In: *Synchrotron Radiation-Useful and Interesting Applications*. IntechOpen, 2019.

[17] A.K. Bhatia and G.A. Doschek. “Atomic data and spectral line intensities for Ne-like Fe XVII”. In: *Atomic Data and Nuclear Data Tables* 52.1 (1992), pp. 1–23. ISSN: 0092-640X. DOI: `https://doi.org/10.1016/0092-640X(92)90007-5`.

[18] R.L. Blake et al. “Spectral and photometric measurements of solar X-ray emission below 60 Å”. In: *The Astrophysical Journal* 142 (1965), p. 1. DOI: `10.1086/148258`.

[19] M. Blessenohl et al. “An electron beam ion trap and source for re-acceleration of rare-isotope ion beams at TRIUMF”. In: *Review of Scientific Instruments* 89.5 (2018), p. 052401. DOI: `10.1063/1.5021045`.

[20] C. F. Bradshaw, E. B. Fomalont, and B. J. Geldzahler. “High-Resolution Parallax Measurements of Scorpius X-1”. In: *The Astrophysical Journal* 512.2 (1999), pp. L121–L124. DOI: `10.1086/311889`.

[21] N.S. Brickhouse et al. “Coronal structure and abundances of Capella from simultaneous EUVE and ASCA spectroscopy”. In: *The Astrophysical Journal* 530.1 (2000), p. 387. DOI: `10.1086/308350`.

[22] A.C. Brinkman et al. “First light measurements with the XMM-Newton reflection grating spectrometers: Evidence for an inverse first ionisation potential effect and anomalous Ne abundance in the Coronae of HR 1099”. In: *Astronomy & Astrophysics* 365.1 (2001), pp. L324–L328. DOI: `10.1051/0004-6361:20000047`.

[23] G.V. Brown. “A brief review of the intensity of lines 3C and 3D in neon-like Fe XVII”. In: *Canadian Journal of Physics* 86.1 (2008), pp. 199–208. DOI: `10.1139/p07-158`.

[24] G.V. Brown, P. Beiersdorfer, and K. Widmann. “Systematic measurement of the relative electron-impact excitation cross section of the 3 d→ 2 p 1 P 1 resonance and 3 D 1 intercombination lines in mid-Z neonlike ions”. In: *Physical Review A* 63.3 (2001), p. 032719. DOI: `10.1103/PhysRevA.63.032719`.

[25] G.V. Brown et al. "Diagnostic utility of the relative intensity of 3C to 3D in Fe XVII". In: *The Astrophysical Journal Letters* 557.1 (2001), p. L75. DOI: `10.1086/323004`.

[26] G.V. Brown et al. "Energy-dependent excitation cross section measurements of the diagnostic lines of Fe XVII". In: *Physical review letters* 96.25 (2006), p. 253201. DOI: `10.1103/PhysRevLett.96.253201`.

[27] G.V. Brown et al. "Laboratory measurements and modeling of the Fe XVII X-ray spectrum". In: *The Astrophysical Journal* 502.2 (1998), p. 1015. DOI: `10.1086/305941`.

[28] J. Buck. *Performance of the variable polarization XUV beamline P04: Benchmarking and studies on stability*. 2017.

[29] J. Buck. *Personal Communication*. 2021.

[30] B Bulbul, M Sezer, and W Greiner. *Relativistic Quantum Mechanics—Wave Equations*. 2000. DOI: `10.1007/978-3-662-04275-5`.

[31] M. Carrier. *Nikolaus Kopernikus*. Vol. 558. CH Beck, 2001.

[32] G.X. Chen. "Converged dirac R-matrix calculation of electron impact excitation of Fe XVII". In: *Physical Review A* 76.6 (2007), p. 062708. DOI: `10.1103/PhysRevA.76.062708`.

[33] G.X. Chen. "X-ray line ratio 3C/3D in Fe XVII". In: *Monthly Notices of the Royal Astronomical Society: Letters* 386.1 (2008), pp. L62–L66. DOI: `10.1111/j.1745-3933.2008.00461.x`.

[34] G.X. Chen and A.K. Pradhan. "Influence of resonances on spectral formation of X-ray lines in Fe XVII". In: *Physical review letters* 89.1 (2002), p. 013202. DOI: `10.1103/PhysRevLett.89.013202`.

[35] GX Chen et al. "Reply to "Comment on 'Dirac R-matrix method for the calculation of x-ray line polarization'"". In: *Physical Review A* 82.3 (2010), p. 036702. DOI: `10.1103/PhysRevA.82.036702`.

[36] C. Cheung, M. Safronova, and M.G. Kozlov. *"Calculations of the 3C/3D and 4C/4D oscillator-strength ratios of Fe16+ and Ni18+"*. 2021.

[37] Charles Cheung, Marianna Safronova, and Sergey Porsev. "Scalable codes for precision calculations of properties of complex atomic systems". In: *Symmetry* 13.4 (2021), p. 621.

[38] A. Cieluch. "Aufbau und Charakterisierung der permanenten Magnetsysteme zweier kompakter Elektronenstrahl-Ionenfallen". In: *Bachelor thesis. Ruprecht-Karls-Universität Heidelberg* (2016).

[39] K Codling. "Applications of synchrotron radiation (ultraviolet spectral light source)". In: *Reports on Progress in Physics* 36.5 (1973), p. 541. DOI: `10.1088/0034-4885/36/5/002`.

[40] M. Cornille, Jacques Dubau, and Sylvie Jacquemot. "Radiative and collisional atomic data for neon-like ions". In: *Atomic data and nuclear data tables* 58.1 (1994), pp. 1–66. DOI: 10.1006/adnd.1994.1022.

[41] J.L. Cronin. *Practical aspects of modern dispenser cathodes*. 1979.

[42] C. Curceanu et al. "X-ray Detectors for Kaonic Atoms Research at DAΦNE". In: *Condensed Matter* 4.2 (2019), p. 42. DOI: 10.3390/condmat4020042.

[43] A. Danilenko. "Alignment correction for plane grating monochromator using the cff parameter". In: *Bachelor thesis. School of Physics and Astronomy, University of St Andrews, Scotland* (2017).

[44] D. Deacon et al. "First operation of a free-electron laser". In: *Physical Review Letters* 38.16 (1977), p. 892. DOI: 10.1103/PhysRevLett.38.892.

[45] W. Demtröder. *Experimentalphysik 3: Atome, Moleküle und Festkörper*. Springer-Verlag, 2016. DOI: 10.1007/978-3-662-49094-5.

[46] W. Demtröder. *Laser spectroscopy: basic concepts and instrumentation*. Springer Science & Business Media, 2013. DOI: 10.1007/978-3-540-73418-5.

[47] Z. Deng and J. H. Eberly. "Multiphoton absorption above ionization threshold by atoms in strong laser fields". In: *J. Opt. Soc. Am. B* 2.3 (1985), pp. 486–493. DOI: 10.1364/JOSAB.2.000486.

[48] *Deutsches Museum: Der Geheimcode der Sterne*. Viewed on 24.02.2021. URL: https://www.deutsches-museum.de/presse/pressearchiv/presse-2017/fraunhofer-linien/.

[49] F. Díaz et al. "High-accuracy MR-MP perturbation theory energy and radiative rates calculations for core-excited transitions in Fe XVI". In: *The Astrophysical Journal Supplement Series* 207.1 (2013), p. 11. DOI: 10.1088/0067-0049/207/1/11.

[50] S. Dobrodey. "Charge-exchange studies of bare and hydrogen-like low-Z ions in the X-ray and extreme-ultraviolet ranges inside an electron beam ion trap". PhD thesis. 2019.

[51] C.Z. Dong et al. "A theoretical study of the 3d–2p resonance to intercombination line-intensity ratio in mid-Z Ne-like ions". In: *Nuclear Instruments and Methods in Physics Research Section B: Beam Interactions with Materials and Atoms* 205 (2003), pp. 87–92. DOI: 10.1016/S0168-583X(02)01982-1.

[52] P. Emma and LCLS Commissioning Team. "First lasing of the LCLS X-ray FEL at 1.5 Å". In: *Proceedings of PAC09, Vancouver, to be published in http://accelconf. web. cern. ch/AccelConf* (2009).

[53] S.W. Epp et al. "Soft X-ray laser spectroscopy on trapped highly charged ions at FLASH". In: *Physical review letters* 98.18 (2007), p. 183001. DOI: 10.1103/PhysRevLett.98.183001.

[54] Synchrotron Soleil EPSIM 3D/JF Santarelli. *Scheme of synchrotron principle*. 2021. URL: `https://commons.wikimedia.org/wiki/File:Sch%C3%A9ma_de_principe_du_synchrotron.jpg`.

[55] *Fast ComTec GmbH MPA4*. Viewed on 05.08.2020. URL: `https://www.fastcomtec.com/mpa4`.

[56] R. Follath. *Resolving power at the diffraction limit*. 1998.

[57] Harald Friedrich. *Theoretische Atomphysik*. Springer-Verlag, 2013.

[58] E. Gatti and P. Rehak. "Semiconductor drift chamber—An application of a novel charge transport scheme". In: *Nuclear Instruments and Methods in Physics Research* 225.3 (1984), pp. 608–614. DOI: `10.1016/0167-5087(84)90113-3`.

[59] J.D. Gillaspy. "Highly charged ions". In: *Journal of Physics B: Atomic, Molecular and Optical Physics* 34.19 (2001), R93. DOI: `10.1088/0953-4075/34/19/201`.

[60] J.D. Gillaspy et al. "Fe XVII X-ray line ratios for accurate astrophysical plasma diagnostics". In: *The Astrophysical Journal* 728.2 (2011), p. 132. DOI: `10.1088/0004-637X/728/2/132`.

[61] O. Gingerich. "From Copernicus to Kepler: Heliocentrism as model and as reality". In: *Proceedings of the American Philosophical Society* 117.6 (1973), pp. 513–522.

[62] I. P. Grant and N.C. Pyper. "Breit interaction in multi-configuration relativistic atomic calculations". In: *Journal of Physics B: Atomic and Molecular Physics* 9.5 (1976), p. 761. DOI: `10.1088/0022-3700/9/5/019`.

[63] F. Grilo. "High-temperature plasmas of interest to astrophysics and fusion reactors". PhD thesis. 2020.

[64] M. F. Gu. *Calculations of the 3C/3D and 4C/4D oscillator-strength ratios of Fe16+ and Ni18+*. 2021.

[65] M. F. Gu. "The flexible atomic code". In: *Canadian Journal of Physics* 86.5 (2008), pp. 675–689. DOI: `10.1139/p07-197`.

[66] M.F Gu. "New benchmark of X-ray line emission models of Fe XVII". In: *arXiv preprint arXiv:0905.0519* (2009).

[67] M.F. Gu et al. "Inner-shell absorption lines of Fe VI-Fe XVI: A many-body perturbation theory approach". In: *The Astrophysical Journal* 641.2 (2006), p. 1227. DOI: `10.1086/500640`.

[68] M.F. Gu et al. "Laboratory measurements of 3→2 X-ray emission lines of Ne-like Ni XIX". In: *The Astrophysical Journal Letters* 607.2 (2004), p. L143. DOI: `10.1086/421975`.

[69] D. Habs et al. "First experiments with the Heidelberg test storage ring TSR". In: *Nuclear Instruments and Methods in Physics Research Section B: Beam Interactions with Materials and Atoms* 43.3 (1989), pp. 390–410. DOI: `10.1016/0168-583X(89)90383-2`.

[70] H.. Haken and Hans Christoph Wolf. *Atom-und Quantenphysik: eine Einführung in die experimentellen und theoretischen Grundlagen*. Springer-Verlag, 1987.

[71] D.E. Harris and D. Irwin. *Einstein Observatory Revised User's Manual*. Harvard-Smithsonian Center for Astrophysics, 1984.

[72] D.R. Hartree. "The wave mechanics of an atom with a non-Coulomb central field. Part I. Theory and methods". In: (1928). DOI: `10.1017/S0305004100011919`.

[73] *Heidenhain: Angle Encoders with Integral Bearing*. Viewed on 10.03.2021. URL: `https://www.heidenhain.de/fileadmin/pdb/media/img/591109-24_Angle_Encoders_with_Integral_Bearing.pdf`.

[74] B.L. Henke, Eric M Gullikson, and John C Davis. "X-ray interactions: photoabsorption, scattering, transmission, and reflection at E= 50-30,000 eV, Z= 1-92". In: *Atomic data and nuclear data tables* 54.2 (1993), pp. 181–342. DOI: `10.1006/adnd.1993.1013`.

[75] G. Herrmann. "Optical theory of thermal velocity effects in cylindrical electron beams". In: *Journal of Applied Physics* 29.2 (1958), pp. 127–136. DOI: `10.1063/1.1723053`.

[76] R. Hilborn. "Einstein coefficients, cross sections, f values, dipole moments, and all that". In: *American Journal of Physics* 50.11 (1982), pp. 982–986. DOI: `10.1119/1.12937`.

[77] D. Hoffmann. "100 Jahre Quantenphysik: Schwarze Körper im Labor: Experimentelle Vorleistungen für Plancks Quantenhypothese". In: *Physikalische Blätter* 56.12 (2000), pp. 43–47. DOI: `10.1002/phbl.20000561215`.

[78] K. Hübner. "Gustav Robert Kirchhoff". In: *Das gewöhnliche Leben eines außergewöhnlichen Mannes. Schriften, Archiv und Museum der Universität Heidelberg* 16 (2010).

[79] D.P. Huenemoerder et al. "TGCat*: THE CHANDRA TRANSMISSION GRATING DATA CATALOG AND ARCHIVE". In: *The Astronomical Journal* 141.4 (2011), p. 129. DOI: `10.1088/0004-6256/141/4/129`.

[80] HeatWave Labs Inc. *Notes on Dispenser and Oxide Cathodes*. 1999.

[81] Spectra-Mat Inc. *Technical Bulletin: Emission Characteristics — Dispenser Cathodes*. 2014.

[82] Spectra-Mat Inc. *Technical Bulletin: Handling and Care of Cathodes*. 2014.

[83] Spectra-Mat Inc. *Technical Bulletin: HEATER POWER SUPPLY RECOMMENDATIONS A.C. or D.C?* 2014.

[84] Spectra-Mat Inc. *Technical Bulleting: Guidelines for Processing of Dispenser Cathodes*. 2014.

[85] D Iwanenko and I Pomeranchuk. "On the maximal energy attainable in a betatron". In: *Physical Review* 65.11-12 (1944), p. 343. DOI: `10.1103/PhysRev.65.343`.

[86] N. Jagoda and W.D. Antrim Jr. "An evolution of X-ray astronomy instrumentation." In: *Journal of the British Interplanetary Society* 28 (1975), pp. 299–318.

[87] F. Jansen et al. "XMM-Newton observatory-I. The spacecraft and operations". In: *Astronomy & Astrophysics* 365.1 (2001), pp. L1–L6. DOI: `10.1051/0004-6361:20000036`.

[88] R Jiang Y.H .and Püttner et al. "Isotope shifts of double-excitation resonances in helium". In: *Physical Review A* 69.5 (2004), p. 052703. DOI: `10.1103/PhysRevA.69.052703`.

[89] P. Jönsson et al. "Relativistic CI calculations of spectroscopic data for the 2p6 and 2p53l configurations in Ne-like ions between Mg III and Kr XXVII". In: *Atomic Data and Nuclear Data Tables* 100.1 (2014), pp. 1–154. DOI: `10.1016/j.adt.2013.06.001`.

[90] J. Kaastra and F. Paerels. *High-resolution X-Ray Spectroscopy: Past, Present, and Future*. Springer New York, 2011.

[91] J.S. Kaastra, R. Mewe, and H. Nieuwenhuijzen. "SPEX: a new code for spectral analysis of X & UV spectra." In: *UV and X-ray Spectroscopy of Astrophysical and Laboratory Plasmas* (1996), pp. 411–414.

[92] Y.S. Kim and R.H. Pratt. "Direct radiative recombination of electrons with atomic ions: Cross sections and rate coefficients". In: *Physical Review A* 27.6 (1983), p. 2913. DOI: `10.1103/PhysRevA.27.2913`.

[93] G. Kirchhoff and R. Bunsen. "XLII. Chemical analysis by spectrum-observations.—Second memoir". In: *The London, Edinburgh, and Dublin Philosophical Magazine and Journal of Science* 22.148 (1861), pp. 329–349.

[94] P. Kirkpatrick and A. V. Baez. "Formation of optical images by X-rays". In: *JOSA* 38.9 (1948), pp. 766–774. DOI: `10.1364/JOSA.38.000766`.

[95] S. Kühn. "Inbetriebnahme und Charakterisierung einer Elektronenkanone mit optischem Zugang zur Strahlachse in einer kompakten Elektronenstrahlionenfalle". In: *Master thesis. Ruprecht-Karls-Universität Heidelberg* (2017).

[96] S. Kühn et al. "High Resolution Photoexcitation Measurements Exacerbate the Long-Standing Fe XVII Oscillator Strength Problem". In: *Physical Review Letters* 124.22 (2020), p. 225001. DOI: `10.1103/PhysRevLett.124.225001`.

[97] E. Landi and M.F. Gu. "Atomic data for high-energy configurations in Fe XVII-XXIII". In: *The Astrophysical Journal* 640.2 (2006), p. 1171. DOI: `10.1086/500286`.

[98] J. Larmor. "On the radiation from moving ions". In: *Phil Mag* 44.503 (1897), p. 12.

[99] P. Lechner et al. “Silicon drift detectors for high count rate X-ray spectroscopy at room temperature”. In: *Nuclear Instruments and Methods in Physics Research Section A: Accelerators, Spectrometers, Detectors and Associated Equipment* 458.1-2 (2001), pp. 281–287. DOI: 10.1016/S0168-9002(00)00872-X.

[100] P. Lechner et al. “Silicon drift detectors for high resolution room temperature X-ray spectroscopy”. In: *Nuclear Instruments and Methods in Physics Research Section A: Accelerators, Spectrometers, Detectors and Associated Equipment* 377.2-3 (1996), pp. 346–351. DOI: 10.1016/0168-9002(96)00210-0.

[101] M. Leutenegger et al. “High-Precision Determination of Oxygen K_α Transition Energy Excludes Incongruent Motion of Interstellar Oxygen”. In: *Phys. Rev. Lett.* 125 (24 2020), p. 243001. DOI: 10.1103/PhysRevLett.125.243001.

[102] M. Levine et al. “The electron beam ion trap: A new instrument for atomic physics measurements”. In: *Physica Scripta* 1988.T22 (1988), p. 157. DOI: 10.1088/0031-8949/1988/T22/024.

[103] M.A. Levine et al. “The use of an electron beam ion trap in the study of highly charged ions”. In: *Nuclear Instruments and Methods in Physics Research Section B: Beam Interactions with Materials and Atoms* 43.3 (1989), pp. 431–440. DOI: 10.1016/0168-583X(89)90386-8.

[104] G.Y. Liang and N.R. Badnell. “R-matrix electron-impact excitation data for the Ne-like iso-electronic sequence”. In: *Astronomy & Astrophysics* 518 (2010), A64. DOI: 10.1051/0004-6361/201014170.

[105] A. Liénard. “Champ électrique et Magnétique”. In: *L’éclairage électrique* 16.27-29 (1898), pp. 5–14.

[106] S. D. Loch et al. “NON-EQUILIBRIUM MODELING OF THE FE XVII 3C/3D LINE RATIO IN AN INTENSE X-RAY FREE-ELECTRON LASER EXCITED PLASMA”. In: *The Astrophysical Journal* 801.1 (), p. L13. DOI: 10.1088/2041-8205/801/1/l13.

[107] S.D. Loch et al. “The effects of radiative cascades on the X-ray diagnostic lines of Fe16+”. In: *Journal of Physics B: Atomic, Molecular and Optical Physics* 39.1 (2005), p. 85. DOI: 10.1088/0953-4075/39/1/009.

[108] W. Lotz. “An empirical formula for the electron-impact ionization cross-section”. In: *Zeitschrift für Physik* 206.2 (1967), pp. 205–211. DOI: 10.1007/BF01325928.

[109] W. Lotz. “Electron-impact ionization cross-sections and ionization rate coefficients for atoms and ions from hydrogen to calcium”. In: *Zeitschrift für Physik* 216.3 (1968), pp. 241–247. DOI: 10.1007/BF01392963.

[110] M. Loulergue and H. Nussbaumer. “A study of Fe xvii and Ni xix coronal lines”. In: *Astronomy and Astrophysics* 45 (1975), pp. 125–134.

[111] A. Lutman et al. “Polarization control in an X-ray free-electron laser”. In: *Nature photonics* 10.7 (2016), pp. 468–472. DOI: 10.1038/nphoton.2016.79.

[112] V. Mäckel et al. “Laser spectroscopy on forbidden transitions in trapped highly charged Ar 13+ ions”. In: *Physical review letters* 107.14 (2011), p. 143002. DOI: `10.1103/PhysRevLett.107.143002`.

[113] *Magnet data sheet S-45-30-N*. Viewed on 18.03.2021. URL: `https://www.supermagnete.de/eng/data_sheet_S-45-30-N.pdf`.

[114] J.E. McClintock. “Marriage of X-ray and optical astronomy.” In: *Technology Review* 78 (1975), pp. 26–33.

[115] D.L. McKenzie et al. “Solar flare X-ray spectra between 7.8 and 23.0 Ångstroms”. In: *The Astrophysical Journal* 241 (1980), pp. 409–416. DOI: `10.1086/158354`.

[116] C Mendoza and MA Bautista. “Theoretical Confirmation of the Low Experimental 3 C/3 D f-Value Ratio in Fe xvii”. In: *Physical review letters* 118.16 (2017), p. 163002. DOI: `10.1103/PhysRevLett.118.163002`.

[117] R. Mewe et al. “CHANDRA-LETGS X-ray observations of Capella-Temperature, density and abundance diagnostics”. In: *Astronomy & Astrophysics* 368.3 (2001), pp. 888–900. DOI: `10.1051/0004-6361:20010026`.

[118] P Micke et al. “Coherent laser spectroscopy of highly charged ions using quantum logic”. In: *Nature* 578.7793 (2020), pp. 60–65.

[119] P. Micke et al. “The Heidelberg compact electron beam ion traps”. In: *Review of Scientific Instruments* 89.6 (2018), p. 063109. DOI: `10.1063/1.5026961`.

[120] S. Mobilio, F. Boscherini, and C. Meneghini. *Synchrotron Radiation*. Springer, 2016.

[121] Peter J Mohr, Günter Plunien, and Gerhard Soff. “QED corrections in heavy atoms”. In: *Physics Reports* 293.5-6 (1998), pp. 227–369.

[122] A. Müller et al. “Photoionization of Ne Atoms and Ne+ Ions Near the K Edge: Precision Spectroscopy and Absolute Cross-sections”. In: *The Astrophysical Journal* 836.2 (2017), p. 166. DOI: `10.3847/1538-4357/836/2/166`.

[123] J.U. Ness et al. “Are stellar coronae optically thin in X-rays? A systematic investigation of opacity effects”. In: *Astronomy & Astrophysics* 407.1 (2003), pp. 347–358. DOI: `10.1051/0004-6361:20030880`.

[124] F. Nicastro et al. “Observations of the missing baryons in the warm–hot intergalactic medium”. In: *Nature* 558.7710 (2018), pp. 406–409. DOI: `10.1038/s41586-018-0204-1`.

[125] N. Oreshkina et al. “Astrophysical Line Diagnosis Requires Nonlinear Dynamical Atomic Modeling”. In: *Phys. Rev. Lett.* 113 (14 2014), p. 143001. DOI: `10.1103/PhysRevLett.113.143001`.

[126] N. Oreshkina et al. “X-ray fluorescence spectrum of highly charged Fe ions driven by strong free-electron-laser fields”. In: *Journal of Physics B: Atomic, Molecular and Optical Physics* 49.9 (2016), p. 094003. DOI: `10.1088/0953-4075/49/9/094003`.

[127] *Ortec Spectroscopy Amplifier 672*. Viewed on 05.08.2020. URL: `https://www.ortec-online.com/products/electronics/amplifiers/672`.

[128] *P04 Variable Polarization XUV Beamline*. Viewed on 17.01.2021. URL: `https://photon-science.desy.de/facilities/petra_iii/beamlines/p04_xuv_beamline/cluster-03_eng.html`.

[129] F. Paerels and S. Kahn. "High-resolution x-ray spectroscopy with Chandra and XMM-Newton". In: *Annual Review of Astronomy and Astrophysics* 41.1 (2003), pp. 291–342. DOI: `10.1146/annurev.astro.41.071601.165952`.

[130] F. Pajot et al. "The Athena X-ray integral field unit (X-IFU)". In: *Journal of Low Temperature Physics* 193.5 (2018), pp. 901–907. DOI: `10.1117/12.2232432`.

[131] J.H. Parkinson. "New observations of Fe XVII in the solar X-ray spectrum". In: *Astronomy and Astrophysics* 24 (1973), p. 215.

[132] H. Petersen. "The plane grating and elliptical mirror: a new optical configuration for monochromators". In: *Optics Communications* 40.6 (1982), pp. 402–406. DOI: `10.1016/0030-4018(82)90040-2`.

[133] *PETRA III - Facility Information*. Viewed on 14.01.2021. URL: `https://photon-science.desy.de/facilities/petra_iii/facility_information/index_eng.html`.

[134] *Petra IV. Upgrade of PETRA III to the Ultimate 3D X-ray Microscope. Conceptual Design Report*. Viewed on 27.04.2021. URL: `https://bib-pubdb1.desy.de/record/426140/files/DESY-PETRAIV-Conceptual-Design-Report.pdf`.

[135] A. Pradhan and S. Nahar. *Atomic astrophysics and spectroscopy*. Cambridge University Press, 2011.

[136] R. Reininger and A. de Castro. "High resolution, large spectral range, in variable-included-angle soft X-ray monochromators using a plane VLS grating". In: *Nuclear Instruments and Methods in Physics Research Section A: Accelerators, Spectrometers, Detectors and Associated Equipment* 538.1-3 (2005), pp. 760–770. DOI: `10.1016/j.nima.2004.09.007`.

[137] K. Rosner. "Production and preparation of highly charged ions for re-trapping in ultra-cold environments". In: *Master thesis. Ruprecht-Karls-Universität Heidelberg* (2019).

[138] J. Rudolph et al. "X-ray resonant photoexcitation: Linewidths and energies of K α transitions in highly charged Fe ions". In: *Physical review letters* 111.10 (2013), p. 103002. DOI: `10.1103/PhysRevLett.111.103002`.

[139] Jan K Rudolph. "Fluoreszenzspektroskopie an K-Schalen-Übergängen hochgeladener Eisenionen". PhD thesis. Justus-Liebig-Universität Gießen, 2013.

[140] U.I. Safronova et al. "Electric-dipole, electric-quadrupole, magnetic-dipole, and magnetic-quadrupole transitions in the neon isoelectronic sequence". In: *Physical Review A* 64.1 (2001), p. 012507. DOI: `10.1103/PhysRevA.64.012507`.

[141] J. Santana et al. “Electron-correlation effects on the 3 C to 3 D line-intensity ratio in the Ne-like ions Ar 8+ to Kr 26+”. In: *Physical Review A* 91.1 (2015), p. 012502. DOI: `10.1103/PhysRevA.91.012502`.

[142] C. Schmitz-Antoniak. “X-ray absorption spectroscopy on magnetic nanoscale systems for modern applications”. In: *Reports on Progress in Physics* 78.6 (2015), p. 062501. DOI: `10.1088/0034-4885/78/6/062501`.

[143] L. Schmöger et al. “Coulomb crystallization of highly charged ions”. In: *Science* 347.6227 (2015), pp. 1233–1236.

[144] V. Schonfelder et al. “Instrument description and performance of the imaging gamma-ray telescope COMPTEL aboard the Compton Gamma-Ray Observatory”. In: *Astrophysical Journal Supplement Series* (1993). DOI: `10.1086/191794`.

[145] S. Schreiber and B. Faatz. “The free-electron laser FLASH”. In: *High Power Laser Science and Engineering* 3 (2015). DOI: `10.1017/hpl.2015.16`.

[146] H. Schulte-Schrepping et al. *Commissioning of the APPLE II undulator*. Tech. rep. Tech. Rep. 1, 2002.

[147] Ch. Schweiger et al. “Production of highly charged ions of rare species by laser-induced desorption inside an electron beam ion trap”. In: *Review of Scientific Instruments* 90.12 (2019), p. 123201. DOI: `10.1063/1.5128331`.

[148] N. Scoville et al. “COSMOS: Hubble space telescope observations”. In: *The Astrophysical Journal Supplement Series* 172.1 (2007), p. 38. DOI: `10.1086/516580`.

[149] C. Shah et al. “Revisiting the Fe xvii Line Emission Problem: Laboratory Measurements of the 3s–2p and 3d–2p Line-formation Channels”. In: *The Astrophysical Journal* 881.2 (2019), p. 100. DOI: `10.3847/1538-4357/ab2896`.

[150] C D. Sherrill and H. F. Schaefer. “The configuration interaction method: Advances in highly correlated approaches”. In: *Advances in quantum chemistry* 34 (1999), pp. 143–269. DOI: `10.1016/S0065-3276(08)60532-8`.

[151] Shevchuk, I. and Scholz, F. and Seltmann, J. and Glaser, L. and Deinert, S. *Focus Finder for Microfocus Characterization @ P04*. 2013.

[152] P. Söding. “On the discovery of the gluon”. In: *The European Physical Journal H* 35.1 (2010), pp. 3–28. DOI: `10.1140/epjh/e2010-00002-5`.

[153] J. Stark et al. “An ultralow-noise superconducting radio-frequency ion trap for frequency metrology with highly charged ions”. In: *arXiv preprint arXiv:2102.02793* (2021).

[154] R. Steinbrügge. “Bestimmung von absoluten Auger-und radiativen Zerfallsraten K-Schalen-angeregter hochgeladener Eisenionen”. PhD thesis. Ruprecht-Karls-Universität Heidelberg, 2015.

[155] R. Steinbrügge et al. “Absolute measurement of radiative and Auger rates of K- shell- vacancy states in highly charged Fe ions”. In: *Physical Review A* 91.3 (2015), p. 032502. DOI: `10.1103/PhysRevA.91.032502`.

[156] S. Stenholm. *Foundations of laser spectroscopy*. Courier Corporation, 2012.

[157] T. Takahashi et al. “The ASTRO-H (Hitomi) x-ray astronomy satellite”. In: *Space Telescopes and Instrumentation 2016: Ultraviolet to Gamma Ray*. Vol. 9905. International Society for Optics and Photonics. 2016, 99050U. DOI: 10.1117/12.2232379.

[158] M. Tashiro et al. “Status of x-ray imaging and spectroscopy mission (XRISM)”. In: *Space Telescopes and Instrumentation 2020: Ultraviolet to Gamma Ray*. Vol. 11444. International Society for Optics and Photonics. 2020, p. 1144422. DOI: 10.1117/12.2565812.

[159] XRISM Science Team. “Science with the X-ray Imaging and Spectroscopy Mission (XRISM)”. In: *arXiv preprint arXiv:2003.04962* (2020).

[160] F. Tyrén. “Die optischen L-spektren der Elemente Chrom bis Kobalt im extremen Ultraviolett”. In: *Zeitschrift für Physik* 111.5 (1938), pp. 314–317.

[161] L. Vályi. “Atom and ion sources”. In: (1977).

[162] J. Viefhaus et al. “The Variable Polarization XUV Beamline P04 at PETRA III: Optics, mechanics and their performance”. In: *Nuclear Instruments and Methods in Physics Research Section A: Accelerators, Spectrometers, Detectors and Associated Equipment* 710 (2013), pp. 151–154. DOI: 10.1016/j.nima.2012.10.110.

[163] Kai Wang et al. “Comment on “Theoretical Confirmation of the Low Experimental 3 C/3 D f-Value Ratio in Fe xvii””. In: *Physical review letters* 119.18 (2017), p. 189301. DOI: 10.1103/PhysRevLett.119.189301.

[164] M. Weisskopf et al. “Chandra X-ray Observatory (CXO): overview”. In: *X-Ray Optics, Instruments, and Missions III*. Vol. 4012. International Society for Optics and Photonics. 2000, pp. 2–16. DOI: 10.1117/12.391545.

[165] P. Willmott. *An introduction to synchrotron radiation: techniques and applications*. John Wiley & Sons, 2019. DOI: 10.1002/9781119970958.

[166] K. Wittenburg. *Beam instrumentation workshop*. 2008.

[167] C. Wu and X. Gao. “Change of the relative line strengths due to the resonance induced population transfer between Fe XVII and Fe XVI ions”. In: *Scientific reports* 9.1 (2019), pp. 1–9. DOI: 10.1038/s41598-019-43916-x.

[168] H. Xu et al. “High-resolution observations of the elliptical galaxy NGC 4636 with the reflection grating spectrometer on board XMM-Newton”. In: *The Astrophysical Journal* 579.2 (2002), p. 600. DOI: 10.1086/342828.

[169] H. L. Zhang and D. Sampson. “Relativistic distorted wave collision strengths for excitation to the 88 n= 3 and n= 4 levels in all 71 neon-like ions with 21 Z 93]”. In: *Atomic data and nuclear data tables* 43.1 (1989), pp. 1–69. DOI: 10.1016/0092-640X(89)90014-4.

[170] Hong Lin Zhang, Christopher J Fontes, and Connor P Ballance. "Comment on "Dirac R-matrix method for the calculation of x-ray line polarization"". In: *Physical Review A* 82.3 (2010), p. 036701. DOI: 10.1103/PhysRevA.79.062715.

[171] K. Zhukovsky. *Undulators for Short Pulse X-Ray Self-Amplified Spontaneous Emission-Free Electron Lasers*. IntechOpen, 2016. DOI: 10.5772/64439.

[172] *Zur Geschichte der Astronomie*. Viewed on 23.02.2021. URL: https://www.uibk.ac.at/historische-sternwarte/zur-geschichte-der-astronomie/.

Acknowledgements

Es ist geschafft! Auch wenn ich es nicht gedacht hätte, aber die Daten sind tatsächlich im Kasten, ausgewertet und die Arbeit geschrieben. Auch wenn auf der Titelseite nur ein Name steht, so ist dieses Projekt nur durch die Zusammenarbeit vieler erfolgreich gemeistert worden, denen ich auf den letzten Seiten dieser Abschlussarbeit danken möchte.

Lieber José, die abenteuerliche Reise vom Praktikanten zum Doktoranden begann vor 8 Jahren. Seitdem habe ich es sehr zu schätzen gelernt, Teil deiner Arbeitsgruppe zu sein. Deine unerlässliche Förderung junger Wissenschaftler im Rahmen von Messkampagnen, Tagungen und Konferenzen ist nicht selbstverständlich und setzt ein großes Vertrauen voraus. Besonders deine Hands-On Mentalität, die du eins zu eins an deine Studenten und Studentinnen überträgst, weiß ich sehr zu schätzen und wird mich weiterhin auf meinen Wegen begleiten.

Prof. André Butz möchte ich dafür danken, dass er sich bereit erklärt hat, sich auf diese Arbeit außerhalb seines Fachbereichs der Umweltphysik als Zweitgutachter einzulassen.

Liebe EBITTERS, ihr seid der Hauptgrund, warum ich jeden Tag gerne aufgestanden und ins Institut gefahren bin. Ob gemeinsame Essen in der Kantine, Kaffeetisch mit fragwürdigen Gesprächsthemen, fachliche Gespräche, der tägliche Schabernack oder Stammtische im Schnookeloch. Langweilig wurde es nie mit euch!

Annegret, Bernhard, Frank, Jan, Jörg, Steffi, Stephan, Marion und Walle, euch möchte ich für unsere wöchentlichen Sitzungen danken, die mich einiges über den Ablauf und die Strukturen eines Instituts gelehrt haben, ohne dabei den Spaß aus den Augen zu verlieren.

Dem PolarX-Strahlzeit Team danke ich für das unermüdliche Helfen beim Vorbereiten der Strahlzeiten, beim Transport und Aufbau des Experimentes und bei der eigentlichen Durchführung der Experimente. Die Tatsache, dass man selbst nach 14 Tagen zusammen in einem Hutch ohne jeglichen privaten Ausgleich sich nicht komplett die Köpfe einschlägt zeugt davon, dass ihr mehr als nur Kollegen seid.

Sonja danke ich besonders für all das Wissen, das ich seit Bachelor- und Masterarbeit aber auch während der Doktorarbeit durch ihre Betreuung erhalten habe.

Allen Korrekturlesenden, Peter, Stepan, Sonja, Michael, Chintan und Maurice gilt mein Dank.

Daniela und Urs danke ich für die Beherbergung und mentale Unterstützung in der kritischen Schreibphase dieser Arbeit auf ihrer Finca.

Meinen Eltern Stephanie und Bertram sowie meinem Bruder Christoph gilt ebenfalls der höchste Dank, die zu jeder Zeit an mich geglaubt haben, mich in jeglicher Weise unterstützt haben und mir den Rücken freihielten.

Zu guter Letzt danke ich noch der wichtigsten Person in meinem Leben. Flurina, egal in welchen Zeiten, du warst immer für mich da und hast mich bedingungslos unterstützt! Dafür danke ich dir zu tiefst. Ich weiß nicht, ob ich es ohne dich geschafft hätte. Ich freue mich auf die gemeinsamen Abenteuer, die wir noch zusammen erleben werden.